

# **Liquid Oxygen Droplet Combustion in Hydrogen under Microgravity Conditions**

Verbrennung von flüssigen Sauerstofftropfen in  
Wasserstoff unter Mikrogravitationsbedingungen

Dissertation for receiving the degree of “Doktor der  
Ingenieurwissenschaften (Dr.-Ing.)” approved by the Department of  
Production Engineering of the University of Bremen

by

**M.Sc. Florian Meyer**

## **Reviewers:**

Prof. Dr. Marc Avila (University of Bremen, Germany)

Prof. Dr. Hiroshi Nomura (Nihon University, Japan)

## **Day of oral examination:**

December 2<sup>nd</sup>, 2022

**Florian Meyer**

# **Liquid Oxygen Droplet Combustion in Hydrogen under Microgravity Conditions**

## Acknowledgments

First, I would like to thank my mentor Christian Eigenbrod for encouraging me and giving me the chance to do this research project. Thank you very much for the motivation, the valuable discussion, and the tireless support during the last years. Your scientific as well as engineering experience and your enthusiasm for both have helped me a lot and serve as a role model for me. I would also like to thank my supervisor Marc Avila, who has supported and motivated me enormously over the last few years. Thank you for the fruitful discussions, your persistence, and sharing your expertise. In addition, I would like to express my sincere gratitude to Hiroshi Nomura as the second examiner for his efforts and engagement. I also want to thank Michael Dreyer for his review of this thesis and the valuable discussion. Thank you for taking the time and sharing your knowledge.

This research has been funded by the German Federal Ministry for Economic Affairs and Climate Action through the German Space Agency (DLR) in the framework of “HYDRA” and “HYDRA-II” (grants: 50 WM 1645 and 50 WM 2065). I thank the whole HYDRA team for the friendly and great cooperation during the last years as well as for the dedicated discussion during joint publications. Many thanks to Jim Hermanson, Volker Wagner, Wolfgang Paa, and Shion Ando, I learned a lot from you. In addition, I would like to thank the team at DLR in particular Thomas Driebe, Karin Kiewisch, Alexander Kreplin, Rainer Forke, and Wolfgang Dreier for supporting this research and for the always friendly and constructive cooperation. The collaboration between the University of Bremen and the University of Washington was supported by the US Fulbright Scholars Program. This program enabled several research periods of the project partner Jim Hermanson at ZARM, which also benefited this thesis in the context of scientific exchange.

I would also like to thank my colleagues at ZARM, in particular Günther Marks, who developed the initial design of the cryogenic combustion chamber, Michael Peters, Andrea Fischer, Peter Prengel, Holger Faust, Ronald Mairose, Frank Ciecior, Martin Castillo, Jakob Hauschildt as well as the entire workshop team and the entire team of ZARM FAB for their irreplaceable help, productive discussions, and friendly support. I want to thank Nick Kleemann and Sepehr Ariaei for their work on the project as well as Roswitha Krebs-Goldbecker from the university's glass workshop for the laborious process of making the suspender blanks.

Finally, a special thanks goes to my fiancée Alina, to my family, and to my friends, all of whom have always been supportive and understanding. Thank you all!



## Publications

### Journal Papers (Peer Review):

- F. Meyer, C. Eigenbrod, V. Wagner, W. Paa, J. C. Hermanson, S. Ando, M. Avila, Oxygen droplet combustion in hydrogen under microgravity conditions, *Combustion and Flame* 241, 112081 (2022).
- F. Meyer, C. Eigenbrod, V. Wagner, W. Paa, J. C. Hermanson, Apparatus to investigate liquid oxygen droplet combustion in hydrogen under microgravity conditions, *Review of Scientific Instruments* 91, 105110 (2020).

### International Conferences – Papers:

- F. Meyer, C. Eigenbrod, V. Wagner, W. Paa, J. D. Hall, M. Zody, J. Frydman, J. C. Hermanson, Combustion of Single Oxygen Droplets in Hydrogen under Microgravity Conditions, AIAA SciTech 2021 Forum, AIAA 2021-0548 (2021).
- F. Meyer, C. Eigenbrod, V. Wagner, W. Paa, J. D. Hall, M. Zody, J. Frydman, J. C. Hermanson, Combustion of Single Liquid Oxygen Droplet in Hydrogen under Microgravity Conditions, The 31st International Symposium on Transport Phenomena, Honolulu, USA, Virtual Event (2020).
- F. Meyer, C. Eigenbrod, J. C. Hermanson, J. Frydman, W. Paa, V. Wagner, Microgravity Experiments and Numerical Simulations on the Combustion of Single Oxygen Droplets in Hydrogen, 69th International Astronautical Congress (IAC), IAC-18-A2.2.7 (2018).

### International Conferences – Presentations:

- F. Meyer, C. Eigenbrod, W. Paa, J. C. Hermanson, S. Ando, M. Avila, Single Droplet Combustion of Liquid Oxygen in Hydrogen under Microgravity Conditions, 44th COSPAR Scientific Assembly, Presentation, Athens, Greece, 2022.
- F. Meyer, C. Eigenbrod, V. Wagner, W. Paa, J.D. Hall, M. Zody, J. Frydman, J.C. Hermanson, Liquid Oxygen Droplet Combustion in Hydrogen under Microgravity Conditions, 72nd Annual Meeting of the APS DFD, Presentation, Seattle, USA, 2019.
- J.D. Hall, M. Zody, J. Frydman, J.C. Hermanson, F. Meyer, C. Eigenbrod, V. Wagner, W. Paa, Numerical Simulation of Liquid Oxygen Droplet Combustion in Hydrogen, 72nd Annual Meeting of the APS DFD, Presentation, Seattle, USA, 2019.
- F. Meyer, C. Eigenbrod, V. Wagner, W. Paa, J.D. Hall, M. Zody, J. Frydman, J.C. Hermanson, Liquid Oxygen Droplet Combustion in Hydrogen under Microgravity Conditions, 35th Annual Meeting of the ASGSR, Presentation, Denver, USA, 2019.

- 
- J.D. Hall, M. Zody, J. Frydman, J.C. Hermanson, F. Meyer, C. Eigenbrod, V. Wagner, W. Paa, Numerical Simulation of Liquid Oxygen Droplet Combustion in Hydrogen in Microgravity, 35th Annual Meeting of the ASGSR, Presentation, Denver, USA, 2019.
  - F. Meyer, C. Eigenbrod, J. Frydman, J.C. Hermanson, V. Wagner, W. Paa, Combustion of Single Oxygen Droplets in Hydrogen at Sub- and Supercritical Conditions, 37th International Symposium on Combustion, Work in Progress Poster, Dublin, Ireland, 2018.

## Abstract

The combustion of hydrogen and oxygen is important in the field of liquid rocket propulsion and in the near future also in aeronautical and automotive propulsion as well. In a rocket engine, a spray combustion process with gaseous hydrogen and liquid oxygen is formed as a result of the vaporization of the liquid hydrogen before it enters the combustion chamber. To optimize engine performance by improving combustion efficiency and aiming for smaller combustion chambers as well as to avoid combustion instabilities, a fundamental understanding of the vaporization and combustion processes at relevant ambient pressures is necessary.

In order to study these fundamental processes focusing on the most central element of the technical spray combustion process, the single droplet, an experimental apparatus was developed which allows the combustion of single liquid oxygen droplets in a hydrogen atmosphere. It is shown that the dimensions of a single droplet in a technical spray ( $\text{\O}5\text{-}150\ \mu\text{m}$ ) can be scaled up in reduced gravity conditions. The experimental setup was integrated into a drop capsule to perform experiments under microgravity conditions at the drop tower in Bremen to allow for the application of sophisticated diagnostics on large stationary and mostly spherical droplets. The main component of the setup is the cryogenic combustion chamber, which is surrounded by a liquid nitrogen jacket. The temperature of 77 K allowed gaseous oxygen to condense and to generate a liquid oxygen droplet at the tip of a quartz suspender. The droplet with a diameter of about 0.7 mm was ignited by a laser-induced plasma breakdown at different ambient pressures in the sub- and supercritical regime (0.1 to 5.7 MPa), and the combustion during the free-fall phase was investigated by shadowgraph imaging and  $OH^*$  chemiluminescence diagnostics (hydroxyl radical).

Despite a wide flammability range of the hydrogen/oxygen system, the ignition had to take place very close to the droplet surface due to the high diffusion rate of hydrogen. As a consequence of the ignition, the burning droplet detached from the suspender in all experiments and burned free-floating next to the suspender. This was initially seen as a problem but the detachment meant that the droplet was no longer affected by the suspender. At low pressures ( $< 0.8\ \text{MPa}$ ), it was observed that the shape of the droplet changed significantly during combustion, which is attributed to the formation of a (water) ice crust in close vicinity to the droplet surface. In a parametric study, it was found that the burning rate in the subcritical regime increases significantly with increasing pressure, whereas the flame standoff ratio decreases only slightly. In the supercritical regime, the measured data indicate a slight decrease in the burning rate. However, due to the vanishing of the surface tension, no defined detachment of the droplet from the suspender occurred, so that the subcritical experiments are not directly comparable with the experiments under supercritical conditions. An alternative evaluation method indicates a continuous increase of the burning rate in the transition to the supercritical regime.

So far, only numerical simulations on single liquid oxygen droplet combustion have been performed and reported in the literature. By means of the developed experimental

apparatus it has become possible to provide a first experimental database (exploiting microgravity conditions). These data provide key combustion research parameters, such as the flame standoff ratio or the burning rate constant, which can be used for validation and future development of numerical models. These fundamental models form the basis for advanced simulations that also include the interactions in a spray and can lead to an improvement in the volumetric heat release and thus of the efficiency of an engine.

## Kurzfassung

Die Verbrennung von Wasserstoff und Sauerstoff ist insbesondere für kryogenen Raketentriebwerke wichtig, spielt aber auch in naher Zukunft Flugzeuge und Fahrzeuge eine wichtige Rolle. Im einem Raketentriebwerk bildet sich durch das Verdampfen des flüssigen Wasserstoffs vor dem Eintritt in die Brennkammer ein Sprayverbrennungsprozess mit gasförmigem Wasserstoff und flüssigem Sauerstoff. Um die Leistung eines Triebwerks durch Verbesserung der Verbrennungseffizienz und Verkleinerung der Brennkammer zu optimieren und um Verbrennungsinstabilitäten zu vermeiden, ist ein grundlegendes Verständnis der Verdampfungs- und Verbrennungsprozesse bei relevanten Umgebungsdrücken nötig.

Zur Untersuchung dieser grundlegenden Prozesse anhand des zentralsten Elementes des technischen Sprayverbrennungsprozesses, dem Einzeltropfen, wurde ein Experimentaufbau entworfen, der die Verbrennung von einzelnen flüssigen Sauerstofftropfen in einer Wasserstoffatmosphäre ermöglicht. Es wird gezeigt, dass sich die Dimensionen eines Einzeltropfens in einem technischen Spray ( $\text{Ø}5\text{-}150\ \mu\text{m}$ ) unter reduzierter Schwerkraft hochskalieren lassen. Der experimentelle Aufbau wurde in eine Fallkapsel integriert, um Experimente unter Mikrogravitation am Fallturm in Bremen durchzuführen, welche die Anwendung geeigneter Diagnostik an großen stationären und meist kugelförmigen Tropfen ermöglichen. Die Hauptkomponente des Aufbaues ist die kryogene Brennkammer, die von einem flüssigen Stickstoffmantel umgeben ist. Die Temperatur von 77 K ermöglichte es, gasförmigen Sauerstoff zu kondensieren und einen flüssigen Sauerstofftropfen an einem Quarz-Suspender zu erzeugen. Der Tropfen mit einem Durchmesser von zirka 0.7 mm wurde bei verschiedenen Umgebungsdrücken im unter- und im überkritischen Bereich (0.1 bis 5.7 MPa) durch einen laserinduzierten Plasmadurchbruch gezündet und die Verbrennung während des freien Falles mit einer Shadowgraphie und einer  $\text{OH}^*$ -Chemilumineszenz-Diagnostik (Hydroxyl-Radikal) untersucht.

Trotz der weiten Zündgrenzen des Wasserstoff-Sauerstoff-Systems musste die Zündung aufgrund der hohen Diffusionsgeschwindigkeit des Wasserstoffs sehr nahe an der Tropfenoberfläche erfolgen. Dies hatte zur Folge, dass sich der brennende Tropfen bei allen Experimenten nach der Zündung vom Suspender ablöste und freischwebend neben dem Suspender verbrannte. Dies wurde zunächst als Problem angesehen, aber die Ablösung bewirkte, dass der Tropfen nicht mehr vom Suspender beeinflusst wurde. Es wurde beobachtet, dass sich die Form des Tropfens während der Verbrennung bei niedrigen Drücken ( $< 0.8\ \text{MPa}$ ) signifikant änderte, was auf die Bildung von einer (Wasser-)Eiskruste in unmittelbarer Nähe zur Tropfenoberfläche zurückzuführen ist. In einer parametrischen Studie wurde festgestellt, dass die Brennrate im unterkritischen Bereich mit steigendem Druck deutlich ansteigt, wohingegen das Flammenabstandsverhältnis leicht abnimmt. Im überkritischen Bereich weisen die Messdaten auf eine leichte Abnahme der Brennrate hin. Jedoch erfolgte durch das Verschwinden der Oberflächenspannung keine definierte Ablösung des Tropfens vom Suspender, sodass die unterkritischen Experimente nicht direkt mit den Experimenten

unter überkritischen Bedingungen vergleichbar sind. Eine alternative Auswertemethode weist auf einen kontinuierlichen Anstieg der Brennrate im Übergang zum überkritischen Bereich hin.

Bislang wurden ausschließlich numerische Simulationen zur Verbrennung einzelner flüssiger Sauerstofftropfen durchgeführt und in der Literatur veröffentlicht. Mit Hilfe der entwickelten Versuchsanordnung ist es möglich geworden, eine erste experimentelle Datenbasis bereitzustellen (unter Ausnutzung der Mikrogravitationsbedingungen). Diese Daten liefern wichtige Kenngrößen für die Verbrennungsforschung, wie z.B. das Flammenabstandsverhältnis oder die Brennrate, die für die Validierung und zukünftige Entwicklung numerischer Modelle verwendet werden können. Diese grundlegenden Modelle bilden die Basis für weiterführende Simulationen, die auch die Wechselwirkungen in einem Spray einbeziehen und zu einer Verbesserung der volumetrischen Wärmefreisetzung und damit der Effizienz eines Triebwerks führen können.

# Contents

<b>Acknowledgments</b> .....	<b>ii</b>
<b>Publications</b> .....	<b>iii</b>
<b>Abstract</b> .....	<b>v</b>
<b>Kurzfassung</b> .....	<b>vii</b>
<b>Nomenclature</b> .....	<b>xii</b>
<b>1. Introduction</b> .....	<b>1</b>
1.1. Motivation .....	1
1.2. Thesis scope.....	4
1.3. Outline .....	4
<b>2. Fundamentals</b> .....	<b>6</b>
2.1. Heat and mass transfer mechanisms .....	6
2.1.1. Molecular transport mechanisms.....	6
2.1.2. Convective transport mechanisms.....	8
2.1.3. Radiation.....	9
2.2. Supercritical fluids and mixing .....	10
2.3. Droplet vaporization .....	13
2.3.1. Mass and heat transport processes in droplet vaporization .....	14
2.4. Combustion.....	17
2.4.1. Classification .....	18
2.5. Droplet combustion .....	19
2.5.1. Mass and heat transport processes in droplet combustion.....	20
2.5.2. $d^2$ -law.....	22
2.6. Microgravity approach .....	26
2.6.1. Grashof number .....	26
2.6.2. Fourier number .....	27
2.6.3. Reynolds number.....	28
2.7. Optical diagnostics .....	29
2.7.1. Shadowgraph imaging .....	30
2.7.2. $OH^*$ chemiluminescence.....	31

---

2.7.3.	Background oriented Schlieren .....	32
<b>3.</b>	<b>State of the art.....</b>	<b>34</b>
3.1.	Droplet vaporization .....	34
3.1.1.	Experimental studies .....	34
3.1.2.	Numerical studies .....	38
3.2.	Droplet combustion .....	42
3.2.1.	Experimental studies .....	42
3.2.2.	Numerical studies .....	47
3.2.3.	Water condensation .....	52
3.3.	Summary and contrast of the reviewed studies .....	54
3.4.	Droplet generation and suspension techniques.....	55
3.5.	Droplet ignition techniques .....	58
3.6.	Combustion diagnostics.....	60
3.6.1.	Density-based diagnostics .....	61
3.6.2.	Emission spectroscopy .....	62
3.6.3.	Absorption spectroscopy .....	63
3.6.4.	Laser-based diagnostics.....	63
3.6.5.	Other diagnostic techniques .....	64
<b>4.</b>	<b>Experimental setup.....</b>	<b>66</b>
4.1.	Cryogenic combustion chamber .....	66
4.2.	Droplet generation and suspension.....	73
4.3.	Droplet ignition .....	82
4.4.	Drop tower capsule.....	88
<b>5.</b>	<b>Measurement techniques .....</b>	<b>95</b>
5.1.	Shadowgraph imaging .....	96
5.2.	$OH^*$ chemiluminescence.....	100
5.3.	Pressure measurement .....	103
<b>6.</b>	<b>Results and discussion.....</b>	<b>107</b>
6.1.	Ignition process .....	107
6.2.	Suspender effect .....	111
6.3.	Combustion process.....	119

---

6.4.	Droplet regression .....	127
6.5.	Flame position .....	130
6.6.	Supercritical combustion effects .....	135
6.7.	Pressure effects .....	139
6.7.1.	Reproducibility .....	139
6.7.2.	Burning rate constant.....	141
6.7.3.	Flame standoff ratio.....	148
<b>7.</b>	<b>Conclusions .....</b>	<b>152</b>
7.1.	Summary of the experimental results .....	152
7.2.	Progress and future work.....	153
	<b>References .....</b>	<b>156</b>
	<b>List of figures .....</b>	<b>169</b>
	<b>List of tables .....</b>	<b>181</b>
	<b>Student work.....</b>	<b>182</b>
	<b>Appendices .....</b>	<b>183</b>

# Nomenclature

## Chemical Symbols

H	Hydrogen
H <sub>2</sub> O	Water
He	Helium
M	Non-reacting element for balancing
N	Nitrogen
O	Oxygen
OH	Hydroxyl
OH*	Excited hydroxyl

## Latin Characters

<i>a</i>	Area
<i>A</i>	Pre-exponential factor
<i>B<sub>c</sub></i>	Spalding transfer number for combustion
<i>B<sub>v</sub></i>	Spalding transfer number for vaporization
<i>c</i>	Speed of sound
<i>c<sub>p</sub></i>	Specific heat capacity at constant pressure
<i>d</i>	Droplet diameter
<i>d<sub>0</sub></i>	Initial droplet diameter
<i>d<sub>f</sub></i>	Suspender fiber diameter
<i>D<sub>AB</sub></i>	Binary diffusion coefficient
<i>Da</i>	Damköhler number
<i>D<sub>m</sub></i>	Mass diffusion coefficient
<i>E</i>	Activation energy
<i>f</i>	Flame diameter
<i>F</i>	Focal length
<i>Fo</i>	Fourier number
<i>g</i>	Gravitational acceleration
<i>Gr</i>	Grashof number
<i>i</i>	Reaction order
<i>I</i>	Light intensity
$\vec{j}$	Diffusion flux
<i>Ja</i>	Jakob number
<i>k</i>	Rate constant
<i>k<sub>c</sub></i>	Burning rate constant (based on the combustion lifetime)
<i>k<sub>g</sub></i>	Gasification rate constant (based on the droplet lifetime)
<i>k<sub>ideal</sub></i>	Rate constant at ideal (spherical) conditions
<i>k<sub>v</sub></i>	Vaporization rate constant
<i>K</i>	Reaction rate constant

$K''$	Pseudo first-order reaction rate
$K_B$	Boltzmann constant
$K_{GD}$	Gladstone-Dale constant
$K_{SB}$	Stefan-Boltzmann constant
$l$	Distance
$l_{BG}$	Distance between background and object
$l_{d,l}$	Longest droplet dimension line
$l_{d,s}$	Shortest droplet dimension line
$l_L$	Distance between lens and object
Le	Lewis number
$\dot{m}$	Mass flow rate
$m$	Total mass
$M$	Molecular mass
$n$	Refractive index
$n_0$	Reference refractive index
$N$	Number of moles per unit volume
$p$	Pressure
$P$	Power
$p_c$	Critical pressure
$p_{O_2}$	Partial pressure of oxygen
$p_r$	Reduced pressure
$p_{r,vap}$	Reduced vapor pressure
$p_{vap}$	(Saturation) vapor pressure
$\vec{q}$	Heat flux
$q_c$	Specific enthalpy of condensation
$q_g$	Specific gasification energy
$q_r$	Specific enthalpy of chemical reaction
$q_t$	Specific enthalpy to bring the surface to the temperature of vaporization
$q_v$	Specific enthalpy of vaporization
$r$	Radius
$r_d$	Droplet radius
$r_f$	Flame radius
$R$	Universal gas constant
$R_d$	Droplet shape ratio
$R_s$	Specific gas constant
Re	Reynolds number
$S$	Net rate of various sources
$t$	Time
$t_1$	Time of droplet disappearance
$T$	Temperature
$T_b$	Boiling temperature
$T_c$	Critical temperature

$T_f$	Adiabatic flame temperature
$T_r$	Reduced temperature
$T_s$	Surface temperature
$T_\infty$	Ambient temperature
$v$	Velocity
$\vec{v}_{diff}$	Diffusion velocity
$x, y, z$	Spatial dimensions
$v_{rel}$	Relative velocity
$X$	Mole fraction
$Y$	Mass fraction

### Greek Characters

$\alpha$	Thermal diffusivity
$\gamma$	Isentropic expansion factor
$\varepsilon$	Refraction angle
$E$	Emissivity
$\epsilon$	Characteristic energy (Lennard-Jones potential)
$\zeta_1$	Entrance coordinates
$\zeta_2$	Exit coordinates
$\theta$	Contact angle
$\Lambda$	Absorption coefficient
$\kappa$	Thermal conductivity
$\nu$	Kinematic viscosity
$\rho$	Density
$\rho_\infty$	Ambient density
$\sigma$	Fuel-to-oxidizer ratio
$\phi$	Equivalence ratio
$\tau$	Total time
$\tau_c$	Total time for combustion (combustion lifetime)
$\tau_g$	Total time for gasification (droplet lifetime)
$\tau_s$	Total time for single-phase combustion (single-phase combustion lifetime)
$\tau_v$	Total time for vaporization (droplet lifetime)
$\Psi$	Collision diameter (Lennard-Jones potential)
$\Omega_D$	Collision integral for diffusion

### Abbreviations

1D	One-dimensional
1g	Normal gravity
2D	Two-dimensional
3D	Three-dimensional

---

$\mu\text{g}$	Microgravity
BOS	Background oriented Schlieren
CAD	Computer aided design
CMOS	Complementary metal-oxide semiconductor
CSS	Capsule control system
DAQ	Data acquisition system
FEM	Finite element method
fps	Frames per second
FSP	Flame spray pyrolysis
GUI	Graphical user interface
IPHT	Leibniz Institute of Photonic Technology
IR	Infrared
ISS	International Space Station
LabVIEW	Laboratory Virtual Instrument Engineering Workbench
LED	Light-emitting diode
LH <sub>2</sub>	Liquid hydrogen
LIF	Laser-induced fluorescence
LII	Laser-induced incandescence
LN <sub>2</sub>	Liquid hydrogen
LOX	Liquid oxygen
Nd:YAG	Neodymium-doped yttrium aluminum garnet
NUC	Next Unit of Computing
OpenFOAM	Open Source Field Operation and Manipulation
PCTFE	Polychlorotrifluoroethylene
PEEK	Polyether ether ketone
PET	Polyethylene terephthalate
PIV	Particle image velocimetry
PLIF	Planar laser-induced fluorescence
PTFE	Polytetrafluoroethylene
px	Pixel
PXI	Peripheral Component Interconnect eXtensions for Instrumentation
TFP	Thin filament pyrometry
TTL	Transistor-transistor logic
USB	Universal Serial Bus
UV	Ultraviolet
Yb:YAG	Ytterbium-doped yttrium aluminum garnet
ZARM	Center of Applied Space Technology and Microgravity

# 1. Introduction

## 1.1. Motivation

Combustion is an essential component of human mobility. Internal combustion engines in automobiles as well as aircraft and rocket engines are based on the conversion of combustion energy (heat) into mechanical energy. The same holds for the generation of electric power in stationary gas-turbines where the thermal expansion is converted into the generator driving torque. Since the early 1970s, there has been extensive development for more efficient and cleaner-burning internal combustion engines based on fundamental research on hydrocarbon fuel systems [1]. On the way towards a carbon-free mobility, alternative propulsion technologies and fuel systems are currently being developed. In addition to its use with a fuel cell, the combustion of hydrogen ( $H_2$ ) is a topic of current research for the aeronautical industry [2] or for the automotive industry as a gap technology for long-distance and commercial vehicles [3], since neither carbon dioxide nor carbon monoxide is emitted. For rocket propulsion systems, however, another characteristic is crucial. Hydrogen can be used to achieve a very high specific impulse, which is the ratio of the thrust produced to the mass flow rate of the propellants (unit: m/s) [4]. To compare different propulsion systems, the specific impulse is often given in seconds as the ratio of thrust produced to the weight flow rate (based on the Earth's gravitational acceleration).

In general, four categories are identified with respect to high-thrust rocket motors: solid-propellant motors, liquid-propellant engines, gaseous-propellant engines, and hybrid-propellant engines (propellants are stored in at least two of the three physical states of matter) [4]. The highest specific impulse combined with relatively high thrust can be achieved by liquid propulsion systems (for high-thrust rocket motors). A liquid-propellant rocket engine essentially consists of a feed system for the propellants, such as turbopumps, and the thrust chamber assembly, which in turn consists of an injector, a combustion chamber, and a thrust nozzle [4]. The fuel and the oxidizer are fed into the combustion chamber through the injector. Usually, the (cryogenic) fuel is in gaseous state, as it is used to cool the nozzle and the combustion chamber walls, causing it to vaporize. The oxidizer, on the other hand, is injected into the combustion chamber in liquid state. The combination of liquid hydrogen ( $LH_2$ ) and liquid oxygen (LOX) exhibits a very high specific impulse and is often used as a propellant combination, such as for Aerojet Rocketdyne's RS-25 engines, which were used for the Space Shuttle and will be used for the Space Launch System. This engine achieves a specific impulse of 451 s (4424 m/s) in vacuum [4]. Another example is Ariane Group's HM7B engine, which is used as the upper stage on the Ariane 5 rocket and has a specific impulse of 446 s (4375 m/s) in vacuum [5]. For comparison, Energomash's RD-180 engine serves as the first stage of the Atlas V rocket and is powered by LOX and kerosene. This engine has a specific impulse of 338 s (3316 m/s) in vacuum, which is significantly less than hydrogen-fueled engines [6]. The main reasons for the high specific impulse of  $LH_2$ -LOX systems include the low molar mass of hydrogen and the high combustion temperature. In addition, the specific impulse also depends on the combustion efficiency in the

combustion chamber, the expansion of the exhaust gases in the nozzle, and other design factors [4, 7]. However, the low density of hydrogen is also a disadvantage, because on the one hand it limits the thrust of the engine and on the other hand it requires large tank volumes, which increases the structural mass of the rocket. An alternative to hydrogen is methane, which has a higher density, a higher boiling temperature, and reduced handling and safety constraints [8] as well as the possibility of in-situ methane production on Mars [7]. The disadvantage of methane, however, is a lower performance compared to hydrogen. Rockets with a hydrocarbon fuel in the first stage and LH<sub>2</sub> in the upper stage can therefore combine the advantages of both fuels [9].

In the development of new liquid rocket engines, efforts are being made to improve burnout efficiency, since combustion in the divergent part of the nozzle reduces thrust and thus overall efficiency. Furthermore, better mixture formation can contribute to smaller and lighter combustion chambers, which increases the payload. With respect to the LH<sub>2</sub>-LOX main engine of Ariane, it is estimated that every second of specific impulse adds about 100 kg of payload [8]. To increase thrust, high combustion chamber pressures are used, which are often above the thermodynamical critical points of the reaction fluids [10]. A higher combustion chamber pressure leads to an increase in the expansion rate in the nozzle and ultimately to an increase in thrust and thus also in the specific impulse [7]. At the same time, the demands on the turbopump and the cooling performance of the combustion chamber (or on the temperature resistance of the materials) also increase, which in turn limits efficiency [4]. The oxidizer (LOX) is injected at subcritical temperatures, however, the fluid can heat up very quickly and experience a transcritical state transition to the supercritical regime [10]. Beyond the critical point, the thermodynamic properties of the fluid change drastically due to the absence of a phase change [11]. During injection into the combustion chamber, numerous small ligaments, lumps, and droplets are formed [12]. The atomization increases the heat and mass exchange between the liquid and the surrounding gas and leads to an increase of the overall vaporization rate [1].

The design and development process of liquid rocket engines today is still characterized by an expensive experimental trial-and-error approach to determine the stability limits of the system. Crucial to the design is the predictive determination of the occurrence of combustion instabilities that limit the engine's operating conditions. These instabilities occur due to the strong coupling between the fluid, the volumetric heat release, and the acoustic modes of the combustion chamber [11]. The volumetric heat release can vary depending on the instantaneous and local degree of premixing of the combustion. The associated fluctuations in thermal expansion are both driving and amplifying forces of the resonant instabilities.

Optimizing rocket engines requires a detailed understanding of the spray combustion, which is characterized by the multiple superposition and non-linearly coupled interactions of individual sub-processes, including liquid jet disruption, atomization, droplet formation, vaporization, ignition, and combustion. The spray combustion for LOX and hydrogen is shown schematically in Figure 1.

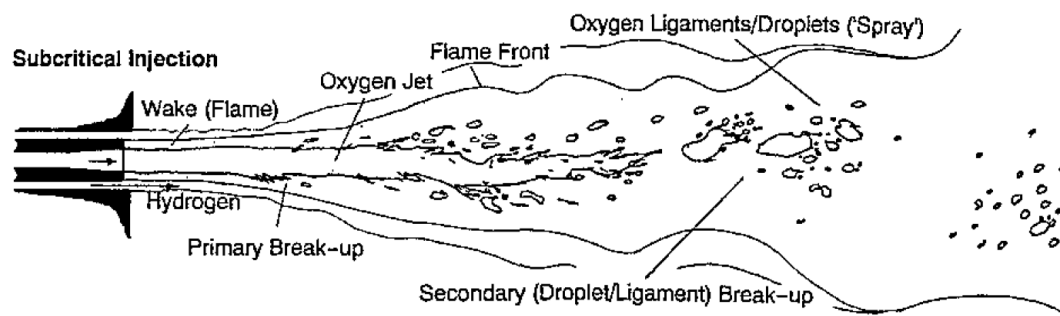


**Figure 1:** Schematic of the subcritical injection process. Reprinted from [12] with permission from the American Institute of Aeronautics and Astronautics (AIAA).

Here, detailed knowledge of mixture formation and combustion is at a much lower level than in internal engine combustion or in gas turbines, and so the technical development status of injectors has also remained almost unchanged for decades. Because of the complexity of these sub-processes, even the latest numerical simulations on modern supercomputers are not able to reproduce spray combustion in full detail [13]. Therefore, simplified models are usually employed to describe combustion in rocket engines, e.g., [11, 13-17]. Such numerical models are currently used only as complementary verification in the design process of rocket engines [11]. In order to improve the accuracy of numerical models, it is necessary to represent the aforementioned sub-processes as simply and accurately as possible. Thus, to better understand the complex spray combustion, it is essential to first understand how a single droplet, as the most basic element of a spray, interacts with its gaseous environment and how it exchanges heat, mass, and momentum [1, 18]. The single droplet case is the most basic configuration to study vaporization and combustion, as well as the position of the flame and the influence of water as combustion product of hydrogen and oxygen. To date, there is no experimental database on the combustion of a single oxygen droplet in a hydrogen atmosphere. Fundamental investigations of single droplets can be used to validate and develop (numerical) models, which in turn can be used for improved spray combustion models. This approach has been used over decades to improve internal combustion engines (based on the study of single hydrocarbon droplets) [1].

To study the combustion of single droplets, quiescent microgravity conditions offer possibilities to simplify the problem. For example, free (natural) and forced convection are suppressed with mainly diffusion as the remaining mass transport mechanism, since the residual accelerations in the Bremen drop tower are in the order of  $10^{-6}$  g. As a consequence, single droplets and their corresponding flames are spherical and can be accurately modeled with a single spatial dimension (the radius). At the same time, microgravity conditions allow for comparatively large and long-lived droplets (millimeter length scale), which enables the application of sophisticated diagnostics. The first systematic droplet combustion experiments under microgravity conditions were performed by Kumagai & Isoda [19] back in 1957. Considerable progress has been made since their pioneering work and microgravity has been repeatedly shown to be an

appropriate and powerful tool to understand the influence of diffusion and convection in combustion processes. Examples include the demonstration that large droplets undergo self-extinction and then continue to burn in the cool-flame regime [20], or studies on the interaction between neighboring droplets during ignition [21, 22] and combustion [23], or the flame spread between large droplet clouds [24, 25].

## 1.2. Thesis scope

The aim of this thesis is to investigate the combustion of a LOX droplet in a hydrogen atmosphere at different ambient pressures under microgravity conditions to gain a basic understanding of the combustion process of a LH<sub>2</sub>-LOX rocket engine. By determining combustion parameters, such as the burning rate or the flame standoff ratio, an initial database is created that can be used to validate numerical models. These parameters can also be used to compare the LOX-H<sub>2</sub> system with other fuel systems. In addition, the analysis of the combustion experiments serves to identify combustion phenomena and to assess their significance on the overall process. By varying the ambient pressure, the effects in both the subcritical and supercritical regimes are investigated to evaluate possible efficiency improvements. These data are important to increase the accuracy and validity of future numerical models.

Since no experiments on LOX single droplet combustion have been reported in the literature, the main aim of this thesis is to design a new apparatus and apply new methods to conduct LOX combustion experiments under microgravity conditions in the Bremen drop tower. By using suitable optical diagnostic techniques, the required combustion parameters are to be determined at high temporal resolution.

## 1.3. Outline

Chapter 2 of this thesis is devoted to the theoretical background, specifically, thermodynamic and fluid mechanic concepts necessary to describe the problem of droplet combustion are introduced. Based on this, the case of droplet vaporization is considered, before the fundamentals of combustion are explained. Subsequently, the case of droplet combustion is considered in detail. The similarity of droplets with technical dimensions ( $\mu\text{m}$  length scale) to large droplets under microgravity (mm length scale) is shown using dimensionless numbers. Then, the basics of the optical diagnostics used in this thesis are outlined. In chapter 3, a discussion of the state of the art is provided, which includes advances in the fields of experimental and numerical droplet vaporization and combustion, as well as droplet generation, suspension, and ignition techniques. This part is concluded with a discussion of advances in combustion diagnostics. Chapters 4 and 5 contain a description of the experimental setup and the measurement techniques. The development of the combustion chamber as well as of the droplet generation and suspension method are explained in detail. The droplet ignition, which was developed together with the Leibniz Institute of Photonic Technology (IPHT), as well as the overall setup of the drop capsule, are described. Shadowgraph imaging and  $OH^*$  chemiluminescence (hydroxyl radical) were used to measure the droplet diameter and the flame zone, respectively. The integration of these techniques as well as pressure

---

measurement into the experimental setup is presented. In chapter 6, the results of the drop tower experiments are shown and discussed. The combustion process at a pressure of 0.1 MPa is highlighted in detail before the effects of ambient pressure on droplet regression and flame position, as well as on the overall combustion process, are discussed. Special attention is also given to the supercritical droplet combustion before the conclusions of the thesis are drawn in chapter 7.

## 2. Fundamentals

Combustion research is divided into many different areas and involves various disciplines, such as thermodynamics, fluid mechanics, materials science, chemical kinetics, transport phenomena, diagnostics, and numerical analysis. The field of droplet combustion represents only a small section of decades of research on combustion. In chapter 2.1, the dominant mass and heat transport mechanisms relevant to describe the problem are explained. The characteristics of supercritical fluids are introduced in chapter 2.2. In the case of single droplet combustion under microgravity conditions, simplifying assumptions can be made. Specifically, due to the almost completely suppressed natural convection, a spherical droplet shape can be assumed. The flame and the layering of the gas phase around the droplet can also be assumed to be spherical. Therefore, droplet vaporization is discussed using a simplified one-dimensional (1D) spherically-symmetric system in chapter 2.3. The principles of combustion relevant to this thesis are explained in chapter 2.4. In addition, the dominant transport mechanisms are pointed out in the case of isolated droplet combustion in chapter 2.5. This also includes the classical model of Spalding [26] used to describe droplet vaporization and combustion in the steady-state. In chapter 2.6, the microgravity approach in relation to droplet combustion using dimensionless numbers is introduced. Finally in chapter 2.7, the fundamentals of the optical diagnostic techniques relevant to this work are outlined.

### 2.1. Heat and mass transfer mechanisms

The description of combustion problems relies on the conservation laws of thermodynamics and fluid mechanics, including transport properties and chemical kinetics [27]. The relevant equations describe the conservation of mass, momentum energy, and the concentration of individual species and are either solved approximately by numerical methods or are greatly simplified so that an analytical solution is possible. Since no detailed numerical description of the combustion process is included in this thesis, the derivation of these equations is omitted and reference is made to the existing literature, e.g., [1, 27, 28]. In this subchapter, the relevant mass and heat transport mechanisms are summarized.

#### 2.1.1. Molecular transport mechanisms

In a quiescent ambient, gas transport is primarily by mass diffusion. When considering the diffusion of molecules of species A, e.g., oxygen vapor, into an atmosphere of molecules of species B, e.g., hydrogen, the result is a binary system. According to the first Fick's law [29], the diffusion flux between A and B is proportional to the concentration gradient and progresses from areas of high to areas of low concentration. The local diffusion flux for species A can be calculated using Fick's law [30]:

$$\vec{J}_A = -D_{AB}\nabla N_A \quad (1)$$

where  $D_{AB}$  is the binary diffusion coefficient of molecules A and B and  $N_A$  is the number of moles per unit volume of species A. The binary diffusion coefficient can be calculated based on the Chapman-Enskog theory and increases with increasing temperature. However, the pressure has an inversely proportional effect, so that the binary diffusion coefficient decreases rapidly with increasing pressure [31]. Assuming the ideal gas law, the binary diffusion coefficient can be approximated with the Chapman-Enskog theory based on the Lennard-Jones potential [32]:

$$D_{AB} = 0.18583 \sqrt{T^3 \left( \frac{1}{M_A} + \frac{1}{M_B} \right) \frac{1}{p \Psi_{AB}^2 \Omega_{D,AB}}} \quad (2)$$

where  $T$  is the temperature,  $M$  is the molecular mass,  $p$  is the pressure,  $\Psi$  is the collision diameter, and  $\Omega_D$  is the collision integral for diffusion. The derivation of the equation as well as the Lennard-Jones potential parameters can be found elsewhere [32]. This equation is used in chapter 6.1 to estimate diffusion velocities. An example calculation of the binary diffusion coefficient is given in Appendix A.

A special case is the equimolar counter-diffusion. In the diffusion of two ideal gases at constant pressure and temperature in a closed system, the mean molar velocity is zero [28]. This is only the case if the molar volumes of the two species are equal. However, there can be a net flux of mass by diffusion if the molar masses of the two species differ. The total number of moles is assumed to be constant [30]:

$$N = N_A + N_B = \text{constant} \quad (3)$$

This leads to:

$$\nabla N = 0 \quad (4)$$

$$\nabla N_A = -\nabla N_B \quad (5)$$

$$\vec{J}_A = -\vec{J}_B \quad (6)$$

As derived elsewhere [30], the net mass flux by diffusion can be written as:

$$\rho \vec{v}_{diff} = \vec{J}_A M_A + \vec{J}_B M_B = \vec{J} (M_A - M_B) \quad (7)$$

where  $\rho$  is the local density of the gas mixture and  $\vec{v}_{diff}$  is the diffusion velocity.

In analogy to mass diffusion, temperature diffusion (thermal conduction) is due to the transport of thermal energy between neighboring molecules in the presence of a

temperature gradient [28]. The heat flux  $\vec{q}$  is from higher temperature regions to lower temperature regions and is given by Fourier's law:

$$\vec{q} = -\kappa\nabla T \quad (8)$$

where  $\kappa$  is the thermal conductivity.

In addition to these two first-order diffusion mechanisms, there are also second-order diffusion phenomena. Above, it has been assumed that thermal diffusion only occurs in the presence of a temperature gradient, and mass diffusion only occurs in the presence of a concentration gradient. However, thermal diffusion can also occur in the presence of a concentration gradient, and mass diffusion in the presence of a temperature gradient. These second-order effects are known as Dufour and Soret effects, respectively [1]. For example, low-molecular-weight hydrogen can induce counter-gradient diffusion in the presence of steep temperature gradients around the flame. However, the second order diffusion coefficients are generally much smaller than the first order Fickian diffusion coefficients [1]. Therefore, the Dufour and Soret effects are neglected in the context of this basic thermodynamic description of the studied system.

An important dimensionless parameter in heat and mass transfer is the Lewis number, which represents the ratio of heat conduction to diffusion and often serves as a simplifying assumption in analytical or numerical models. The Lewis number is defined as follows [32]:

$$\text{Le} = \frac{\alpha}{D_{AB}} = \frac{\kappa}{\rho c_p D_{AB}} \quad (9)$$

where  $\alpha$  is the thermal diffusivity and  $c_p$  is the specific heat capacity at constant pressure.

### 2.1.2. Convective transport mechanisms

In addition to the molecular transport mechanism, there is also convective mass and energy transport. Convective flows are also called bulk flows and describe the transport due to a fluid velocity. In contrast, diffusion describes the transport due to concentration gradients, as shown above. A distinction is made between forced and free flow. A forced flow is caused by external forces, e.g., by a fan. Free flow is caused by density differences, which in turn are due to temperature, pressure, or concentration differences [28].

In the case of droplet combustion under microgravity considered here, the droplet is burned in a quiescent environment, i.e., no forced flow is present. In addition, free (natural) flows in reduced gravity are mostly suppressed. However, a bulk flow occurs during the phase change at the droplet surface, which results in convective mass and energy transport. This flow is called Stefan flow and is an outcome of the mass balance at an interface with mass transfer. Due to the difference in density in the liquid and gaseous phases, expansion occurs. This expansion acts in the radial direction away from the droplet surface and causes a convective flow [33]. In the droplet case considered, the continuity equation in a 1D, spherically-symmetric system can be written as [27]:

$$\dot{m} = 4\pi r^2 \rho v = \text{constant} \quad (10)$$

where  $\dot{m}$  is the mass flow rate (in the radial direction),  $r$  is the radius, and  $v$  is the radial fluid velocity. This equation is derived elsewhere, see e.g., [27].

The mass flow rate corresponds to the amount of liquid that changes into the gas phase. Therefore, Equation (10) can be used to estimate the velocity of the Stefan flow. Using the rate constant  $k = 8rv$  (introduced later in chapter 2.5.2), this equation can also be written as [27]:

$$\dot{m} = \frac{1}{2} k \pi \rho r = \text{constant} \quad (11)$$

Based on this equation the quasi-steady Stefan flow velocity at the droplet surface can be determined as [34]:

$$v_{Stefan\ flow} = \frac{\rho_{liquid}}{\rho_{vapor}} \frac{k}{8r} \quad (12)$$

where  $\rho_{liquid}$  is the density of the liquid,  $\rho_{vapor}$  is the density of the vapor at the surface and  $r$  is the droplet radius. This equation is used in chapter 6.7 to calculate the Stefan flow at the droplet surface for various conditions.

### 2.1.3. Radiation

Another energy transport mechanism is radiation, which describes the transport of energy by electromagnetic waves. Thus, the emission of radiation is a conversion of the internal energy into electromagnetic energy. Based on the Stefan-Boltzmann law, the heat flux  $\vec{q}$  can be calculated as follows [28]:

$$\vec{q} = EK_{SB}T^4\vec{e}_r \quad (13)$$

where  $E$  is the emissivity and  $K_{SB}$  is the Stefan-Boltzmann constant. In the case of droplet combustion, a radiant heat flux is emitted from the flame. By multiplying by the radiating area, the radiation power  $P$  can be calculated [28]:

$$P = aEK_{SB}T^4 \quad (14)$$

where  $a$  is the surface area of the flame shell.

When the radiation energy reaches the droplet, a part is reflected, a part is absorbed, and a part is transmitted. The absorbed heat flux can be calculated using the absorption coefficient  $\Lambda$  instead of the emissivity based on the previous equations. The droplet also emits radiation into the ambience, but due to the much lower temperature of the droplet

(compared to the flame temperature), this heat flux is several orders of magnitude less than the heat flux from the flame.

## 2.2. Supercritical fluids and mixing

The state of a fluid and thus the process of phase change is primarily determined by the ambient pressure and temperature. A general distinction is made between subcritical, transcritical, and supercritical conditions. Figure 2 shows the phase diagram for oxygen in the relevant pressure and temperature regime. The boiling line marks the transition between the liquid and the vapor phase. It ranges from the triple point, at which the solid, liquid, and vapor phases of a species can coexist in thermodynamic equilibrium, to the critical point. The critical point, in turn, marks the maximum temperature and pressure at which liquid and vapor phases can coexist in thermodynamic equilibrium [35].

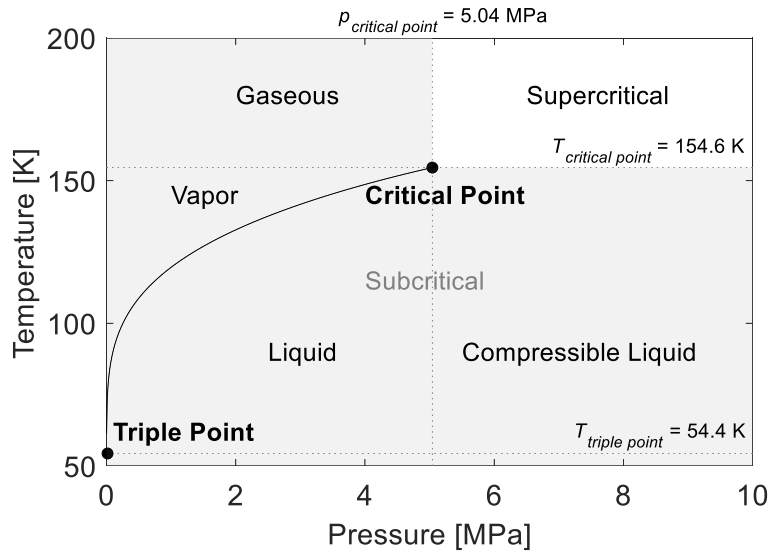


**Figure 2:** Pressure-temperature phase diagram for oxygen. Data from [36] via NIST Chemistry WebBook [37].

The density-temperature diagram for oxygen at three different pressure levels is shown in Figure 3. The pressure values are given as reduced pressures  $p_r$  according to the following definition:

$$p_r = \frac{p}{p_c} \quad (15)$$

where  $p_c$  is the critical pressure of the corresponding species (in the context of this thesis, this is always the disperse phase, i.e., the droplet species). This definition also applies to the reduced temperature  $T_r$  accordingly. In the subcritical regime, pressure and temperature are below the critical point ( $p_r < 1$ ) and the phase change occurs with a discontinuity in density. As the pressure increases, this step change in density decreases until the critical pressure is reached. At pressures at and above the critical pressure ( $p_r \geq 1$ ), the density decreases continuously with increasing temperature, as shown in Figure 3.

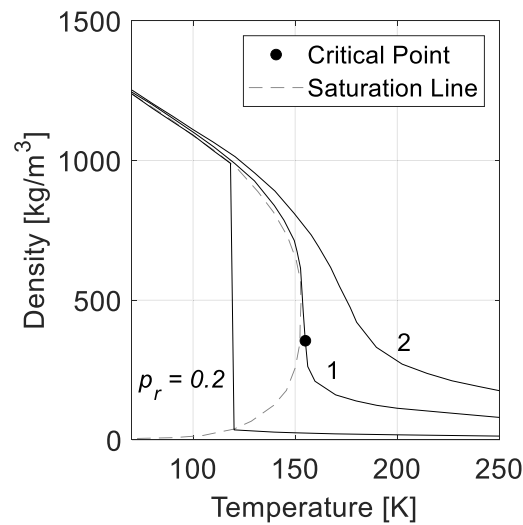


**Figure 3:** Density-temperature diagram calculated with a modified Benedict-Webb-Rubin equation for oxygen at three different reduced pressures  $p_r$ . Adapted from [38].

As the supercritical regime is approached, phase change no longer occurs and the enthalpy of vaporization, which is the amount of energy required for phase change, vanishes [39]. For example, when a droplet with a temperature below the critical temperature is exposed to an environment with critical conditions, the droplet remains in the liquid phase until the critical temperature  $T_c$  is reached. If the temperature at the surface exceeds the critical value, the liquid becomes a supercritical fluid. Since there is no step change in enthalpy and density, the supercritical fluid has no interface with the surrounding gas or with the subcritical liquid droplet. It forms a cloud around the droplet into which the ambient gas diffuses in a quiescent atmosphere due to the lack of surface tension [40].

The transition to the supercritical regime in a single-species system is characterized by the critical temperature and the critical pressure, both of which must be exceeded. However, if more than one species is involved, these limits can be shifted. In a binary system, such as the oxygen droplet in a gaseous hydrogen atmosphere considered in this thesis, the solubility of gaseous hydrogen in LOX at a given pressure above the critical point ( $p_r \geq 1$ ) increases with increasing temperature. At the same time, the amount of hydrogen in the vapor phase of oxygen decreases. This transition zone is the transcritical region. The maximum temperature, at which a phase equilibrium can exist, is the critical mixing temperature and marks the transition to the supercritical regime [38, 41]. With increasing pressure, this maximum temperature decreases, resulting in a critical mixing line, as shown in Figure 4.

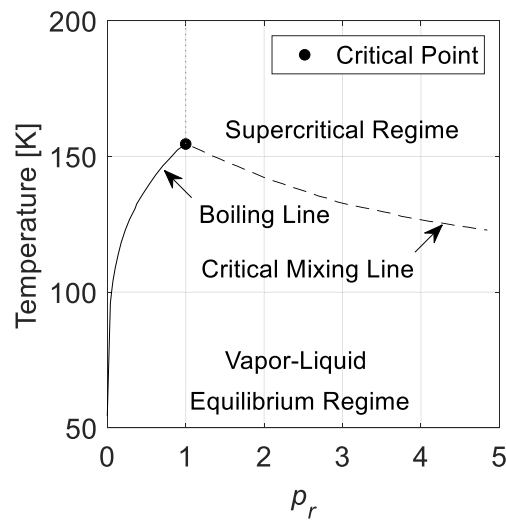


**Figure 4:** Pressure-temperature diagram for the phase behavior of the hydrogen-oxygen system in equilibrium. Adapted from [38].

In the field of liquid rocket propulsion, supercritical properties are often used to improve mixing during fuel and oxidizer injection [12, 41, 42]. In the supercritical regime, the lack of surface tension leads to a drastic increase in solubility, which can be further increased significantly by convective flows. This effect is important for atomization and spray processes, where the surface tension is a dominant factor [42].

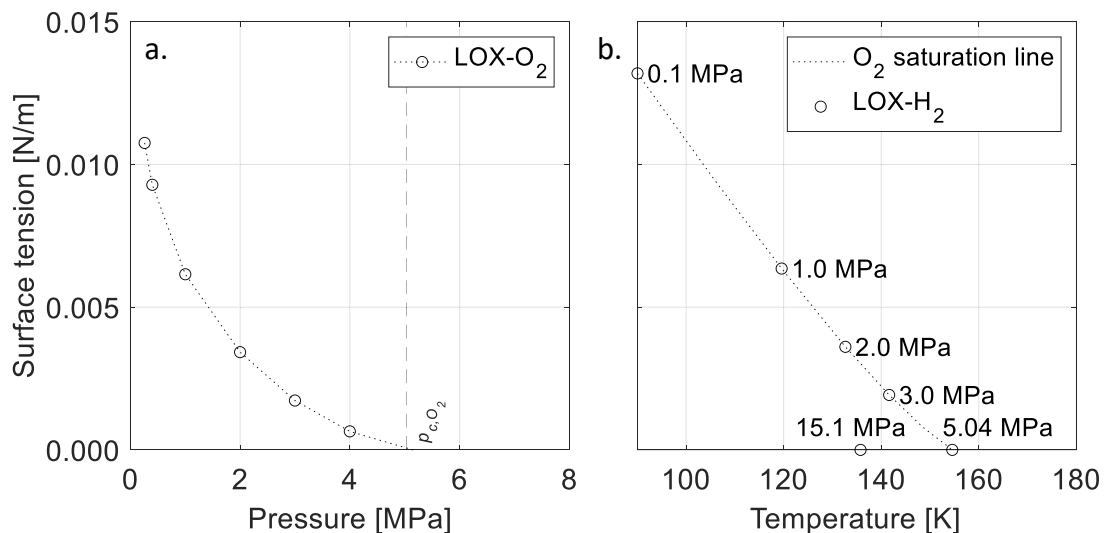


**Figure 5:** a. Measured values of surface tension as a function of pressure for a LOX droplet in a gaseous oxygen environment at saturation temperature. Adapted from [43] based on [44]. b. Computed values of surface tension as a function of temperature for a LOX droplet in hydrogen. Adapted from [41].

The vanishing of the surface tension can be significantly affected by the surrounding atmosphere. In the equilibrium system of liquid oxygen and oxygen vapor, the surface tension decreases continuously with increasing pressure and vanishes at the critical point,

as shown in Figure 5b. Thus, the oxygen is not significantly affected by the hydrogen in the gas phase. It should be noted, however, that surface tension is still present above the critical pressure as long as the critical mixing temperature is not exceeded [41].

### 2.3. Droplet vaporization

Based on the thermodynamic and fluid mechanical fundamentals in the previous subchapter, the droplet vaporization is described in the following. The vaporization is an essential part of the droplet combustion process and therefore important to describe the experiments in this thesis.

In general, vaporization is divided into evaporation and boiling. Evaporation occurs below the boiling temperature and takes place solely at the interface between the gas and liquid phases. Evaporation is triggered when the partial pressure in the surrounding gas mixture is less than the saturation partial pressure, also called the (saturation) vapor pressure, which depends on the temperature at the droplet surface, as shown in Figure 6. In a closed system, the (saturation) vapor pressure is the pressure that is established when the vapor is in thermodynamic equilibrium with the associated liquid phase. When the boiling temperature is reached, the vapor pressure corresponds to the ambient pressure [45].

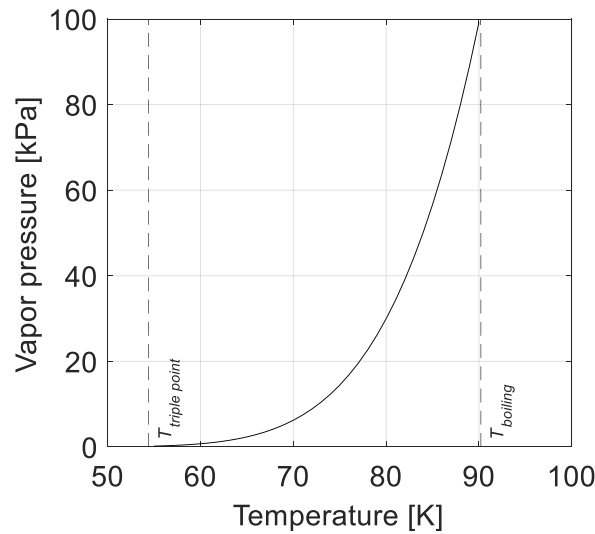


**Figure 6:** Vapor pressure of oxygen as a function of temperature at 0.1 MPa. Data based on [46].

To estimate the vapor pressure of LOX the following equation by Chung [46] can be used:

$$\ln p_{r,vap} = 6.372408 - \frac{6.637925}{T_r} - 1.97576 \ln T_r + 0.265517T_r^5 \quad (16)$$

where  $p_{r,vap}$  is the reduced vapor pressure and  $T_r$  is the reduced temperature of oxygen. This equation is based on the empirical determination of the constants and exponent of the modified Frost-Kalkwarf equation and is used in chapter 6.1 to calculate vapor pressures at various conditions.

Boiling, on the other hand, occurs when the liquid phase reaches the boiling temperature and occurs not only at the interface, but also in the bulk of the liquid. In many cases, both evaporation and boiling processes are present at the same time. Figure 7 schematically shows oxygen droplet vaporization in spherically-symmetric configuration subdivided into evaporation and boiling.

In the case shown for boiling, the heat input is only from the ambience to the droplet surface. Thus, although the surface and possibly also the entire liquid reaches the boiling temperature, the energy required for the phase change is still only transported to the surface. In combination with a high mass transport rate in the gas phase, it is therefore assumed that the boiling process takes place only near the droplet surface and that vapor bubble formation in the droplet interior is unlikely. Therefore, the case shown can also be referred to as evaporation at saturated conditions (saturated evaporation). In the context of this thesis, the phase change at the droplet surface is always referred to as vaporization.

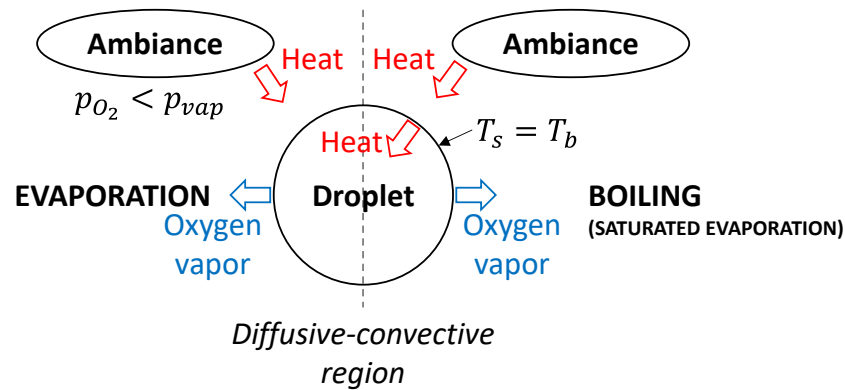


**Figure 7:** Schematic representation of spherically-symmetric oxygen droplet vaporization (divided into evaporation and boiling), where  $p_{O_2}$  is the partial pressure of oxygen,  $p_{vap}$  is the vapor pressure,  $T_s$  is the surface temperature, and  $T_b$  is the boiling temperature. Adapted from [33] and modified.

In both cases, the energy required for the phase change without a rise in the temperature of the liquid is the enthalpy of vaporization. There must be a constant supply of heat to the liquid in order to sustain boiling [1]. Also, evaporation requires heat from outside or from the droplet itself to maintain the phase change. The enthalpy of vaporization decreases with increasing temperature of the liquid. Since the ambient pressure affects the boiling temperature, as shown in Figure 2, the surface temperature of the droplet increases with increasing pressure in the case considered. Thus, the enthalpy of vaporization decreases with increasing pressure (surface temperature) and approaches zero at the critical point [39].

### 2.3.1. Mass and heat transport processes in droplet vaporization

In order to illustrate the mass and heat transport processes in droplet vaporization, a simplified representation of the relevant transport mechanisms is given below. For this purpose, the problem is assumed to be quasi-steady, i.e., the droplet has a constant

diameter and the temperature of the droplet is assumed to be constant and equal to the surface temperature. Important quantities for describing the gas composition are the mole fraction  $X$  and the mass fraction  $Y$ , which are defined as follows:

$$X_A = \frac{N_A}{N}, \quad Y_A = \frac{m_A}{m} \quad (17)$$

where  $N$  is the total number of moles per unit volume and  $m$  is the total mass.

Figure 8 shows qualitative plots of the quasi-steady temperature, the mole fraction of the involved species, and the Stefan flow velocity. With regard to temperatures, the following applies:

$$T_\infty \gg T_s \quad (18)$$

$$T_s = T_b \quad (19)$$

where  $T_\infty$  is the ambient temperature,  $T_s$  is the temperature at the droplet surface, and  $T_b$  is the boiling temperature. To vaporize the liquid, energy in the form of heat must be introduced into the droplet (at the surface), which in this case is accomplished by heat conduction based on Equation (8):

$$q = \frac{\dot{m}}{a} q_g = \kappa \left( \frac{\partial T}{\partial r} \right)_s \quad (20)$$

where  $\dot{m}$  is the mass flow rate of LOX (to satisfy the steady-state condition),  $a$  is the surface area of the droplet, and  $q_g$  is the overall energy per unit mass required to vaporize the liquid, which consists of the (specific) enthalpy of vaporization  $q_v$  and the (specific) enthalpy required to bring the surface to the temperature of vaporization (sensible heat)  $q_t$  [30]:

$$q_g = q_v + q_t \quad (21)$$

Since the LOX has already reached the boiling temperature, it is assumed that the energy transported to the surface is solely used for the phase change. Thus, the temperature gradient at the droplet surface (via heat conduction) determines the LOX mass flow rate (or the droplet regression rate in the real case) [30].

With respect to the mole fraction of the species involved, as shown in Figure 8b, it is assumed that a  $X_{O_2,s} = 1$  applies at the droplet surface (the subscript  $s$  indicates the droplet surface), since the surface has reached the boiling temperature and thus the vapor pressure is equal to the ambient pressure. Due to the fast diffusion of hydrogen and oxygen, a steep concentration gradient is established in the gas phase, so that an increased oxygen content is only present very close to the surface.

The mass and heat transport processes are dominated by diffusion. Due to the higher molar mass of oxygen (compared to hydrogen), a diffusive net mass transport away from the droplet is formed. However, the Stefan flow also contributes to the overall mass and heat transport. As shown above, the density step during the phase change results in a bulk flow (Stefan flow) normal to the droplet surface. For example, at 0.1 MPa the density ratio between the liquid and the vapor phase at saturation conditions (90 K) is about 260 ( $\rho_{liquid} = 1141.8 \text{ kg/m}^3$  and  $\rho_{vapor} = 4.4 \text{ kg/m}^3$ ). Based on Equation (10), the Stefan flow velocity in the gas phase can be determined depending on the mass flow rate, which can be estimated from the droplet regression, with:

$$v_{Stefan\ flow} = \frac{\dot{m}}{4\pi r^2 \rho} \quad (22)$$

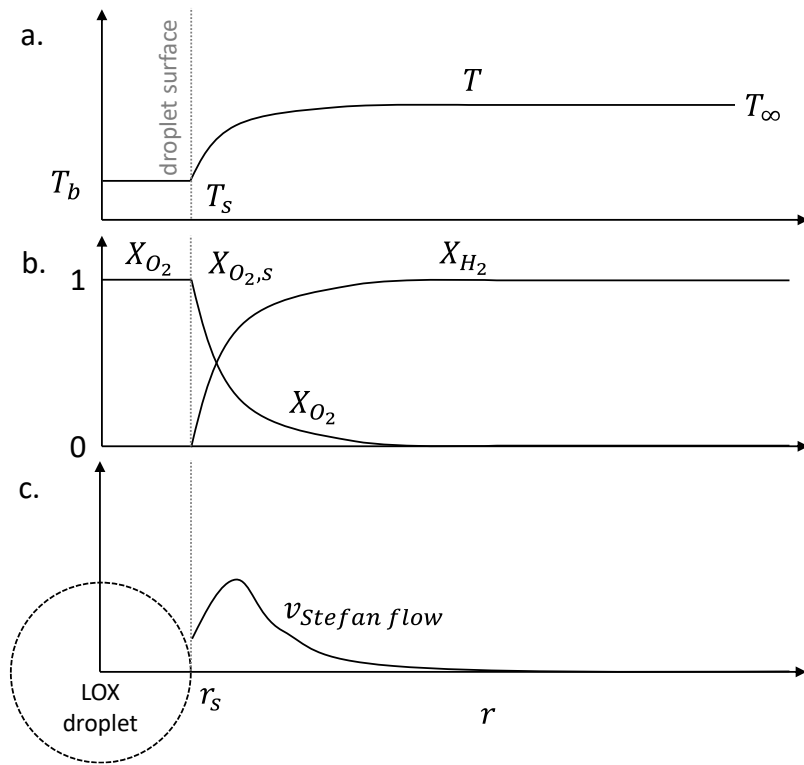
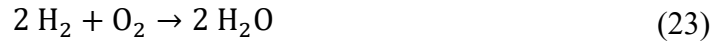


**Figure 8:** Simplified qualitative profiles of the mass and heat transport processes during vaporization of a LOX droplet in hydrogen at subcritical ambient pressure. a. Temperature. b. Mole fraction. c. Stefan flow velocity.

The Stefan flow velocity decreases quadratically with radius, but also depends on density, as shown in Figure 8c. As a result of the sharp drop in density with increasing radius due to the temperature and the gas composition (density of oxygen around 16 times higher than hydrogen), the flow velocity first increases before it decreases again. In addition to Stefan flow, there is also net mass transport by diffusion, based on Equation (7). Due to the higher molar mass of oxygen compared to hydrogen, the flux induced by diffusion also acts in the same direction as the Stefan flow.

## 2.4. Combustion

In general, combustion is defined as a rapid exothermic reaction that releases considerable energy in the form of heat [31]. It is a complex interaction of chemical and physical processes supporting and conditioning each other. Individual reactions proceed with either an absorption or a release of energy, which usually manifests as heat [30]. The combustion of hydrogen and oxygen is described by the basic stoichiometric reaction equation:



Stoichiometry describes the exact ratio of oxygen and fuel without excess oxygen or fuel remaining after complete combustion [31]. To comply with the law of conservation of mass, exact quantities of reactants and products are obtained. In the case of hydrogen-oxygen combustion, exactly two molecules of the fuel, hydrogen, are required to react with one molecule of oxygen to form two molecules of water. The stoichiometric fuel-to-oxidizer ratio for this combination is 2. The equivalence ratio  $\phi$  results from the relation of the actual fuel-to-oxidizer ratio  $\sigma_{actual}$  to the stoichiometric fuel-to-oxidizer ratio  $\sigma_{stoichiometric}$  [1, 31]:

$$\phi = \frac{\sigma_{actual}}{\sigma_{stoichiometric}} \quad (24)$$

According to this definition, it follows that an equivalence ratio below unity ( $\phi < 1$ ) corresponds to a fuel-lean system because there is less fuel than the stoichiometric amount of fuel. Accordingly, an equivalence ratio above unity ( $\phi > 1$ ) indicates a fuel-rich system. The equivalence ratio affects the flame temperature. In general, an under- or over-oxidized system will result in a drop in flame temperature. In an under-oxidized system ( $\phi > 1$ ), there is a lack of oxidizer to burn all the fuel and thus the maximum energy (heat) cannot be extracted. In the opposite case ( $\phi < 1$ ), there is enough oxygen to burn all the fuel, but the excess oxygen is also heated without participating in the reaction, which leads also to a drop in flame temperature [30].

All chemical reactions proceed at a defined (kinetic) rate and depend on the system conditions, such as the concentration of the reactants, the temperature, and the presence of a catalyst or inhibitor [30]. Once a reaction has been triggered, this reaction can trigger several sub-reactions, which in turn result in further follow-up reactions. Depending on the problem and complexity, these sub-reactions can play an important role in the investigation of certain combustion phenomena, such as the ignition phase. In the field of chemical kinetics, many reaction mechanisms are developed which, on the one hand, represent the respective process to be observed, such as autoignition, as precisely as possible, but, on the other hand, are as reduced and efficient as possible. For example, the one-step reaction of hydrogen and oxygen shown in Equation (23) is only a simplification of the complete process. There is also an extended, but still simplified 3-step kinetics for hydrogen-oxygen combustion [47]:



where  $M$  is a non-reacting element used for balancing and  $\rightleftharpoons$  indicating a reaction equilibrium. More detailed reaction mechanisms of the hydrogen-oxygen reaction consist of 12 [47], 16 [1] or 21 [48] steps.

This example only concerns the rather simple reaction of a pure fuel, consisting of only one chemical element, with a pure oxidizer without further elements, such as nitrogen. In the field of hydrocarbon combustion, the number and complexity of reaction steps increases significantly. For modeling real fossil fuels, such as diesel or gasoline, some kinetics mechanisms include over 600 species and over 27,000 reactions [49-51].

For actual, mostly numerical, calculations of the reaction sequences, the determination of the reaction rates of the individual reaction steps is important. The reaction rate constant  $K$  is generally given by the simple Arrhenius equation [52] or by the modified Arrhenius equation [53], the latter being given here in the most common form [54]:

$$K = AT^i e^{-\frac{E}{RT}} \quad (28)$$

where  $A$  is a pre-exponential factor,  $i$  is the reaction order,  $E$  is the activation energy, and  $R$  is the universal gas constant. In the field of reaction kinetics, new simplified and computationally efficient reaction mechanisms, e.g., [54], and more detailed mechanisms that capture as many combustion phenomena as possible, e.g., [51] are being developed.

The ratio of the reaction rate to the mass transport rate is described by the Damköhler number. Here  $Da_I$  represents the ratio to the convective mass transport rate, whereas  $Da_{II}$  represents the reaction rate in relation to the diffusive mass transfer rate [32]:

$$Da_{II} = \frac{K''}{D_{AB}} \quad (29)$$

where  $K''$  is the pseudo-first-order reaction rate. The Damköhler number is often used for simplifying assumptions, e.g.,  $Da_{II} \gg Da_I \gg 1$ .

#### 2.4.1. Classification

In order to split the large field of combustion, different classifications are made. With regard to the flame, a distinction is made between premixed flames, where the reactants are already mixed before they reach the flame, e.g., a Bunsen burner, and diffusion flames, where the mixing of the reactants takes place at the interface, e.g., a candle [31],

a droplet flame, or a solid fuel fire. A further classification can be made according to the flow condition, i.e., whether the fluid flow is laminar or turbulent. Both premixed and diffusion flames can occur in either flow condition. The mixing of reactants is significantly increased in a turbulent flow, which in non-premixed systems usually leads to a significantly higher flame speed, compared to combustion under laminar flow conditions [39]. However, the final mixing of the reactants occurs by molecular diffusion processes independent of the type of flow [1]. A further distinction is made between the phases of fuel and oxidizer. Homogeneous combustion occurs when both reactants are initially in the same fluid phase, i.e., either gas or liquid. This is the case, e.g., with a Bunsen burner, where both the fuel and the oxygen/air are gaseous. Heterogeneous combustion, on the other hand, occurs when the reactants are in different phases. This can be solid and gaseous, e.g., as in the combustion of coal particles [1]. Consequently, the combustion of liquid oxygen and gaseous hydrogen can be classified as heterogeneous with the fuel in gaseous state and the oxidizer (initially) in liquid state. A diffusion flame forms based on the diffusive transport of the two reactants. Since the oxygen droplet burns in a quiescent environment in the context of this thesis, the flow conditions can be classified as laminar. This and other effects of microgravity on the flow field are discussed in detail in chapter 2.6.

## 2.5. Droplet combustion

Apart from the reactions in the gas phase, the mass transport mechanisms within and around the droplet and the phase change process at the droplet surface are qualitatively similar in combustion as well as in vaporization. In simplified terms, the flame during combustion represents a hotter “ambiance” located at a closer distance, strongly accelerating the process [33].

In common droplet combustion, such as hydrocarbon droplets in air, the disperse phase, i.e., the droplet, is represented by the fuel, while the oxidizer is the homogeneous phase. For the case of hydrogen-oxygen combustion in a rocket engine, the fluid phases of fuel and oxidizer are often inverted. A schematic diagram of the oxygen droplet combustion in a spherically-symmetric configuration is shown in Figure 9. Of crucial importance in droplet combustion is the coupling between chemical reactions in the flame zone and vaporization. After ignition, a flame forms around the droplet and the heat from the hot reaction zone is transported to the droplet surface. This heat input, which heats up the droplet surface near to boiling temperature [10], drastically increases the vaporization rate. The oxygen vapor is transported within the inner diffusive-convective region from the droplet surface to the flame region, where it mixes with the surrounding fuel until the mixture reacts. This creates a positive feedback loop as the flame promotes vaporization and the vaporization feeds the flame. As for the pure vaporization case, the transport in the gas phase consists of both diffusion and convection (Stefan flow).

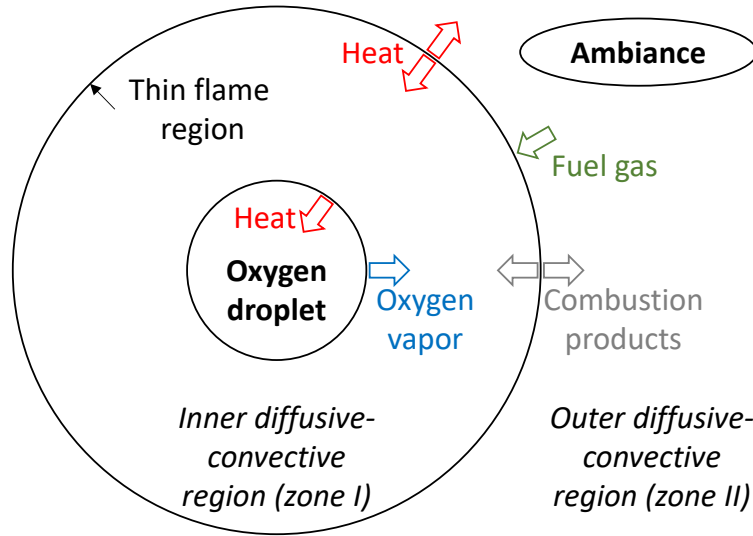


**Figure 9:** Schematic representation of spherically-symmetric oxygen droplet combustion. Adapted from [33].

### 2.5.1. Mass and heat transport processes in droplet combustion

As in the case of pure vaporization in chapter 2.3, a simplified representation of the relevant transport mechanisms is shown in Figure 10 to illustrate the mass and heat transport in droplet combustion. The problem is assumed to be quasi-steady with a constant temperature of the droplet. In addition, the flame-sheet approximation is assumed, which states that the oxidizer and the fuel are transported from opposite sides in stoichiometric proportion to the flame ( $\phi = 1$ ). The reaction zone is assumed to be a thin reaction sheet [27]. The problem is divided into two zones inside and outside the flame shell (zone I and II).

The temperature in the gas phase is largely determined by the flame temperature, as shown in Figure 10a-b. Outside the flame shell, the energy is transported to the ambience primarily by heat conduction. Inside the flame shell, however, a significant amount of energy is also transferred by radiation. Based on Equations (13) + (20), the radial energy transport to the droplet surface is described by [30]:

$$q = \frac{\dot{m}}{a} q_g = \underbrace{\kappa \left( \frac{\partial T}{\partial r} \right)_s}_{\text{conduction}} + \underbrace{\Lambda K_{SB} T^4}_{\text{radiation}} \quad (30)$$

where  $\Lambda$  is the absorption coefficient of the LOX droplet.

The mole fractions are shown in Figure 10c-d. Due to the flame-sheet approximation, only oxygen and water (as product of the combustion) are present as in zone I. Outside the flame shell, in zone II, only water and hydrogen are present. Both reactants have a mole fraction of zero at the position of the flame sheet, as they are consumed and react to form water. The quasi-steady mass transport can be explained in terms of the individual

species. The oxygen vapor is transported from the surface of the LOX droplet to the flame and consumed there. Hydrogen, on the other hand, is transported from the environment to the flame zone and is consumed. The resulting water vapor is transported both inwards (towards the droplet surface, zone I) and outwards (zone II). As for the vaporization case, mass transport is primarily controlled by diffusion. A diffusive counterflow is formed both in zone I and in zone II. Based on Equation (2), the diffusion rate is significantly affected by the ambient temperature. Therefore, the diffusion flux is significantly increased in the region of the hot flame.

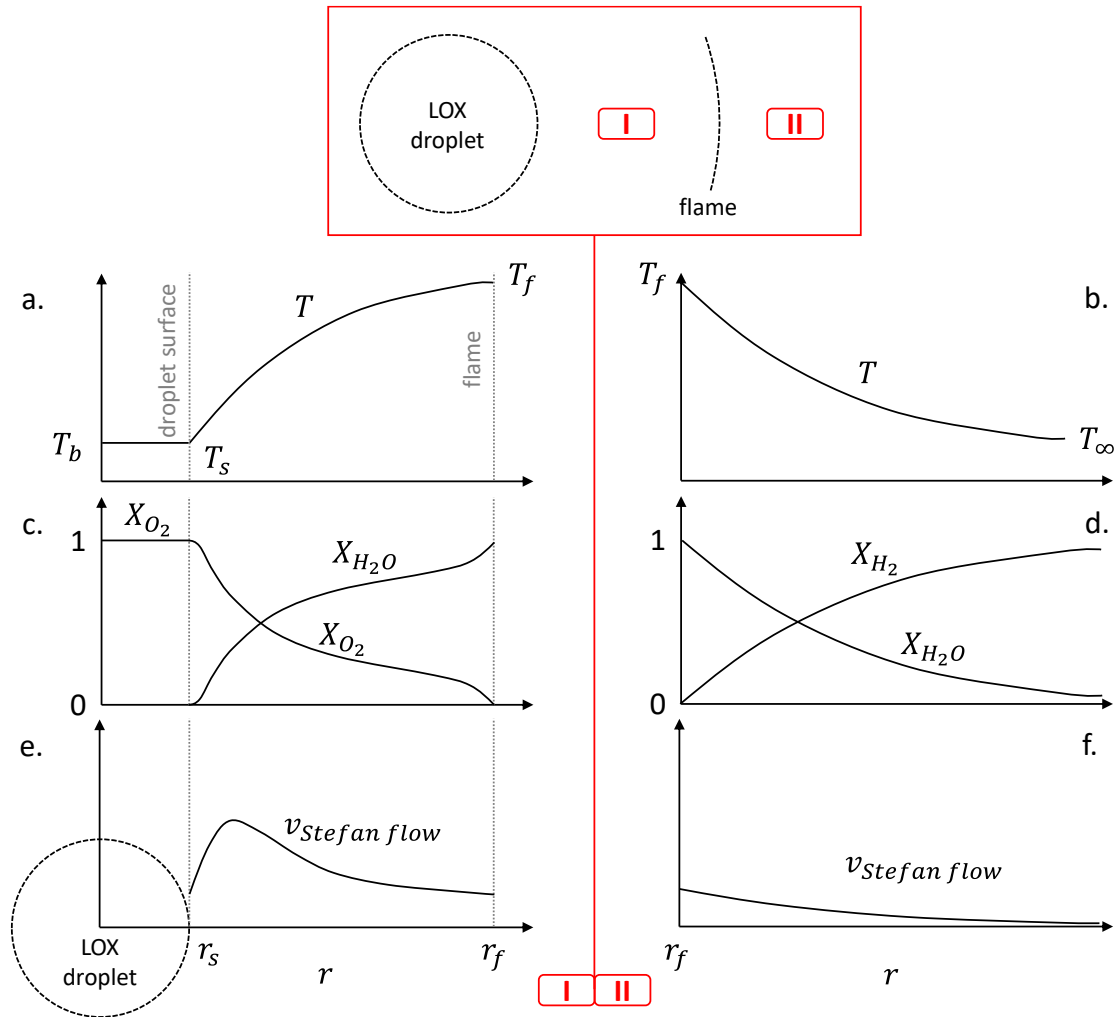


**Figure 10:** Simplified qualitative profiles of the mass and heat transport processes during combustion of a LOX droplet in hydrogen at subcritical ambient pressure. I. Inside flame shell: a. Temperature. b. Mole fraction. c. Stefan flow velocity. II. Outside flame shell: d. Temperature. e. Mole fraction. f. Stefan flow velocity. Adapted from [27, 55].

However, convective mass (and heat transport) also occurs due to Stefan flow at the droplet surface and thermal (gas) expansion in the flame region and superimposes the diffusive transport process. Due to the strong heating of the gas phase by the flame, a convective flow away from the flame towards the droplet and also into the ambience is induced by thermal expansion. At the same time, however, diffusive mass transport is

greatly enhanced by the higher temperature, so it is assumed that the effect of thermal expansion on the overall mass transport is not significant.

In Figure 10e-f the velocity profile of the Stefan flow is shown. Based on Equation (22), the Stefan flow velocity is dependent on both radius and density. Due to the strong temperature increase in the flame region (Figure 10a-b), the Stefan flow velocity also increases. The bulk flow leads to a decrease of mass transport of water vapor from the flame to the droplet surface and an increase of oxygen vapor mass transport away from the droplet (zone I). Thus, the water vapor is mainly transported into the ambience (zone II).

### 2.5.2. $d^2$ -law

One of the first well-defined single droplet combustion experiments were performed independently by Godsave [56] and Spalding [26] in 1953. Their work led to the formulation of the classical theory of droplet vaporization and droplet combustion (later referred to as  $d^2$ -law). This theory represents a simplified model based on the following assumptions [33]:

1. **Spherical symmetry:** Forced and natural convection are neglected and the diffusion is only radial. This reduces the analysis to 1D.
2. **No spray effects:** The droplet is modeled as an isolated droplet in an infinite oxidizing environment.
3. **Diffusion being rate-controlling:** Diffusion is the primary transport mechanism (convective transport mechanisms are neglected).
4. **Isobaric process:** The pressure during the vaporization or combustion is constant.
5. **Flame-sheet combustion:** Chemical reaction rates are infinitely fast compared to gas-phase diffusion rates ( $Da_{II} = \infty$ ). The flame has an infinitesimal thickness and is modeled as a sink for the reactants and a source of chemical heat release and products.
6. **Constant gas phase properties:** The specific heat and thermal conductivity are constant and the Lewis number is unity ( $Le = 1$ ).
7. **Quasi-steady gas phase processes:** The processes at the liquid surface are much slower than the gas phase transport processes.
8. **Simultaneous fuel vaporization and consumption:** The amount of the fuel vaporized at the surface (oxidizer in the LOX/H<sub>2</sub> case) is instantly consumed by the flame.
9. **Single fuel species:** The droplet consists of a single-component droplet with no internal flows.
10. **Constant and uniform droplet temperature:** The droplet temperature is close to the saturation point and the (transient) heating up period is neglected.
11. **Saturation vapor pressure at droplet surface:** The phase change process is much faster than the gas phase transport. The vaporization at the droplet surface is at equilibrium producing vapor which is at its vapor pressure.
12. **No Soret, Dufour, and radiation effects:** All these effects are neglected.

These assumptions are used to solve the 1D energy, fuel, and oxidizer conservation equations, which leads to the formulation of the following equations (derived elsewhere [1]):

$$d^2 = d_0^2 - kt \quad (31)$$

where  $d^2$  is the squared droplet diameter,  $d_0^2$  is the square of the initial droplet diameter,  $k$  is the rate constant, and  $t$  is the time. The Equation (31) is known as the  $d^2$ -law.

The rate constant can be calculated for combustion  $k_c$  as well as for vaporization  $k_v$  and is defined as:

$$k = 8\alpha_{gas} \frac{\rho_{gas}}{\rho_{liquid}} \ln(1 + B) \quad (32)$$

where  $\alpha$  is the thermal diffusivity of the gas:

$$\alpha = \frac{\kappa}{\rho c_p} \quad (33)$$

and  $B$  is the Spalding transfer number, which is different for vaporization ( $B_v$ ) and combustion ( $B_c$ ):

$$B_v = \frac{c_p(T_\infty - T_s)}{q_v} \quad (34)$$

$$B_c = \frac{c_p(T_\infty - T_s)}{q_v} + \frac{Y_{O_2, \infty} q_r}{\sigma_{stochiometric} q_v} \quad (35)$$

where  $Y_{O_2, \infty}$  is the ambient oxygen mass fraction and  $q_r$  is the (specific) enthalpy of chemical reaction (heat of combustion). The Spalding heat transfer number for vaporization is similar to the Jakob number, which is the ratio of sensible heat absorbed by the liquid  $q_t$  to latent heat absorbed by the gas  $q_v$  [57]:

$$Ja = \frac{q_t}{q_v} = \frac{c_p \Delta T}{q_v} \quad (36)$$

Dividing Equation (31) by the initial droplet diameter squared  $d_0^2$ , leads to a dimensionless droplet diameter as a function of time:

$$\left(\frac{d}{d_0}\right)^2 = 1 - \frac{k}{d_0^2} t \quad (37)$$

The time span between the start of the droplet regression and the vanishing of the droplet is introduced as the total time  $\tau$ . The total time of vaporization  $\tau_v$  is obtained from

Equation (31) using the vaporization rate constant  $k_v$  and the total time of combustion  $\tau_c$  using the combustion rate constant  $k_c$ , respectively:

$$\tau_v = \frac{d_0^2}{k_v}, \quad \tau_c = \frac{d_0^2}{k_c} \quad (38)$$

The flame standoff ratio is:

$$\frac{f}{d} = \frac{\ln(1 + B_c)}{\ln\left(1 + \frac{Y_{O_2, \infty}}{\sigma_{stochastic}}\right)} \quad (39)$$

where  $f$  is the flame diameter.

These equations can be used to calculate the main vaporization or combustion characteristics. The calculations are based on the Spalding number, which is calculated differently for the combustion case and for the vaporization case, respectively. The model assumes that during quasi-steady droplet combustion, the droplet regression rate and the flame standoff ratio  $f/d$  are constant. This results in a linear decrease in squared droplet diameter over time, as shown in Figure 11.

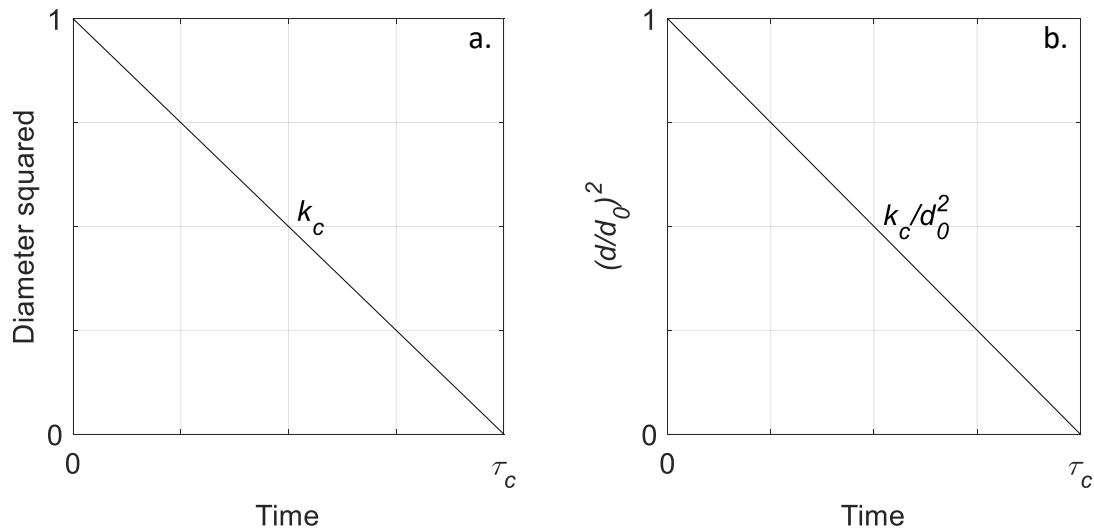


**Figure 11:** Droplet regression during combustion according to the  $d^2$ -law. a. Dimension-based diameter. b. Dimensionless diameter. Adapted from [10].

Compared to experimental results, the simplified assumptions of the  $d^2$ -law can lead to qualitative and quantitative deviations. A main concern is the assumption of quasi-steady processes. Especially with respect to the initial phase of combustion or vaporization, neglecting transient droplet heating leads to a deviation in the droplet regression. Due to the significantly lower initial temperature of the droplet, the droplet diameter initially remains constant or even increases slightly as the liquid expands [33, 58]. Only after the droplet surface is heated to the steady-state droplet temperature, often referred to as the (pseudo) wet-bulk temperature [59], the squared droplet diameter decreases linearly over

time. However, since the heating is fairly rapid during the droplet lifetime (for 1 mm droplets), taking droplet heating into account leads only to a slight increase in the total burning time of the droplet [33]. In addition to the transient heating of the droplet, the formation of a soot shell (with hydrocarbon fuels) and radiation heat losses can also lead to the unsteadiness of droplet combustion and thus to a continuous increase in the instantaneous burning rate over the entire combustion lifetime. Furthermore, experiments have shown that the burning rate constant could also be influenced by the initial droplet diameter, the igniter, the suspender, and the measurement method [60].

The neglect of radiation in the  $d^2$ -law must be questioned with respect to large droplets. While for small droplets with a size of 100  $\mu\text{m}$  the radiative heat flux only accounts for about 1 % of the total energy flux required for gasification, this portion increases to about 40 % for large droplets with a size of 1 mm [61]. Thus, radiation is an important factor in this case, which is not covered by the  $d^2$ -law. To account for this in the model, the energy flux term would have to be extended to include radiation, as in Equation (30).

Another point is the assumption of a constant flame standoff ratio. Experiments have shown that in many cases the flame standoff ratio increases slightly during burning. This is attributed to the transient accumulation of fuel vapor in the region between the droplet and the flame. The increase is also related to the ambient oxygen concentration. At high oxygen environments, the flame standoff ratio approaches a constant value [58]. With respect to the flame position, the predictions of the  $d^2$ -law can significantly deviate qualitatively as well as quantitatively from real experiments. To take the vapor accumulation effect into account in the analytical model the overall mass conservation for the vapor at the surface would have to be extended [1]:

$$\dot{m}_{vapor} = \dot{m}_{flame} + \frac{d}{dt} \int_{r_d(t)}^{r_f(t)} (Y_{vapor}\rho) 4\pi r^2 dr \quad (40)$$

where  $\dot{m}_{flame}$  is the consumption rate at the flame,  $r_f$  is the radius of the flame and  $r_d$  is the radius of the droplet, and the second term is the accumulation/depletion rate in the inner region.

A strong simplification is also made for the properties in the gas phase. Despite high temperature gradients in the region between droplet surface and flame, only averaged transport properties are used in the model. Even using accurate transport properties at a predefined elevated temperature, uncertainties in calculated burning rates can be about 10-20 % [62]. Under extreme environmental conditions, such as trans- or supercritical conditions, unsteady diffusion processes are not represented by the model [33]. Despite the known inaccuracies, the simplified model predicts, e.g., the droplet burning rate, the flame standoff ratio or the flame temperature. Especially with regard to the large number of different real fuels and ambient conditions, it is extremely difficult to describe the different vaporization and combustion effects precisely with only one model. The assumptions made in the  $d^2$ -law result in very simple equations, which can be calculated quickly and can give an approximate result, at least in many cases.

The definition of the vaporization or burning rate constant  $k$  from the  $d^2$ -law is also frequently used in the literature to describe experimental or numerical results. However, sometimes droplet lifetimes and sometimes combustion lifetimes are used as the basis for calculation. To clearly distinguish these terms, the following notation is used in this thesis:

- **Vaporization rate constant  $k_v$ :** Used only for pure vaporization cases and based on the total time for vaporization (droplet lifetime)  $\tau_v$ ,
- **Combustion rate constant  $k_c$ :** Used for combustion cases and based on the total time for combustion (combustion lifetime)  $\tau_c$ ,
- **Gasification rate constant  $k_g$ :** Introduced to differentiate from vaporization without reactions in the gas phase and used only for combustion cases and based on the total time for gasification during the combustion event (droplet lifetime)  $\tau_g$ . In the context of this thesis, gasification and vaporization both refer to the physical phase change of the droplet without chemical reactions.

The calculation of the different rate constants is based on Equation (38) and is the ratio of the initial droplet diameter squared to the respective total time:

$$k_v = \frac{d_0^2}{\tau_v} , \quad k_c = \frac{d_0^2}{\tau_c} , \quad k_g = \frac{d_0^2}{\tau_g} \quad (41)$$

## 2.6. Microgravity approach

The detailed processes of vaporization and combustion in sprays can only be studied to a limited extent in real technical combustors. On the one hand, the droplet sizes in technical sprays are in the order of 5-150  $\mu\text{m}$  and thus is too small for most diagnostics, and on the other hand, the turbulent flow conditions in such technical combustion chambers do not allow for quasi-stationary diagnostics [63]. The droplet size can be increased if the gravity is greatly reduced at the same time. This is the microgravity approach, which offers a way to study the essential processes of spray combustion on large droplets under microgravity conditions. With the help of dimensionless numbers, the comparability of these two systems can be shown. Another difference between the single droplets of a technical spray and those under microgravity is due to the flow conditions around the droplet. Other parameters, such as ambient pressure, temperature, composition of the atmosphere or of the droplet, can be predefined to match those in the particular technical system.

### 2.6.1. Grashof number

One effect that depends on the droplet size is natural thermal convection in the gas phase. The resulting buoyancy forces are proportional to the volume of the heated gas and therefore increase cubically with the droplet diameter. This implies that the effect of natural convection is almost negligible for small droplets as they occur in technical sprays. With large droplet diameters, however, as required for detailed diagnostics, natural convection has a major effect. To estimate the importance of flows in thermal convection, the dimensionless Grashof number is used, based on [1]:

$$Gr = \frac{gd^3}{\nu_\infty^2} \left( \frac{\rho_\infty - \rho}{\rho_\infty} \right) \approx \frac{gd^3}{\nu_\infty^2} \left( \frac{T_f - T_\infty}{T_\infty} \right) \quad (42)$$

where  $g$  is the gravitational acceleration,  $d$  is the droplet diameter,  $T_f$  is the flame temperature,  $\rho_\infty$ ,  $\nu_\infty$ , and  $T_\infty$  are the density, kinematic viscosity, and the temperature of the surrounding gas, respectively. At constant pressure, the density ratio can be approximated by the temperature ratio. When comparing different cases, the material properties (kinematic viscosity) and the ambient conditions (temperature ratio) remain constant. Thus, the effect of natural convection depends only on the droplet diameter and the gravitational acceleration. To evaluate the effect of natural convection, the Grashof numbers are calculated for three different cases:

1. The small droplet of a technical spray
2. The large droplet in normal gravity
3. The large droplet in microgravity

For the calculation, the combustion case of an oxygen droplet in a hydrogen atmosphere is assumed. Realistic temperatures and a corresponding viscosity were selected. The results are shown in Table 1. If the droplet diameter is increased, the gravitational acceleration must be reduced correspondingly to obtain similarity. Experiments on large droplets under microgravity ( $\mu\text{g}$ ) thus have physical similarity to the processes on small droplets and normal gravity conditions (1g). In both cases, natural or thermal convection plays only a negligible role.

**Table 1:** Example calculation of the Grashof number for hydrogen-oxygen combustion in various cases.

Case	$d$	$g$ [m/s <sup>2</sup> ]	$\nu$ [m <sup>2</sup> /s]	$T_f$ [K]	$T_\infty$ [K]	$Gr$
Spray	5...150 $\mu\text{m}$	9.81	$1 \times 10^{-6}$	3000	77	0.04...1100
1g experiment	0.7 mm	9.81	$1 \times 10^{-6}$	3000	77	$1.1 \times 10^5$
$\mu\text{g}$ experiment	0.7 mm	$9.81 \times 10^{-6}$	$1 \times 10^{-6}$	3000	77	0.112

### 2.6.2. Fourier number

As the size of the droplets increases, the time required for vaporization or combustion increases. Since combustion processes are largely determined by transient heat transfer processes, the Fourier number can be considered for a comparison of different combustion chambers and experimental systems, based on [30, 64]:

$$Fo = \alpha \frac{t}{d^2} \quad (43)$$

The Fourier number expresses the ratio of the time of an ongoing thermal process  $t$  to the time of the molecular diffusion of energy [64]. In terms of technical sprays with droplet

lifetimes in the order of microseconds, this would give a lifetime in the order of a few hundred milliseconds for larger droplets, as shown in Table 2. Experiments have shown that the temporal differences of different initial droplet diameters can be scaled with a constant Fourier number and therefore results from large droplets can also be transferred to small droplets, at least over a wide range of diameters [65].

**Table 2:** Example calculation of the Fourier number for hydrogen-oxygen combustion in various cases.

Case	$d$	$\alpha$ [m <sup>2</sup> /s]	$t$	$ Fo$
Spray	5...150 $\mu\text{m}$	$7.8 \times 10^{-5}$	$\sim 5 \mu\text{s} \dots \sim 5 \text{ms}$	15.6...17.4
$\mu\text{g}$ experiment	0.7 mm	$7.8 \times 10^{-5}$	$\sim 100 \text{ms}$	16.0

### 2.6.3. Reynolds number

Another important effect to be compared is the forced convection, caused by the relative motion between droplet and surrounding gas. The essential parameter for this is the Reynolds number, based on [64]:

$$Re = \frac{d v_{rel}}{\nu} \quad (44)$$

where  $v_{rel}$  is the relative velocity between the droplet and the surrounding gas. The Reynolds number expresses the ratio of the fluid inertia to the viscosity [64]. Since in a system with technical injection, such as a rocket injector, the relative velocity drops rapidly after droplet formation. This leads to small Reynolds number values in the order of  $Re < 5$  [66]. Droplets with technical dimensions are therefore exposed to only minor flow effects and follow the turbulent flow field quite well. With the goal of better observability and easier diagnosis, when the droplet diameter is increased from the micrometer to the millimeter scale, the relative velocities must decrease accordingly, as shown in Table 3. These flow velocities are within the range of the remaining imperfections when trying to establish quiescent conditions in the microgravity experiment.

**Table 3:** Example calculation of the Reynolds number for hydrogen-oxygen combustion in various cases.

Case	$d$	$\nu$ [m <sup>2</sup> /s]	$v_{rel}$	$ Re$
Spray	5...150 $\mu\text{m}$	$5 \times 10^{-7}$	0.5 m/s ... 15 mm/s	4.5...5.0
$\mu\text{g}$ experiment	0.7 mm	$5 \times 10^{-7}$	4 mm/s	5.0

With the help of the three dimensionless numbers calculated above, it can be demonstrated that small technical droplets are similar to large droplets under microgravity

conditions. Conversely, it is also possible to transfer the findings from experiments with large droplets to technical dimensions. This is one reason for the decades of combustion research on droplets under reduced gravity.

Another reason is that both the classical theory, described in chapter 2.5.2, and other models, which are used to calculate vaporization and combustion processes, often include the important assumption of spherical symmetry of both the liquid droplet and the surrounding gas phase. This assumption significantly simplifies the calculations, since the equations need to be computed for only one, rather than two or even three, spatial dimensions. Therefore, basic spherical-symmetric experimental results are helpful to develop and validate fundamental computational tools for modeling droplet combustion. However, the combustion of single isolated droplets under normal gravity conditions, even in an initially quiescent environment, usually generates sufficient heat to cause natural convective flows, which destroy the spherical symmetry of the experiment, as shown in Table 1 using the Grashof number calculation. Under normal gravity, buoyancy enhances heat and mass transfer in the gas phase, resulting in an increase in burning rate. The flame shape is also clearly distorted, which makes it difficult to determine the flame position. Since the effects of buoyancy vary significantly with droplet diameter, as shown in Equation (42), experiments under normal gravity are entirely transient. Under quiescent microgravity conditions, droplets and correspondingly, the flames have a spherical shape since natural convection is almost completely suppressed. This results in nearly spherical-symmetric experimental conditions that can be accurately modeled with a single spatial dimension (the radius) [33, 34].

## 2.7. Optical diagnostics

In the field of combustion research, optical diagnostics or measurements (are used synonymously in the following) are of crucial importance. The combustion process has many special characteristics that significantly complicate the measurement of different quantities. The major limitation entails the high sensitivity of the combustion process. Since the process is spatially extremely inhomogeneous, with the flame extending to only a few micrometers, placing measurement sensors near the flame will significantly disrupt the process. Therefore, non-invasive diagnostics are widely used to minimize the effect on the combustion. But on the one hand, a high spatial resolution is required to investigate these tiny structures. On the other hand, the time scales are often very small, which leads to the requirement of a simultaneously high temporal resolution of the required measurement systems [67]. In experiments under microgravity conditions, the diagnostics are additionally subject to space constraints and must be very robust. However, under these conditions the objects are usually spherical and therefore easier to reconstruct in contrast to the otherwise often complex structures, e.g., under turbulent conditions. Thus, line-of-sight methods are in principle also suitable to reconstruct the geometry of the investigated object. In the following, the basics of the three optical measurement methods relevant to this thesis are explained.

### 2.7.1. Shadowgraph imaging

Shadowgraph imaging, or shadowgraphy, is a measurement method based on changes in fluid density and thus the index of refraction. These changes affect the optical phase and the propagation direction of a light wave and can be made visible accordingly. The refractive index  $n$  can be related to the density of the fluid  $\rho$  by the Clausius-Mosotti equation [68]:

$$n - 1 = K_{GD}\rho \quad (45)$$

where  $K_{GD}$  is the Gladstone-Dale constant, which is specific for a fluid. Thus, various physical quantities, such as pressure and temperature differences or concentrations of different species in the medium, can be visualized via their effect on the density of the fluid. However, to enable quantitative measurements of individual density-based quantities, the exact relationship between refractive index and density must be known [68].

Shadowgraph imaging represents the simplest form of density-based optical diagnostics. With this technique, shadow patterns caused by an inhomogeneous density field are made visible. Figure 12 shows a basic setup and the deflection of light by the density gradient. The light from a point light source is transmitted through a test region, where a density inhomogeneity causes a refraction of light. This reflection then caused a shadow on the image plane, which can be made visible by using a camera focused to this plane (not shown in the setup).

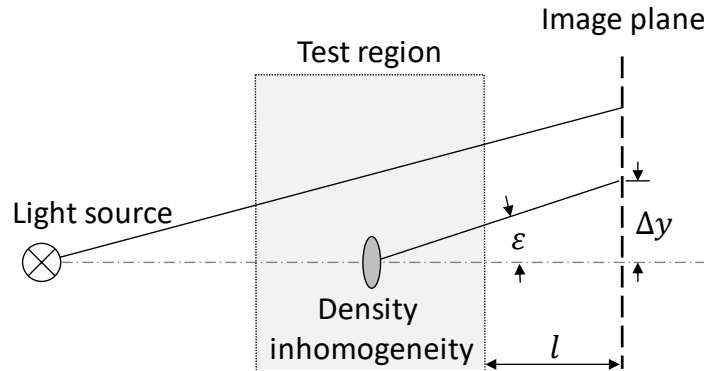


**Figure 12:** Schematic setup of the direct shadowgraph imaging technique. The density inhomogeneity causes a refraction of light with an angle  $\epsilon$ , which leads to a displacement on the image plane from its original position by distance  $\Delta y$ . The image plane is located at a distance of  $l$  from the test region. Adapted from [68, 69].

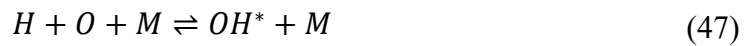
This setup can also be adjusted in order to generate an arrangement with parallel light through the test region. The relative change of light intensity on the image plane can be calculated according to the following equation [68]:

$$\frac{\Delta I}{I} = l \int_{\zeta_1}^{\zeta_2} \left( \frac{\partial^2}{\partial x^2} + \frac{\partial^2}{\partial y^2} \right) (\ln n) dz \quad (46)$$

where  $I$  is the light intensity,  $l$  is the distance from the image plane,  $\zeta_1$  and  $\zeta_2$  are the entrance and exit coordinates, respectively, of the light transmitted through the test region, and  $z$  is the optical axis (the direction of light), whereas  $x$  and  $y$  are the coordinated in the planes normal to the optical axis. Shadowgraph imaging can be used to visualize density gradients, but the method is only sensitive to changes of the second derivative of density [67, 68]. Thus, this technique is not suitable for a direct quantitative measurement of the density [68]. However, due to its simplicity, the method can be used to qualitatively visualize density gradients and to determine the dimensions of much denser fluids, such as the diameter of a liquid droplet in a gaseous environment.

### 2.7.2. $OH^*$ chemiluminescence

Chemiluminescence is the emission of light triggered by chemical reactions. This is in contrast to fluorescence, where light is absorbed, resulting in excitation [70]. During combustion, the flame emits self-radiation caused by the chemical excitation of specific intermediates. The rate at which a chemically excited molecule or radical is produced is temperature dependent and thus the detectable radiation of the characteristic spectra of the intermediate radicals, e.g.,  $OH^*$ , is a product of thermal and chemical excitation [67]. As shown in chapter 2.4, the reaction mechanism of hydrogen and oxygen is divided into many sub-reactions. An important intermediate molecule is hydroxyl ( $OH$ ), which is formed in many different reactions steps [47]. The most dominant reactions to form  $OH$  in the excited state ( $OH^*$ ) are [71, 72]:



By detecting the  $OH^*$  chemiluminescence during combustion, the reaction zone can be visualized. In combustion processes where soot is produced, the broadband soot radiation overlaps the intensity of the chemiluminescence, which is about three orders of magnitude smaller. However, the chemiluminescence portion of the light emission becomes dominant when no soot is produced, as in the hydrogen-oxygen combustion [73]. Figure 13 shows a spectral profile of a hydrogen-air combustion over a wide wavelength range. The bandwidth of the  $OH^*$  chemiluminescence is very narrow and has a significant peak in the ultraviolet (UV) spectrum near 310 nm [70, 73].

By using suitable optical filters, the visible and infrared (IR) spectrum of the flame radiation can be blocked, so that only the narrow range around the  $OH^*$  signal around 310 nm is detected. Since this signal is very weak, image intensified cameras are often used to detect the  $OH^*$  signal at high speed. Theoretically, the absolute intensities of the  $OH^*$  spectral line can be used to determine gas temperatures. In the hydrogen-oxygen

system in particular, there is almost no interference of the signal from other light emission sources in this spectral range. However, it is very difficult to determine the absolute intensities in experimental setups [73].

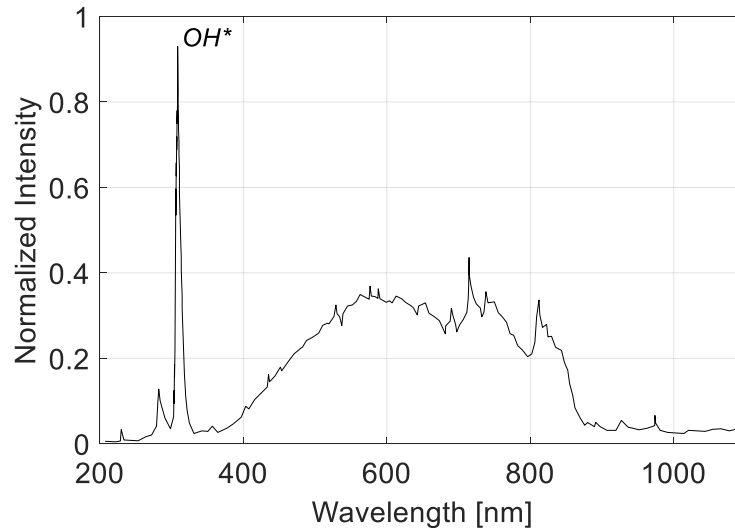


**Figure 13:** Spectral profile of hydrogen-air combustion in a car engine. Data adapted from [74] and filtered.

But the technique can be used to locate the reaction zone in the flame. Since the  $OH^*$  radiation is generated by the flame itself, only integral measurements along the line of sight can be performed.

### 2.7.3. Background oriented Schlieren

Schlieren methods are at first sight very similar to the shadowgraph method presented in chapter 2.7.1. Both methods visualize inhomogeneities in the density field and can give information about temperature, pressure or chemical composition of the gas. However, since these quantities are all related via the density, it is necessary for the measurement of one quantity that the other two quantities are known at the same time. Both methods determine the density inhomogeneities via the change of the refractive index. In shadowgraph imaging, the illuminance level responds to the second spatial derivative of the refractive index, whereas in Schlieren methods the illuminance level responds to the first derivative and is therefore more sensitive in most cases [69].

Background oriented Schlieren (BOS) is a Schlieren method suggested by Meier in 1999 [75]. This technique differs from the classical Schlieren method, often referenced to as the Toepler Schlieren method [68], and based on the local displacement of patterns throughout the image [76]. The BOS setup is schematically shown in Figure 14.

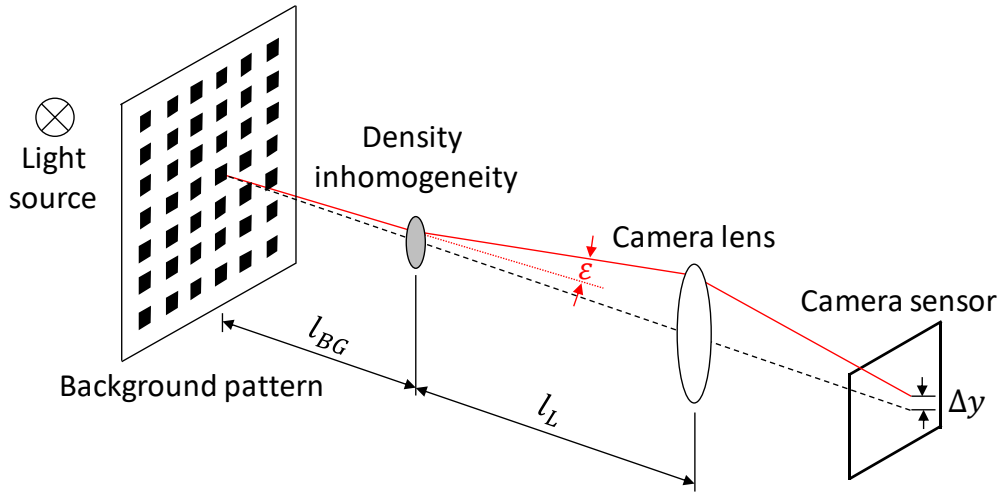


**Figure 14:** Schematic BOS setup. The density inhomogeneity causes a refraction of light with an angle  $\varepsilon$ , which leads to a displacement on the camera sensor from its original position by distance  $\Delta y$ . The background pattern is located at a distance of  $l_{BG}$  and the camera lens at a distance of  $l_L$  from the density inhomogeneity, respectively. Adapted from [76] and modified.

A printed ordered or random background pattern is backlit with a light source and is focused by a camera. Due to the changed refractive index of a density inhomogeneity, a part of the light is deflected, which leads to a local shift of the background pattern on the camera sensor. This deflection is determined by the spatial gradients of the refractive index integrated along the line of sight and can be calculated with this equation [76]:

$$\varepsilon = \frac{1}{n_0} \int \frac{\partial n}{\partial y} dz \quad (49)$$

where  $\varepsilon$  is the refraction angle and  $n_0$  is a reference refractive index. Based on the refraction angle as well as the distances in the optical setup and the focal length of the camera lens, the displacement on the camera sensor  $\Delta y$  can be calculated [76]:

$$\Delta y = F \left( \frac{l_{BG}}{l_{BG} + l_L - F} \right) \varepsilon \quad (50)$$

where  $F$  is the focal length of the camera lens,  $l_{BG}$  is the distance between the background and the object and  $l_L$  is the distance between the camera lens and the object. Unlike the Toepler Schlieren methods, the camera images of the BOS method do not directly provide an extractable signal. They have to be processed with the help of a reference image, which was taken without the density inhomogeneity. Usually, algorithms for cross-correlation are used for this purpose, as they are also used in other measurement methods, e.g., in Particle Image Velocimetry (PIV) [76]. The individual structures of the background pattern are compared with those of the reference image, thus making the density-related displacement visible.

### 3. State of the art

The first published combustion studies on single droplets were performed back in the middle of the 20<sup>th</sup> century [77]. Since then, significant progress has been made in the analytical and numerical modeling, as well as in the experimental diagnostics for the detailed description of vaporization and combustion effects over a wide range of environmental conditions and fluid systems. In this chapter, the relevant experimental and numerical studies on droplet vaporization as well as droplet combustion are reviewed. The focus is on studies of the hydrogen-oxygen system and partly of hydrocarbon vaporization and combustion, when appropriate. These studies are summarized and contrasted in a combined subchapter. The chapter is concluded with a review of experimental methods for droplet generation and ignition as well as combustion diagnostics.

#### 3.1. Droplet vaporization

The vaporization of droplets has been intensively studied in different configurations, at different environmental conditions, and for a variety of species systems. In the following, the studies relevant for this work are presented and divided into experimental and numerical studies.

##### 3.1.1. Experimental studies

The handling of LOX and hydrogen requires stringent safety measures. In addition, the experimental effort is increased since suitable thermal insulation and in many cases a coolant, usually liquid nitrogen, must be used to generate cryogenic oxygen droplets. Therefore, the experimental database for the vaporization or combustion of oxygen droplets, even under 1g, is very limited. To reduce safety requirements, inert ambient gases, such as nitrogen or helium, were often used for vaporization experiments.

Yang *et al.* [78] examined the vaporization of LOX in an inert environment of helium under subcritical and supercritical conditions in 1g. They used a pool-like configuration based on an oxygen feed tube to create a constant liquid surface at a fixed position. This setup was used in a convective environment with a defined flow velocity of 0.2 cm/s and a fixed temperature of 290 K ( $T_r = 1.88$ ). The measurements of the vaporization rates, which are shown in Figure 15, indicate an almost linear increase with increasing pressure ranging from 0.5 to 6.9 MPa (reduced pressure of oxygen  $p_r = 0.1$  to 1.4). In addition, the surface temperature of the LOX was measured. At subcritical pressures, a temperature slightly below the boiling temperature of pure oxygen was found. In the supercritical regime, on the other hand, a temperature very close to the calculated critical mixing temperature for oxygen and helium was found. The oxygen mole fraction was measured to compare the species profile the gas phase at different pressures. They found that near the liquid surface the decreasing slope of the oxygen mole fraction is steeper at high pressure ( $p_r = 1.4$ ) compared to lower pressures ( $p_r = 0.6$ ). They concluded that the gas velocity and diffusion coefficient is reduced at high pressures [18, 78].

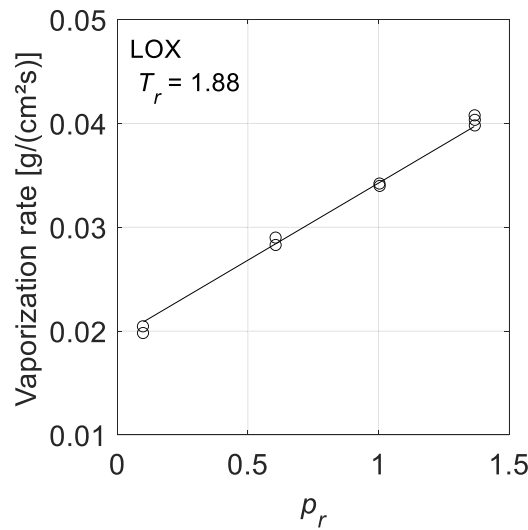


**Figure 15:** Effect of reduced ambient pressure on the vaporization rate of LOX in helium at 290 K with a purge flow velocity of 0.2 cm/s. Adapted from [78].

In another experimental work under 1g conditions, Chesneau *et al.* [79] studied the vaporization of single oxygen droplets in stagnant air, nitrogen, and helium at room temperature. The initial droplet diameters ranged from 0.8 to 1.4 mm. They also found a significant increase in the vaporization rate with increasing pressure from 0.1 to 1.75 MPa ( $p_r = 0.02$  to 0.35), as shown in Figure 16.

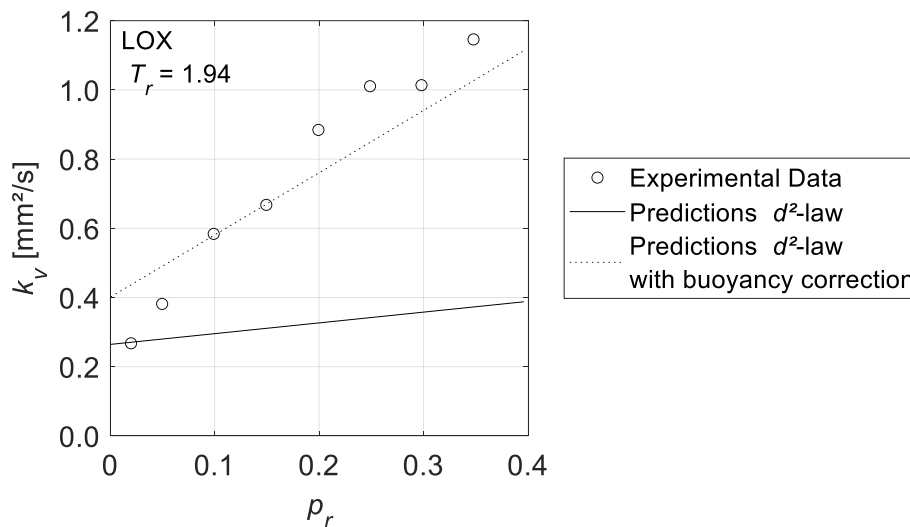


**Figure 16:** Variation of the average vaporization rate constant of LOX droplets with pressure in helium at 300 K. Adapted from [79].

To compare these findings with predictions of the  $d^2$ -law, they applied a buoyancy correction based on the Grashof number. This correction includes gravity effects and leads to a rough agreement of the measured data with the prediction of the  $d^2$ -law. The increasing average vaporization rates of LOX with increasing pressure are in contrast to

the results obtained with n-heptane droplets under the same ambient conditions, i.e., at room temperature. They explained this difference by the higher reduced temperature of the gaseous environment, which was  $T_r = 2$  in the LOX experiments and 0.6 in the hydrocarbon experiments [79]. However, this study cannot be directly compared quantitatively with the previous study because Yang *et al.* [78] studied a stationary surface rather than vaporization on a single droplet.

The vaporization effects have been studied much more extensively with respect to hydrocarbons. Sato [80] summarizes extensive vaporization studies on n-heptane droplets under  $\mu\text{g}$  and 1g. Figure 17 shows the difference between  $\mu\text{g}$  and 1g droplet vaporization experiments. After an initial heating phase, the square of the droplet diameter decreases almost linearly and thus corresponds to the course of the  $d^2$ -law.

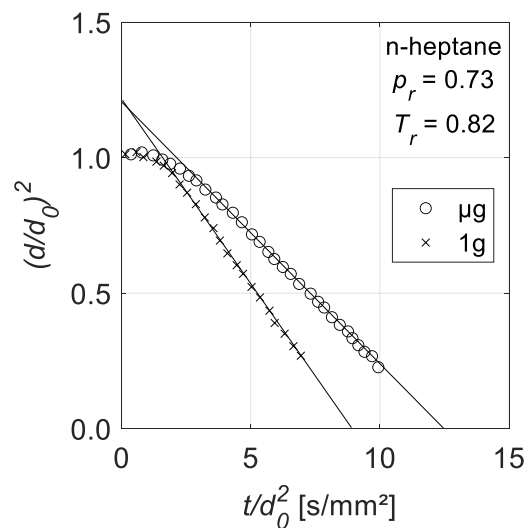


**Figure 17:** Droplet regression of vaporizing n-heptane droplets at 2 MPa and 445 K under  $\mu\text{g}$  and 1g. Adapted from [80].

As noted in the study by Chesneau *et al.* [79] on vaporization of oxygen droplets, ambient temperature has a major effect on the vaporization rate constant, as shown in Figure 18 for n-heptane. Both under  $\mu\text{g}$  and under 1g, the vaporization rate constant increases with increasing ambient temperature. Consistent with Figure 17, the vaporization rate constant under microgravity conditions is slightly lower than at 1g. The effects of ambient pressure on the vaporization rate constant of n-heptane droplets at different ambient temperatures at 1g are shown in Figure 19. At low ambient temperatures, the vaporization rate constant first decreases with increasing pressure, then reaches a minimum before increasing again. From a temperature  $T_r < 0.69$  on, the vaporization rate constant no longer reaches a minimum, but increases monotonically. When the temperature exceeds the critical value  $T_r > 1$ , the vaporization rate constant first increases and then reaches a maximum, which is above the critical pressure. As the temperature continues to rise, the initial increase in the vaporization rate increases more rapidly. The pressure at which the vaporization rate reaches the maximum at high ambient temperatures decreases as the ambient temperature increases in the direction towards the critical pressure [80].

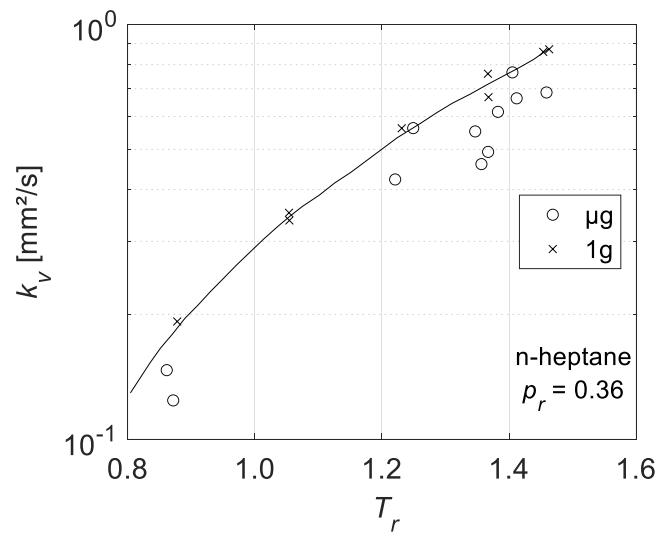


**Figure 18:** Effects of the ambient temperature on the vaporization rate constant of n-heptane droplets at 1 MPa under  $\mu\text{g}$  and  $1\text{g}$ . Adapted from [80].

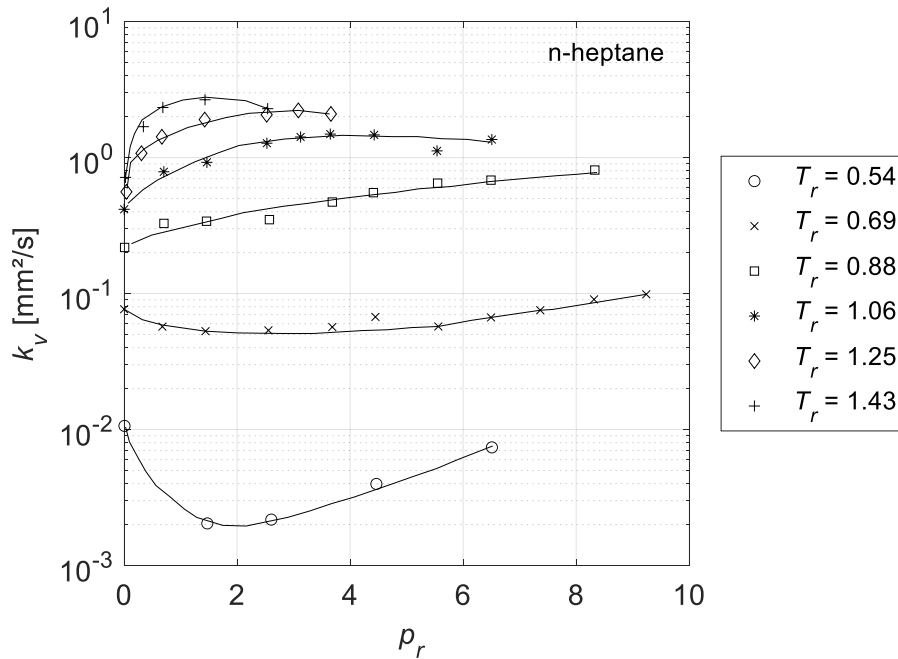


**Figure 19:** Effects of the ambient pressure on the vaporization rate constant of n-heptane droplets at different ambient temperatures under  $1\text{g}$ . Adapted from [80].

Another detailed study on the effects of temperature and pressure was conducted by Nomura *et al.* [81]. They investigated suspended n-heptane droplets under microgravity at pressures in the range of 0.1-5.0 MPa ( $p_r = 0.04$  to 1.83) and at temperatures varying from 400 to 800 K ( $T_r = 0.74$  to 1.48). At high pressures and high temperatures, the outer edge of the droplet became gradually obscured by the dense vapor surrounding the droplet. They measured the ratio of the initial heat-up time to the vaporization lifetime,

which was almost independent of the ambient temperature at a pressure of  $p_r = 0.04$ . However, at higher pressures, the ratio increases as the ambient temperature increases [81].

In a more recent study, Nomura *et al.* [82] investigated the droplet vaporization of n-hexadecane at subcritical and supercritical conditions in  $\mu\text{g}$ . The pressure was varied from 1 to 3 MPa ( $p_r = 0.71$  to 2.13) and a temperature of 773 K ( $T_r = 1.07$ ) was set. They found that the vaporization rate constant increases linearly with ambient pressure, reaches a maximum slightly above the critical pressure, and then decreases linearly. These results are consistent with findings on n-heptane [80]. They also studied the droplet lifetime and initial heat-up period and found that at subcritical ambient pressures, the droplet vaporization lifetime increases with increasing pressure, although the vaporization rate constant also increases. This is due to the increase in initial heating time overtaking the increase in quasi-steady-state vaporization period. They concluded that for fuels with a high critical temperature, the initial heating time determines the dependence of ambient pressure on the droplet vaporization lifetime in the vicinity of the critical point of the fuel [82].

### 3.1.2. Numerical studies

In contrast to the very limited number of experimental studies, there have been many numerical studies on LOX droplet vaporization. The numerical studies discussed here are mostly based on 1D models (assuming spherical symmetry). These results can only be compared with experiments under microgravity in a quiescent environment. In all models, radiation was neglected because the effect is small in the pure vaporization case.

One of the first numerical investigations of the vaporization of an LOX droplet in hydrogen under subcritical and supercritical conditions and high ambient temperatures was carried out by Delplanque & Sirignano [83]. In addition to unsteady effects at subcritical pressure conditions, such as transient droplet heating, they also studied vaporization effects near the critical point. In their model they assumed spherical symmetry (1D) as well as constant pressure and used Fick's law in the species transport equation. Dufour effects and viscous dissipation were neglected in the model and the momentum equation was not solved in the gas phase where the pressure is constant. In addition, convection in the droplet was also neglected [83]. They found that the fractional difference between the droplet surface and droplet core temperature is larger compared to hexane droplets and remains significant during most of the droplet lifetime. In the supercritical pressure regime, neglecting gas-phase solubility in the droplet results in significant underestimation of the critical mixing temperature, which is reached very quickly by the droplet surface at hot ambient temperature [83].

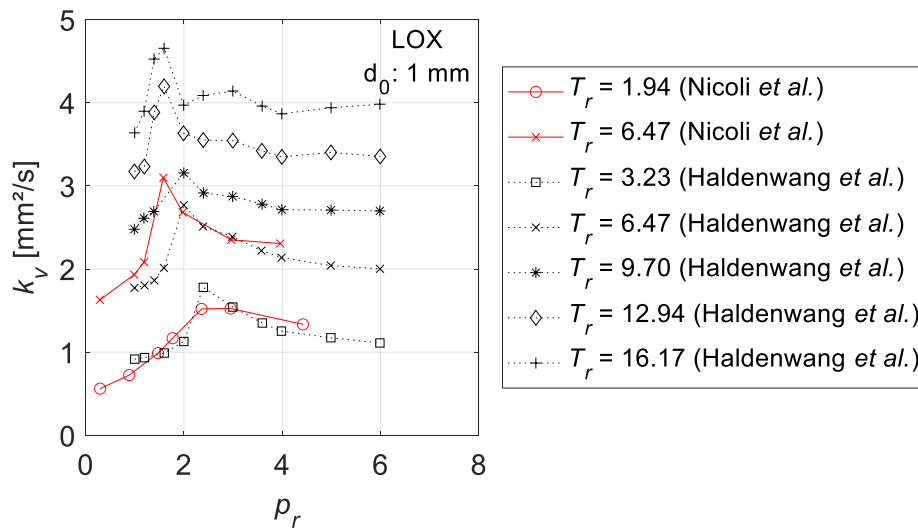
Yang *et al.* [78] performed numerical studies on gas solubility at the surface of a LOX droplet in helium to compare these results with their experimental results, which are discussed in chapter 3.1.1. In their two-dimensional (2D) model they considered the influence of gravity on the axial momentum equation due to the large temperature gradient between the LOX surface and the surrounding flow. They assumed that the flows are steady state, the flow field is axisymmetric, Fick's law of mass diffusion is valid, and

the LOX surface is in thermodynamic phase equilibrium. Additionally, they neglected viscous dissipation, Dufour and Soret effects as well as radiation and turbulence. Based on these assumptions, they calculated the mole fraction of helium dissolved in the LOX at different pressures. For  $p_r = 0.60$  they determined a mole fraction of 0.7 % and for  $p_r = 1.37$  a mole fraction of 8.4 %. They concluded that the gas solubility in the liquid becomes significant with increasing pressure [78]. Oschwald *et al.* [84] came to the same conclusion when studying the phase behavior of the oxygen-hydrogen system in equilibrium.

In another study, Harstad & Bellan [85] investigated the behavior of an isolated oxygen droplet in a hydrogen atmosphere at supercritical conditions. Based on a 1D model, their results showed that the supercritical behavior is that of a slow diffusion process. Parametric studies varying initial liquid droplet size, ambient pressure, and ambient temperature showed that gradients increase with increasing pressure and lower temperatures. Considering practical applications, they concluded that, given the long characteristic time associated with diffusion, increasing turbulence is required to mix LOX and hydrogen in liquid rocket engines at higher pressures [85].

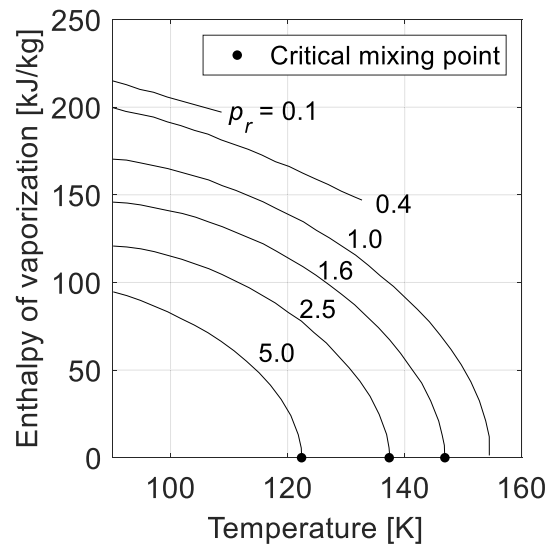
Nicoli *et al.* [86] investigated possible substitute mixtures for LOX droplet vaporization studies in hydrogen to enable “safe” experiments. They numerically studied the vaporization of liquid oxygen in a hydrogen atmosphere (LOX-H<sub>2</sub>) and compared the results with those of liquid oxygen in a helium atmosphere (LOX-He) and in a nitrogen atmosphere (LOX-N<sub>2</sub>) as well as liquid nitrogen in a hydrogen atmosphere (LN<sub>2</sub>-H<sub>2</sub>). The comparisons showed that nitrogen is not a good substitute for hydrogen. However, the combinations of LOX-He, LN<sub>2</sub>-H<sub>2</sub>, and LOX-H<sub>2</sub> showed good qualitative agreement. They concluded that liquid nitrogen as a substitute for liquid oxygen, i.e., the LN<sub>2</sub>-H<sub>2</sub> system, seems to be the best way to obtain meaningful data [86].

Figure 20 shows the influence of ambient pressure on the vaporization rate constant at different ambient temperatures for LOX droplets with a diameter of 1 mm based on two different studies [86, 87]. Similar to the experimental results of vaporization of n-heptane droplets at high ambient temperatures shown in Figure 19, the numerical results also indicate a maximum in the vaporization rate constant for oxygen droplets. Haldenwang *et al.* [87] termed this phenomenon, which occurs at high temperatures close to the critical pressure, “transcritical minimum”. However, they found that the chosen definition of the droplet surface under supercritical conditions (based on temperature or mass fraction) strongly affects the appearance of this phenomenon.



**Figure 20:** Comparison of different numerical studies on the effect of the ambient pressure on the vaporization rate constant of LOX droplets with a diameter of 1 mm at different ambient temperatures from 300 K to 2500 K. In the supercritical regime, the droplet surface is defined at position of the critical mixture composition. Adapted from Nicoli *et al.* [86] and Haldenwang *et al.* [87]. Vaporization rate constant calculated from droplet lifetimes based on Equation (41).

Yang *et al.* [88] also studied the pressure effects on oxygen droplet vaporization in hydrogen environments. For an initial droplet diameter of 100  $\mu\text{m}$ , they found that the droplet lifetime decreases significantly with increasing pressure in the subcritical regime before decreasing very rapidly in the supercritical regime up to a pressure of 8 MPa ( $p_r = 1.6$ ). Above that pressure, the droplet lifetime then increases slightly with increasing pressure. In the supercritical regime, the rate is roughly 5 times higher compared to the results presented in Figure 20. However, in their study, the critical mixing temperature was used as the criterion for the droplet surface in the supercritical regime. The authors explained the increase in the vaporization rate in the subcritical regime by the decreasing enthalpy of vaporization with increasing pressures, as shown in Figure 21. This effect dominates the counteracting effect of decreasing mass diffusivity with increasing pressure and leads to the observed increase in vaporization rate. At  $p_r \geq 1.6$ , the droplet surface quickly reaches the critical mixing temperature, so that the enthalpy of vaporization approaches zero. Now, the droplet behavior is dominated by mass and thermal diffusion, which are affected by pressure [88]. Yang summarized that pressure affects the droplet lifetime and thus the vaporization rate through its influence on the critical mixture temperature and the ambient thermal diffusivity [38].



**Figure 21:** Numerical results showing the effect of pressure and temperature on the enthalpy of vaporization of oxygen in an equilibrium mixture of oxygen and hydrogen. Adapted from [88].

Lafon *et al.* [89, 90] also studied the vaporization effects of a small oxygen droplet in a hot hydrogen atmosphere, including the effects of the Dufour and Soret cross-diffusion terms [90]. Their model results showed a steady increase in the vaporization rate and a corresponding decrease in the droplet lifetime with increasing pressure even above the critical pressure of oxygen, as shown in Figure 22.

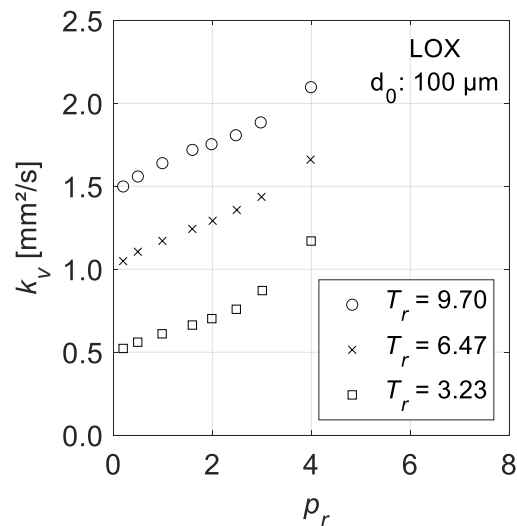


**Figure 22:** Numerical results on the effect of the ambient pressure on the vaporization rate constant of LOX droplets with a diameter of 100  $\mu\text{m}$  at different ambient temperatures. Vaporization rate constant calculated from droplet lifetimes based on Equation (41). Adapted from [89].

In the supercritical regime, the droplet lifetime was seen to decrease more rapidly with increasing pressure [89, 90]. This trend depends on the ambient temperature and the

definition of the droplet surface. The droplet lifetime may even increase slightly in the supercritical pressure regime, at a low ambient temperature below 500 K. In this case, a minimum droplet lifetime occurs at an intermediate pressure above the critical pressure of oxygen [90]. The Dufour and Soret cross-diffusion terms were estimated to have a negligible effect on the determination of the droplet lifetime [90].

In summary, these numerical studies exhibit significant differences with respect to supercritical vaporization rate constants. Some studies [78, 83, 89, 90] report monotonically increasing vaporization rates, whereas other studies [86-88] indicate local maxima in the supercritical regime. Possible factors influencing the profile of the vaporization rates are the ambient temperature and most important the definition of the droplet surface in the supercritical regime [87].

In addition to these studies on droplet vaporization in quiescent environments, numerous numerical studies have been performed to investigate other aspects of LOX droplet vaporization. Examples include studies on vaporization characteristics under convective conditions, e.g., by Litchford [91], Delplanque & Sirignano [92], and Meng *et al.* [93, 94], or the study by Lafon *et al.* [95] on pressure-coupled responses of vaporizing droplets. However, these studies are only indirectly relevant in the context of this thesis and are mentioned here only for the sake of completeness.

## 3.2. Droplet combustion

As in the previous chapter, the state of the research on droplet combustion is divided in this subchapter into experimental and numerical studies. In addition to a review of published studies on LOX combustion, some studies on hydrocarbon droplet combustion relevant to this thesis are also reviewed. These studies relate to individual phenomena in droplet combustion research, such as the influence of the ambient pressure, and thus represent only a small fraction of the extensive research on droplet combustion of hydrocarbons. Finally, the topic of water condensation is treated separately at the end of this subchapter.

### 3.2.1. Experimental studies

The experimental studies on droplet combustion are divided into experiments under reduced gravity conditions and under normal gravity conditions. The reduced gravity conditions include both experiments in a drop tower with residual accelerations in the order of  $10^{-6}$  g, and parabolic flights with residual accelerations of  $\sim 10^{-2}$  g [96].

#### 3.2.1.1. Reduced gravity conditions

Early experiments on single droplet combustion were conducted in the 1950s [26, 56, 97]. Godsave [56] investigated burning droplets of several fuels with shadowgraph imaging and found that the droplet lifetime is proportional to the square of the droplet diameter. His work and the work of Spalding [26] led to the formulation of the  $d^2$ -law, as described in chapter 2.5.2. To enable comparison with theoretical (spherically symmetric) droplet combustion models, convection must be eliminated, since otherwise the influence of natural convection on the droplet burning rate is too severe to be neglected [19]. For this

reason, Kumagai & Isoda [19] performed the first systematic droplet combustion experiments on n-heptane and ethanol under microgravity conditions back in 1957. They applied Schlieren imaging and direct photograph imaging in a free-falling combustion chamber to track the flame as well as the droplet regression. In their study, they investigated the effect of natural convection on droplet combustion by varying the acceleration of the combustion chamber. They found that the burning rates decrease as acceleration decreases. As the acceleration approaches zero leading to a spherical flame, the fuel droplet is not affected by natural convection [19].

Faeth *et al.* [98] studied the influence of ambient pressure and ambient oxygen concentration on single n-decane droplets in a free-fall apparatus under microgravity conditions ( $\sim 1$  s of test time). They used droplets with initial diameters in the range of 0.6 to 1 mm and varied the pressure between 0.7 to 13.8 MPa ( $p_r = 0.3$  to 6.6) at room temperature. When measuring the combustion lifetimes, they found that the lifetimes gradually decrease with increasing pressure and reach a minimum near the critical pressure of the droplet. In Figure 23 the dependence of the burning rate constant on the pressure is shown.

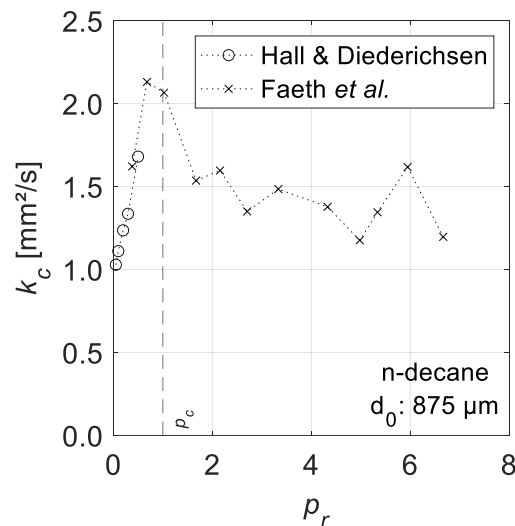


**Figure 23:** Experimental results on the effect of the ambient pressure on the burning rate constant of n-decane droplets with a diameter of 875  $\mu\text{m}$  in air at room temperature under  $\mu\text{g}$ . Combustion rate constant calculated from combustion lifetimes based on Equation (41). Adapted from Hall & Diederichsen [99] and Faeth *et al.* [98].

They explained this phenomenon by the reduced mass diffusivity and the increased vaporization rate with increasing pressure [100]. Above the critical pressure, the combustion lifetime increases again with increasing pressure, which is due to the reduced diffusion rates in the gas phase at higher pressures. The authors attribute the scatter in the data at high pressures to variations in the droplet temperature at the time of ignition and to interference effects from hot wire ignition. In addition, they observed that as the oxygen content in the ambient atmosphere increased, the combustion lifetime was increasingly

reduced. This was attributed to the higher droplet temperature due to the reduced flame distance [98, 100].

These results are in agreement with the experimental data of Sato *et al.* [101], who studied the combustion of n-octane droplets in air under  $\mu\text{g}$ . The burning rate constant, as determined from the  $d^2$ -law, was seen to increase with increasing ambient pressure and to reach a maximum near the critical pressure of the fuel, as shown in Figure 24. Beyond the critical pressure, in the supercritical regime, the burning rate decreases slightly. Law [1] summarized these results and attributed the increase in burning rate in the subcritical regime to the reduced enthalpy of vaporization. In contrast, he attributed the decreasing burning rate constant in the supercritical regime to the dependence of the mixture between fuel vapor and ambient gas on the mass diffusivity, which decreases with increasing pressure in this inherently transient regime.

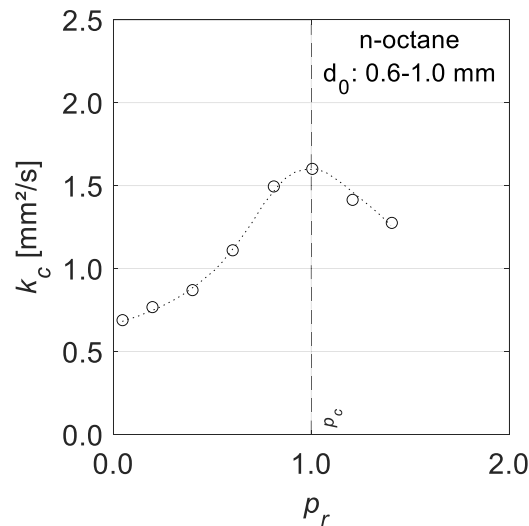


**Figure 24:** Experimental results on the effect of the ambient pressure on the burning rate constant of n-octane droplets with a diameter between 0.6 to 1.0 mm in air under  $\mu\text{g}$ . Adapted from [101].

In addition to n-octane, it was found that also n-heptane, n-decane, n-hexadecane, ethanol, and methanol showed a similar pattern of changes in burning rate with pressure under microgravity conditions [80]. Vieille *et al.* [96] also studied several of these fuels under reduced gravity on parabolic flights (gravity level  $\sim 10^{-2} \text{ g}$ ) and also found an increasing burning rate constant with increasing pressure in the subcritical regime. In the supercritical regime, however, the burning rate constant remains almost constant and the scatter prevents a general statement on the trend. In a review study, Givler & Abraham [59] concluded that the available data indicate a minimum combustion lifetime occurring exactly at the critical pressure for all hydrocarbons. However, in another review study, Bellan [100] found no clear maximum in the burning rate constant near the critical point in the data of Vieille *et al.* [96] and referred to different levels of microgravity compared to the studies of Faeth *et al.* [98] and Sato *et al.* [80, 101]. A similar sensitivity to residual accelerations was detected by Chauveau *et al.* [102] who found a significant effect of buoyancy even with reduced gravity in parabolic flights. Williams [27]

developed a burning rate correction for free convection conditions based on the Grashof number for  $Gr < 1$ :

$$k = k_{ideal}(1 + 0.533Gr^{0.52}) \quad (51)$$

where  $k_{ideal}$  is the burning rate constant at ideal (spherical) conditions based on the  $d^2$ -law.

Another issue that has been intensively discussed in the literature is the evolution of the flame standoff ratio. According to the  $d^2$ -law, the ratio between flame diameter and droplet diameter, i.e., the flame standoff ratio, is constant, as described in chapter 2.5.2. However, some studies on single droplet combustion under  $\mu g$  have demonstrated that the flame standoff ratio increases continuously during the droplet lifetime, e.g., [58, 103, 104]. Law [1] identified two areas: At low oxygen concentrations, the flame standoff ratio increases continuously, whereas at high oxygen concentrations it levels off. In both cases, the flame size first increases and then decreases. This can be attributed to the fact that at the time of droplet ignition only little fuel is present in close vicinity of the droplet surface due to the low droplet temperature. Thus, after ignition, the flame initially forms very close to the droplet. However, with ignition, the vaporization rate is rapidly increased and more fuel gas is produced. As a result, the flame expands and increases the distance to the droplet [1]. This effect depends on the ambient oxygen concentration, since at low concentrations more fuel gas is vaporized than burned. As a result, fuel vapor accumulates in the inner region of the flame, causing the flame standoff ratio to increase, as the flame moves towards the stoichiometric mixture [58]. It was also pointed out that the combustion lifetime and the droplet lifetime may be different due to residual fuel vapor that needs additional time to burn [80]. A comparison of the total time of combustion (combustion lifetime)  $\tau_c$  and the total time of gasification (droplet lifetime)  $\tau_g$  for the combustion of n-heptane droplets under  $\mu g$  is shown in Figure 25a. In the subcritical pressure regime, both the combustion and the droplet lifetimes decrease. In the supercritical regime, the combustion lifetime increases with increasing ambient pressure, whereas the droplet lifetime decreases continually. The time difference between combustion lifetime and droplet lifetime is the time required to burn the remaining fuel vapor. It was concluded that the increase in combustion lifetime with increasing pressure could be attributed to decreasing diffusion rates of the fuel vapor and the surrounding oxygen at high pressures [80]. These findings on droplet and combustion lifetimes are consistent with the results from Faeth *et al.* [98] on n-decane droplets.

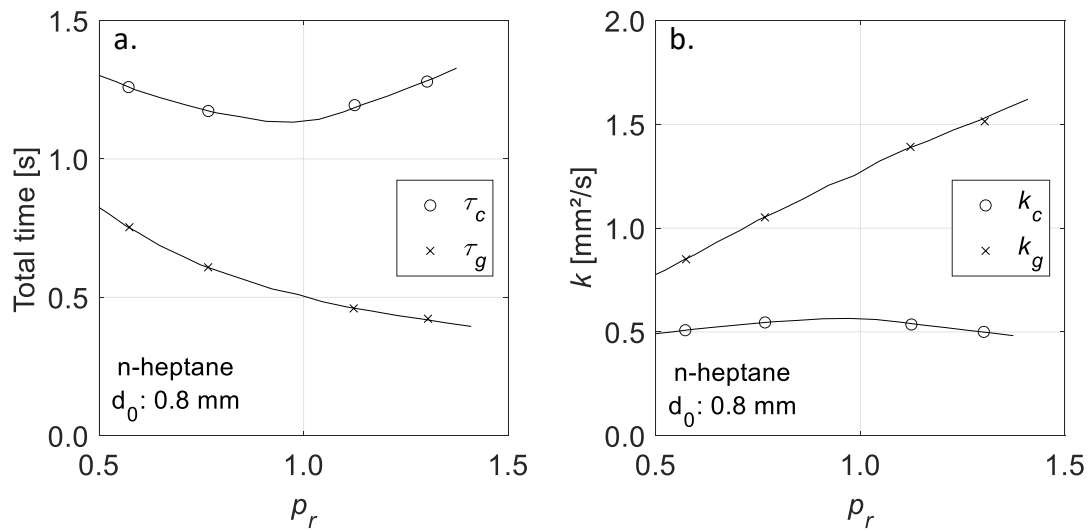


**Figure 25:** Comparison of the ambient pressure effects on the total time of combustion/gasification (a.) and on the burning/gasification rate constant (b.) of n-heptane droplets with a diameter of 0.8 mm in 13 % oxygen under  $\mu g$ . Adapted from [80].

In addition to the single droplet combustion studies on hydrocarbons presented, detailed studies on droplet interactions under  $\mu g$  have been performed, e.g., by Mikami *et al.* [23, 105], Okai *et al.* [106], or Eigenbrod *et al.* [21, 22]. The results were compared with observations from single droplet studies as a first step towards a better understanding of the interactions in technical spray combustion, however, these studies are only indirectly relevant in the context of this thesis.

### 3.2.1.2. Normal gravity conditions

As explained above, to study spherically symmetric droplet combustion, the technique of gravity-minimized environments, such as free-fall experiments in a drop tower, experiments on parabolic flights, or on the International Space Station (ISS), has often been used and is well established. In addition to this complex and costly technique, studies on single droplets or droplet interaction have been carried out under 1g conditions, e.g., in the field of flame spray pyrolysis (FSP), e.g., [107-109]. In these studies, droplets with initial diameters of about 100  $\mu m$  were generated and burned in a free-floating configuration. Due to the very small droplet size, the buoyancy effects under normal gravity were strongly reduced, as already shown in chapter 2.6 using the Grashof number. Recently, Li *et al.* [108] studied the interactions of two p-xylene droplets, which is a common solvent used in FSP. They used a three-dimensional (3D) measurement system based on two high-speed cameras to track the 3D trajectories, velocities, and diameters of the droplets as well as the diameters of the visual flames. By changing the droplet spacing and ambient oxygen concentration, different interaction scenarios could be identified and described. For example, they found that in a pure oxygen atmosphere, the flame size and brightness as well as the flame standoff ratio increase with decreasing flame spacing. The droplet burning rate constant, on the other hand, decreases, which is

attributed to the competition of oxygen in the environment [108]. In this study, the free-floating configuration eliminated the influence of the fiber, which is often used in 1g and  $\mu\text{g}$  experiments to suspend and position (comparably) large droplets. However, buoyancy effects and the velocity differentials between the droplet and the co-flowing atmosphere affect the combustion process and must be considered in fundamental studies.

The experimental studies discussed here were related exclusively to the combustion of hydrocarbon or alcohol droplets. As already noted in the review of experimental studies on droplet vaporization of LOX, on the one hand, the safety requirements for handling oxygen and hydrogen are very high, and on the other hand, the general experimental effort required to generate and combust cryogenic droplets is also very high. In the field of spray combustion research, several studies have been conducted on the oxygen-hydrogen system. In addition to some studies on injection as well as on the mixing and atomization processes of LOX in inert environments, e.g., [84, 110], many studies on combustion and ignition in miniaturized and optically accessible rocket motors have been conducted, e.g., [12, 41, 111-115]. However, no experimental studies on single droplet combustion of LOX in hydrogen atmosphere have been carried out to date.

Yang *et al.* [18, 116] chose an alternative approach to study LOX combustion. They considered a limiting case where the radius of the droplet curvature is very large. A column of LOX was used to create a constant liquid surface which was held in a fixed location. A hydrogen-helium mixture was supplied around the central tube in which the LOX was fed. By this means, an axisymmetric diffusion flame could thus be generated at the outlet of the oxygen feed tube (diameter of 6.35 mm) under normal gravity conditions. With this setup, they investigated the steady-state burning behavior of LOX in a hydrogen-helium mixture at a pressure of 3.0 MPa ( $p_r = 0.6$ ) using a gas-sampling probe for gas chromatograph analysis and several thermocouples. The surrounding gas flow velocity of the hydrogen-helium mixture was 1.5 cm/s with a temperature of 295 K. In the experiments, the flame showed a very sensitive holding behavior when the LOX surface was held exactly at the exit opening of the feed tube. Detachment of the flame from the tube rim resulted in quenching effects that ultimately caused the flame to extinguish. Therefore, the LOX surface was held 1.5 mm below the feed tube outlet to obtain a stable diffusion flame stabilized at the hot outlet rim. At a pressure of  $p_r = 0.6$ , a temperature of 136.2 K was measured at the LOX surface. This is slightly below the boiling temperature of oxygen of 142.0 K at this pressure. In addition to the shape of the flame, the hydrogen concentration above the flame measured with a gas chromatograph was also compared with numerical simulation results, which showed good agreement [18, 116].

### 3.2.2. Numerical studies

The numerical studies on droplet combustion are subdivided according to the droplet species (LOX or hydrocarbons) and according to the ambient (flow) conditions.

### 3.2.2.1. LOX droplet combustion in a quiescent environment

Despite the lack of single droplet experiments, numerous numerical studies have been performed on the combustion of LOX droplets in hydrogen due to its relevance in the field of rocket propulsion. Lafon & Habiballah [89] used a 1D numerical model to study the combustion of LOX droplets in hydrogen. They employed a one-step kinetic and considered the condensation of water vapor, which is generated as the product of the combustion. This phenomenon is discussed in detail in chapter 3.2.3. They found that due to the high diffusion rate of hydrogen, the flame is very close to the droplet surface. The flame standoff ratio is about 3, which is considerably less compared to hydrocarbon droplets, which have a flame standoff ratio of 15 to 20. This results in no significant vapor accumulation in the gaseous phase, so they concluded that the droplet lifetime and the combustion lifetime are almost the same [89]. This is in contrast to the results for hydrocarbon droplet combustion discussed in chapter 3.2.1.

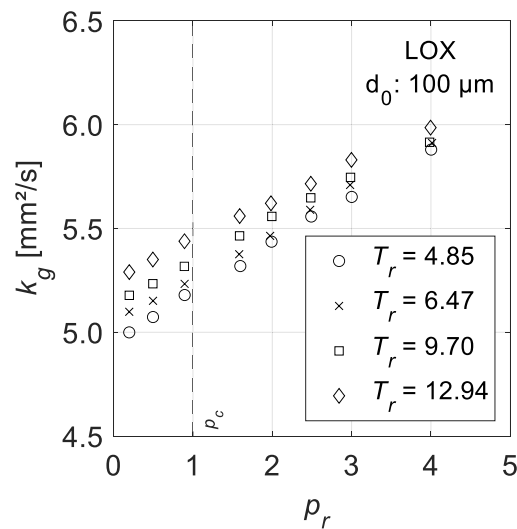


**Figure 26:** Numerical results on the effect of the ambient pressure on the gasification rate constant of burning LOX droplets with a diameter of 100  $\mu\text{m}$  at different ambient temperatures. Gasification rate constant calculated from droplet lifetimes based on Equation (41). Adapted from [89].

The effect of pressure was intensively studied at different ambient temperatures. The results are shown in Figure 26 in the form of the gasification rate constant, which is based on the droplet lifetime. The absolute values of droplet lifetime in this case are of the same order of magnitude as for pure vaporization at high ambient temperature (compare Figure 22). In the case of combustion, the gasification rate constant increases monotonically and there is no significant change in the transition from the subcritical to the supercritical regime. In contrast to results for hydrocarbon droplet combustion, where a minimum in combustion time was observed experimentally and predicted numerically, the model results showed no such phenomenon. Lafon & Habiballah explained this by the strongly reduced vapor accumulation for the hydrogen-oxygen system. They explained that for this fuel system, the gasification process is mainly controlled by heat diffusion. They

attributed the increase in gasification rate to the increase in thermal conductivity and the decrease in enthalpy of vaporization [89].

Daou *et al.* [55] performed a numerical study to investigate the combustion of an LOX droplet in a quiescent hydrogen environment under supercritical conditions with detailed chemistry. They studied the ignition as well as the flame structure and addressed the effect of ambient pressure. They found that for a droplet with a diameter of 50  $\mu\text{m}$ , the combustion time increased by less than 4 % with an increase in pressure from 10 to 20 MPa ( $p_r = 2.0$  to 4.0). They compared this with experimental results of Faeth *et al.* [98] and Sato *et al.* [101] who also found a slight increase in combustion lifetime for hydrocarbon droplets in the supercritical regime. In addition, they investigated the ignition behavior of the droplet. They showed that first a premixed flame is formed, which is initiated on the hydrogen-rich hot side. After ignition, a quasi-steady diffusion flame is formed. In contrast to the case of a single irreversible reaction, a complete chemistry model leads to a very thick flame that splits into two zones [55]. In more recent numerical studies by the author of this thesis and collaborators it was shown that the initial premixed flame may split into two individual flames shortly after ignition ( $\mu\text{s}$  scale), before the actual diffusion flame is formed. This phenomenon was explained by the wide ignition limits of the hydrogen-oxygen system, so that (for a moment) individual flames form on the lean and the rich side [117, 118].

### 3.2.2.2. LOX droplet combustion in convective environments

In contrast to the previous studies, which focused on single droplets in a quiescent atmosphere, several other studies were conducted that addressed other aspects of hydrogen-oxygen droplet combustion. As an example, Aouina *et al.* [119] studied the heating, vaporization, ignition, and subsequent combustion of a LOX droplet with a diameter of 25  $\mu\text{m}$  injected into a laminar uniform hydrogen flow with a temperature of 1500 K. An initial velocity of 20 to 70 m/s and a pressure of 0.1 MPa ( $p_r = 0.2$ ) was set, corresponding to conditions similar to liquid rocket propulsion systems. They used an axisymmetric, 2D numerical model and a detailed chemical reaction system for this purpose. Prior to ignition, it was found that the oxygen vapor concentration in the gas phase is almost circular around the droplet. In contrast, the concentration profile in the gas phase for a methanol droplet in air is strongly affected by convection. They attributed this to the different ambient pressure in the two cases and to the low Lewis number of the gaseous hydrogen and the associated high diffusion rate in the gas phase. Furthermore, they found that the ignition time reaches a minimum at an initial droplet diameter of about 50  $\mu\text{m}$ . For small droplets, this time is mainly determined by the time to reach an ignitable mixture, whereas for large droplets, the ignition time is primarily determined by the droplet heating process. In addition, they studied the interactions between two adjacent droplets and found that if droplets are sufficiently close together, one common diffusion flame forms instead of two independent flames. They concluded that droplet interactions play an important role in dense spray combustion processes [119].

Other numerical studies, e.g., Kim *et al.* [120] or Lafon *et al.* [95] addressed the dynamic responses of vaporizing or burning LOX droplets to external pressure oscillations in the

gaseous phase. These studies provided important data to improve the understanding of acoustic instabilities, which are often observed during rocket engine tests and thus of high practical relevance. In a review paper [38], Yang summarized several numerical studies on modeling vaporization, mixing, and combustion processes in the supercritical regime. In his work, in addition to the topics already mentioned, many other aspects of supercritical droplet combustion have been addressed, however, these studies are not directly relevant to this thesis and are cited as for the sake of completeness.

### 3.2.2.3. Hydrocarbon droplet combustion

In a review paper from 2000, Bellan [100] summarized many studies on modeling subcritical and supercritical fluids in various configurations, such as droplets, droplet clusters, sprays, and jets. In addition to studies on the hydrogen-oxygen system, studies on hydrocarbon combustion were also discussed. One of the first numerical studies on supercritical droplet combustion of n-pentane in air was conducted by Shuen *et al.* [61], who investigated a pressure range from 0.5 to 14.2 MPa ( $p_r = 0.15$  to 4.21). The effects of ambient pressure on different time scales are shown in Figure 27.

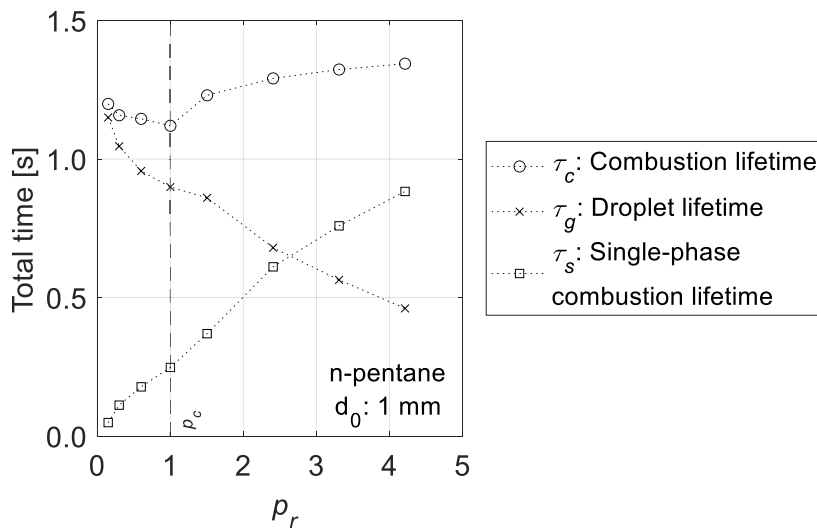


**Figure 27:** Numerical results on the effect of the ambient pressure on different time scales for the combustion of a n-pentane droplet with a diameter of 1 mm in air at a ambient temperature of 1000 K. Adapted from [61].

They found a minimum of the combustion lifetime near the critical pressure of the liquid fuel, which is in qualitative agreement with experiments reported in chapter 3.2.1. In contrast, the droplet lifetime decreases monotonically over the entire pressure range investigated, which is mainly caused by the decrease in enthalpy of vaporization. This effect overrides the counteracting effect of the decrease in mass diffusivity with increasing pressure, resulting in a net increase of the surface regression rate and a decrease of the droplet lifetime, respectively. Looking at the very early phase of the droplet lifetime, the relatively fast increase of temperature at the droplet surface can lead to a rapid decrease of the liquid density and thus to a volume expansion. In the initial phase, this effect may offset the regression due to vaporization and cause the droplet to exceed

its initial size. Due to the decreasing mass diffusivity and the associated increasing vapor accumulation, the single-phase combustion lifetime, i.e., the (gaseous) combustion lifetime after the droplet has vanished, increases significantly with increasing pressure, as shown in Figure 27. The droplet lifetime and single-phase combustion lifetime characteristics lead to the irregular behavior of the total combustion lifetime [61].

Another effect observed by Shuen *et al.* is the decrease of the peak flame temperature with increasing pressure due to the increase of the Lewis number. They found a monotonic decrease from 2885 K at  $p_r = 0.15$  to 2202 K at  $p_r = 4.21$  and attributed this to the slower diffusion of fuel vapor to the flame zone at high pressures. However, the authors of the study concluded that a quantitative comparison of their numerical results with experimental data is rather difficult because they neglect radiation effects in their model. They estimated that the ratio of the radiative heat flux to the total energy flux required for vaporization is only 1 % for droplets with a diameter of 100  $\mu\text{m}$  at a pressure of 5.0 MPa ( $p_r = 1.5$ ). Whereas for large droplets with a diameter of 1 mm this fraction increases significantly to 40 % for the temperature range considered in that study. Another simplification in the model was the use of one-step kinetics. However, Shuen *et al.* concluded that the simplified kinetics primarily affect the ignition processes, and since these only occupy a small portion of the droplet lifetime, they assumed that the influence on their results was not significant [61]. Bellan reviewed this study and noted that in addition to Soret and Dufour effects, also solubility effects at the droplet surface were neglected. In addition, thermodynamic equilibrium was assumed when the critical conditions were not present. These assumptions may have affected the accuracy of the results. However, a comparison with an experimental study by Canada & Faeth [121] showed that the predicted continuous increase in gasification rate with increasing pressure from the subcritical to the supercritical regime is consistent with the experimental data [100].

#### 3.2.2.4. Recent advances in numerical modeling

In recent years, more and more powerful computational resources have become available and the numerical models for the simulation of droplet combustion have been continuously improved. As an example, Moriue *et al.* [122] numerically studied the spontaneous ignition of single n-heptane droplets of technical dimensions ( $d_0 = 1$  to 100  $\mu\text{m}$ ). Experimental studies have shown that the phenomenon of two-stage ignition with the appearance of the cool-flame occurs for large droplets with a diameter of 0.7 to 1 mm, e.g., [123]. By using reduced kinetics with 437 reactions and 92 species, validated by comparison with experiments on large droplets ( $d_0 \sim 0.7$  mm), the two-stage ignition behavior as well as the ignition delay time of the cool-flame and also of the hot-flame could be reproduced for small droplets of a size for practical use [122]. More recently, this numerical model was further developed by Klinkov *et al.* [124] and was used to study the autoignition of n-heptane droplets in technical sprays. The single droplet model, which includes the droplet related physics and chemistry, was coupled with an external flow simulation to represent the spray formation, turbulence, and droplet trajectories. The initial parameters and boundary conditions were chosen to approximate the spray effects

of neighboring droplets in the flow [124]. The results of this study are not directly relevant to this thesis, but they demonstrate the importance of single droplet experiments. This study is an example that highlights the potential of numerical model development for real technical applications based on fundamental experimental data.

Another study demonstrated the possibilities based on the latest computational advances and the development of new numerical models and tools. Saufi *et al.* [125] investigated the combustion of a fuel droplet suspended in normal gravity using an OpenFOAM<sup>®</sup> solver. They modeled a methanol droplet on a vertical quartz fiber in a 2D axisymmetric domain and ignited the droplet with a simulated spark. In the model, in addition to the conservation equations of momentum, energy, and mass of the species, a detailed description of the interfacial thermodynamics based on cubic equations of state were implemented. Moreover, the volume-of-fluid method was used for interface advection. The model included reduced kinetics (20 species, 129 reactions), a radiation model, and the heat transfer from the suspender fiber to the droplet. The detailed modeling enabled the investigation of the flame-suspender interaction, the effect of gravity on the flame properties, the main species distribution around the droplet, the velocity field inside the droplet, and the water absorption in the liquid phase [125]. By taking into account the suspender effect, the combustion characteristics of the experiments, such as the droplet regression, could be numerically determined with good agreement. This study demonstrates the progress in modeling capabilities and the possibilities that can be enabled by modern numerical tools.

### 3.2.3. Water condensation

A special phenomenon that can occur during the combustion of LOX is the condensation of water vapor as product of the combustion process with hydrogen. As shown in Equation (23), the reaction of gaseous oxygen with hydrogen produces water, which is also in the gaseous state near the flame (water vapor). However, condensation of water vapor during droplet combustion can occur either outside or also inside the hot flame shell near the cryogenic droplet surface. In both cases, the ambient temperature must be below the boiling temperature and the vapor pressure must be exceeded, as shown qualitatively in Figure 10. When the temperature is below the melting temperature of water, the phase change occurs first from gaseous to liquid and then from liquid to solid (water ice), as long as the partial water pressure is above the triple point pressure of water (0.61 kPa [126]). Below this pressure, there is no liquid phase and the water vapor deposits directly to ice.

Powell [127] attempted to experimentally simulate the condensation of water vapor on the oxygen droplet surface using liquid nitrogen as a substitute. He injected cryogenic nitrogen droplets with a diameter of 0.6 mm into a superheated steam chamber and attempted to visualize a layer of water or ice on the droplet surface. However, with the diagnostic technique used, he was only able to detect small ice or water particles in the wakes of the liquid nitrogen droplets and not on the droplet surface. Powell concluded that if layers of condensed water did form, they were likely only a few micrometers thick and beyond the resolution of the imaging techniques used [127].

Litchford & Jeng [91] studied numerically the vaporization of LOX droplets in hydrogen at subcritical and supercritical pressures under convective conditions. They also considered the effects of water vapor near the droplet surface and suggested that significant water vapor concentrations can occur near the droplet and therefore this effect should be considered in equilibria computations. This could lead to two scenarios: first, supersaturated water vapor exists at the droplet surface, or second, the water vapor condenses and forms ice crystals at the surface. Calculations on this indicated no vapor-liquid equilibria conditions are allowed if supersaturated water vapor is present above trace concentrations. They concluded that the formation of ice crystals seems to be a likely possibility. With regard to possible droplet experiments, Litchford & Jeng pointed out that the importance of considering not only the ice formation on the surface during vaporization, but also any remaining ice particles after the droplet vanishes, which might be easier to detect and could serve as a first indication of ice formation [91].

Daou *et al.* [55] showed with numerical simulations in the supercritical regime using species profiles that water is transported close to the droplet surface. Since they did not consider condensation in their model, they did not address the issue further. Lafon *et al.* also reported the condensation or freezing of water vapor near the oxygen droplet surface in several numerical studies [89, 90, 95]. They assumed that the nucleation process takes place almost instantaneously and condensed water is subjected to thermophoretic and viscous forces [90]. They also pointed out that water or ice particles are continuously blown away from the droplet surface by the gaseous flow of oxygen induced by droplet vaporization [89]. Therefore, the water or ice layer was assumed to be very thin since the high diffusivity of hydrogen leads to a flame zone close to the droplet surface, resulting in a steep local temperature gradient [95]. Lafon & Habiballah [89] found that the condensation limit for water is reached in the direct vicinity of the droplet, at about 0.3 times the instantaneous droplet radius, and attribute this to the Stefan flow at the surface. This location has a local temperature of about 400 K. Due to the release of the enthalpy of condensation of the water, an increase of the vaporized mass flow rate of about 5-10 % was determined. In addition, they compared the phenomenon of water or ice formation around the droplet to a phenomenon that can occur during hydrocarbon droplet combustion [89]. In some studies [128, 129], it was observed that carbon particles formed at the flame diffused to the droplet surface and agglomerated in the direct vicinity of the surface. This shell could hide the droplet surface for optical visualization. The position of the shell is determined by thermophoretic effects and is particularly efficient for large molecules or particles diffusing towards the cold droplet surface [89].

Other studies reported micro-explosions with burning alcohol droplets where the exhaust water outmatches the droplet's blowing and accumulates in the droplet's surface as it is soluble in alcohol. The layer in this case forms a vaporization barrier as it has a higher boiling temperature than pure alcohol, which leads to micro-explosions [106, 130]. This could also occur with burning oxygen droplets when oxygen vapor breaks through a potential ice shell, but this has neither been numerically predicted nor experimentally observed so far.

### 3.3. Summary and contrast of the reviewed studies

In the case of pure vaporization, the essential comparison variable is the vaporization rate constant and its pressure as well as temperature dependence. The reviewed experimental studies under 1g conditions on LOX vaporization in helium show a linear increase of the vaporization rate in the subcritical pressure regime as well as into the supercritical regime [78, 79]. In contrast, experimental studies under  $\mu\text{g}$  conditions on the vaporization of various hydrocarbons, e.g., n-heptane, in air found a maximum in the vaporization rate constant above or near the critical point of the fluid [80-82]. However, the occurrence and pressure value of a maximum depends on the ambient temperature [79, 80]. For the hydrocarbon case, it was concluded that the initial heating time determines the dependence of ambient pressure on the droplet vaporization rate in the vicinity of the critical point of a fuel with a high critical temperature [82]. Compared to hydrocarbons, the critical temperature of LOX is very low. And the reduced ambient temperatures were also significantly higher in the LOX studies with  $T_r = 1.88$  and  $1.94$ , respectively, compared to the hydrocarbon studies with a maximum of  $T_r = 1.43$ . Therefore, the numerical studies on the pressure effect on the vaporization rate of LOX droplets are only comparable with the experimental studies to a very limited extent. First, in the numerical studies, the vaporization was calculated in a hydrogen environment, instead of helium. Second, the simulations were performed under the assumption of spherical symmetry and thus cannot reproduce the 1g experimental results. In some numerical studies, monotonically increasing vaporization rates were found [78, 83, 89, 90]. In other studies, a local maximum of the vaporization rate in the supercritical regime was found [86-88]. The main difference is the definition of the droplet surface in the supercritical regime, for which no unified definition has been used (critical temperature or mass fraction as a criterion) [87]. In summary, the pressure effect on the vaporization rate of a LOX droplet is controversially discussed in the literature, and the experimental and numerical studies do not provide a clear conclusion.

In the case of droplet combustion, the main characteristics are the burning (or gasification) rate constant and the flame standoff ratio. In the absence of experimental studies on individual LOX droplets, only studies on hydrocarbon droplets can be used to experimentally evaluate these characteristics and transfer them to the LOX-H<sub>2</sub> system. In several studies under  $\mu\text{g}$  conditions with different hydrocarbons, e.g., n-decane, n-octane, or n-heptane, it was shown that the burning rate constant reaches a maximum near the critical point of the fuel [59, 80, 98, 101]. With respect to flame position, it has been shown both experimentally and numerically that for hydrocarbon droplets in low oxygen concentration, vapor accumulation leads to an increasing flame standoff ratio [58, 61]. With increasing ambient pressure, the vapor accumulation leads to monotonically decreasing droplet lifetimes, but to a minimum in the combustion lifetime at the critical point. Transferred to the rate constants, this means that the burning rate constant has a maximum at the critical point, whereas the gasification rate constant increases monotonically. For the LOX-H<sub>2</sub> system, numerical simulations have shown that the flame standoff ratio is significantly smaller than for hydrocarbons. Due to the proximity of the flame to the droplet surface, it is assumed that there is no significant vapor accumulation

and the droplet lifetime is approximately equal to the combustion lifetime. The gasification rate constant increases monotonically into the supercritical regime [89]. In another numerical study, an almost constant combustion lifetime was found in a pressure range between  $p_r = 2$  to 4, i.e., well beyond the critical point. A similar behavior was observed in the combustion of hydrocarbon droplets [55]. This is in contrast to the previously discussed study on LOX combustion, where a significant increase in droplet lifetime was found. However, it should be noted that one study refers to droplet lifetime and one to combustion lifetime. The relationship between combustion and droplet lifetime is only discussed in the first study. Overall, significant differences in flame position and vapor accumulation were observed when comparing the LOX-H<sub>2</sub> system to the combustion of hydrocarbon droplets in air. A monotonic increase from the subcritical to the supercritical regime, similar to the pure vaporization case, is assumed [89]. However, this has not yet been confirmed either by other numerical studies or experimentally.

### 3.4. Droplet generation and suspension techniques

One of the most essential challenges in conducting experimental studies on droplet combustion or vaporization under microgravity conditions is to remotely generate a single droplet and to position it. Since droplet experiments have been performed for decades, there are many different techniques for both droplet generation and suspension that have been described in the literature.

A basic technique for droplet generation is the use of a syringe in combination with a needle. This setup has been used in many studies, e.g., [103, 131], and is based on the automation of the manual droplet generation as performed in the laboratory under normal gravity conditions. For example, Mikami *et al.* [131] used a syringe to transport and dispense the fluid to a supply needle. After droplet generation, the needle was rapidly retracted to detach the droplet from the needle [131]. The syringe is usually driven by a stepper motor [103].

In order to dispense the liquids even more precisely, piezo pumps were used. For example, Nomura *et al.* [82] used a piezo pump to feed fluid from a fuel reservoir to thin glass needles for droplet generation. Ulmke *et al.* [132] developed a piezo-electric droplet generator consisting of a piezo-ceramic tube and a continuous glass capillary. The device was used to create droplets with a diameter between 10-100  $\mu\text{m}$ . Single droplets as well as droplet chains with a frequency between 1 Hz and 3 kHz could be generated. This piezo-electric droplet generator was used to inject single floating droplets in the field of FSP, e.g., [107-109]. Other studies in the field of droplet vaporization [133], combustion [134], and autoignition [22] used similar piezo-electrical injectors to generate and suspend larger droplets. By injecting a large number of micron sized droplets to the suspender, the desired size of the final droplet could be precisely adjusted [22].

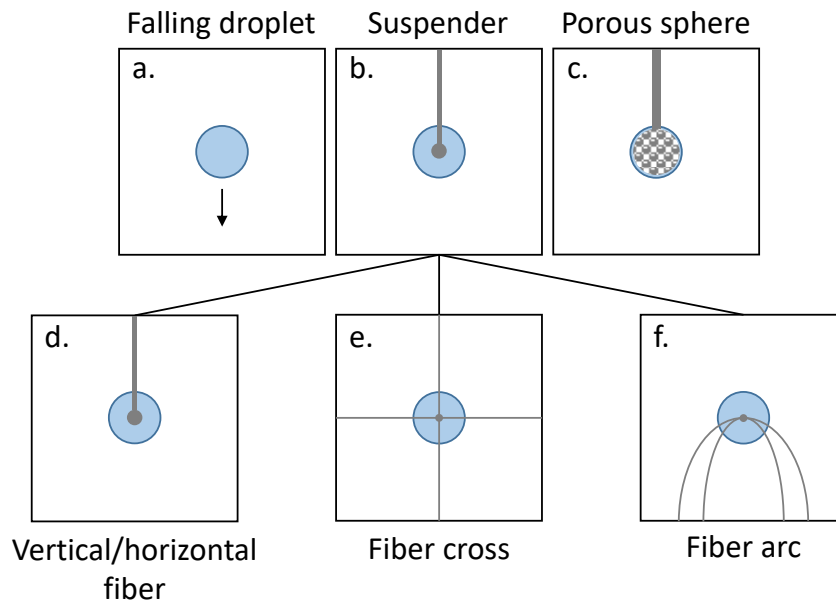


**Figure 28:** a-c. Various experimental techniques to study droplet combustion. d-f. Different suspender configurations. Droplet shown idealized in blue without the effect of gravity or wetting forces. Adapted from [27, 82, 133].

After separating a droplet from the liquid reservoir, different methods were used to position the droplet in order to apply various diagnostics. Williams [27] described three different main experimental techniques, shown schematically in Figure 28a-c. The most ideal method for droplet combustion compared to a 1D numerical model would be a stationary free-floating droplet (Figure 28a). Experiments aboard the ISS used two opposing needles to generate a droplet, which were rapidly retracted just before ignition. In the ideal case, a motionless, free-floating droplet was positioned and then ignited [104]. This technique required very good microgravity quality and a relatively long experimental time. Marchese *et al.* [135] also used this technique for drop tower experiments and were able to generate and ignite a floating droplet during the free-fall phase. However, the usable experiment time was reduced to about 1.5 s [135]. Another example is the study of Jackson & Avedisian [136], who ejected a droplet in a vertical trajectory and released the experiment capsule in a drop tower near the apex of the droplet trajectory, which required precise timing.

Under normal gravitational conditions, a floating droplet was used, e.g., in experiments on FSP [107, 108]. Here, one or more tiny droplets with a diameter of  $\sim 100 \mu\text{m}$  were created and transported through the surrounding gas stream. The movement of the droplet and the small diameter resulted in high requirements to limit the variation of the droplet trajectory in the depth position, which was less than  $9 \mu\text{m}$ . The depth of field of the optical diagnostic system camera was  $\pm 4.5 \mu\text{m}$  [107].

To investigate the steady-state, spherically symmetric combustion of droplets, another experimental technique was used, in which the droplet was created around a porous sphere which is internally supplied with liquid fuel [27], as shown in Figure 28c. As an example, Canada & Faeth [121] used a porous sphere of aluminum oxide supplied with

various fuels through a water-cooled hypodermic tube. The fuel flow rate was adjusted so that the surface of the sphere was completely wetted without dripping [121]. Using this technique, the (vaporization or burning) rate constant  $k$  can thus be calculated based on the  $d^2$ -law with the measured mass flow rate for ideal steady-state conditions by means of this equation [27]:

$$k = 2 \frac{\dot{m}}{\pi \rho r} \quad (52)$$

The most commonly used technique for stationary droplet positioning is the use of a suspender, as shown in Figure 28b. Suspenders usually consisted of a thin fiber and were often made of quartz, sapphire, or silicon carbide. The tip of the fiber was fused into a sphere to hold the droplet, as shown in Figure 28d. This basic method of a vertical or horizontal suspender fiber has been used in many experimental studies, e.g., [81, 133, 137]. In the case of droplet vaporization, it was found that there is a transient heating phase that precedes the steady-state. During this initial phase of droplet lifetime, the heat initially absorbed by the droplet is used to heat the liquid to its equilibrium temperature. Once this temperature is reached, all the heat transferred into the droplet is used to gasify the liquid. Experiments were performed to validate the numerical predictions about the presence and duration of the heating phase of the droplet. However, the use of a suspender led to some additional effects that changed the mechanisms of heat transfer in the droplet [133].

Chauveau *et al.* [133] investigated the influence of the diameter of different suspender configurations on the vaporization of n-decane droplets under 1g. The normalized droplet histories for three different suspenders are shown in Figure 29. They found an increase in vaporization rate with increasing fiber diameter and attributed this to heat conduction from the fiber into the droplet interior. They compared the results of the vertical suspender with a fiber cross arrangement consisting of two orthogonal very thin fibers (compare Figure 28e) [133].

This fiber cross configuration was used in some studies, e.g., Liu *et al.* [134], and reduced the influence of the suspender on the droplet. Especially in combustion experiments, a lot of heat can be conducted into the droplet due to the heating of the suspender by the flame. When comparing experimental data with a suspender and unsupported spherical-symmetric numerical simulations, the effect of the suspender must be included. In addition to thermodynamic effects, a suspender also affects the shape of the droplet due to the wetting behavior of the liquid [138].

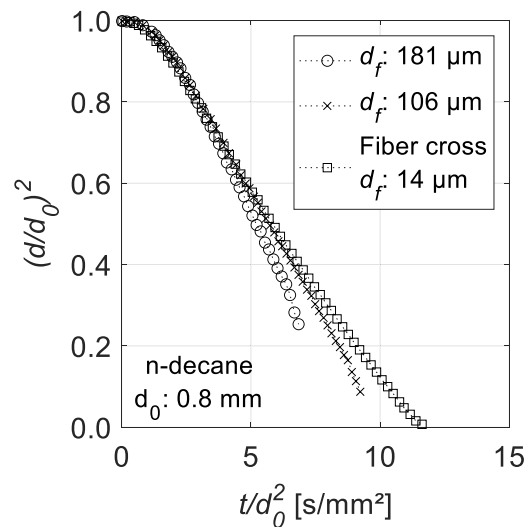


**Figure 29:** Normalized droplet time histories for the vaporization of n-decane droplets at an ambient temperature of 570 K and a pressure of 0.1 MPa under 1g. Adapted from [133].

More recently, Nomura *et al.* [82] conducted an experimental study of droplet vaporization under microgravity conditions. They used a fiber arc suspender, as shown in Figure 28f, by stretching two silicon carbide fibers with a diameter of 7  $\mu\text{m}$  into an arc and fixing them at the intersection point with a small glass bead. Since the droplet suspension fiber was very thin, the spherical shape of the droplet was rarely affected.

In addition to the droplet positioning methods presented, other methods such as acoustically suspended droplets have been used in some studies, e.g., [139-141], to minimize the impact on the droplet. However, this technique also has some drawbacks, such as the high experimental and control complexity and the effect of the standing sound wave to the gas phase as well.

### 3.5. Droplet ignition techniques

The ignition of a droplet is classified into two categories [142]:

- spontaneous ignition (also called autoignition or self-ignition) and
- forced ignition.

In the event of spontaneous combustion, the temperature of the system is raised to the point where heat generation exceeds heat loss, without the use of an external heat source [142]. As one example, Eigenbrod *et al.* [22] studied the autoignition of n-decane droplet pairs under microgravity conditions. They used a droplet elevator that rapidly transported the suspended droplets into a preheated oven to study the ignition delay time and the autoignition process at different ambient conditions [22].

More relevant for this thesis are the methods of forced ignition, which are based on a local temperature increase. After localized ignition, the entire combustible system inflames without additional external heat input. The source of this temperature increase can be, among others, a spark or a plasma torch, or also an external flame [142]. In many droplet

combustion studies, the hot wire method was used for ignition, e.g., [96, 98, 102-104, 131]. In these studies, a hot wire was electrically heated in the direct vicinity of the droplet, so that the gas mixture around the vaporizing droplet was heated and finally ignited. In some cases [104, 131], the ignition wire was retracted after ignition was complete to avoid interfering with the combustion process. Farouk *et al.* [143] performed both experiments and numerical studies on the combustion of methyl butanoate. Among other things, they compared different ignition methods using a numerical model and concluded that spark ignition adds significantly less enthalpy to the system than ignition with a hot wire. For the experiments, they used two electrical spark ignition sources that were placed symmetrically around the droplet and retracted after ignition [143]. The spark ignition method was also used in many other studies, e.g., [136] or very similar methods such as arc discharge ignition [101] or plasma arc ignition [137]. In an experimental study, Yates *et al.* [144] investigated the spark ignition of hydrogen in oxygen and nitrogen mixtures at 100 K between 0.03 to 0.28 MPa. They found that when the temperature was lowered from 289 to 100 K, the quenching distance of hydrogen mixtures was not significantly affected and the flammable range remained wide, i.e., hydrogen concentration between 10 to 90 % in pure oxygen [144]. Schröder *et al.* [145] investigated the explosion limits of hydrogen-oxygen mixtures at pressures up to 20 MPa ( $p_r = 4.0$ ) at room temperature under 1g conditions. The results of their experimental study are shown in Figure 30. They found that the pressure has only a marginal effect on the course of the lower and upper explosion limits, so that the explosion limits exist over a wide pressure range between 4 and 6 % and between 94 and 95 % [145].

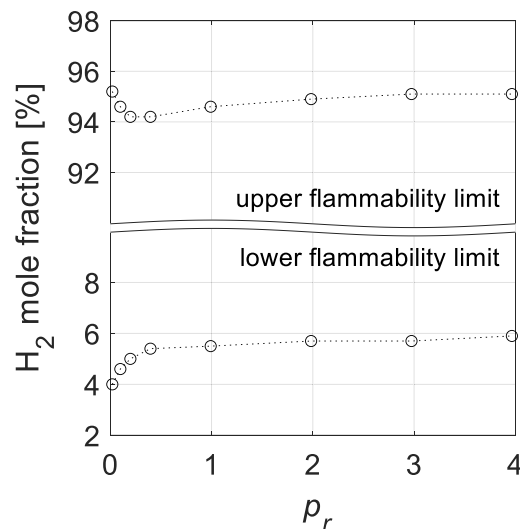


**Figure 30:** Pressure effect on the explosion limits of hydrogen-oxygen mixtures at 293 K between 0.1 to 20 MPa. Adapted from [145].

The forced ignition methods discussed so far are all based on the electrical generation of heat, sparks, or plasma. Another method of generating a spark at a single point is by using a laser beam. The laser-induced spark ignition consists of several sub-processes. If sufficient laser energy is focused on a single point, a gas breakdown occurs, which is followed by plasma expansion. This expansion generates shock waves that propagate into

the surrounding area until pressure equilibrium is reached. The remaining hot gas then leads to ignition and later full scale combustion [142]. Srivastava *et al.* [146] studied the characteristics of laser ignition in hydrogen-air mixtures in a combustion bomb. They used a Nd:YAG laser with a wavelength of 1064 nm and a lens with a focal length of 50 mm to focus the beam. The size and temporal evolution of the plasma were observed and discussed in detail. In addition, also the flame kernel development as a precursor to actual ignition and combustion was investigated. They compared the pressure increase triggered by laser plasma ignition with ignition by spark plug ignition and found that the increase was higher with laser ignition. Possibly, this could be due to the absence of a plasma quenching effect. However, they reviewed several other studies and summarized that laser ignition in general has several benefits compared to conventional spark ignition. The minimum pulse energy required for successful ignition decreases significantly with increasing pressure. If this minimum pulse energy is exceeded, ignition delay times can be shortened and reduced total combustion times can be achieved compared to conventional spark ignition [146]. With regard to laser ignition of LOX, studies to date have focused primarily on the ignition of sprays. For example, Gurliat *et al.* [147] studied the ignition of a cryogenic hydrogen-LOX spray at sea-level conditions using a pulsed Nd:YAG laser emitting at 532 nm. De Rosa *et al.* [148] extended these studies by investigating the transient ignition process of the spray under vacuum conditions using the same experimental setup. The goal of these studies was to better control the overall transient ignition process by precisely controlling the ignition parameters to avoid any pressure spikes or combustion instabilities during ignition [147]. More recently, feasibility studies have been conducted to explore the use of laser ignition in future rocket engines, e.g., [149].

To ultimately ignite a droplet, an ignitable premixture must exist in the gas phase, i.e., the liquid must have vaporized to a certain extent before ignition. If this premixture is not yet fully established, e.g., due to very low ambient temperature, the ignition source can also help to accelerate the vaporization process. Here, the hot wire method has advantages, as the relatively slow heating can significantly increase the vaporization rate of the droplet prior to ignition. In contrast, spark discharges, plasma breakdowns, or laser-induced sparks are very short and only affect a small region, so that the vaporization rate is only increased to a limited extent. Therefore, sometimes several sparks must be generated in order to ignite a droplet.

The methods presented here were the most commonly used in the literature. However, there are other methods or slight variations of the presented methods that are not discussed within the scope of this thesis.

### 3.6. Combustion diagnostics

In recent decades, considerable progress has been made in the field of combustion diagnostics. This has significantly improved the understanding of basic combustion processes as well as practical applications, and has led to the discovery of new combustion processes and mechanisms [67]. Due to the shift from the classical trial-and-error approach to detailed numerical simulations, experimental combustion research has been

increasingly used in recent years to validate (sub-)models and interdependencies between various physical and chemical processes [150]. Today, sophisticated combustion diagnostics can provide valuable data for model validation. In the following, the main combustion diagnostic techniques in the literature are reviewed and the techniques relevant to this thesis are discussed in more detail.

Combustion diagnostics are generally divided into invasive and non-invasive techniques. Invasive techniques typically involve placing mechanical probes at the region of interest, which can lead to a non-negligible effect on the sensitive combustion process if the probe is placed close to the reaction zone. Mechanical probes can be used to measure, e.g., temperature, pressure, species concentration, flow velocity or particulates [67]. The most common way to measure the temperature field around a droplet is to place small thermocouples at the desired positions. Mikami *et al.* [24] developed a method to determine the flame temperature around the burning droplet based on the thin filament pyrometry (TFP) method. For this purpose, they used the SiC-fiber grid, on which the individual droplets were suspended, as a temperature indicator. They calibrated the luminosity of the fibers as a function of temperature using a visible spectrum camera. Therefore, the temperature range of the TFP method was limited to 980 to 1500 K. [24]

The non-invasive techniques are usually more elaborate and complex, but do not affect the combustion process. The fundamental principles of these techniques are based on chemical or physical processes that are caused by interaction with optical radiation or cause radiation themselves. These processes are, e.g., chemiluminescence, fluorescence as well as Mie, Rayleigh, and Raman or anti-Stokes Raman scattering or refraction. The understanding of these processes allows to determine physical or chemical quantities such as species concentration, density, or temperature [67].

### 3.6.1. Density-based diagnostics

Basic visualization techniques such as shadowgraph or Schlieren imaging use the refractive index to visualize differences in density induced, e.g., by temperature gradients [67]. Shadowgraph imaging has often been used in the field of spray combustion to visualize the droplets or to determine the oxygen mass fraction, e.g., [12, 13, 84, 111, 115]. In the field of droplet combustion, the technique has been widely used to track the droplet diameter, e.g., [98, 151-153]. Schlieren imaging was also used as a diagnostic method in spray combustion experiments, e.g., [12, 148]. In the field of single droplet combustion, e.g., Ogami *et al.* [154] studied droplet combustion in an oscillatory flow under microgravity conditions. They used Schlieren imaging in combination with backlit imaging to identify both the flame location and the droplet size [154]. Other examples of the use of Schlieren imaging in the investigation of single droplets are, e.g., [19, 153]. These basic visualization techniques are well suited for qualitative applications as droplet and flame tracking because they require only a relatively simple optical setup. However, shadowgraph and Schlieren imaging often do not allow quantitative measurements, as would be necessary to determine, e.g., the temperature or the concentration field [67]. The physical principles and the optical setup of these density-based methods are explained in more detail in chapter 2.7.

### 3.6.2. Emission spectroscopy

Another non-invasive technique is the emission spectroscopy. Here, the radiation spectrum directly emitted by the flame is detected. Kirchhoff & Bunsen [155] studied the different colors of flames induced by the addition of various metal salts and found that certain elements were related to specific spectral emission lines. This phenomenon can be attributed to thermally excited atoms, however, most emissions spectroscopy of the gas phase is based on the more complex chemiluminescence of molecules [67]. The fundamentals of chemiluminescence are described in more detail in 2.7.2. The technique of  $OH^*$  chemiluminescence, which is relevant to this thesis, has been widely used in combustion research to characterize the flame. For example, De Rosa *et al.* [148] used the chemiluminescence of the  $OH$  radical (spectral range of  $\lambda = 310 \pm 5$  nm) to determine the position of the flame front of a cryogenic hydrogen-liquid oxygen spray. They used an intensified high speed camera and a frame rate of 18000 fps [148].  $OH^*$  chemiluminescence was also used for flame characterization in other studies on spray combustion, e.g., [113-115]. Fiala [71] studied the radiation of high-pressure hydrogen-oxygen flames in the context of combustion instabilities in rocket engines. He found that the behavior of  $OH^*$  radiation at high pressures has been described in the literature in contradictory ways [71]. For example, experiments by Diederichsen & Wolfhard [156] showed that the  $OH^*$  emission from a hydrogen-oxygen diffusion flame increases by a factor of 400 when the pressure is increased from 0.1 to 4.0 MPa. Other studies also showed an increase in  $OH^*$  intensity, albeit with different factors, e.g., [12, 157, 158]. However, some studies showed that the  $OH^*$  radiation remained constant or even decreased with increasing pressure, e.g., [159, 160]. Fiala attributed these inconsistencies of the total amount of  $OH^*$  radiance to the fact that there is no simple correlation between  $OH^*$  radiation and pressure. The intensity results from the peak temperature, the number of  $OH$  molecules and their distribution, each of which is influenced by the ambient pressure. Thus, the total  $OH^*$  radiation can increase, remain constant or decrease depending on the operating conditions and setup [71]. In the field of droplet combustion, Marchese *et al.* [135] used  $OH^*$  chemiluminescence to determine the flame position of a methanol droplet under microgravity conditions. They use an intensified camera with a UV-transmissive lens and a narrow band interference filter centered at 310 nm. In another study by these authors [161], they analyzed the  $OH^*$  signal in detail and compared it with numerical models. The emission signal was processed using the inverse Abel deconvolution algorithm to determine the time evolution of the location of the peak intensity within the flame. Based on this study, they concluded that for methanol and for n-heptane flames the location of maximum  $OH^*$  emission intensity, as shown in Figure 31, coincides with the location of maximum flame temperature, which they therefore assumed to be the flame position [135]. Thus, the technique of emission spectroscopy, e.g., the  $OH^*$  chemiluminescence, is well suited for the detection of flame positions. However, quantitative measurements by emission spectroscopy in general are not possible because there is no thermal equilibrium in the population of the different excited molecular states [67].

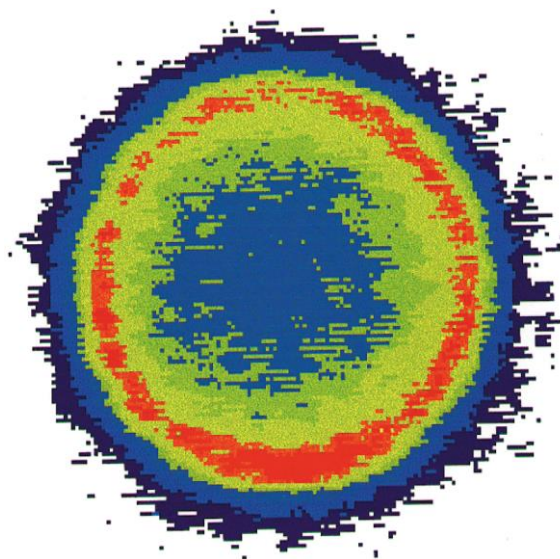


**Figure 31:**  $OH^*$  chemiluminescence image from a microgravity droplet flame surrounding a 1.9 mm n-heptane droplet in 40/60 % mixture of oxygen and helium at 0.025 MPa at 0.53 s after ignition. Reprinted from [161] with permission from Elsevier.

### 3.6.3. Absorption spectroscopy

Another line-of-sight diagnostic is the absorption spectroscopy, which can be used, e.g., for the quantitative measurement of species concentrations. The measuring principle is based on the concentration-dependent attenuation of an induced radiation by partial absorption. [67] For example, Werner & Meier [162] used laser absorption spectroscopy to measure the vapor concentration in the vicinity of vaporizing hydrocarbon droplets. They used a helium-neon laser with a wavelength of  $3.39 \mu\text{m}$  and an IR detector. To quantify the measured absorption signals, they measured the absorption cross sections in a heated gas cell. They concluded that the laser absorption measurements do not need to be calibrated and are relatively simple [162].

### 3.6.4. Laser-based diagnostics

Laser-induced fluorescence (LIF) is another technique for measuring species concentration or even temperature and is based on an absorption-emission process between laser photons and atoms or molecules. LIF is characterized by a high signal strength and a good spectral discrimination between signal and scattered light [67]. This technique was used, e.g., to conduct spray volume and droplet size measurements [163] or to determine the Sauter mean diameter of spray systems [164]. Cannon *et al.* [165] studied the vapor concentration between two neighboring droplets in a droplet stream using LIF. In addition, LIF was also used for single droplet combustion under microgravity in the drop tower to measure flame position and diameter but also droplet diameter and droplet temperature [166, 167]. Eigenbrod *et al.* studied the autoignition of a n-decane [22] and a n-tetradecane [21] droplet pair in microgravity and used the planar laser-induced fluorescence (PLIF) technique. They used a complex laser system, which is described in more detail in another reference [168], consisting of two Yb:YAG disk

lasers to excite formaldehyde at a wavelength of 343.248 nm. The laser generated pulses at a repetition rate of 1 kHz and the laser beam was expanded to a light sheet of 10 mm in height and a thickness of 0.1 mm. The LIF signal was recorded with an intensified camera and the pixel intensities were normalized with the excitation energy profile, which was recorded in parallel. The light sheet allowed the entire surrounding area of the two droplets to be examined in one plane and both cool-flame and hot-flame ignition to be observed [22]. Schulz [150] compared results from  $OH^*$  PLIF and  $OH^*$  chemiluminescence on flame propagation in stoichiometric methane-air mixtures at different turbulence intensities. As the intensity increased different results of the two measurement methods were obtained. Since the flame propagation was no longer symmetric and uniform, the  $OH^*$  PLIF results showed individual flame cusps and handles, whereas the line-of-sight results of  $OH^*$  chemiluminescence were still interpretable as connected and compact flames. Schulz thus presented the advantage over line-of-sight methods [150]. On the other hand, however, it should be noted that, e.g., PLIF involves a considerably more complex setup than the relatively simple optical setups of emission spectroscopy. Another technique, the laser-induced phosphorescence is very similar to LIF, but is based on phosphorescence, which is essentially only distinguished by the longer radiation time scales compared to fluorescence, and thus has not often been used for combustion diagnostics [67].

Interferometry is a technique in which coherent light beams are sent through a test section and the optical path length is compared with a reference [169]. Due to the change in the speed of light as the beam passes through different media, the light experiences a phase shift, which responds to the refractive index of the media [170]. Tanabe *et al.* [123] used a Michelson interferometer to visualize the temperature field around an n-heptane droplet. With this measurement technique, they were able to detect the two-stage ignition behavior of a cool-flame and a hot-flame [123]. The same Michelson interferometer was used in other studies, e.g., [171, 172].

Scattering techniques include different types such as Mie, Rayleigh, or Raman scattering [67]. These techniques have been widely used in combustion diagnostics to measure, e.g., temperature, density, chemical concentration, droplet size, or droplet distribution [84, 112, 173-175]. Primarily, scattering techniques have been used in the field of spray combustion, e.g., [84, 112, 173, 174], or in the field of FSP, e.g., [175], i.e., on very small droplets.

### 3.6.5. Other diagnostic techniques

There are many other measurement techniques that have been used in the field of combustion research, but are less relevant to this thesis. One example is laser-induced incandescence (LII), which is based on Planck radiation emitted by particles triggered by high-energy laser radiation and is mainly used in soot diagnostics [67].

In summary, there are a variety of different techniques for combustion research and considerable progress has been made in recent years in the development of new diagnostic tools. Modern laser diagnostics have significantly contributed to a better understanding of fundamental combustion processes [67]. However, especially with regard to

---

combustion experiments under microgravity, there are also many limitations, such as installation space, robustness and adjustability, which require considerable effort to integrate modern laser diagnostics into experimental apparatus.

## 4. Experimental setup

To study the droplet combustion of LOX in a hydrogen atmosphere under microgravity conditions, a completely new experimental hardware had to be developed and built. The apparatus was designed to fit into a standard ZARM drop tower capsule and therefore the installation space was limited. In addition, all experiment components had to be designed to withstand the maximum vertical deceleration forces of 50 g with a safety factor of 2, i.e., a quasi-steady acceleration of 100 g had to be assumed in the design phase [176]. All experimental procedures had to be performed remotely, as access to the experiment was not possible 2.5 hours before the actual drop of the experiment. Also, special safety measures had to be taken to ensure the safe handling of LOX and hydrogen.

In this chapter, the experimental setup is described in detail. It should be noted that the hardware was continuously further developed and adapted between individual experimental campaigns. Therefore, both the basic design and the corresponding further developments are described. The optical concept for the laser ignition, which is part of chapter 4.3, was designed by the project partner IPHT. Parts of the content was published by the author of this thesis and collaborators in [117, 118, 177-180].

### 4.1. Cryogenic combustion chamber

The main element of the experimental setup is the cryogenic combustion chamber, which is based on a 3-chamber system. As shown in Figure 32, the actual combustion chamber, in which LOX and gaseous hydrogen ( $H_2$ ) were combined and ignited in a controlled manner, is located in the center of the overall setup. The combustion chamber is completely enclosed by a liquid nitrogen ( $LN_2$ ) cooling jacket, which is surrounded, in turn, by an evacuated outer container that provides thermal isolation. The combustion chamber is thus cooled and kept at a fixed temperature of 77 K (the atmospheric boiling temperature of liquid nitrogen).

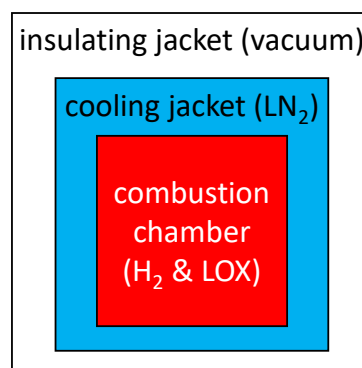


**Figure 32:** Schematic illustration of the principle of the cryogenic combustion chamber.

Figure 33 shows the computer aided design (CAD) half-section of the cryogenic combustion chamber with the various media labeled. The innermost container represents the actual combustion chamber and was designed for a maximum internal pressure of 10 MPa. The inner diameter of the combustion chamber is 43 mm, the height is 60 mm,

and the minimum wall thickness is 6 mm. The other two containers were designed for a pressure of 0.1 MPa and for vacuum, respectively. To provide optical access to the combustion chamber on two axes, the nested containers each have four orthogonal quartz windows with a clear diameter of 15 mm.

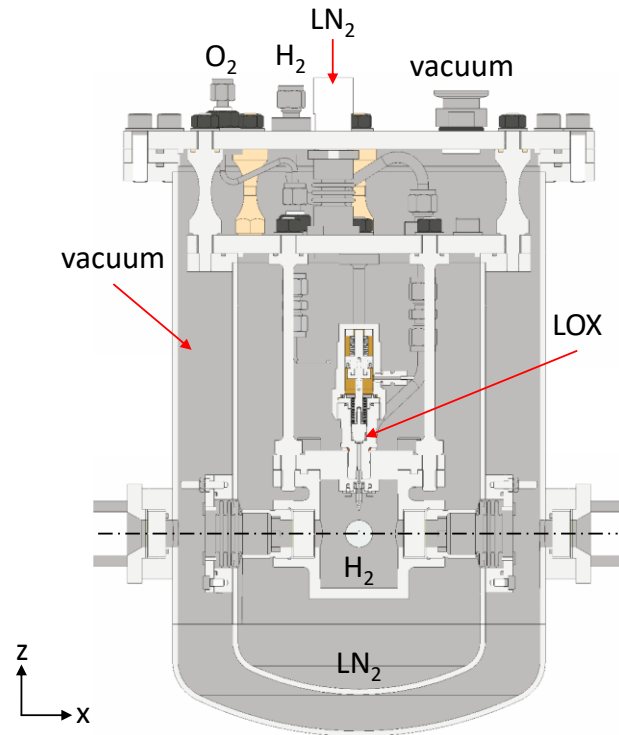


**Figure 33:** Cross-sectional CAD view of the cryogenic combustion chamber (outermost container diameter of 206 mm) with the different compartments and main inlets (helium line not shown). The dashed line indicates the optical axis. Figure published in [177].

In addition to the design constraint of 100 g in the vertical direction ( $z$ -axis in Figure 33), a horizontal acceleration also had to be taken into account for the design in case the drop tower capsule does not enter the deceleration unit exactly straight. Here, an inclination angle of the drop tower capsule of  $1^\circ$  was assumed. In order to consider this in the design, the deceleration force of 100 g, which in the ideal case acts only along the  $z$ -axis of the experiment, was divided into individual components. This resulted in the following design loads for the horizontal  $x/y$ -axes:

$$\tan 1^\circ * 100 \text{ g} = 1.75 \text{ g} \quad (53)$$

As the material for the cryogenic combustion chamber, stainless steel 1.4301 (AISI 304) was chosen because it is suitable for low temperatures around 77 K and for handling hydrogen and oxygen. Only one grade of stainless steel was used to avoid possible differences in thermal expansion. The design of all components of the cryogenic combustion chamber was verified using the finite element method (FEM) in the ANSYS

Mechanical<sup>®</sup> software package. Here, the worst-case material properties were used to meet the strength requirements at both room temperature and cryogenic temperatures.

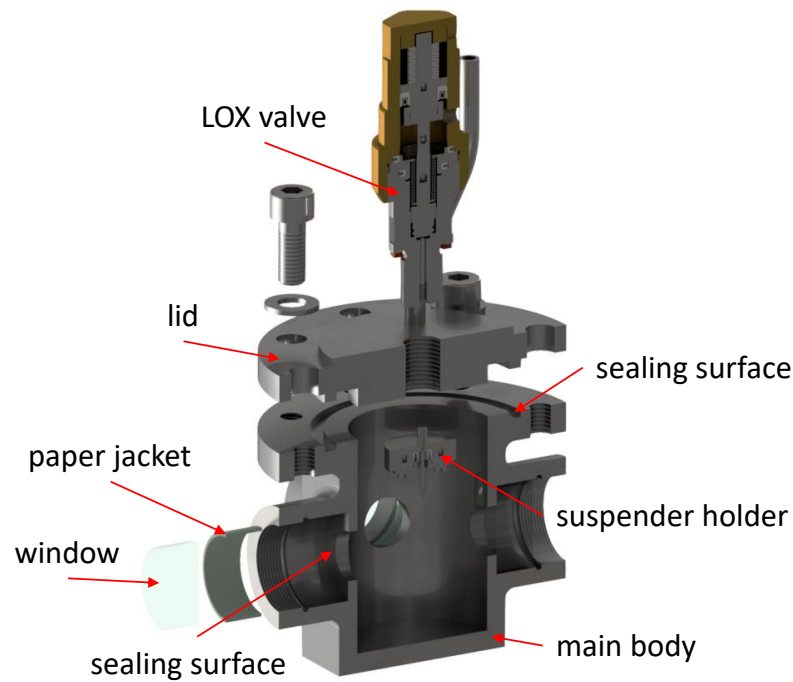


**Figure 34:** CAD exploded view of the combustion chamber. Inner diameter: 43 mm, inner height: 60 mm.

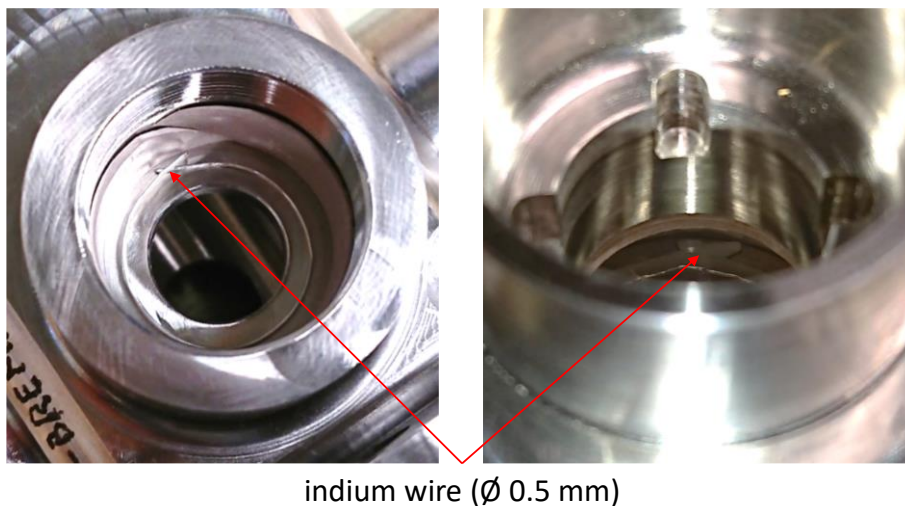


**Figure 35:** Indium wire sealing of the quartz windows in the combustion chamber.

The combustion chamber consists of a milled main body and a lid, as shown in Figure 34. The lid was screwed onto the main body and was sealed with an indium wire with a diameter of 0.5 mm. The LOX valve was screwed into the combustion chamber cover from above and the suspender holder from below, both of which are described in detail in chapter 4.2. The two pipes into the combustion chamber were welded into the combustion chamber lid. Quartz windows (Ø25 x 12 mm) were inserted with a paper jacket into the four lateral sockets of the main body and were also sealed with an indium

wire at the sealing surface. The windows are mechanically polished on both sides with a quality of  $\lambda/4$ . Indium is very suitable as a sealing material in cryogenic conditions. The wire is very ductile and thus adapts exactly to the component surface, as shown in Figure 35. However, a high force had to be exerted to flatten the sealing surface.



**Figure 36:** CAD representation of the combustion chamber piping without vacuum and liquid nitrogen container.

When integrating the individual containers, special attention had to be paid to the piping. The combustion chamber has a total of three connections: for hydrogen, for LOX and for purging. In addition, the LOX valve requires another high-pressure connection for the control pressure. A total of four lines had to be routed from the outside through the vacuum and LN<sub>2</sub> container. For the piping, stainless steel pipes were used, each routed in an S-shape to increase flexibility. This flexibility was necessary with regard to the thermal (temperature range: 77 to 293 K) and mechanical loads (deceleration: up to 100 g). Classical bulkhead fittings are not suitable for this application, since the feedthroughs on the respective container lid have to be specially sealed. For this reason, commercially available fittings were modified and welded to pipe sockets, allowing very small installation dimensions to be realized. Figure 36 shows a rendered representation of the cryogenic combustor piping as it was fabricated and implemented. The gaseous hydrogen is directly supplied to the combustion chamber and allows the chamber to be filled with pure hydrogen or a hydrogen/helium mixture at a prescribed pressure. Gaseous oxygen is supplied to the LOX valve mounted on the combustion chamber lid. During the chill-down of the experiment, the oxygen partially condenses to liquid in the oxygen line and in the valve into the combustion chamber.

The LN<sub>2</sub> container has an inner diameter of 134 mm, a height of 240 mm, and a wall thickness of 3 mm. The container was mounted to the lid plate of the vacuum containment by six bolts made from low heat conductive polyether ether ketone (PEEK). The combustion chamber then was placed inside the LN<sub>2</sub> containment and was connected to the lid plate with four bolts made of stainless steel. A sealed tunnel for optical access,

containing a bellows for mechanical and thermal motion compensation, connects the combustion chamber wall to the LN<sub>2</sub> container wall. The tunnel is shown in Figure 37 and consists of a plate for the LN<sub>2</sub> container flange, a screw-in for the combustion chamber, which at the same time fixes the windows, and a bellows, which connects both parts. The bellows has a thickness of 0.3 mm and was circumferentially welded to both parts. Due to the flexible connection, any relative movements of the combustion chamber and the LN<sub>2</sub> container can be compensated. The tunnels were screwed into the combustion chamber using a special tool. The flange plate was then screwed to the container flange. Here, slotted holes were used to ensure that the holes in the flange were accessible.

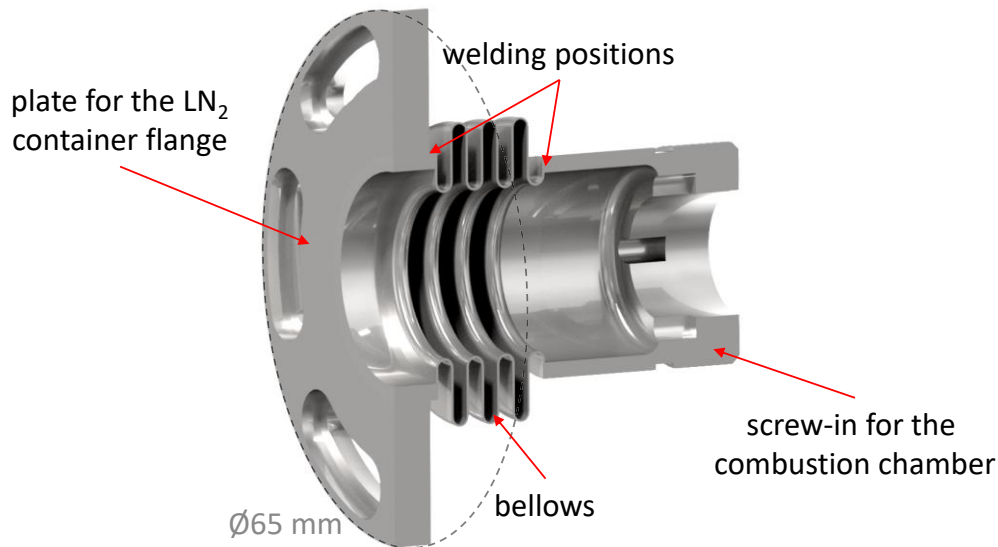


**Figure 37:** CAD view of the sealed tunnel between combustion chamber and LN<sub>2</sub> container for optical access to the combustion chamber.

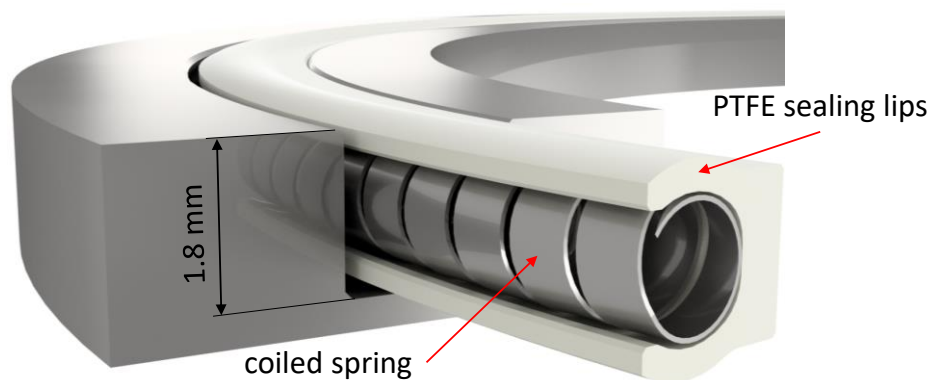


**Figure 38:** CAD view of the spring energized PTFE lip sealings for cryogenic applications in a flange groove.

The tunnel plate seals between LN<sub>2</sub> and vacuum by means of a special sealing, which is shown in Figure 38. These sealings are custom made for the required diameters and groove depths and consist of polytetrafluoroethylene (PTFE) seal lips and a coiled spring. The metal spring can ensure sealing over a wide temperature range, as the different thermal shrinkage of PTFE and stainless steel can be compensated by the elastic deformed

spring. This type of sealing was used for the LN<sub>2</sub> container and also for the LN<sub>2</sub> feedthrough to the vacuum container, which is also subject to a large temperature gradient. Nitrile rubber O-rings were used as sealings for the vacuum container, as this component is not exposed to cryogenic temperatures.

The outer surface of the LN<sub>2</sub> container and the inner surface of the vacuum containment were electro-polished for an improved insulation performance due to the reduced radiation emission and absorption. The vacuum container has an inner diameter of 200 mm, a height of 321 mm, and a wall thickness of 3 mm. The container was additionally covered on the outside with black cell foam to prevent any condensation of atmospheric water vapor from dripping onto the electronics below. The volume of the LN<sub>2</sub> container is approximately 2.8 l and the container was completely filled at the end of experiment chill-down. The insulation performance was adequate to keep the LN<sub>2</sub> level above the lid of the combustion chamber for at least 2.5 h. This is the typical time period between hand-over to the drop tower operators and the end of the experiment and includes the drop capsule's transfer to the top of the drop tower and the subsequent evacuation process in the drop tower.

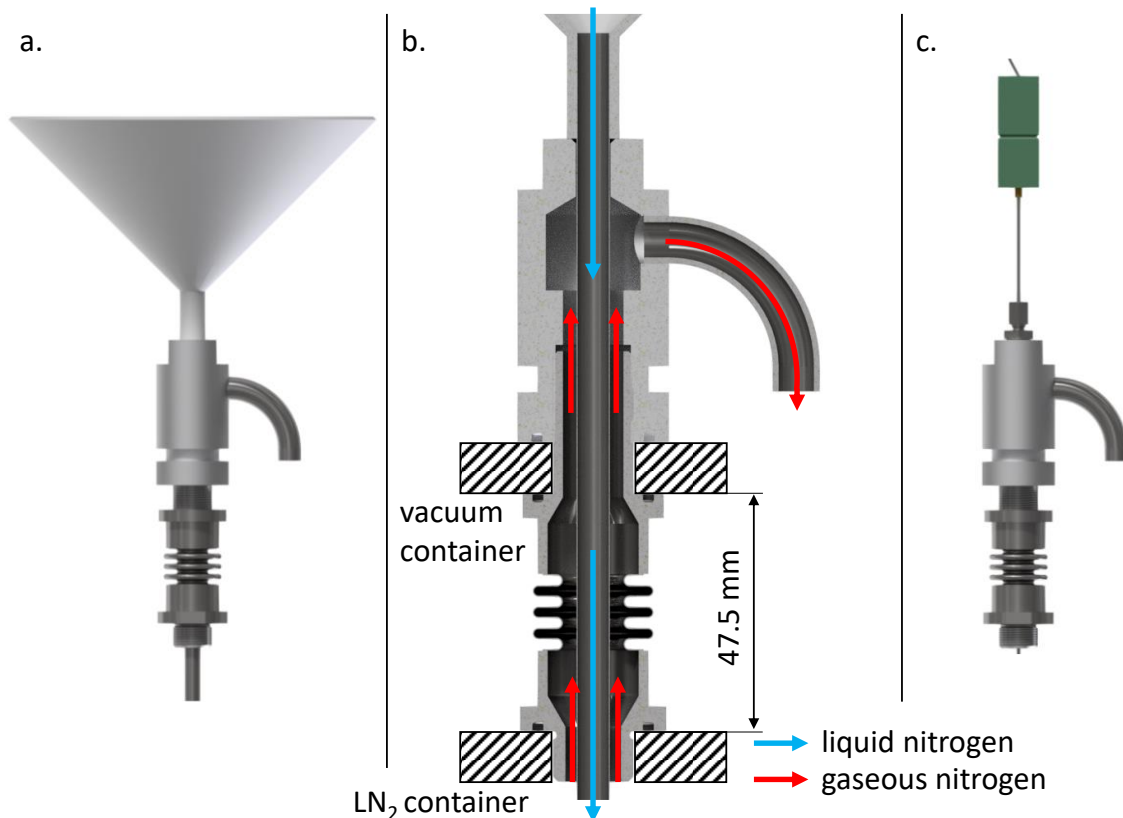


**Figure 39:** CAD view of the nitrogen feedthrough. a. Feedthrough with funnel. b. Sectional view with funnel. c. Feedthrough with thermocouple.

In addition to the gas pipes which are fed into the experiment, a nitrogen feedthrough also had to be integrated into the vacuum container. This feedthrough was used to fill LN<sub>2</sub> into the experiment. The requirements for such a feedthrough were the same as for the piping. The vacuum as well as LN<sub>2</sub> container had to be sealed and the connecting element had to

be flexible to withstand the thermal and mechanical stresses during the experiment operation. Like the four lateral connecting tunnels between the combustion chamber and the LN<sub>2</sub> container, the nitrogen feedthrough was designed as a stainless steel bellows component, as shown in Figure 39. On the one hand, the bellows of the feedthrough ensured elasticity during deceleration and, on the other hand, the low wall thickness of 0.3 mm reduced the heat input into the cryogenic combustion chamber. The nitrogen feedthrough could fulfill several functions. First, it was used to fill the LN<sub>2</sub> container (Figure 39a). For filling, a thin-walled tube with a wall thickness of 0.15 mm was connected to a funnel, which could be placed on the feedthrough. LN<sub>2</sub> flowed through the thin-walled tube into the container and the annular gap between the tube and the feedthrough served as a vent for vaporizing nitrogen (Figure 39b). Especially during chill-down, i.e., when the container was filled for the first time, a great amount of LN<sub>2</sub> vaporized on the still “warm” container walls or on the combustion chamber, which were at room temperature. Due to the clear separation of inlet and outlet, LN<sub>2</sub> could be quickly filled into the container and the boiling of the LN<sub>2</sub> surface in the funnel, caused by rising nitrogen bubbles, was minimized. The nitrogen vapor was directed to the side and then downwards onto the lid of the vacuum container to prevent condensed humidity from entering the feedthrough and freezing there. After the chill-down of the combustion chamber and complete filling of the LN<sub>2</sub> container, the funnel was removed and could be replaced by a thermocouple (Figure 39c). The measuring tip of the type T thermocouple was positioned just above the combustion chamber lid. This allowed to measure if the combustion chamber was still completely surrounded by LN<sub>2</sub> before starting the experiment. While the measuring tip was inside the liquid nitrogen, a constant temperature of approximately 77 K was indicated. However, as soon as the measuring tip was above the liquid level, the temperature dropped by about 0.5 K due to the phase change. This ensured that LOX was introduced into the combustion chamber instead of gaseous oxygen.

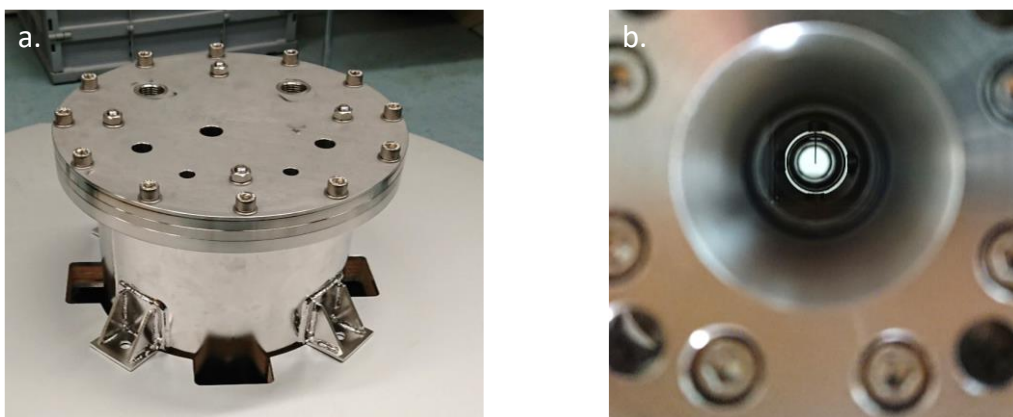


**Figure 40:** a. Integration of the cryogenic combustion chamber (without piping).  
b. View through the cryogenic combustion chamber with dummy suspender.

The outer container of the cryogenic combustion chamber was bolted to a drop capsule platform with welded brackets, as shown in Figure 40a. The positioning of the individual

containers was designed to create two optical axes leading through all containers to the center of the combustion chamber, thus allowing diagnostics of the droplet from several sides, as shown in Figure 40b.

## 4.2. Droplet generation and suspension

To ensure safe experimental operation, the hydrogen and oxygen supply systems had to be separated from each other. Only during droplet generation inside the combustion chamber the two systems were temporarily connected to each other. In order to minimize the diffusion of the hydrogen into the oxygen in this case, it had to be ensured that the two gas phases (hydrogen and oxygen) are separated from each other by a liquid oxygen phase. This could only be achieved by an additional oxygen valve, which was installed in the LN<sub>2</sub> container and thus in the cryogenic environment. A LOX valve allows gaseous oxygen to condense in the valve and in the oxygen feed line before the valve is opened for droplet generation. However, there are high requirements for such a LOX valve:

- High pressure: 6 MPa
- Low temperature: 77 K (inside LN<sub>2</sub> container)
- Limited space (compact design)
- Remote controllability (software controlled)

Although commercial valves are available for the use with cryogenic media or even in a cryogenic environment, the simultaneous satisfaction of all the above requirements cannot be guaranteed by a commercial product for this special application. Therefore, the required valve was developed and manufactured in-house.

The basic principle is based on a needle valve, which is normally closed and can be opened pneumatically. As the pneumatic control medium, helium (critical temperature of 5.2 K) is used to avoid any condensation or freezing in the valve or supply line. During the development phase, various sealing methods were tested. On the one hand, different designs and materials were used for the stem tip. First, a tapered tip made of brass was used, which was pressed into a valve seat made off stainless steel that was also tapered. In the further course of development, a polished ball made of hard metal was then used in combination with the same valve seat. However, both variants led to significant leakage of the valve. This was probably due to insufficient surface quality of the valve seat or stem tip. Therefore, further tests were performed with a tapered PTFE tip. This valve design resulted in a good sealing performance of the valve at room temperature. The LOX valve was then subjected to a real application test inside the cryogenic combustion chamber. This showed significant leakage of the needle valve as soon as the experiment was cooled down with LN<sub>2</sub>. The actual function of the valve, the separation of oxygen and hydrogen before and after droplet generation, was no longer given due to the leakage at cryogenic temperature conditions (77 K). As a result of this test, the design of the valve was revised again. The new version of the LOX valve uses a commercial sealing tip (Swagelok SS-4BA-K5). This sealing tip, available as a replacement part, is made of polychlorotrifluoroethylene (PTCFE) and was screwed into the valve stem in a slightly

modified form. With this design, the sealing performance was significantly improved even at cryogenic temperatures.

On the other hand, different variants for sealing the oxygen to the control medium (helium) and to the environment ( $\text{LN}_2$ ) were also tested. First, spring energized PTFE shaft sealings, similar to those shown in Figure 38, were used to seal the stem. However, it became apparent that due to limited accessibility in the valve body, the surface quality of the sealing surfaces could not be machined sufficiently to ensure a complete seal between the oxygen and helium sections. For this reason, a metallic bellows was used, which separates the oxygen from the control medium helium as a welded unit inside the valve. Like the tunnels between the combustion chamber and the  $\text{LN}_2$  container, the bellows were custom-made by a manufacturer. The sealing of the helium section against the  $\text{LN}_2$ , on the other hand, was realized with spring energized PTFE shaft and lip sealings. The axial sealings have an excellent sealing performance even at 77 K. Whereas there is a small leakage when operating in  $\text{LN}_2$  due to the radial shaft seal. However, this does not affect the function of the actual valve and merely causes some helium to bubble into the  $\text{LN}_2$  when the valve is in the open state.

Figure 41 shows the final CAD design of the valve design and the manufactured valve stem. The technical drawings of all valve components are shown in Appendix B.

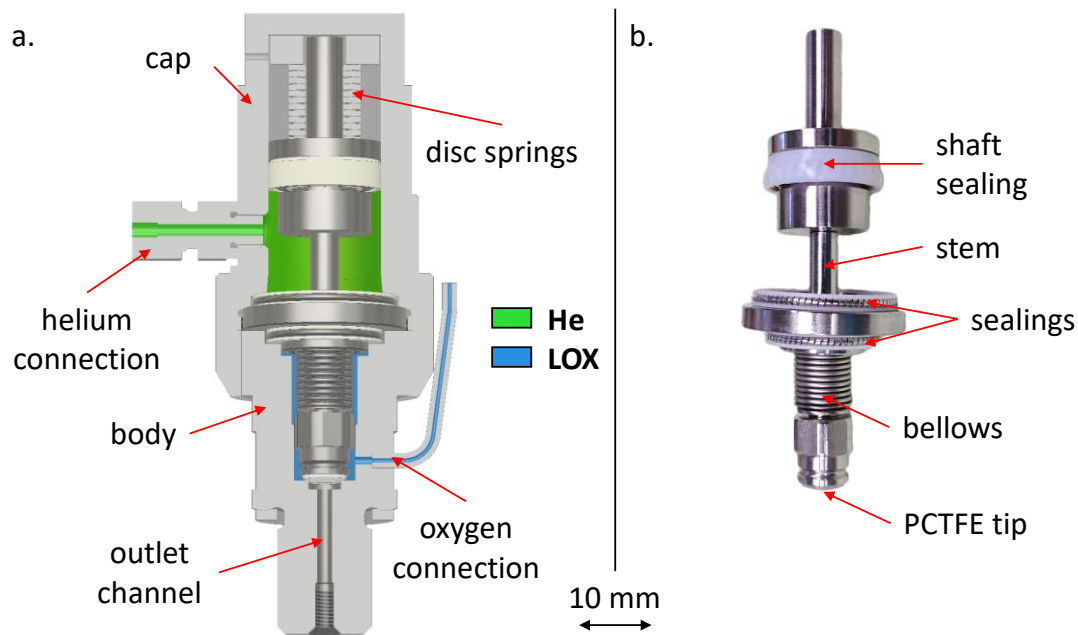


**Figure 41:** a. Cross-sectional CAD view of the LOX valve in closed state. Helium (He) is used to drive the valve. b. Manufactured valve stem with sealings. Figure published in [177] and modified.

The valve essentially consists of three parts: the valve body including the combustion chamber connection, the valve stem including the sealing tip, and the valve cap including the helium connection. Without the oxygen and helium connectors, the valve has a diameter of 30 mm and a total height of 85 mm. The oxygen pipe with an outer diameter of 2 mm and an inner diameter of 0.5 mm was welded to the valve body. For the helium

line, on the other hand, a screw-in connector (SERTO SO 51124-2-M5) was used. The stem, which is shown in Figure 41b, was made of stainless steel and has an overall length of 62 mm. A disc spring assembly ensures that the stem tip is pressed into the sharp-edged valve seat, thus closing the valve (normally closed). By applying a helium pressure of 6 MPa (Figure 41a green area), the spring force is overcome and the shaft is lifted by 0.4 mm. This stroke is sufficient for LOX (Figure 41a blue area) to be transported through the outlet channel into the combustion chamber and is limited in order to minimize the effect of the stem movement on the LOX. As soon as the helium pressure is released, the spring force exceeds the pneumatic pressure and the valve closes again. The welded bellows separates the helium section from the LOX section and consists of 17 corrugations with an outer diameter of 8.2 mm. The nominal wall thickness is 0.12 mm and the total length is  $13.9 \pm 1$  mm. The welded bellows allows on the one hand a perfect sealing and on the other hand the movement of the stem up to 2 mm in axial direction.

The LOX valve was tested under both room temperature and cryogenic conditions. At 77 K, a leakage rate (oxygen against hydrogen) of  $< 10^{-5}$  Pa m<sup>3</sup>/s was determined. However, a more accurate leak rate specification is not possible in the experimental setup, since pressure measurements over longer time periods (in the range of multiple hours) are strongly influenced by the decreasing LN<sub>2</sub> liquid level in the container. Nevertheless, the determined sealing performance of the valve is sufficient to ensure safe experimental operation. The valve has been tested up to a pressure of 6 MPa (hydrogen and oxygen) and 6 MPa against vacuum (for both cases).

As described in the state of the art, typically syringes or piezo pumps are used to generate single droplets for combustion or vaporization experiments. In this experimental setup, a different concept is used, which, on the one hand, is simpler than the use of a piezo pump inside the LN<sub>2</sub> container and, on the other hand, is more flexible with regard to the two-phase system in the oxygen feed line. An essential difference to the droplet experiments reported in the literature, e.g., on hydrocarbons, is that the fluid used for droplet generation is not in a single phase. In a single-phase system where, e.g., the fuel is in the liquid phase, a syringe can be used to adjust the flow rate or dispense the liquid. Due to the approximate incompressibility of the liquid, the stroke of the syringe can be directly correlated with the movement of the liquid. However, this simple correlation is no longer given in a two-phase system, since pressure and temperature changes occur due to the compressibility of the gas phase, and phase change processes are therefore also possible. For this reason, the liquid in this setup was not fed into the combustion chamber by pressure, but rather drawn out of the oxygen pipe by a pressure reduction in the combustion chamber.

Figure 42 shows the simplified circuit diagram for the droplet generation process. The combustion chamber is filled with hydrogen and is then separated from the supply by the main valve. Likewise, gaseous oxygen is also filled into the feedline in the LN<sub>2</sub> container up to the LOX valve. Therefore, the oxygen condenses and a liquid phase is formed in the cryogenic environment, whereas above the LN<sub>2</sub> level the gas phase remains. The LOX valve separates the two closed systems from each other. In order to transport a defined amount of LOX into the combustion chamber, the LOX valve is opened first, before the

outlet valve of the combustion chamber is also opened. Through this valve, hydrogen can be filled from the combustion chamber into an outlet tank in a defined manner using a flow restrictor. As a result, the combustion chamber pressure drops and LOX is drawn into the combustion chamber. When the required amount of oxygen was transported into the combustion chamber, both the LOX and the outlet valve are closed again.

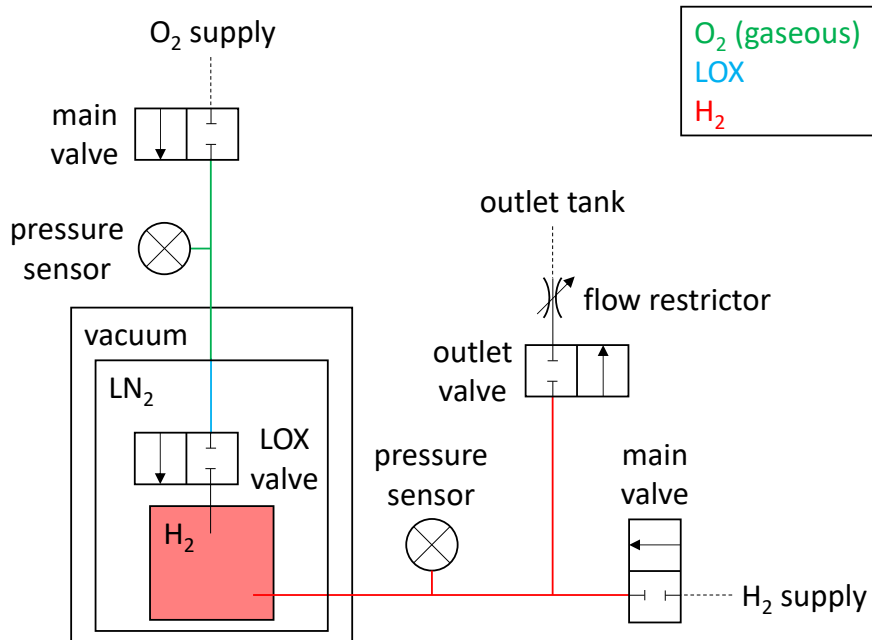


**Figure 42:** Simplified circuit diagram for the pressure control to generate a droplet.

A detailed schematic illustration of the pressure conditions during droplet generation is shown in Figure 43. The process is divided into four phases and is based on different gas volumes of oxygen (approximately  $6 \text{ cm}^3$ ) and hydrogen (approximately  $120 \text{ cm}^3$ ). The hydrogen volume is composed of the combustion chamber volume and the volume of the supply line. The oxygen volume, which results from the volume of the feed line up to the LOX valve, is reduced by the LOX volume in the cryogenic zone. Since the LOX volume can be assumed to be incompressible, pressure differences between hydrogen and oxygen only affect the oxygen volume in the gas phase. In the first phase, the LOX valve is in its closed initial state. A condensation equilibrium is established in the valve and in the oxygen line according to the temperature gradient and the pressure. As soon as the condensation equilibrium is reached, an approximately constant oxygen pressure can be set. The combustion chamber is filled with gaseous hydrogen and can be precisely adjusted to a slightly higher pressure ( $2.5 \text{ kPa}$ ) compared to the oxygen pressure. The higher combustion chamber pressure ensures that no oxygen can enter the combustion chamber in an uncontrolled manner at the moment the LOX valve is opened. In the second phase, pressure equilibrium between hydrogen and oxygen is caused by the opening of the LOX valve. Due to the slightly higher pressure, hydrogen flows into the valve. However, since the oxygen and hydrogen volumes differ greatly, only very little hydrogen enters the valve before pressure equilibrium is reached (Figure 43 phase 2). In the third phase of the process, the pressure of the combustion chamber is reduced in a controlled manner while the LOX valve is still open. By lowering the total pressure, LOX is drawn

out of the valve and transported into the combustion chamber to the suspender (Figure 43 phase 3). After the droplet generation, which is visually observed, the LOX valve is closed again and thus the connection to the remaining LOX in the oxygen is interrupted (Figure 43 phase 4). If necessary, the combustion chamber pressure can then be reduced to the target pressure.

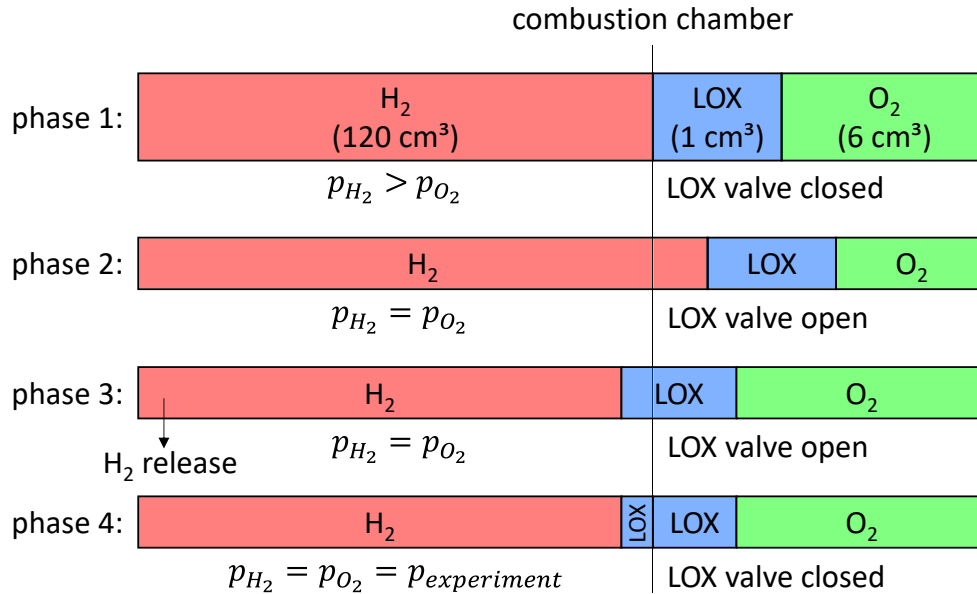


**Figure 43:** Schematic illustration of the pressure levels during the droplet generation process.

In order to separate a single LOX droplet from the introduced liquid column in the combustion chamber and to position it in the center of the combustion chamber, i.e., in the field of view of the optical diagnostics, a suitable suspender had to be developed. In this case, handling with LOX was a particular challenge, since different suspender geometries could only be tested under cryogenic conditions. For this reason, model fluids were identified which have similar properties at room temperature to LOX at 77 K and 0.1 MPa in terms of key characteristics. Two appropriate model fluids are 1-methoxyheptafluoropropane (brand name: Novec™ 7000) and hydrofluoroether (brand name: Novec™ 7500), which are usually used as heat transfer fluids. In terms of droplet generation and wetting properties, the most important properties are density, viscosity, and surface tension. These parameters are listed in Table 4 in comparison with the values of LOX at 77 K and 0.1 MPa.

In addition, the table gives the different boiling points of the liquids, which are important for usability in the laboratory. For example, the model fluid Novec 7000 shows relatively good agreement with the properties of LOX. However, due to the low boiling point, the liquid vaporizes very quickly at room temperature, so that the generation or measurement of droplets in the laboratory is highly time-dependent. Novec 7500, on the other hand, has a much higher boiling temperature, a very similar surface tension, a slightly higher density, but a significantly increased viscosity. Thus, Novec 7500 was chosen as the

model liquid for preliminary tests of possible suspender geometries. Later in the design study, Novec 7000 was also used to provide a better indication of the laboratory tests.

**Table 4:** Properties of different model fluids compared to LOX.

Properties	3M Novec 7000 at 298 K [181]	3M Novec 7500 at 298 K [182]	LOX at 0.1 MPa, 77 K [37]
Density [kg/m <sup>3</sup> ]	1400	1614	1205
Viscosity [mm <sup>2</sup> /s]	0.32	0.77	0.24
Surface tension [N/m]	0.0124	0.0162	0.0166
Boiling temperature at 0.1 MPa [K]	307	401	90

The actual suspension of the LOX droplet is divided into two parts. First, the separation of a single droplet and second, the positioning of the droplet at the tip of the suspender. Various concepts for separating the liquid were developed and tested in the laboratory. The basic idea was to construct a cylinder made of PTFE which transfers the liquid to the suspender. This cylinder is screwed into the valve seat inside the combustion chamber from below. This allows LOX to enter the cylinder after the valve is opened and the combustion chamber pressure is lowered. Figure 44 shows schematically different design steps.

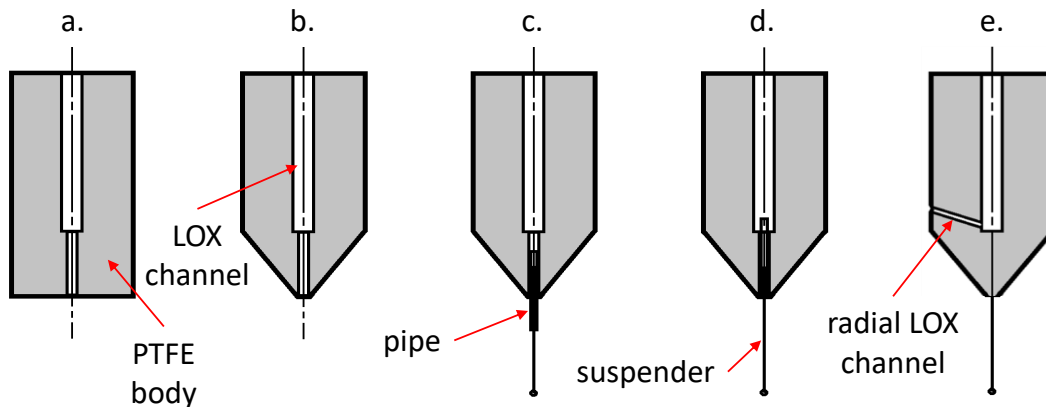


**Figure 44:** Schematic illustration of different approaches for separating a single droplet.

With the first design, shown in Figure 44a, the maximum droplet size at the moment of detachment from the bottom of the cylinder was investigated to test the possibility of transferring a small amount of liquid by dripping onto a suspender below the cylinder. For this purpose, a syringe was inserted into the cylinder so that the model fluid could be fed into the cylinder in a defined manner. However, due to the very good wetting properties of the model fluid, a very large droplet with a diameter of several millimeters

formed at the lower bore (diameter of 0.5 mm), as the fluid wetted the entire underside. Even sharpening the PTFE cylinder, as shown in Figure 44b, could only minimally reduce the droplet size. A new approach was to position the suspender in the PTFE cylinder and hand over a droplet directly. For this purpose, a thin stainless steel tube with a diameter of 0.5 mm) was inserted into the bore of the cylinder and the suspender was glued inside. Two different positioning of the tube were tested, in which the tube was fixed either protruding or flush with the bottom side in the cylinder, as shown in Figure 44c-d. However, in both designs, the model fluid accumulated at the discontinuous shape transition between the cylinder and the tube or between the tube and the suspender, forming a large droplet. Due to manufacturing limitations, this shape transition could not be further reduced in size. Thus, it was not possible to produce a small droplet with this type of cylinder designs. In another design, the bottom bore was replaced by a lateral bore, as shown in Figure 44e. This made it possible to guide a defined amount of liquid to the tip of the cylinder, separating it from the liquid column in the cylinder. The fluid flowed out from the side of the cylinder and ran downward due to gravity and wetting. The shape of the cylinder tip allowed the amount of liquid to be adjusted until dripping.

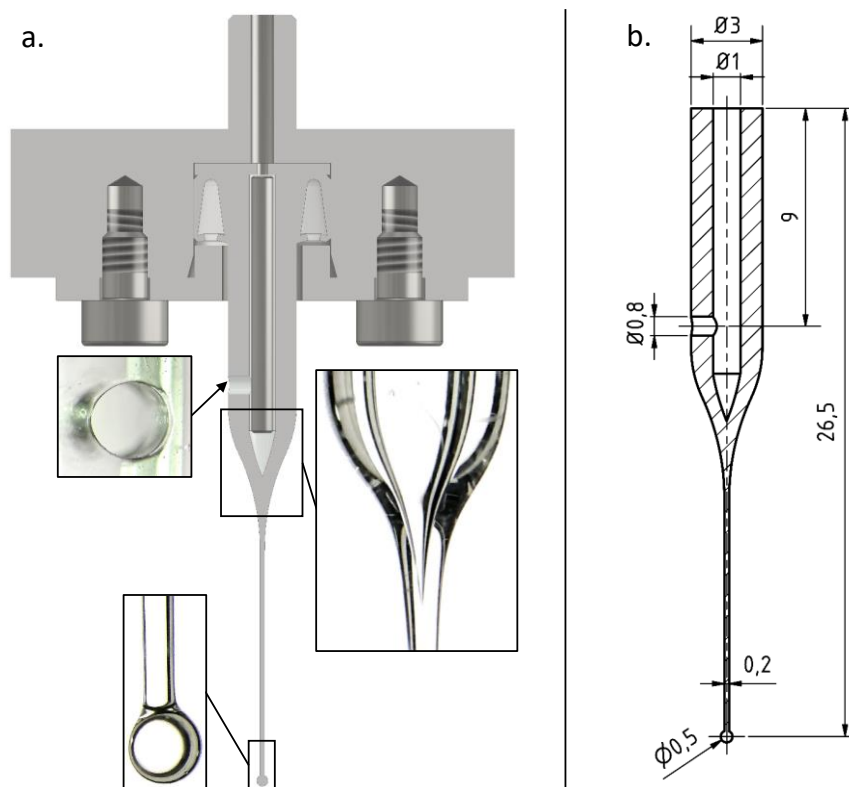


**Figure 45:** a. Cross-sectional CAD view of the suspender holder with a quartz suspender and actual suspender images. b. Suspender dimensions in mm. Figure published in [177].

For the final design of the suspender as used for the drop tower experiments, the cylinder and the suspender were combined and made from one piece. The entire suspender consists of a quartz tube (outer diameter of 3 mm). This tube was drawn into a closed needle of 0.2 mm diameter to provide a smooth shape transition to the suspender tip. The tip of the needle was fused into a sphere with a diameter of 0.5 mm. An outlet bore of 0.8 mm was

drilled horizontally into the upper suspender channel, and its rim was thermally deburred. Quartz was chosen because it has a high melting temperature, a good thermal shock resistance, and very good resistance to oxygen even at high temperatures [183]. In Figure 45 the used suspender is shown together with the suspender holder. The suspender holder is made of stainless steel and is sealed with indium wires. It represents the connection between the LOX valve and the suspender. The suspender is held in place by a spring energized PTFE seal. A metal rod with a diameter of 0.9 mm is inserted into the hollow suspender volume to limit the LOX volume contained in the suspender.

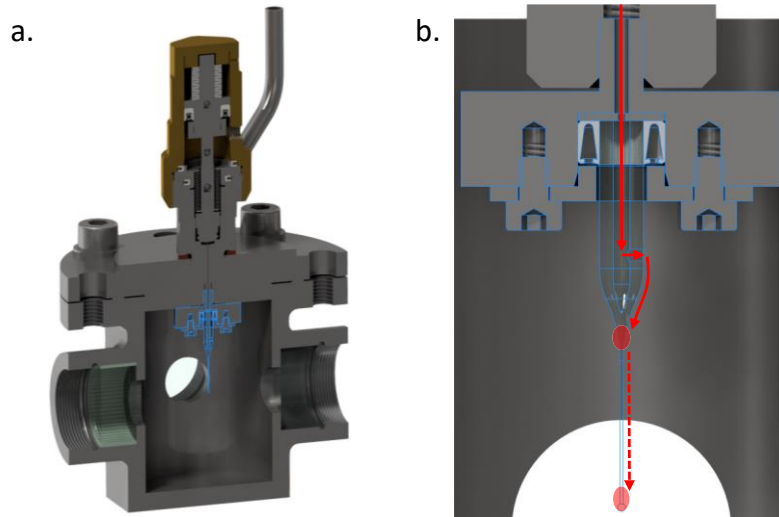


**Figure 46:** a. Cross-sectional CAD view of the integrated suspender (highlighted) in the combustion chamber. b. Suspender detail view with the droplet generation process shown schematically (solid arrows: LOX flow path, ellipses: LOX accumulation, dashed arrow: falling path of the LOX droplet).

For droplet generation, LOX is drawn into the suspender via the outlet channel of the valve and through the lateral bore of the suspender into the combustion chamber, as shown in Figure 46. After exiting the suspender opening, LOX first collects around the diameter transition due to its excellent wetting properties and then drips down along the needle to the rounded suspender tip. The combustion chamber pressure reduction is then stopped, and the LOX supply valve is closed to prevent a second droplet from dripping down to the suspender tip. The pressure profile in the oxygen and hydrogen systems (combustion chamber pressure) is shown in Figure 47.

With this procedure, droplets of specified size can be reliably produced. The standard deviation of the droplet width was  $79.5\ \mu\text{m}$  and standard deviation of the droplet length was  $89.5\ \mu\text{m}$ , based on 40 experiments. Figure 48 shows a LOX droplet of a width of  $0.88\ \text{mm}$  and a length of  $1.27\ \text{mm}$  with a volume that was equivalent to a sphere with a diameter of  $1.0\ \text{mm}$  including the suspender material. The pure oxygen volume was equivalent to a sphere with a diameter of  $0.9\ \text{mm}$ .

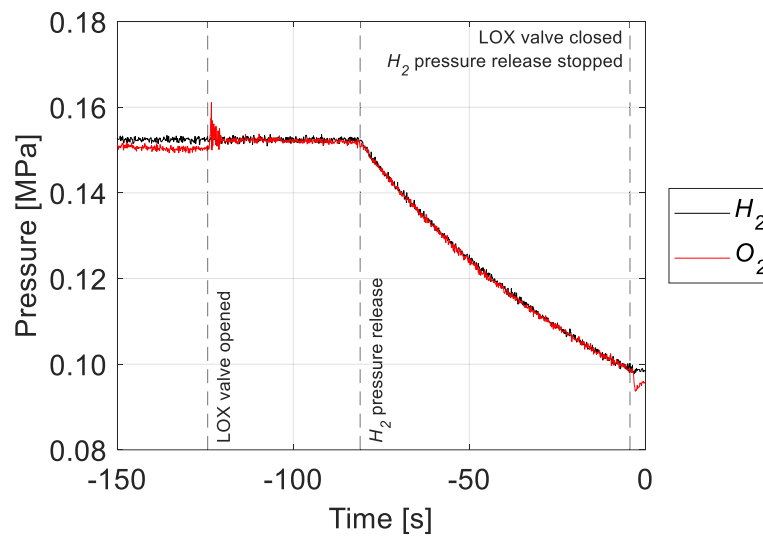


**Figure 47:** Pressure profile during droplet generation. The  $\mu\text{g}$  phase starts at 0 s.

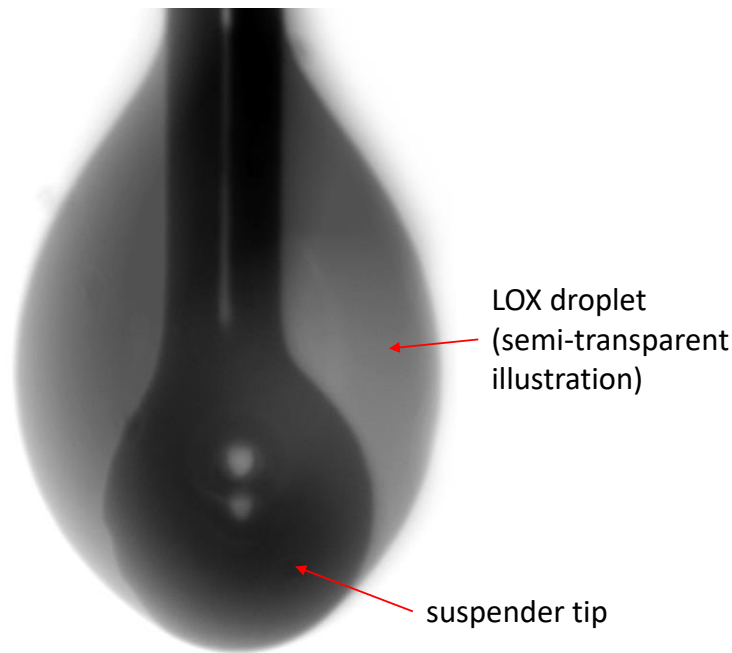


**Figure 48:** Composite image of a LOX droplet backlit image and a suspender tip backlit image in 1g (the image with droplet is displayed semi-transparent to make the suspender tip visible). The droplet width is 0.88 mm and the length is 1.27 mm. Figure published in [177].

In this process, the droplet size depends on several parameters. The most important parameter of the suspender design is the shape of the transition from the suspender tube to the needle. By thermally tapering the tube, a smooth transition without sharp edges could be ensured. This was very important when using LOX, as edges would have led to significantly greater fluid accumulation due to the good wetting properties of LOX. Another important parameter is the speed at which LOX is drawn out of the valve. This parameter is the most difficult to control and to keep constant due to the two-phase system

described above. If the pressure was released too quickly from the combustion chamber, several droplets were generated in quick succession, pulling the previous droplet off the suspender sphere. Finally, the size of the molten suspender sphere and the distance between the liquid accumulation at the transition to the tip of the suspender determine whether the separated droplet can actually be caught and positioned at the tip. The larger the separated droplet and the greater the distance to the tip, the larger the suspender sphere had to be to increase the surface area and thus the catching capability. To minimize the effect of the suspender on the droplet and thus on the combustion, the sphere diameter was kept as small as possible. However, it also had to be ensured that the flame or the hot gas zone did not come close to the upper part of the suspender, where LOX is still present at the time of combustion. Otherwise, this would have significantly affected the combustion process.

The presented suspender design was successfully used in the experiments conducted within this thesis to separate and position a LOX droplet in the center of the combustion chamber. However, this suspender design resulted in an unanticipated detachment of the droplet during combustion, as discussed in chapter 6.2. Therefore, additional suspender designs were developed and tested after the experimental campaigns. These experiments are not part of the scientific evaluation in this thesis and are documented in Appendix C.

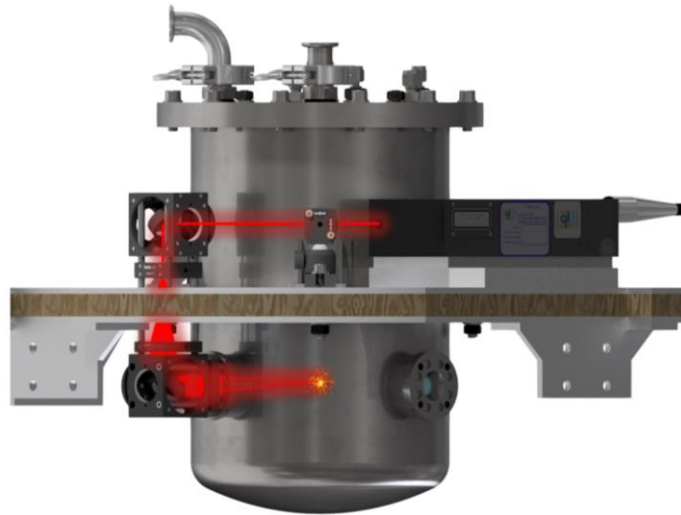
### 4.3. Droplet ignition

For the investigation of the burning LOX droplet during the free-fall phase, a defined ignition position and precise timing is necessary. Given the experimental boundary conditions, the established method of electrical ignition, as discussed in chapter 3.5, is unsuitable in this case for several reasons. An electric ignition spark requires electrodes in the direct vicinity of the droplet, so that its immediate surroundings would be affected and the sphericity of the flame disturbed. This is even more the case when the ignition spot has to be placed very close to the droplet surface, as it is the case for the  $H_2/O_2$  system due to the high diffusion rate of hydrogen. Given the pressure range to be investigated, between 0.1 to 5.5 MPa, the pressure dependence of the high voltage to be applied is also problematic. For these reasons, it was decided to use an optical ignition technique in which the droplet is ignited by a laser-induced plasma breakdown. With this technique, only optical access to the combustion chamber is required and no mechanical parts are needed inside the cryogenic combustion chamber.

The requirements for a suitable laser system resulted on the one hand from the required performance parameters, such as pulse energy, and on the other hand from the limitations of the experimental setup in the drop capsule, such as a compact and robust design with low weight or an integrated cooling system. Based on these requirements, a pulsed diode-pumped Nd:YAG laser from the company Quantel Laser was selected. The main specifications of the laser system are listed in Table 5.

**Table 5:** Main specifications of the Nd:YAG ignition laser system [184, 185].

Parameter	Value	Unit
Product name	Viron™	-
Wavelength	1064	nm
Pulse energy	30	mJ
Pulse width	< 8	ns
Repetition rate	20	Hz
Beam diameter	3.8±1.2	mm
Beam divergence	< 1.5	mrad
Power supply	24	V DC
Cooling	Conductively cooled via base plate	-
Remote access	Telnet commands	-
Dimensions	195 × 89 × 59	mm
Weight	1.7	kg

**Figure 49:** CAD illustration of the integrated laser ignition system with the schematic path of the laser beam in red.

Despite the relatively small dimensions of the laser system, the laser beam had to be deflected several times before it was guided into the combustion chamber. This was necessary so that the other optical accesses to the combustion chamber could be used for different diagnostics and were not blocked by the laser system. Figure 49 shows an illustration of the positioning of the laser system and the beam guidance. For the

optomechanical components the 30 mm cage system from Thorlabs was used, which has proven itself in drop tower operations. The cage components were connected directly to the flange of the outer vacuum container to minimize the relative motion between the laser system and the combustion chamber.

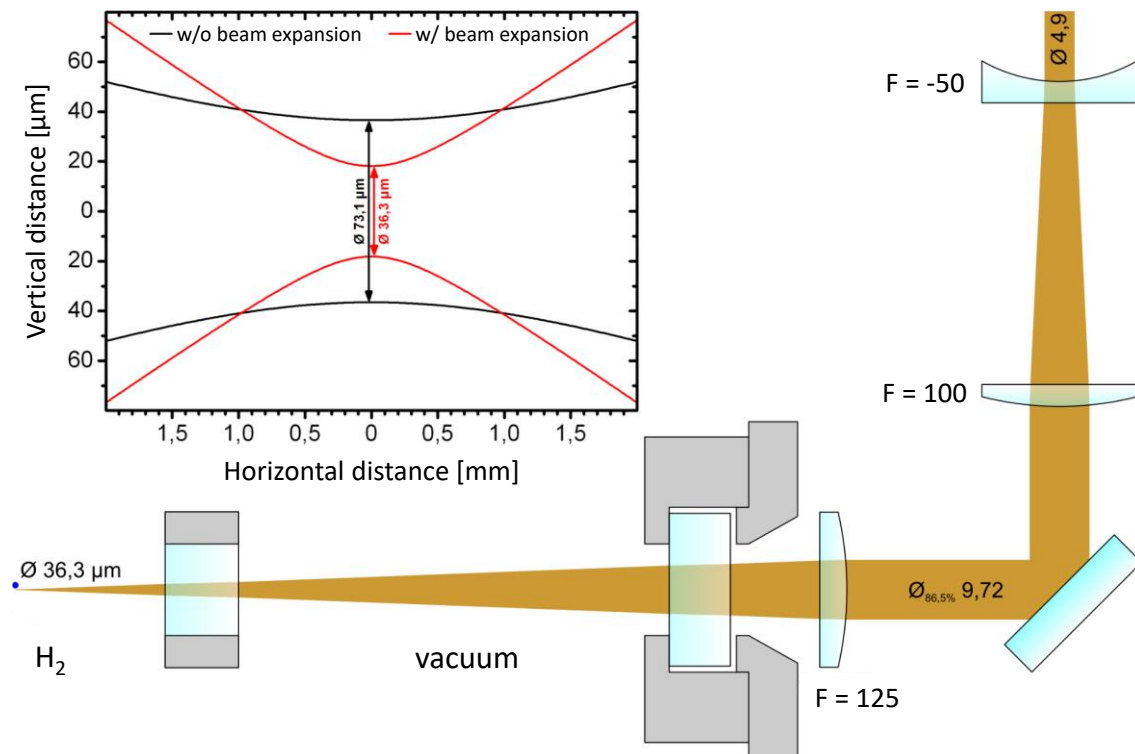


**Figure 50:** Initial concept for beam guidance and influence of the beam expansion on the focus dimensions. Focal lengths in mm. Modified figure from [186].

The actual ignition of the suspended droplet is accomplished by a single laser pulse from the laser system, which is focused to initiate a plasma breakdown for a spatially and temporally defined spark ignition. The integrated laser is dropped together with the combustion setup and is optically aligned relative to the droplet. The laser is mounted to the same platform as the cryogenic combustion chamber, and the exit beam diameter of 4.9 mm is expanded by a factor of 2 by means of a telescope to increase the energy density, as shown in Figure 50. As optical components, anti-reflection coated lenses and highly reflective near-infrared mirrors for 1064 nm were used. The expanded beam is guided along the optical axis of the combustion chamber by a precisely adjustable mirror. Before entering the combustion chamber, the beam is focused with a lens with a focal length of 125 mm, leading to a calculated beam diameter of 36  $\mu\text{m}$  in the focal plane. The adjustable mirror allows for positioning of the spark in the two lateral directions. Shifting the focus lens manually along the optical axis results in an adjustment of the spark along the third axis. The three-dimensional adjustability is necessary since the position of the spark depends on the gas composition and primarily on the pressure in the combustion chamber. The resulting change in the index of refraction can be compensated in this fashion. As the chamber pressure increases, the optimum ignition position, i.e., the position at which an ignitable mixture is present, also changes.

To assess the adjustability of the ignition location and the repeatability of the plasma breakdown, test series were performed without LOX droplets. Figure 51 shows an example of the result of these tests for different chamber pressures and pulse energies.

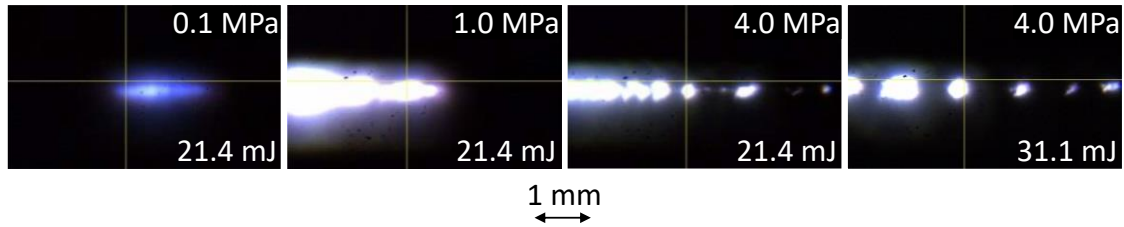


**Figure 51:** Pressure effect on the position and shape of the ignition spark in helium. Laser enters from the left.

The brightness of the ignition spark increases with increasing chamber pressure, with the position shifting in the direction of the focusing lens. At the same time, the shape of the ignition spark changes significantly. The spark becomes longer in the direction of the optical axis and several small sparks are produced in succession, making it difficult to accurately position the ignition location. The pulse energy of the ignition laser also affects the shape and position of the ignition spark. In the literature, the occurrence of multiple successive sparks along the optical axis, which is also called filamentation, is attributed to refocusing cycles. Here, self-focusing and plasma defocusing effects alternate [187]. The extension of the focus along the optical axis, i.e., the drop of the power density to  $1/e^2$ , was calculated to be 2.46 mm [186]. To reduce the focus extension and thus to reduce the filamentation length, the focal length of the focusing lens must be decreased. However, this would require the focus lens to be integrated into the vacuum container, as the distance between the center of the chamber and the outer window is about 120 mm. Therefore, the design of the beam guidance system with regard to the lens position was revised for high pressure experiments so that a lens with a focal length of only 40 mm is positioned directly in front of the inner window of the combustion chamber. This also required minor mechanical adjustments to the combustion chamber to mount this lens. The modifications made to the beam guidance and the effects on the shape of the focus are shown in Figure 52. The shorter focal length results in a reduction of the focus diameter by half with a larger beam divergence after the focus. The estimated extent of the focus along the optical axis is thus reduced to about 440  $\mu\text{m}$ . For the same pulse energy, the power density in the focus increases by a factor of about 4.5 due to the smaller diameter [186]. With the new optical design, the actual focus lens was no longer easily accessible, so the adjustment of the focus position along the optical axis was realized by moving the outer concave lens. However, the three-dimensional adjustability was much more limited with the new design than before. Therefore, the new design was only used for high-pressure experiments.

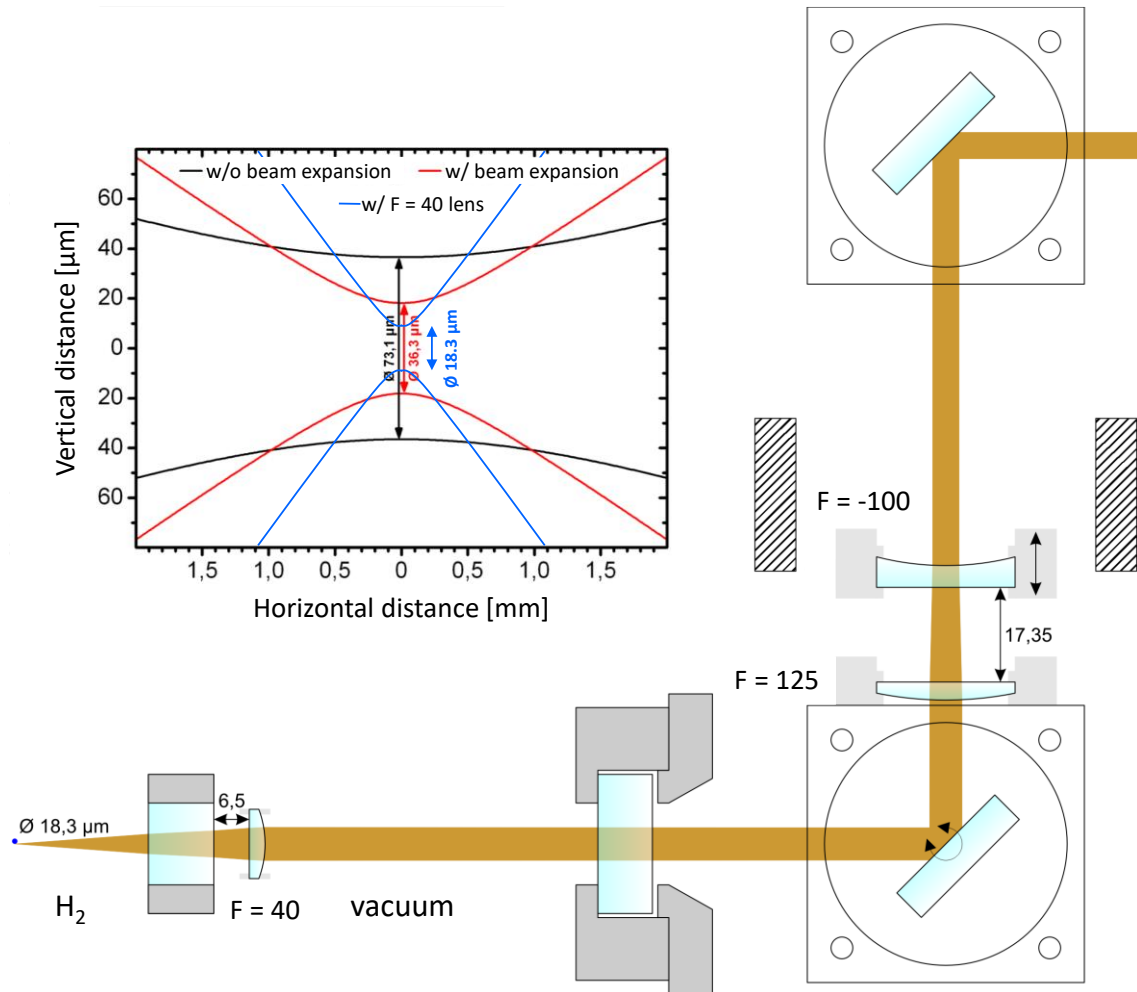


**Figure 52:** New concept for beam guidance and influence of the beam expansion vs. smaller focus lens on the focus dimensions. Focal lengths in mm. Modified figure from [188].

Tests in non-reactive helium atmospheres revealed that the sparks are reproducible with only very small changes in intensity and position. However, this only applied at constant pressure and temperature as well as within a limited period of time. With each change in pressure, the laser optics had to be adjusted accordingly to compensate for the change in refractive index. This also affected the adjustment of the pulse energy, because with increasing pressure the necessary energy to achieve a breakdown decreases. In order to avoid possible local uncontrolled breakdowns, the pulse energy was chosen as low as possible, so that the necessary energy density was only reached at the focal point and not slightly before. In addition, the cryogenic combustion chamber was subject to thermal fluctuations during an experiment run in the drop tower. Due to the long evacuation time in the drop tower, the liquid level of the coolant drops due to the vaporization of the liquid nitrogen. This leads to changes in the thermal expansion of the mounting bolts of the combustion chamber. As a result, the position of the suspender tip varied by approximately 0.1 mm in relation to the externally mounted laser optics. In addition, the relaxation of the drop capsule platforms at the moment of transition to the  $\mu\text{g}$  phase caused minimal movements of the suspender. Overall, all these factors resulted in slight

variations in the position of the ignition spark relative to the droplet in different experiments. Combined with the requirement that the plasma breakdown had to be positioned very close to the droplet surface to allow successful ignition, this resulted in a reduced reliability of the laser ignition when changing experiment parameters, as discussed in more detail in chapter 6.1.

On the one hand, the ignition should be as far away from the droplet as possible in order to minimize the effect on the droplet. On the other hand, however, the plasma spark must be positioned as close as necessary to ensure an ignitable mixture. The probability of achieving successful ignition during the free-fall phase in the drop tower could be increased, if several sparks were generated during one experiment. From shot to shot, the position of the spark was slightly moved toward the droplet surface by the motorized IR mirror, shown in Figure 52. The time between two sparks is adjusted to 250 ms (corresponding to a laser repetition rate of 4 Hz) so that if ignition is successful, the combustion process, which is considerably shorter, is not affected by the subsequent plasma breakdown. In the case of unsuccessful ignition, the pressure wave of the plasma breakdown caused the droplet to oscillate, but this oscillation was damped in less than 50 ms.

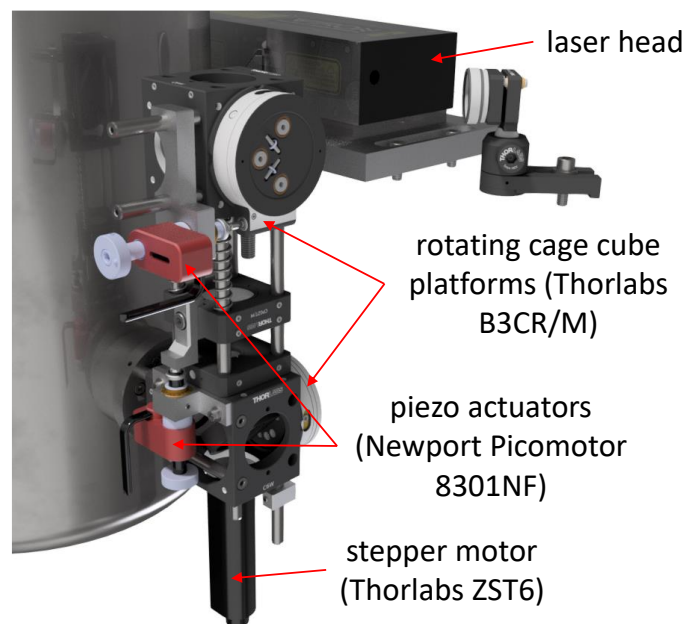


**Figure 53:** CAD representation of the motorized mirror and lens adjustment unit for remote-controlled and high-precision positioning of the ignition spark.

Figure 53 shows the motorized mirror and lens adjustment unit, which allowed the precise adjustment of the laser optics. To move the mirror and thus the vertical position of the plasma breakdown during the  $\mu\text{g}$  phase precisely and quickly, a stepper actuator was used (Thorlabs ZST6). This motor was installed in one of the adjustable mirror holders instead of a micrometer screw. Two piezo linear actuators (Newport Picomotor™ 8301NF) were used to precisely adjust the other two axes for positioning the laser-induced plasma breakdown. The rotation of the mirror during the experiment phase was synchronized

with the ignition laser. Both systems were controlled by the capsule computer, which is explained in more detail in the following subsection.

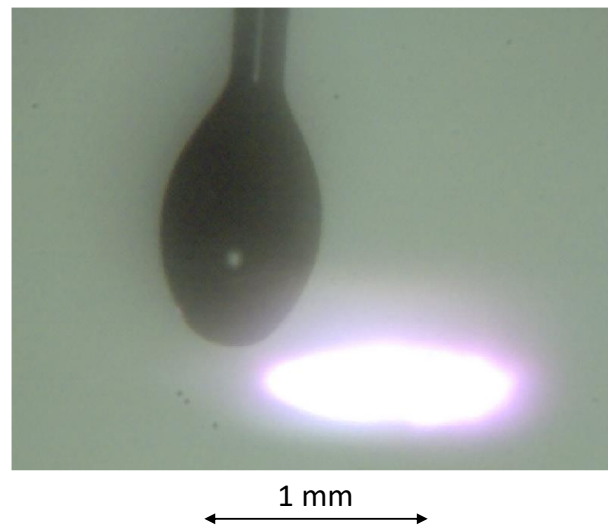


**Figure 54:** Laser-induced plasma spark at 0.15 MPa to ignite the LOX droplet.

With this optical laser system, the LOX droplet was successfully ignited in the investigated pressure range between 0.1 to 5.5 MPa. As an example, Figure 54 shows the plasma breakdown below a suspended LOX droplet in a hydrogen atmosphere at 0.15 MPa.

#### 4.4. Drop tower capsule

All experimental hardware including the electronic components and batteries were integrated into a standard drop tower capsule. The basic structure of this standard drop capsule is shown in Figure 55. The battery packs for the power supply of the experiment and the capsule control system (CCS), a PXI system from National Instruments, were mounted on the base structure. The CCS offers a variety of analog and digital input/output channels as well as serial interfaces, and relay switches. A LabVIEW program was used to control and monitor the experiment, which is explained in Appendix E. The release of the drop capsule as well as the experiment procedure during the  $\mu\text{g}$  phase were also controlled by the software. A radio telemetry and telecommand system was used to communicate with the experiment capsule in the drop tower. The experiment-specific components were mounted on different platforms, which were attached to four stringers (Bosch Rexroth aluminum profiles). The total weight of the experiment including the base and lid structures, the nose cone, additional weights, and the capsule shell was approximately 400 kg. The experiment-specific mechanical and electronic components were distributed over four capsule platforms, which are shown in Figure 56 as a CAD illustration.

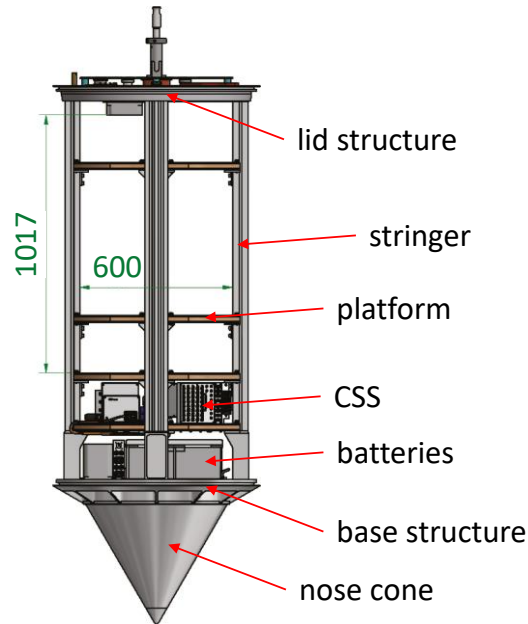


**Figure 55:** Technical drawing of the standard drop tower capsule without pressure-tight capsule shell and experiment-specific hardware. Reprinted from [176] with permission from ZARM FAB mbH.

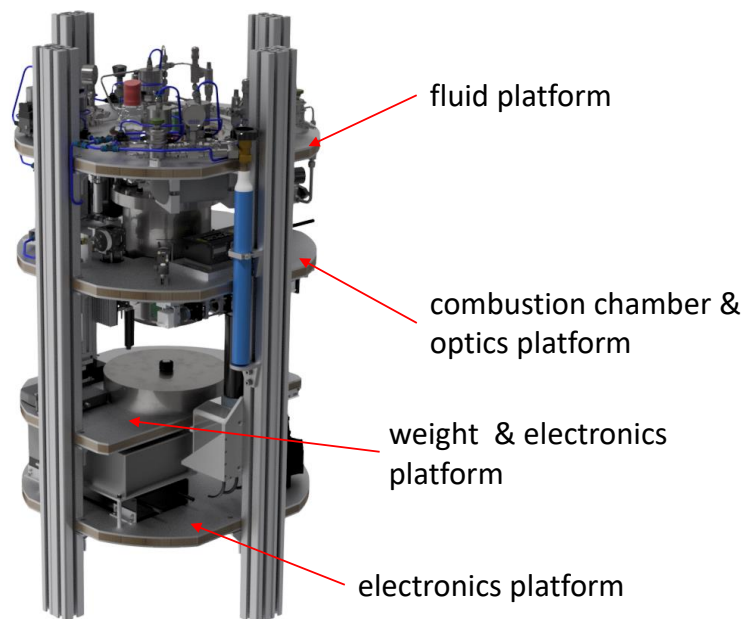


**Figure 56:** CAD illustration of stacked experiment platforms integrated into drop capsule stringer setup.

The top platform is the fluid platform on which the gas supply for the cryogenic combustion chamber was placed. Figure 57 shows the structure of this platform in top view. A complete schematic of the fluid system is shown in Appendix D. The platform was provided with a large cutout to allow the cryogenic combustion chamber to be assembled from above. A total of five compressed gas bottles were installed. The oxygen and helium bottles were each attached to a stringer and have a volume of 0.375 l and a filling pressure of 20 MPa. The hydrogen bottle, as well as another evacuated outlet tank

into which the hydrogen from the combustion chamber is fed for droplet generation, were mounted below the fluid platform. These two bottles have a volume of 1 l and a nominal filling pressure of 20 MPa each. A compressed air bottle with a volume of 1.1 l and a filling pressure of 20 MPa was mounted on the combustion chamber and optics platform. The compressed air served as the control medium for six pneumatically switchable main valves, which were used as inlet and outlet valves for the hydrogen, oxygen, and helium systems. In order to be able to switch these main valves remotely, a solenoid valve was installed in each compressed air line, which could be switched by the LabVIEW software via the CCS. The hydrogen system is connected directly to the combustion chamber, whereas the oxygen and the helium system is fed into the LOX valve. The helium system allows the LOX valve to be opened so that oxygen can enter the combustion chamber for droplet generation. The compressed air system was set up with Festo components, whereas a piping system from Swagelok was used for the other fluid systems.

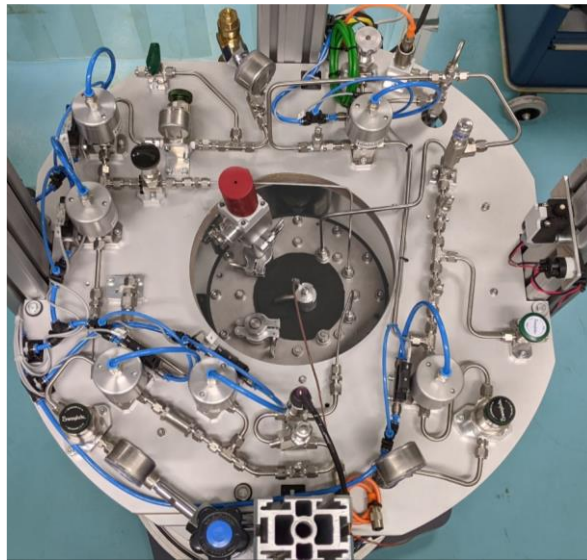


**Figure 57:** Top view of the fluid platform.

All systems are equipped with a pressure reducer to provide the required inlet pressure. Various flow restrictors are then used in the hydrogen, oxygen, and helium supply to limit the pressure rise in the line so that the defined target pressure can be set. A particle filter is also installed in the oxygen system to reduce the risk of an oxygen fire. The hydrogen and the oxygen supply are equipped with absolute pressure sensors. In the hydrogen system, a second flow restrictor is used on the outlet side in order to be able to reduce the pressure in the combustion chamber in a defined manner as part of the droplet generation process. Both the hydrogen and oxygen supply are equipped with a mechanical safety valve so that the pressure can be released in the event of overpressure. In the hydrogen system, the outlet of this safety valve is connected to the evacuated outlet tank to prevent hydrogen from leaking into the drop capsule. All systems were individually tested for leaks. The components for the oxygen system were also specially cleaned. The cryogenic combustion chamber including the fluid supply was designed for an operating pressure of up to 6.0 MPa ( $p_r = 1.19$ ).

The combustion chamber and optics platform were mounted below the fluid platform. The configuration of this platform is shown in Figure 58 as a CAD illustration. The cryogenic combustion chamber was screwed onto the top of the platform. Cutouts in the top of the platform allowed the combustion chamber to be positioned in such a way that the four optical access points are located on the underside of the platform. In addition to the cryogenic combustion chamber, the ignition laser system, and the compressed air supply were also mounted on the top of the platform, as shown in Figure 58a. The optics for the laser ignition, as well as several camera systems and light sources for the optical diagnostics were mounted on the underside. To minimize possible relative movements between the combustion chamber and the platform, as many components as possible were attached directly to the window flange using the 30 mm cage system.

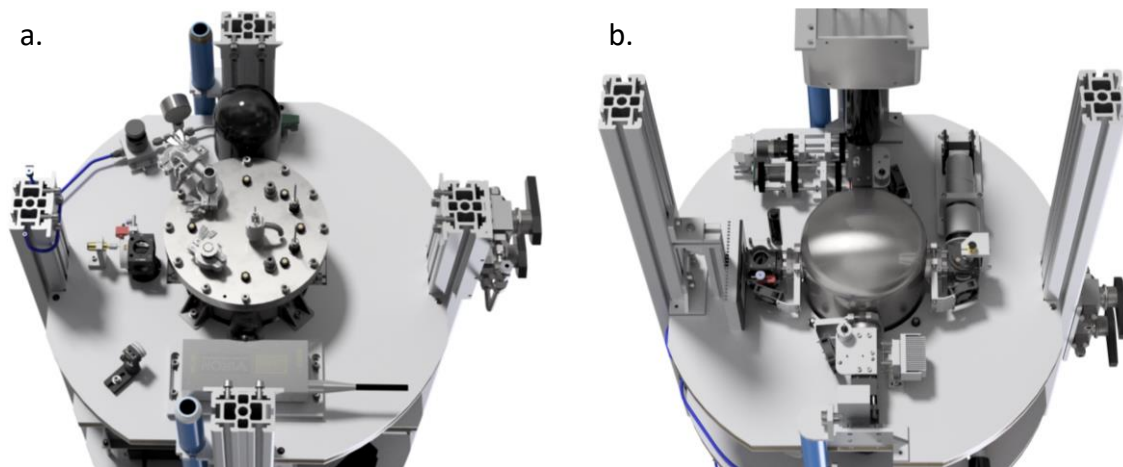


**Figure 58:** CAD illustration of the combustion chamber and optics platform. a. Top view. b. Bottom view.

Additional weights are placed on the weight & electronics platform to increase the overall weight of the capsule and thus enable smoother deceleration in the drop tower. In addition, all electronic components, such as camera recorders, voltage converters, timing devices, stepper motor or piezo actuator controllers, and an additional computer, are installed on the two lower platforms.

The final experimental setup of the drop tower capsule is shown in Figure 59. As already described in the previous subchapters, the experimental setup was continuously developed during the experiment campaigns. Thus, many new components were added to the setup, such as the motorized mirror and lens adjustment unit to be able to remotely adjust the position of the laser-induced plasma breakdown, as described in chapter 4.3. These adjustments also included the measurement techniques, which are described in detail in chapter 5.

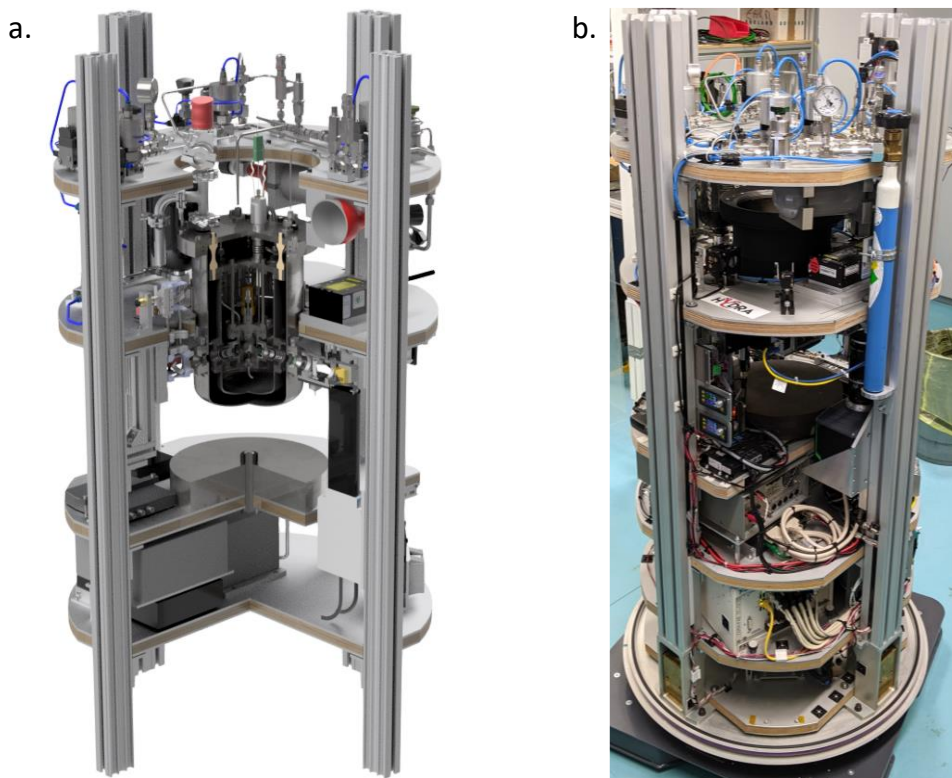


**Figure 59:** Final experimental setup of the drop capsule platforms. a. Cross-sectional CAD view. b. Actual image.

In addition to the supply and handling of the various fluids, the experimental setup also had to ensure precise timing to execute the experiment procedure in a defined manner during the free-fall in the drop tower. Special attention had to be paid to the synchronization of shadowgraph imaging with the very short laser pulse. This is important in order to see the position of the plasma breakdown on the camera images to perform the positioning of the focus relative to the suspender. The pulse width of the Nd:YAG laser is  $< 8$  ns, as shown in Table 5. This suggests a plasma emission duration on the order of  $< 1$   $\mu$ s [146]. Therefore, the camera system had to be precisely synchronized with the ignition laser to capture every plasma breakdown in the shadowgraph images. On the other hand, it was necessary for the  $OH^*$  chemiluminescence to protect the intensified camera from the bright plasma breakdown. Therefore, the exposure of the camera had to be controlled in a way that no radiation could hit the sensitive intensifier and the camera sensor at the moment of the plasma breakdown.

In order to ensure this high precision in the timing of the experiment sequences, several timing devices were built into the setup. Before the drop in the drop tower, the experiment was monitored and controlled using a remote access to the LabVIEW graphical user interface (GUI), shown in Appendix E. For this purpose, a radio connection was established with the CCS so that the commands could be executed from the control room. This also included the droplet generation process, which was performed manually via the LabVIEW interface prior to the drop. Two camera systems were used for visual control

of the droplet generation. Immediately after successful droplet generation and suspension, the experiment sequence was started, which automatically initiated the drop. Since the platforms typically oscillate slightly for approximately 300 ms after capsule release during the transition to the  $\mu\text{g}$  phase, which would negatively affect  $\mu\text{g}$  quality, the laser ignition was only initiated after this time. A  $\mu\text{g}$  switch was used to signal the CCS that the release of the capsule had occurred. In response, a transistor-transistor logic (TTL) signal was sent from the CCS to a delay and pattern generator (Quantum Composers 9214+). Up to this point, all actions were controlled by the CCS, i.e., with a low time precision and a typical delay time in the millisecond range. As soon as the delay and pattern generator, which is equipped with a high-precision clock (resolution and accuracy of 5 ns [189]), received the command, all subsequent actions were executed with a high time precision. The logic of the time control and the devices used are shown schematically in Figure 60.

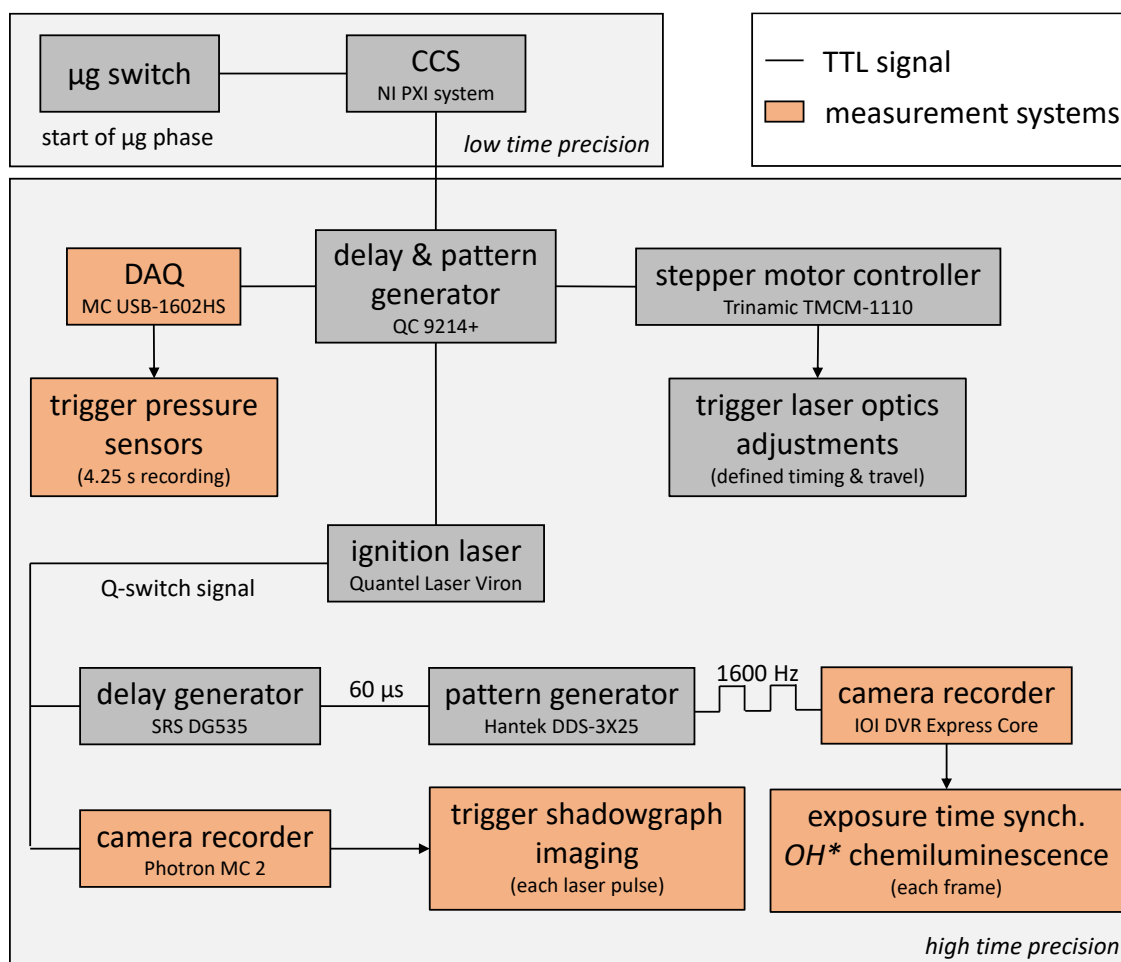


**Figure 60:** Timing diagram of the experiment sequence and the different measurement systems.

The delay and pattern generator triggered several devices after receiving the signal from the CCS. A TTL signal was sent to the armed ignition laser to trigger a predefined series of laser pulses. The synchronized Q-switch signal of the laser was then transmitted to several other devices. On the one hand, the signal was used as trigger input for the Photron

MC 2 camera recorder, which was used for shadowgraph imaging. The recorder was set to record a fixed number of images with each trigger signal, i.e., with each laser pulse. This ensured that every plasma breakdown was captured. On the other hand, the Q-switch signal was also used as a trigger signal for another delay generator. The Stanford Research Systems DG535 pulse delay generator was used to delay the laser signal for a defined period of time. As previously discussed, this was necessary to protect the intensified camera from the bright spark. A delay of 60  $\mu\text{s}$  was chosen for this purpose. The delayed TTL signal was then passed to a pattern generator (Hantek DDS-3X25). This device generated a predefined square wave pattern with a frequency of 1600 Hz. The camera recorder (IO Industries DVR Express Core) used this signal as a synchronized exposure time signal for the  $OH^*$  chemiluminescence diagnostics. With each rising edge of the signal, an image was exposed for a predefined amount of time. In addition, the Quantum Composers delay and pattern generator provided trigger signals for the laser optics adjustment unit and will also be used for the high-speed pressure measurement in the future. A stepper motor controller (Trinamic TMC2130) was used to adjust the laser optics during the experiment phase. After receiving the trigger TTL signal, the predefined travel of the motor was executed with a defined acceleration and velocity profile. For first tests of the new pressure measurement, as described in chapter 5.3, a data acquisition unit (DAQ) from Measurement Computing (USB-1602HS) was used. The trigger signal started the data recording with a duration of 4.25 s. The pattern generator can also be used to control the future planned background oriented Schlieren diagnostics. However, this technique was not used in the experiments discussed in this thesis, and therefore the corresponding components are not shown in Figure 60.

In addition to the CCS, another computer (Intel NUC) was integrated into the experimental setup. This miniaturized computer was used to configure the Photron MC 2 recorder, the pattern generators, and the stepper motor controller. Additionally, another LabVIEW program ran on this computer to control the DAQ for the pressure measurement. In the future, the camera recordings for the background oriented Schlieren diagnostics will also be acquired via this computer. The NUC was accessed remotely from the control room, as was the intensified camera recorder (IO Industries DVR Express Core), which also had its own operating system.

A mechanical contact switch was integrated into the experimental setup to allow the laser to operate only in the closed drop capsule. Detailed work procedures were developed for conducting the laboratory tests and the experiments in the drop tower. For example, procedures were defined on how to evacuate the combustion chamber after a combustion test. Due to the amount of LOX introduced into the suspender tube during the droplet generation process, it had to be assumed that an ignitable mixture was present in the combustion chamber even after a successful droplet combustion experiment. Therefore, the mixture was first diluted by helium before being drained through a cleaned pipe into a bucket of water to ambient pressure. This should prevent a possible ignition or explosion at the outlet of the pipe. After that, the combustion chamber was filled again with helium to a pressure of 5 MPa and the procedure was repeated. Only after two complete cycles the combustion chamber was evacuated with a vacuum pump.

## 5. Measurement techniques

The most essential quantities in droplet combustion are the droplet diameter and the flame position relative to the droplet. Based on the time evolution of these two quantities, the combustion process can be fundamentally characterized or parameter studies can be evaluated. The key indicators that can be derived from this are, e.g., the combustion rate constant or the flame standoff distance. A variety of diagnostics can be used to measure these basic variables, as discussed in chapter 3.6. In addition, modern optical measurement techniques also offer the possibility to investigate much more than just these basic quantities, such as the composition of species involved in the gas phase or the temperature profile around the droplet. However, the use of sensitive optical diagnostics in a drop tower experiment presents a particular challenge. Due to the very limited space, the severely restricted optical accessibility to the combustion chamber, and the harsh environmental conditions, such as the hard deceleration (approximately 50 g), the measurement techniques have to be very robust [67, 176].

Some laser-based diagnostics, such as  $OH^*$  PLIF, have already been successfully used in droplet combustion experiments in the drop tower [22, 168]. With this technique, a laser is used to create a light sheet around the droplet.  $OH$  molecules are excited by this light sheet resulting in an emission of UV radiation, which is then visible to an intensified camera. In contrast to line-of-sight methods, this technique does not provide integral  $OH^*$  signals, but along a 2D plane [150]. However, this requires the droplet to be shielded from the light sheet (to protect the intensified camera from direct irradiation through scattered laser light), which implies that the droplet is stationary. As discussed in more detail in chapter 6.2, in the LOX droplet combustion experiments evaluated in this thesis, the droplet detached from the suspender after ignition. Therefore, this technique could not be used because the droplet was not stationary during combustion.

Within the scope of the experiments conducted for this thesis, shadowgraph imaging and  $OH^*$  chemiluminescence were employed. Shadowgraph imaging was the primary diagnostic system with the images transmitted as a live video signal from the experiment capsule to observe the droplet generation. Two shadowgraph systems were installed in the experimental setup: a high spatial resolution and a high-speed system. The shadowgraph images were primarily used to determine the droplet diameter and shape. Since the calculation of the combustion rate depend on the initial droplet size, the generated LOX droplet size was precisely measured with the high-resolution camera system. The combustion, in turn, had to be recorded with high temporal resolution since the duration of the LOX droplet combustion process is very short. In addition to the two shadowgraph systems,  $OH^*$  chemiluminescence was employed. The chemically excited  $OH$  radicals produced during combustion were imaged with a two-stage intensified camera system (II-CMOS). This information was used to determine the structure and size of the flame. The setup of the employed diagnostic systems is shown schematically in Figure 61.

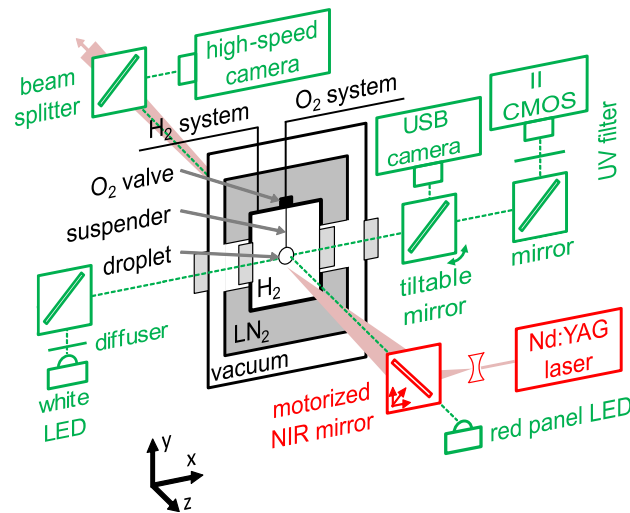


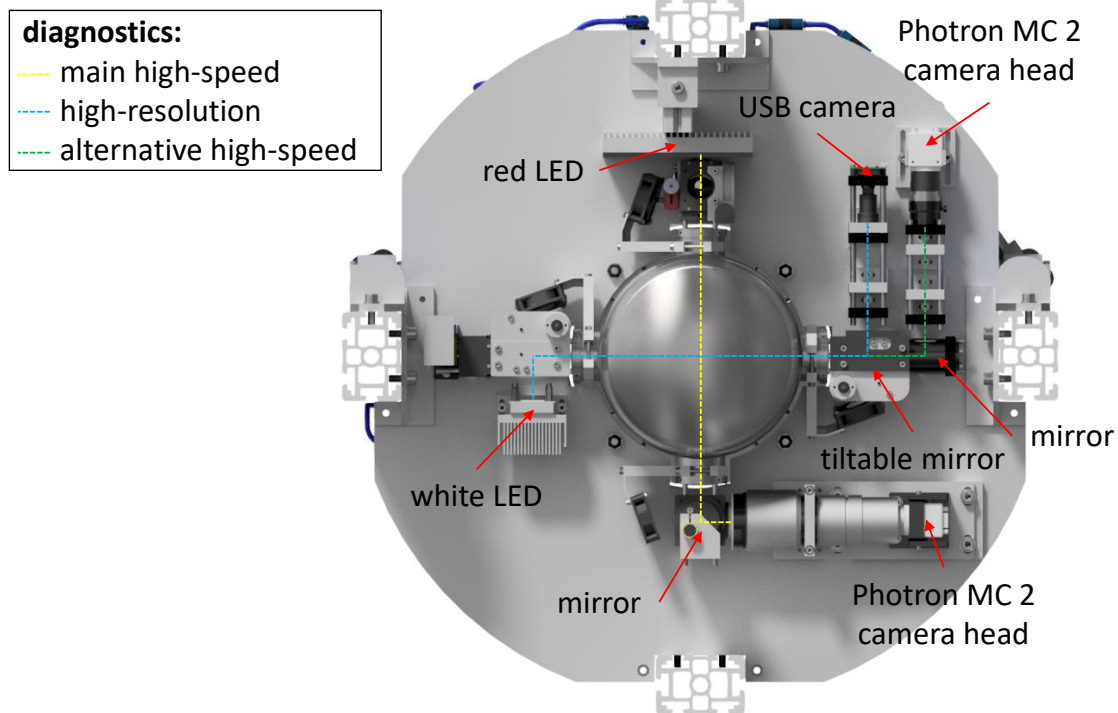
**Figure 61:** Schematic overview of the optical setup. Red: ignition system with illustrated laser beam path (z-axis). Green: diagnostics with indicated optical beam paths (dashed lines, x/z-axis).

In the following subchapters, the setup of the optical diagnostics is described in detail. In addition, different methods for the pressure measurement in the combustion chamber are described. To investigate the concentration field during LOX droplet vaporization and also the temperature field around the droplet during combustion, a BOS diagnostic was integrated into the experimental setup. However, this diagnostic was not used in the experiments evaluated for this thesis. Therefore, the BOS setup is described in Appendix F. Parts of the content was published by the author of this thesis and collaborators in [117, 118, 177-180].

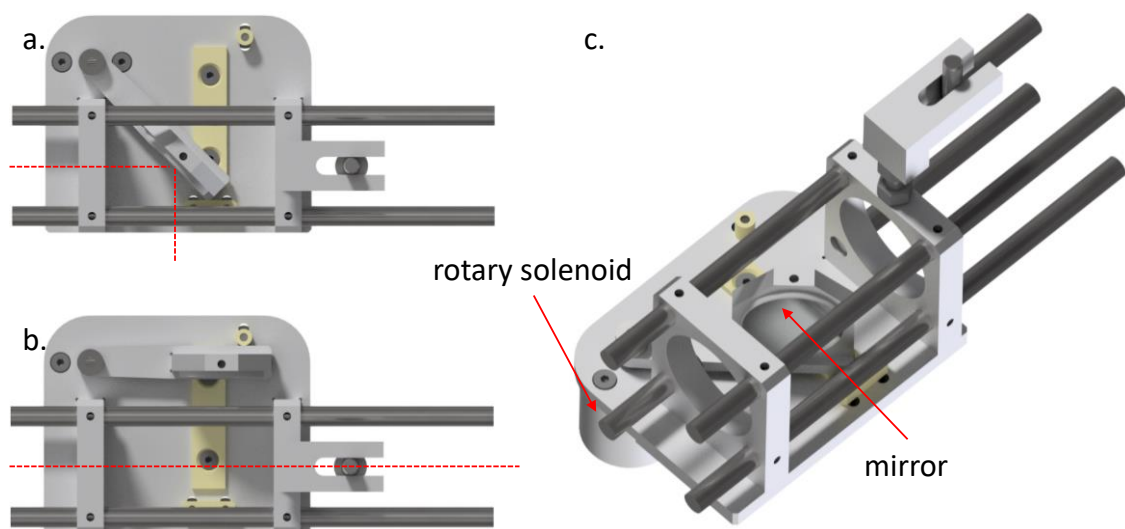
## 5.1. Shadowgraph imaging

Figure 62 shows the setup of the shadowgraph imaging diagnostics which was integrated into the drop capsule. The high-resolution shadowgraph optics consists of a white area light-emitting diode (LED) as backlight. The light is directed into the combustion chamber through a diffuser and a mirror. On the other side of the cryogenic combustion chamber, a tiltable mirror is used to guide the light into the high-resolution camera UI-1491LEM-GL from Imaging Development Systems. The tiltable mirror was developed in-house and consists of a rotary solenoid (Kuhnke D 24-BOR-F-DS9420-24VDC) that moves a mirror attached to an arm in or out of the optical path, as shown in Figure 63. The resolution of the camera including magnification optics is  $0.61 \mu\text{m}/\text{px}$  at 5 fps and the image size is  $2144 \times 2150 \text{ px}$  (field of view:  $1.31 \times 1.31 \text{ mm}$ ). The camera optics consists of a 50 mm camera lens and a telescope consisting of a concave and a convex lens. This setup minimizes the space required for the optics while allowing for a large magnification. The system was used to measure the LOX droplet in detail before initiating the experiment. For this purpose, the volume of the suspender was first determined. Immediately after the droplet suspension, an image of the suspender including the LOX droplet was taken, as shown in Figure 48. By calculating the integral volume of the droplet

and the suspender, and by determining the wetted suspender area, the initial LOX droplet volume could be precisely determined.



**Figure 62:** CAD illustration of the integrated shadowgraph imaging diagnostics with indicated optical beam paths (dashed lines).



**Figure 63:** CAD illustration of the functional principle and structure of the tiltable mirror. Optical path is shown as dashed line. a. Normal position of the mirror (rotary solenoid not powered). b. Alternative position of the mirror (rotary solenoid powered). c. Main components of the design.

In addition to the high-resolution shadowgraph system, a high-speed shadowgraph system was employed. In this case, the light source, a red area LED with a diffuser, was placed behind the motorized IR mirror for laser ignition, as shown in Figure 61. The high-speed

camera (Photron MC2) was positioned on the opposite side of the window where the ignition laser is directed into the combustion chamber. To protect the camera system from the high-intensity IR radiation of the ignition laser, a beam splitter system was used that directed the IR radiation away from the camera. This system consists of a 45° cold mirror (Thorlabs M254C45), a 0° hot mirror (Thorlabs M254H00), and a short pass filter (Thorlabs FESH0750). A 108 mm zoom lens (Kowa LMZ45T3) is used to image the droplet. This camera system has a spatial resolution of 16.1  $\mu\text{m}/\text{px}$  and was operated at 2000 fps and 512  $\times$  512 px (field of view: 8.24  $\times$  8.24 mm). The camera was synchronized with the ignition laser to ensure that every ignition spark was recorded so that the position of the sparks could be verified. Both camera systems, the high-resolution and the high-speed system, could be operated in parallel and were transmitted as live video to the control room.

After the high-resolution droplet measurement just before dropping the experiment, the tiltable mirror was actuated, allowing another diagnostic to be applied during the combustion. Thus, in addition to the primary shadowgraph diagnostic, either  $OH^*$  chemiluminescence, described in detail in chapter 5.2, or a second shadowgraph imaging system could be used, as shown in Figure 62. Similar to the high-resolution system, the second shadowgraph high-speed camera was equipped with a telescope and allowed the investigation of the combustion process from two sides. The second camera system has a spatial resolution of 7.8  $\mu\text{m}/\text{px}$  and was also operated at 2000 fps and 512  $\times$  512 px (field of view: 3.99  $\times$  3.99 mm). Figure 64 shows examples of shadowgraph images recorded by both high-speed camera systems.

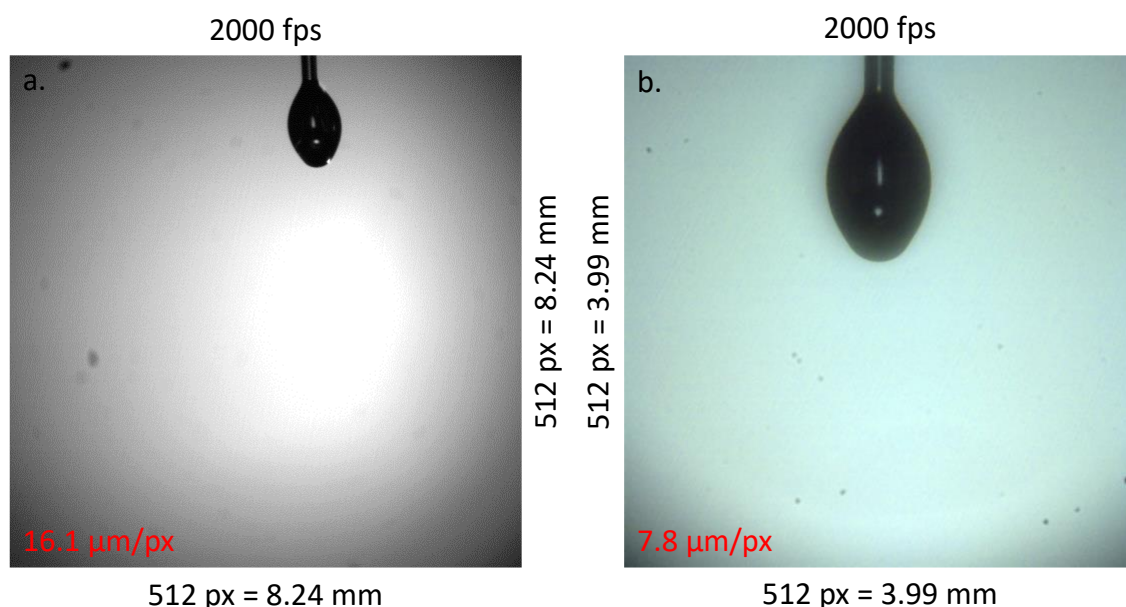


**Figure 64:** High-speed shadowgraph images of a suspended LOX droplet. a. Main camera system (monochrome). b. Second camera system (color).

However, the shadowgraph systems were not used for actual density measurements in the gas phase because the flame created a second light source that overlapped the

measurement. Therefore, this technique was only used for droplet analysis, ignition and flame observation, and analysis of the effect of water as product of the combustion.

For the evaluation of the acquired images, a MATLAB tool was developed to determine the droplet diameter and the flame zone diameter. The source code can be found in Appendix G. The particular challenges in image evaluation were the detachment of the droplet, the strong brightness changes during the combustion process due to water condensation in the combustion chamber, both discussed in chapter 6.2, and the significant deviation from spherical shape under certain conditions, as discussed in chapter 6.3. For this reason, a semi-automatic evaluation process was used to calculate the equivalent droplet diameter. This process is based on a manual selection of an evaluation area in which the droplet to be detected is located, as shown in Figure 65.

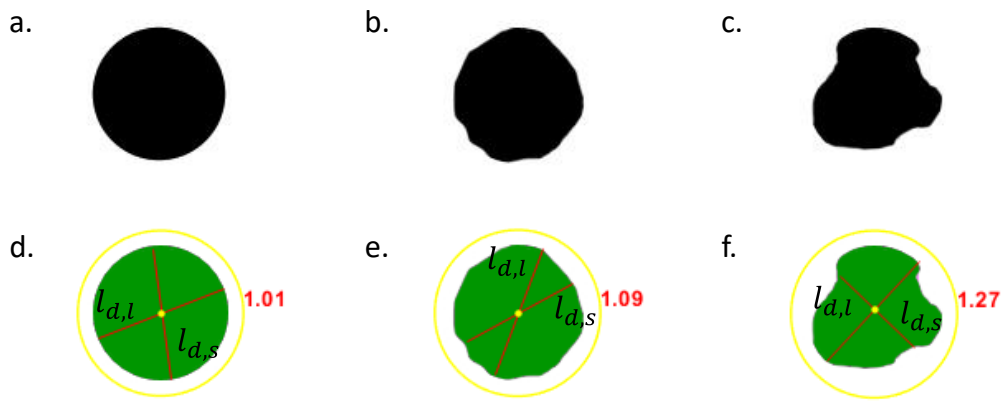


**Figure 65:** Equivalent droplet diameter detection algorithm demonstration. a-c. Generated example images. d-f. Evaluated images (yellow circle: manually selected evaluation area, green area: detected droplet area, yellow dot: calculated droplet centroid, red lines: shortest  $l_{d,s}$  and longest  $l_{d,l}$  dimension line, red value: droplet shape ratio  $R_d$ ).

Within this area, the image is then binarized to separate the droplet from the background. For this purpose, a brightness threshold is calculated. Due to the absorption of the background light, the droplet appears dark on the camera. However, a bright spot may appear in the center of the droplet due to the transparency of the liquid. To identify this point also as part of the droplet, enclosed gaps are closed in the binarized image. Using this method, non-circular shapes can also be detected and an equivalent droplet diameter can be calculated based on the sum of all droplet pixels. To evaluate the droplet shape, the centroid of the identified droplet pixels is calculated and used as a center point to determine the shortest and the longest dimension line of the droplet within a resolution of  $1^\circ$ , i.e., 360 lines. The ratio between the longest and the shortest line is defined as:

$$R_d = \frac{l_{d,l}}{l_{d,s}} \quad (54)$$

where  $l_{d,l}$  is the longest droplet dimension line and  $l_{d,s}$  is the shortest droplet dimension line. For an exact circular shape (resulting in a spherical droplet shape),  $R_d$  is unity. Thus,

the droplet shape ratio  $R_d$  is used as a two-dimensional measure of the deviation from a spherical shape, as shown in Figure 65.

The automatic detection of the size of the droplet was verified manually for certain time steps of each experiment. Due to the changes in brightness during the combustion caused by the water cloud, there could be minimal fluctuations in the diameter determination using this algorithm. The most significant measurement uncertainty of the shadowgraph diagnostic was the non-spherical droplet shape at low pressures. The deviation of the droplet shape ratio from unity can give an indication at which time the measurement uncertainty was increased, because the complex shape of the droplet could not be determined unambiguously using only one camera. In some experiments, the droplet partially burned behind the suspender so that the suspender partly or fully obscured the view to the droplet. However, this effect occurred rarely and affected only short phases during combustion, during which no reliable data could be obtained in any case. Due to the free floating of the burning droplet, the droplet also moved within the depth of field of the cameras, which could cause slight deviations in the diameter determination. However, these effects are considered to be very small since the droplets burned in the direct vicinity of the suspender, i.e., in the focal plane, and no significant blurring was apparent. In contrast, the determination of the droplet lifetime and the initial droplet diameter was not significantly affected by these effects. Due to the framerate of 2000 fps the maximum temporal error was  $< 500 \mu\text{s}$ .

## 5.2. $OH^*$ chemiluminescence

In order to perform  $OH^*$  chemiluminescence imaging of the combustion zone simultaneously with the high-speed shadowgraph imaging during the free-fall phase, the LED light source for the high-resolution shadowgraph imaging was switched off and the mirror was tilted, as shown in Figure 61. This unblocked the beam path from the combustion chamber into a two-stage intensified camera (II-CMOS) with two micro-channel plates. This camera (Lambert HiCAM 500 ST) is used to image the  $OH^*$  chemiluminescence at a wavelength of 308 nm and has a maximum photon gain of 320,000 (ph/ph) applying fiber-taper coupling of the intensifier to the phosphor-screen. An UV-bandpass filter (Schott UG11) protects the camera from the bright flame luminosity. The transmission spectrum is shown in Figure 66. In addition, the timing of the camera shutter is slightly delayed compared to the ignition laser to protect the sensitive camera from the bright ignition spark, as described in chapter 4.4.

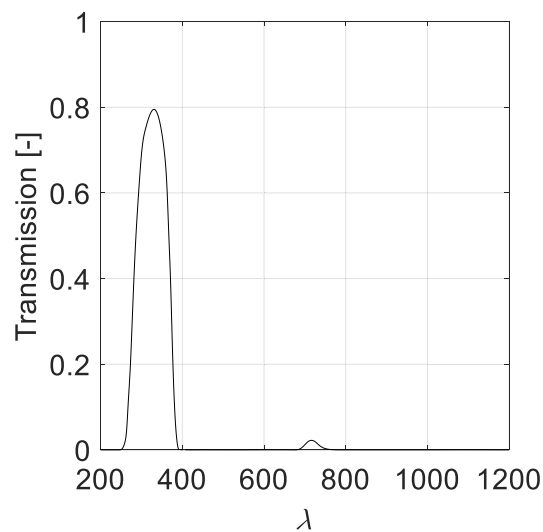


**Figure 66:** Transmission characteristics of the UG11 UV-bandpass filter with a thickness of 3 mm. Adapted from [190].

For magnification, a UV-optimized camera lens (UV-Nikkor) with a focal length of 105 mm is used. The resolution of the intensified camera is  $24.2 \mu\text{m}/\text{px}$  at 1600 fps. The integrated setup of the  $OH^*$  chemiluminescence diagnostics is shown in Figure 67.

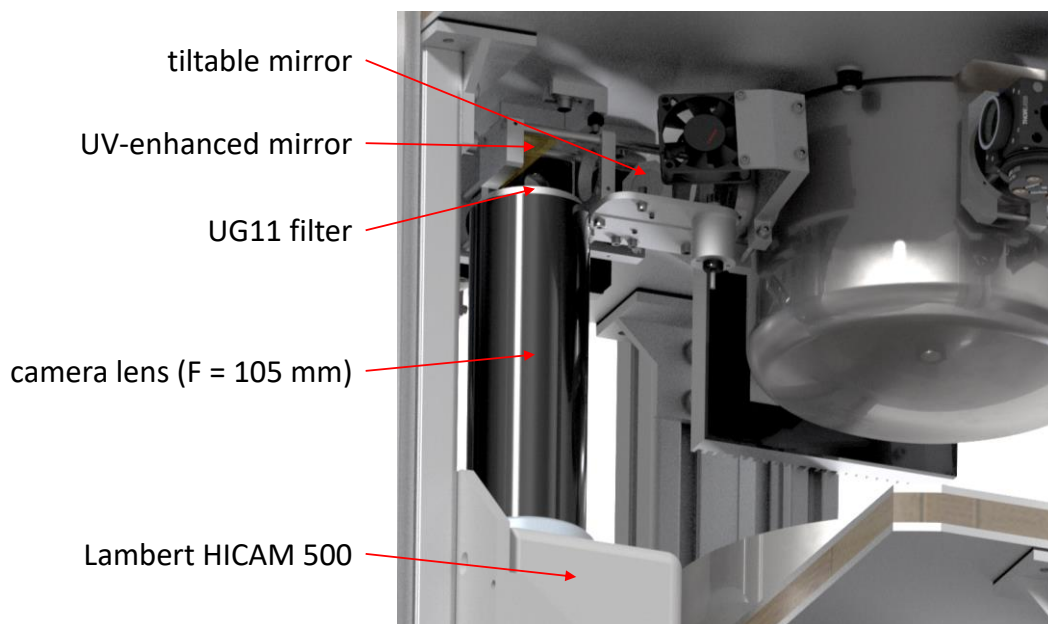


**Figure 67:** CAD illustration of the integrated  $OH^*$  chemiluminescence diagnostics with highlighted main components.

The camera is mounted vertically at a stringer and is looking into the combustion chamber via a UV-enhanced mirror when the tilted mirror is actuated. To prevent the weak UV chemiluminescence signal from being absorbed, the combustion chamber and the vacuum container are equipped with UV-transmissive quartz windows. The UV filter is mounted directly on the camera lens. Figure 68 shows a test image with the camera setup for  $OH^*$  chemiluminescence without the UV filter, i.e., in the visible spectrum.

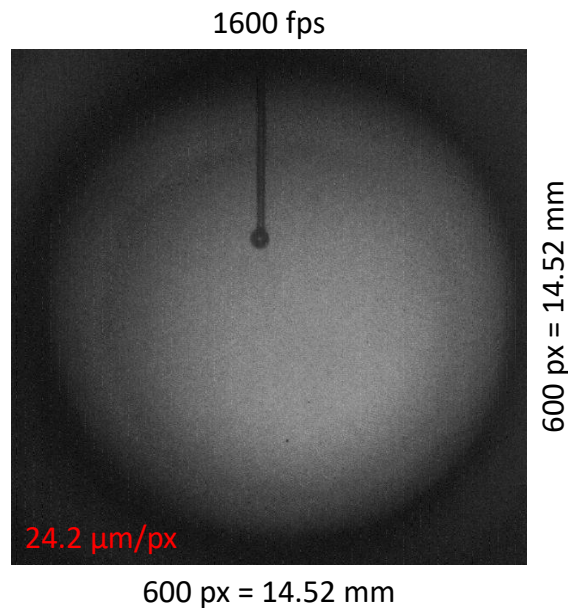


**Figure 68:** Test image with the intensified camera for  $OH^*$  chemiluminescence without UV filter attached.

The intensifier of the camera was operated with a temporal gate width between  $5 \mu\text{s}$  at 0.1 MPa and 40 ns at 5.7 MPa depending on the luminosity of the flame. This parameter and the camera gain were adjusted accordingly for each experiment. In contrast, the exposure time was fixed at  $600 \mu\text{s}$  and the intensifier gain was fixed at 800 V. Both parameters were not adjusted during the experimental campaigns.

To analyze the acquired images, the MATLAB tool presented in Appendix G was also used here to determine the flame zone diameter. Since only the self-radiation of the flame was recorded, no other objects, such as the suspender, can be seen in the images. Therefore, a Hough transformation was performed to determine the diameter of the spherical flame. The Hough transformation is a feature extraction technique and is a proven method for recognizing geometric figures, such as circles, in a binary gradient image after edge detection [191]. For this transformation, the images must first be binarized. Since the brightness of the  $OH^*$  signal changed during the experimental campaigns due to the pressure effect and the corresponding adjustments of the camera system, no fixed threshold value could be selected for binarization. Therefore, the method of Otsu [192] was used, which calculated an automatic threshold value for each image. Using the binarized images, the algorithm detected each pixel that represents an edge of the signal. All circle centers that could lead to an edge pixel within a predefined radius range were then determined. The last step was to analyze the distribution of all detected circle centers and to derive the global center of the detected circle. With this algorithm, the center point as well as the radius could be determined on each frame.

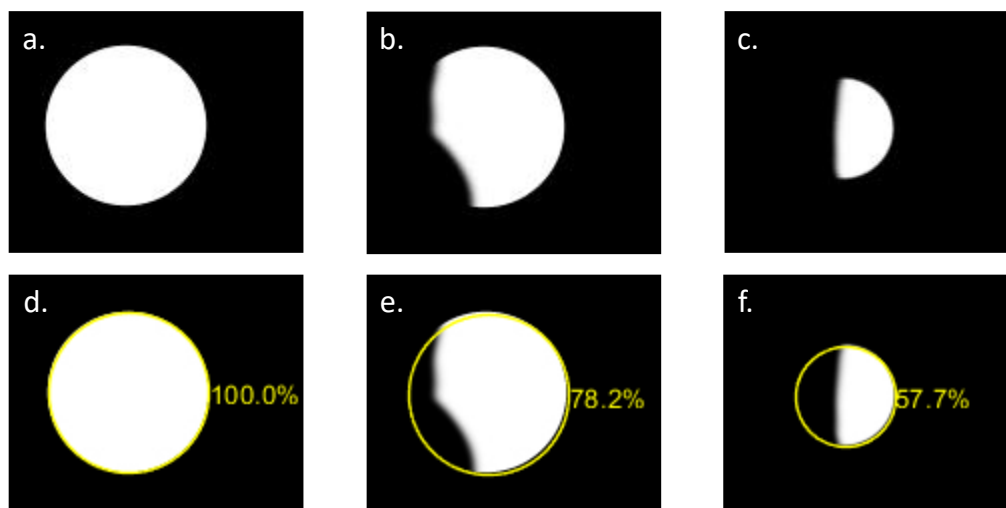


**Figure 69:** Flame diameter detection algorithm demonstration. a-c. Generated example images. d-f. Evaluated images (yellow circle: detected circle, yellow value: filling level).

The detachment of the LOX droplet from the suspender during combustion could lead to the case that the suspender partially (or even completely) obscured the  $OH^*$  signal. However, the use of this evaluation method allowed a precise evaluation, because even incomplete circles could also be detected, as shown by generated example images in Figure 69. Since no sharp signal edge was expected due to the limited resolution of the camera and due to the relatively long lifetime of the  $OH^*$  signal, the evaluation algorithm was also tested on artificially generated images with burred edges, as shown in Figure 70.

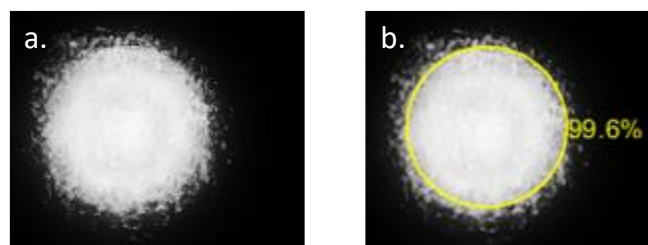


**Figure 70:** Flame diameter detection algorithm demonstration on artificially generated example signal. a. Generated signal. b. Evaluated image (yellow circle: detected circle, yellow value: filling level).

As with the shadowgraph images, individual images were manually reviewed and the automatically determined flame diameter was verified. The water cloud around the burning droplet did not noticeably affect the  $OH^*$  signal. However, as mentioned above, the suspender partially obscured the signal, which resulted in some experiments where flame data could not be determined at the end of the combustion process. Due to the framerate of 1600 fps the maximum temporal error was  $< 625 \mu\text{s}$ .

### 5.3. Pressure measurement

The primary parameters for setting up the experiment were the combustion chamber pressure and the pressure in the oxygen line. In addition, the initial combustion chamber

pressure represents the main parameter in the parametric study performed. Two absolute pressure sensors or two relative pressure sensors were used to measure these pressures, depending on the intended system pressure. Up to an experiment pressure of 1.2 MPa, two U5300 absolute pressure sensors from TE Connectivity with a measuring range from 0 to 1.4 MPa and an accuracy of  $\pm 1.4$  kPa were used. For higher pressures, two 520 pressure sensors from Huba Control with a measuring range from 0 to 6.1 MPa and an accuracy of  $\pm 30.5$  kPa were employed. The pressure sensors were integrated into the piping system outside the cryogenic combustion chamber, as shown in the fluid system schematic in Appendix D.

The measured values were acquired via the CCS, which recorded the pressure values during the free-fall phase at a sampling rate of 2 kHz. However, both sensor types have a natural frequency of  $< 100$  Hz. This means that only relatively slow pressure changes could be detected by the sensors. For the droplet generation process, the differential pressure between the hydrogen in the combustion chamber and the oxygen in the supply line was important. At this point, the combustion chamber pressure is constant and the oxygen pressure also changes only slowly due to condensation. However, during ignition and combustion, dynamic pressure changes can also occur that could not be detected by this rather static pressure measurement system. In addition, a damping effect occurs because the hydrogen sensor was not placed directly in the combustion chamber, but was connected to the combustion chamber via piping.

In order to improve the temporal resolution of the pressure measurement, an additional high-speed pressure measurement system from KULITE was integrated into the experimental setup after the experimental campaigns. This system consists of two cryogenic pressure transducers (CTL-190LM-100A and CTL-312-1000A) and two signal conditioners (KSC-1-BE4). Two different measuring ranges were selected: 0 to 0.7 MPa and 0 to 6.9 MPa. The maximum accuracy errors are  $\pm 3.4$  kPa (typical  $\pm 0.7$  kPa) and  $\pm 34.5$  kPa (typical  $\pm 6.9$  kPa). The pressure transducers were screwed directly into the base of the combustion chamber, as shown in Figure 71. Since the combustion chamber is completely surrounded by liquid nitrogen, the sensors must be suitable and compensated for cryogenic temperatures. Both sensors have therefore been factory compensated for a temperature range of 77 to 311 K. The natural frequency (without the sensor screen) is 380 kHz and 1 MHz, respectively.

The measurement data acquisition for this system is handled by the two-channel DAQ USB-1602HS from Measurement Computing. This device has a maximum sampling rate of 2 MHz per channel and is controlled by a LabVIEW program running on the NUC. The two pressure sensors are connected to the signal conditioners by a cable which is led through the nitrogen feedthrough into the LN<sub>2</sub> container. The signal conditioners in turn are connected to the DAQ via a coaxial signal cable. In addition, the DAQ is connected to a delay and pattern generator to start the measurement precisely, as described in chapter 4.4. Both channels are recorded with the rate of 2 MS/s for 4.25 s. The data evaluation is done by a MATLAB program, which evaluates and displays the data.

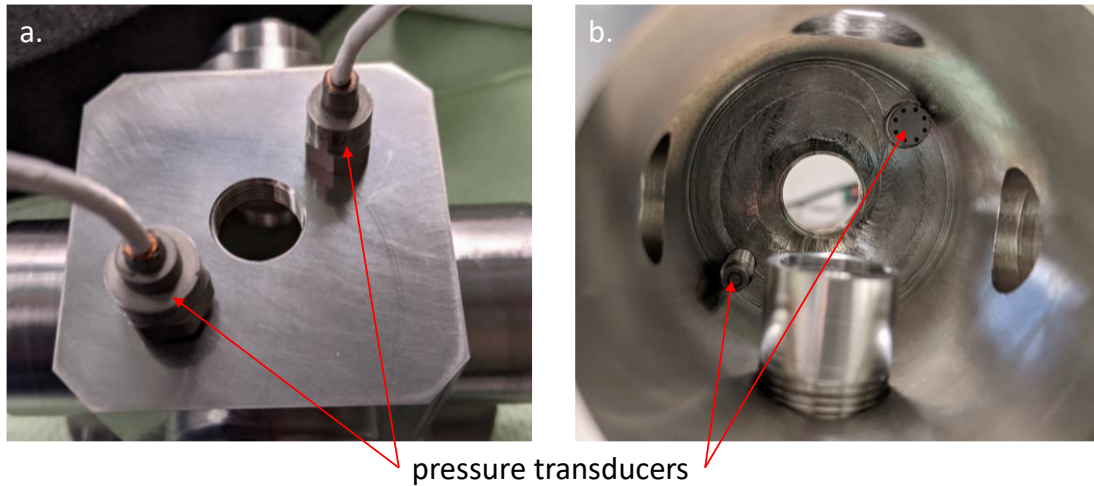


**Figure 71:** Integrated high-speed pressure transducers into the combustion chamber main body. a. Exterior view of the combustion chamber base. b. View into the combustion chamber.

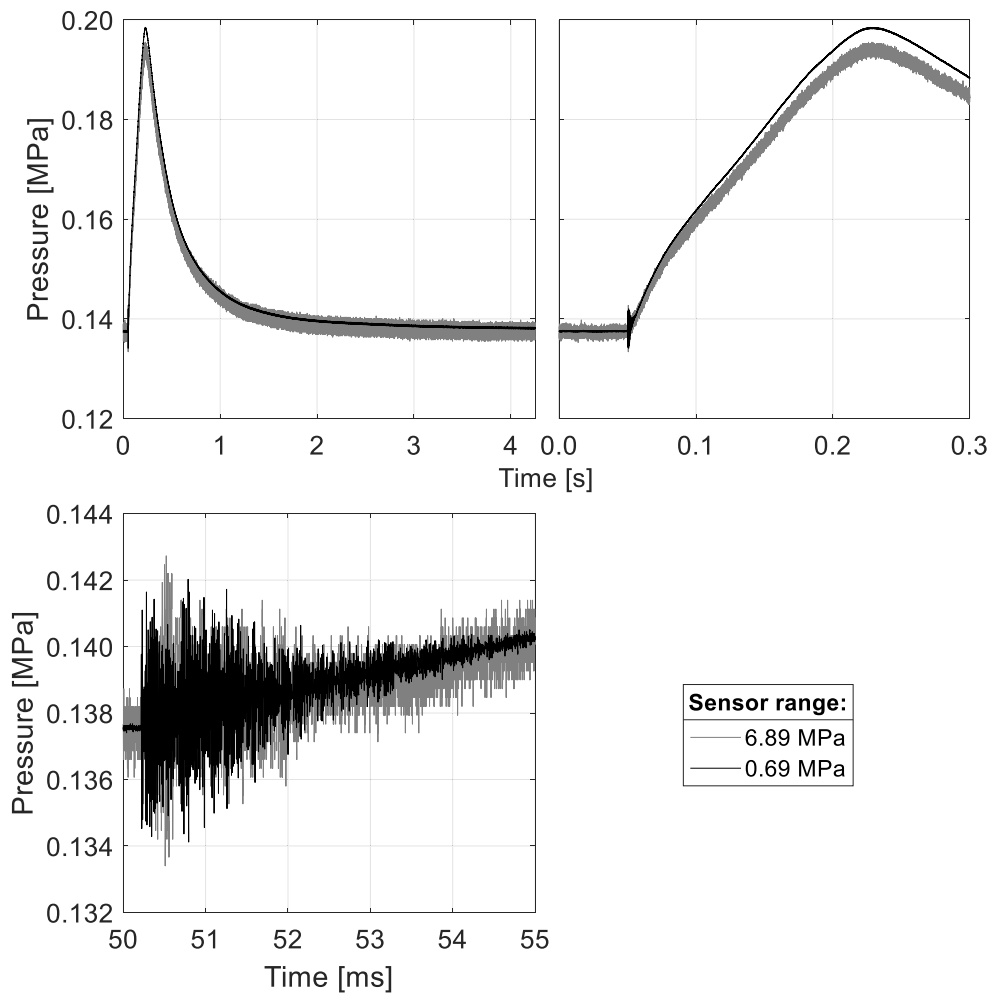


**Figure 72:** Combustion chamber pressure increase during combustion at 0.14 MPa ( $p_r$  0.03) under 1g conditions using the high-speed pressure measurement system. Three different time intervals are shown.

Up to now, the additional pressure measurement system was only used in combustion tests under 1g conditions. Figure 72 shows the pressure profile of the LOX droplet combustion during ignition and combustion at 0.14 MPa. Based on the pressure increase, the combustion lifetime can be precisely determined. In addition, the laser-induced plasma ignition is also visible in the pressure measurement in the test data. This information was not available with the slow pressure measurement used for the drop tower experiments. The additional high-speed pressure measurement will also be used for  $\mu\text{g}$  experiments in the future.

## 6. Results and discussion

In the following, the results from the drop tower campaigns under microgravity conditions are presented and discussed. The results and corresponding discussion are divided thematically into different subchapters. In a few cases, laboratory experiments under normal gravity conditions are also evaluated and discussed.

A total of 59 drop tower experiments were performed in different campaigns, of which 10 experiments were primarily used to test the apparatus and to calibrate the optical diagnostics. The 49 scientific experiments had a success rate of 61.2 %. During the free-fall phase of 4.7 s, a residual acceleration in the order of  $10^{-6}$  g, i.e., microgravity, acted on the experiment capsule. The ambient pressure was varied between 0.10 MPa ( $p_r = 0.02$ ) and 5.66 MPa ( $p_r = 1.12$ ) and was thus in both subcritical and supercritical pressure regimes. The hydrogen content was 100 % and the initial droplet as well as the ambient temperature was 77 K in all experiments, i.e., the droplet was subcooled prior to ignition. 11 experiments were successful, but the initial droplet diameter deviated significantly from the average diameter or the suspender was hit during ignition. These experiments were not considered for evaluation in this thesis. The test matrix of the 19 experiments evaluated in this thesis as well as the essential combustion parameters can be found in Appendix H. Parts of the content and data was published by the author of this thesis and collaborators in [117, 118, 177-180].

### 6.1. Ignition process

The successful execution of an experiment, i.e., the combustion of an oxygen droplet under microgravity conditions, was essentially dependent on the ignition of the droplet during the free-fall phase. In 18 of the 19 cases of an unsuccessful experiment, the cause was due to ignition failure. One reason for this was the problem of creating stationary plasma breakdowns, as described in chapter 4.3. Another reason was the positioning of the plasma spark below the vaporizing droplet. For successful ignition to occur, sufficient energy/heat must be introduced into a zone where an ignitable mixture is present. At an ambient pressure of 0.1 MPa and a temperature of 100 K, the ignition limits of hydrogen in oxygen are about 10 to 90 % (hydrogen concentration) [144]. Thus, the oxygen concentration must be between 10 and 90 % for an ignitable mixture to exist. At first glance, these very wide ignition limits suggest that the ignition location is not particularly sensitive. However, the distribution of oxygen vapor in the vicinity of the droplet is mainly determined by the diffusion velocity, the Stefan flow, and, under normal gravity conditions, also by the natural convection velocity. To estimate diffusion velocity, the binary diffusion coefficient  $D_{AB}$  can be calculated assuming ideal conditions using the Chapman-Enskog theory based on the Lennard-Jones potential in Equation (2). At an ambient pressure of 0.1 MPa and a temperature of 77 K the binary diffusion coefficient is 6.807 mm<sup>2</sup>/s (a detailed calculation can be found in Appendix A). Despite the low ambient temperature, the diffusion rate in this system is comparatively high. This suggests that the oxygen concentration gradient around the droplet is relatively steep. However, it must be taken into account that the droplet was generated before the free-fall phase under

1g conditions. Shortly after the drop of the experiment in the drop tower, the ignition was initiated. Thus, the concentration field around the vaporizing droplet was likely significantly influenced by convective flows.

To evaluate the influence of convection and diffusion on the concentration field around the droplet prior to ignition, a simplified two-stage numerical simulation was performed. The vaporization process was not modeled, but an experimentally determined mass flow rate (based on droplet diameter regression) was assumed. The description of the numerical model and the results can be found.

Based on literature values presented above [144], it is also assumed for a temperature of 77 K that the mixture is ignitable above an oxygen concentration of 10 % (mole fraction). The results from the simplified numerical simulation show that this only applies to the direct vicinity of the droplet surface. Below the droplet, there is a maximum distance of 0.792 mm and above the droplet a maximum distance of 0.493 mm, measured in each case from the stationary droplet surface (see Figure 127 gray sections in Appendix I). Consequently, the laser-induced ignition spark must be positioned within these limits in order to ignite the mixture and subsequently the droplet.

According to these simulation results, it therefore makes sense to generate the spark as close as possible to the droplet surface. However, the close proximity of the laser-induced plasma spark also brings a disadvantage. Experiments in which the droplet was not ignited showed that the thermal expansion of the plasma generated a pressure wave that propagated radially around the spark. This pressure wave caused the droplet to deform strongly and oscillate with a frequency of  $\sim 150$  Hz at the suspender, as shown in Figure 73. The disturbance had the greatest effect in the first 10 ms after the spark was emitted. However, the liquid motion was only completely damped after 30-50 ms and reached the initial position again. The effect of the ignition spark on the oscillation of the droplet increased with decreasing distance of the spark from the droplet surface. Since this influence on the droplet also occurred during successful ignition, as discussed in detail in chapter 6.2, it was therefore desirable to ignite the droplet at the greatest possible distance from the droplet surface. For this reason, the plasma spark was approached to the droplet from below by moving the laser optics during the free-fall phase. The repetition rate of the laser breakdown was set to 4 Hz. This left 250 ms between two breakdowns, enough time to bring the droplet back to rest in the event of unsuccessful ignition, and in the event of ignition, the combustion process was not disturbed by the next breakdown. This technique ensured that the droplet was ignited at the maximum distance from the droplet surface.

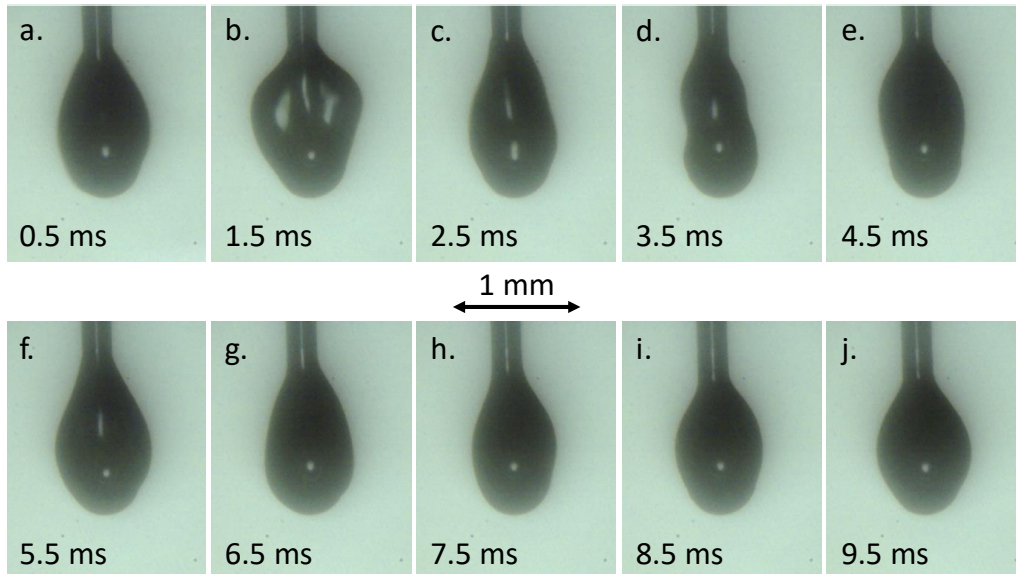


**Figure 73:** Shadowgraph sequence of an unsuccessful ignition of a  $H_2/He$  mixture (50/50 %) at 0.16 MPa ( $p_r = 0.03$ ). Time synchronized with laser-induced spark.

The process of a successful ignition at 0.1 MPa is shown in Figure 74. In this experiment, the distance from the spark to the surface of the droplet was 0.810 mm, which is fairly close to the calculated maximum distance obtained from the numerical model (0.792 mm). The upper row of images, Figure 74a-d, shows the  $OH^*$  chemiluminescence images. To protect the camera from the bright ignition spark, the first image is delayed by 60  $\mu s$ . The lower row of images, Figure 74e-h., shows the shadowgraph images from the moment of ignition. The flame has already expanded completely around the droplet in the first image after 60  $\mu s$ . In the following images, only the intensity of the signal increases, but the shape of the flame remains almost the same. Immediately after ignition, the LOX began to contract, revealing the tip of the suspender below the droplet. Strong oscillations, as they occurred with an unsuccessful ignition (Figure 73), did not occur with successful ignition. In summary, the actual ignition process was not captured by the two camera systems operating at 1600 and 2000 fps. The flame was already fully developed on the first images in each case. However, the spark ignition near the droplet surface detached the liquid from the suspender tip, which had a significant effect on the further course of the combustion and is described in chapter 6.2.

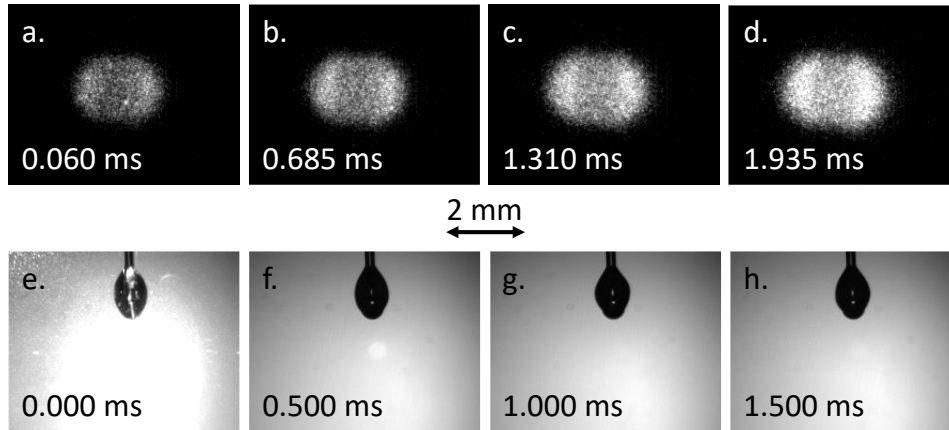


**Figure 74:** Ignition sequence at 0.10 MPa ( $p_r = 0.02$ ). a-d.  $OH^*$  chemiluminescence images. e-h. Shadowgraph images. Time synchronized with laser pulse.

When the ambient pressure was increased, the maximum ignition distance decreased significantly, i.e., the spark had to be positioned even closer to the droplet surface. However, the ignition limits of hydrogen and oxygen barely change in the pressure range between 0.1 and 5.1 MPa according to a study at room temperature [145]. The maximum ignition distance is therefore mainly determined by the concentration field around the vaporizing droplet. At a pressure of 3.0 MPa ( $p_r = 0.6$ ) and a temperature of 77 K, the binary diffusion coefficient drops significantly to a value of 0.226 mm<sup>2</sup>/s (see the exemplary calculation in Appendix A). This corresponds to about 3 % of the value at 0.1 MPa ( $p_r = 0.02$ ) and at the same temperature. Thus, the diffusion rate decreases significantly with increasing pressure, which flattens the concentration gradient around the droplet. At the same time, however, the vaporization process of the LOX droplet is also significantly affected by ambient pressure. With increasing pressure, the boiling temperature of the liquid increases. But since the ambient temperature in the combustion chamber is still 77 K due to cooling with liquid nitrogen, the vapor pressure is constant. In relation to the total pressure, this results in an oxygen saturation concentration of only 0.65 %, which is well below the ignition limit. Thus, the decreasing oxygen saturation concentration causes the maximum ignition distance to decrease with increasing ambient pressure. However, it also becomes apparent, that as soon as the oxygen concentration at the surface of the droplet falls below 10 %, i.e., below the ignition limit, the ignition spark itself must contribute to the vaporization and mixture generation process in order to ignite the droplet at these conditions.

Figure 75 shows the necessary vertical distance of the ignition spark to ignite the droplet at different ambient pressures under  $\mu\text{g}$  conditions. Despite the scattering, the decreasing trend with increasing pressure is clearly visible. At a pressure of 2.0 MPa ( $p_r = 0.4$ ), the spark had to be positioned closer than 0.2 mm to the droplet surface to start the combustion. Due to the small distance of the plasma to the liquid surface, it can be assumed that the vaporization process was locally enhanced by the local increase of the temperature. This effect could also have continued over several unsuccessful ignition attempts during one experiment, so that an ignitable mixture was finally achieved and the

droplet ignited. However, the very close ignition distance also had an effect on the subsequent combustion process. This will be discussed in more detail in the next subchapter.

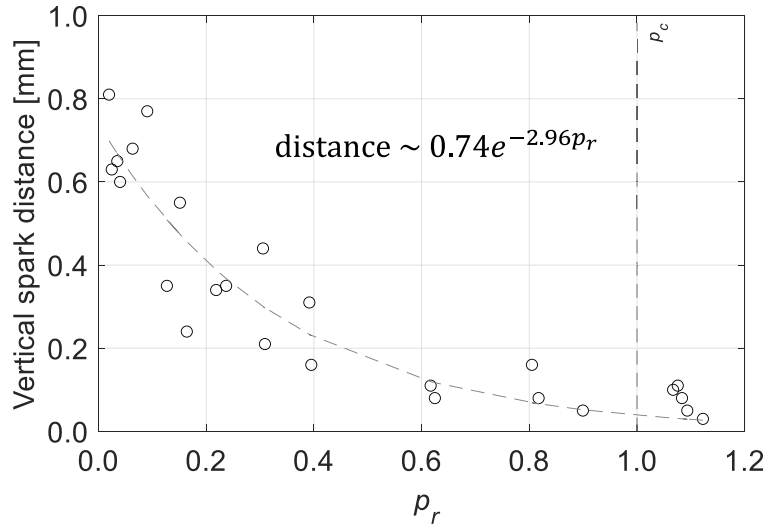


**Figure 75:** Vertical spark distance needed to ignite the droplet at different pressures under  $\mu\text{g}$  conditions. Measured from the bottom of the droplet to the center of the laser-induced plasma spark. Based on experimental data with a gradual decrease in the distance between the ignition spark and the droplet surface.

## 6.2. Suspender effect

After successful ignition, the actual combustion process began by forming a diffusion flame around the droplet. Shortly after ignition, the LOX droplet was observed to detach from the suspender in all experiments. To analyze this behavior in detail, a shadowgraph sequence of the combustion process at 0.10 MPa ( $p_r = 0.02$ ) is shown in Figure 76. After the droplet generation, LOX accumulated not only around the spherical suspender tip, but also along the suspender needle due to the wetting behavior of LOX on quartz. This accumulation was enhanced by the shape of the suspender, as the suspender tip had to be relatively large to ensure that the falling liquid remained on the suspender during droplet generation under 1g conditions, as shown in Figure 48. Incidentally, it was also observed that this droplet shape was similar on a sapphire suspender. Hydrocarbon droplets also show this shape, but less pronounced [60]. As a result, the lower part of the spherical suspender tip was covered only with a thin liquid film. The elongated, ellipsoidal shape of the droplet during droplet generation under 1g conditions apparently became intensified under microgravity conditions as the gravitational pull on the liquid vanished and the Bond number – which is the ratio of gravitational forces to surface tension forces – greatly decreased, see Figure 76a. As described in the previous subchapter, the droplet was deformed by the pressure wave caused by the laser-induced plasma breakdown slightly below the suspender tip. The images taken shortly after ignition suggest that this pressure wave and the ignition in close proximity to the suspender caused the thin liquid film to dry and rupture from the suspender. As a result, the vaporizing liquid that sloshed

back and oscillated for a few milliseconds no longer spread completely around the suspender but contracted to an approximate spherical shape above the suspender sphere after 10 ms, see Figure 76b. The droplet then migrated upward along the spherical tip of the suspender (Figure 76c-e) until it ultimately detached from the suspender approximately 50 ms after ignition (Figure 76f). Complete detachment was indicated by the transition from rapid translational motions to smooth motions and rotations, as well as minor oscillations of the droplet.

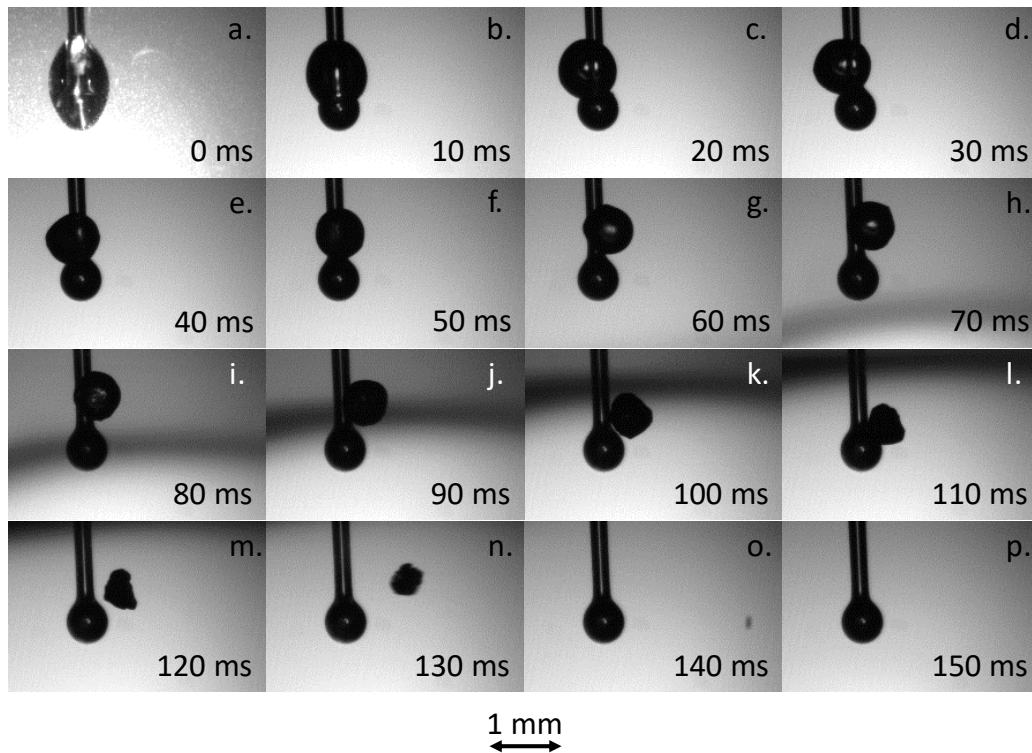


**Figure 76:** High-speed shadowgraph sequence at 0.10 MPa ( $p_r = 0.02$ ). Ignition occurred at 0 ms (a).

This behavior has never been reported in the literature for experiments with suspended hydrocarbon droplets, where a transition from the elongated, wetting shape to an approximate spherical shape was also observed after ignition, but without subsequent detachment. One difference from hydrocarbon droplets is the required close proximity of the ignition spark to the droplet surface in order to ignite the rapidly diffusing ignitable mixture around the vaporizing oxygen droplet, as shown in Figure 75. Although the ignition limits in the hydrogen-oxygen system are much further apart than in the hydrocarbon-air system, the high diffusion rate of hydrogen in oxygen causes both the rich and lean ignition limit to be located in a very small area in the direct vicinity of the droplet surface. Therefore, despite wider ignition limits, the ignition spark must be positioned closer to the droplet than in the hydrocarbon-air system, as explained in chapter 6.1.

For cases without ignition, the droplet was deformed, but returned to its original position, re-enclosing the suspender sphere, and resuming its elongated, ellipsoidal shape due to the wetting of the suspender needle above the suspender sphere (Figure 76a). This

suggests that the heating due to the presence of the flame significantly changed the wetting properties of the burning droplet. Without ignition, the surface temperature of the droplet remained low (subcooled at 77 K) and the adhesive force appear to have dominated over the surface tension. However, after ignition, the droplet surface temperature was increased and the adhesive force became weak, resulting in an increase of the contact angle between the LOX and the quartz suspender and the detachment of the droplet from the suspender. At the same time, also the surface tension was decreased, however, this effect was limited. After detachment from the suspender, only surface tension was effective and the droplet assumed a spherical shape, as expected under microgravity conditions. The droplet detachment occurred over the entire pressure range in all experiments. The time to complete droplet detachment from the suspender was 15 to 50 ms after ignition and depended on the initial diameter of the droplet as well as on the position of the ignition spark.

Figure 77 shows the detachment process at a pressure of 1.20 MPa ( $p_r = 0.67$ ) in detail. In this experiment, it is clearly visible that the contact angle  $\theta$  between the liquid and the suspender has increased within a short time. At the beginning (Figure 77b-c), the droplet was deformed by the pressure wave of the ignition spark, which also affected the contact angle.

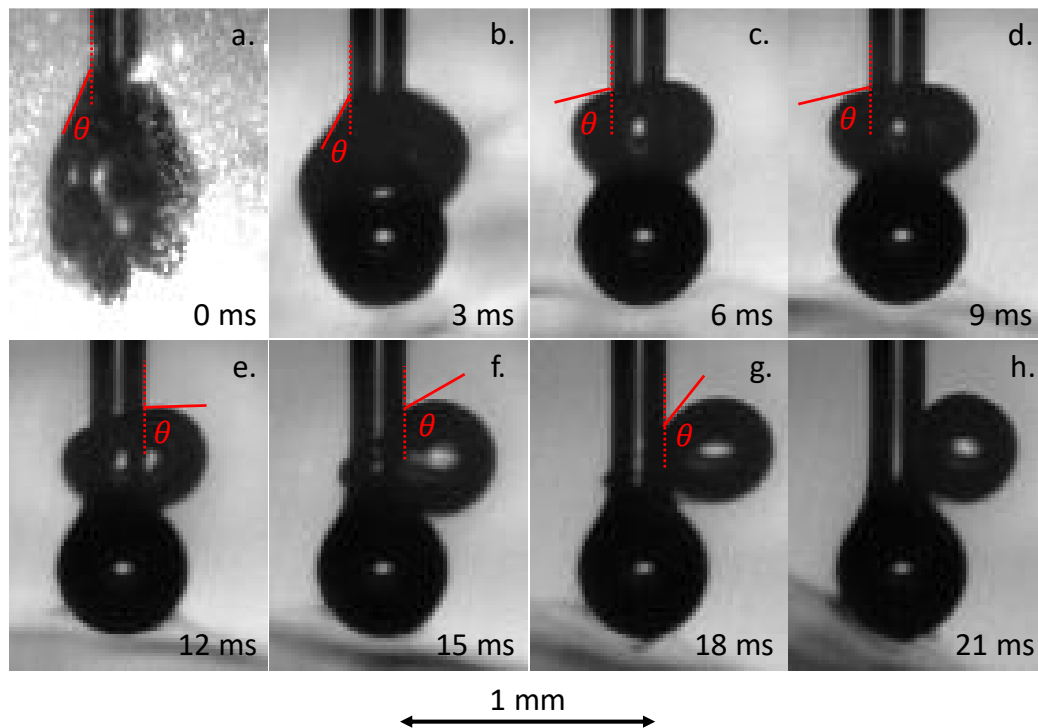


**Figure 77:** High-speed shadowgraph sequence at 1.20 MPa ( $p_r = 0.67$ ). Ignition occurred at 0 ms (a). Contact angle  $\theta$  indicated in red. Complete droplet detachment after 19 ms.

However, the droplet quickly stabilized and the increase of the contact angle started about 9 ms after ignition (Figure 77d). After 12 ms, the droplet began to move to the right side of the suspender needle. On the left side of the needle, the liquid accumulation became

progressively less until the droplet completely detached from the suspender after about 19 ms.

After droplet detachment from the suspender, the droplet burned free-floating next to the suspender in each experiment, as shown for different pressures in Figure 76f-p, Figure 78e-o, and Figure 79d-i. During combustion, the burning droplet was pushed away from the suspender and moved back to the suspender without touching it. The maximum horizontal velocity of this translational movement was approximately 10 mm/s at a pressure of 0.11 MPa. The detachment of the droplet was not anticipated and it complicated the evaluation of the optical diagnostic results. However, the separation of the droplet from the suspender served to protect the suspender from the hot hydrogen-oxygen flame and the simultaneous high oxygen concentration in the direct vicinity of the droplet, which in combination would substantially stress the material. Due to the free-floating of the droplets after droplet detachment, the suspender did not affect the shape of the droplet and also the flame was not noticeably disturbed by the suspender. Only in one experiment did the flame heat the suspender close to the end of the droplet lifetime to the extent that the suspender tip started to glow, as shown in Figure 78.

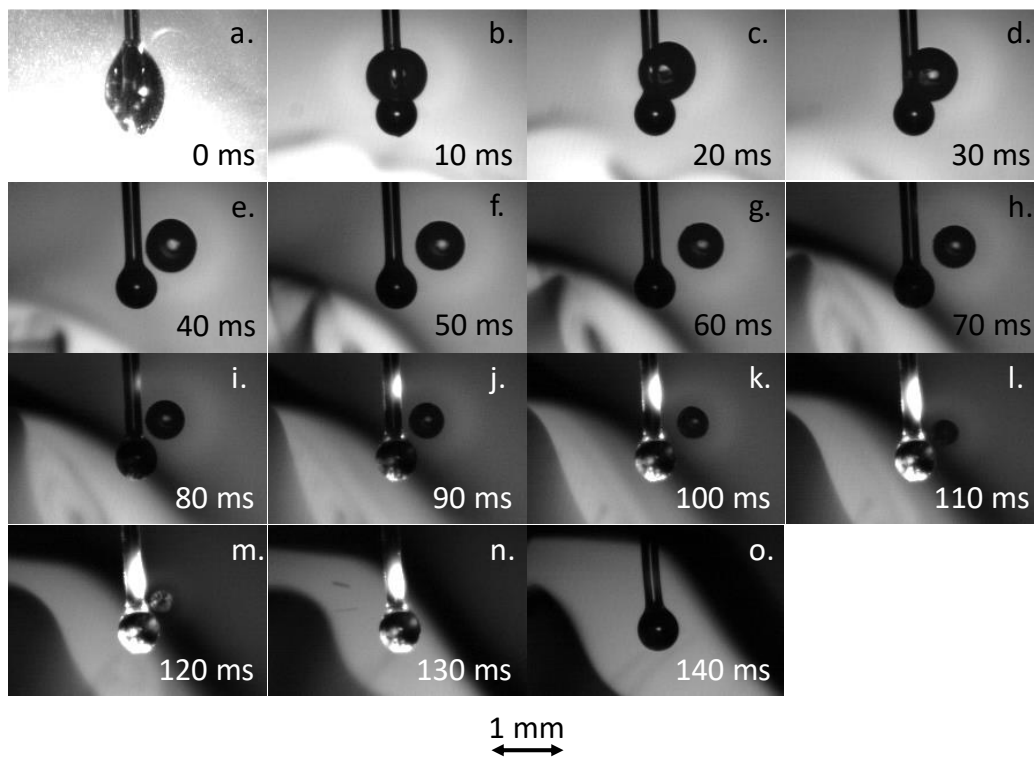


**Figure 78:** High-speed shadowgraph sequence at 0.76 MPa ( $p_r = 0.15$ ). Ignition occurred at 0 ms (a). The flame made contact with the suspender after 80 ms, causing the suspender to glow.

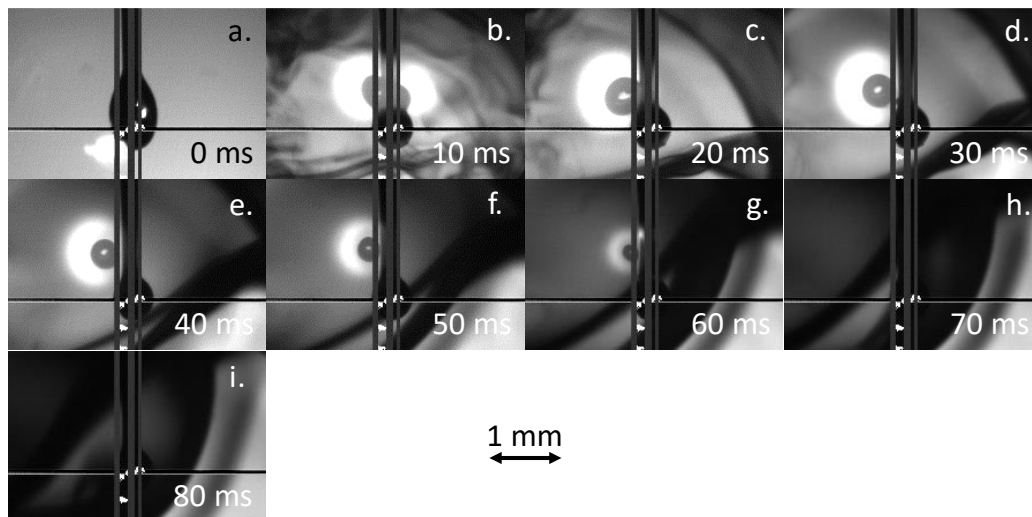


**Figure 79:** High-speed shadowgraph sequence at 3.15 MPa ( $p_r = 0.63$ ). Ignition occurred at 0 ms (a). The lines and dots on the images are defects in the camera sensor.

With this exception, it was therefore assumed that the flame was at a sufficient distance from the suspender and was not affected. In any case, in order to compare all experiments in a consistent manner and to minimize the effect of the suspender, the experimental results, i.e., the droplet regression (chapter 6.4) and the flame position (chapter 6.5), were evaluated only after the complete droplet detachment from the suspender. The average droplet diameter after detachment was  $0.54 \pm 0.08$  mm, which was still large enough to obtain meaningful results with the diagnostics used. After detachment, the LOX droplet no longer had any contact with the suspender, so that consequently no heat transfer could take place from the suspender to the droplet. It has already been shown in the literature that heat conduction through the suspender affects the vaporization and the combustion processes, as shown in Figure 29 [133].

The possible influence of the suspender on the flame can be evaluated more accurately by the  $OH^*$  chemiluminescence images. Figure 80 shows the combustion process at 0.10 MPa ( $p_r = 0.02$ ) on the basis of the  $OH^*$  images. It should be noted that the shadowgraph images were taken orthogonally to the chemiluminescence images, i.e., the diagnostic systems show the combustion process from different sides. The flame contour indicated by the  $OH^*$  signal follows the droplet shape and was therefore initially not spherical, as shown in Figure 80b and Figure 78b, respectively.

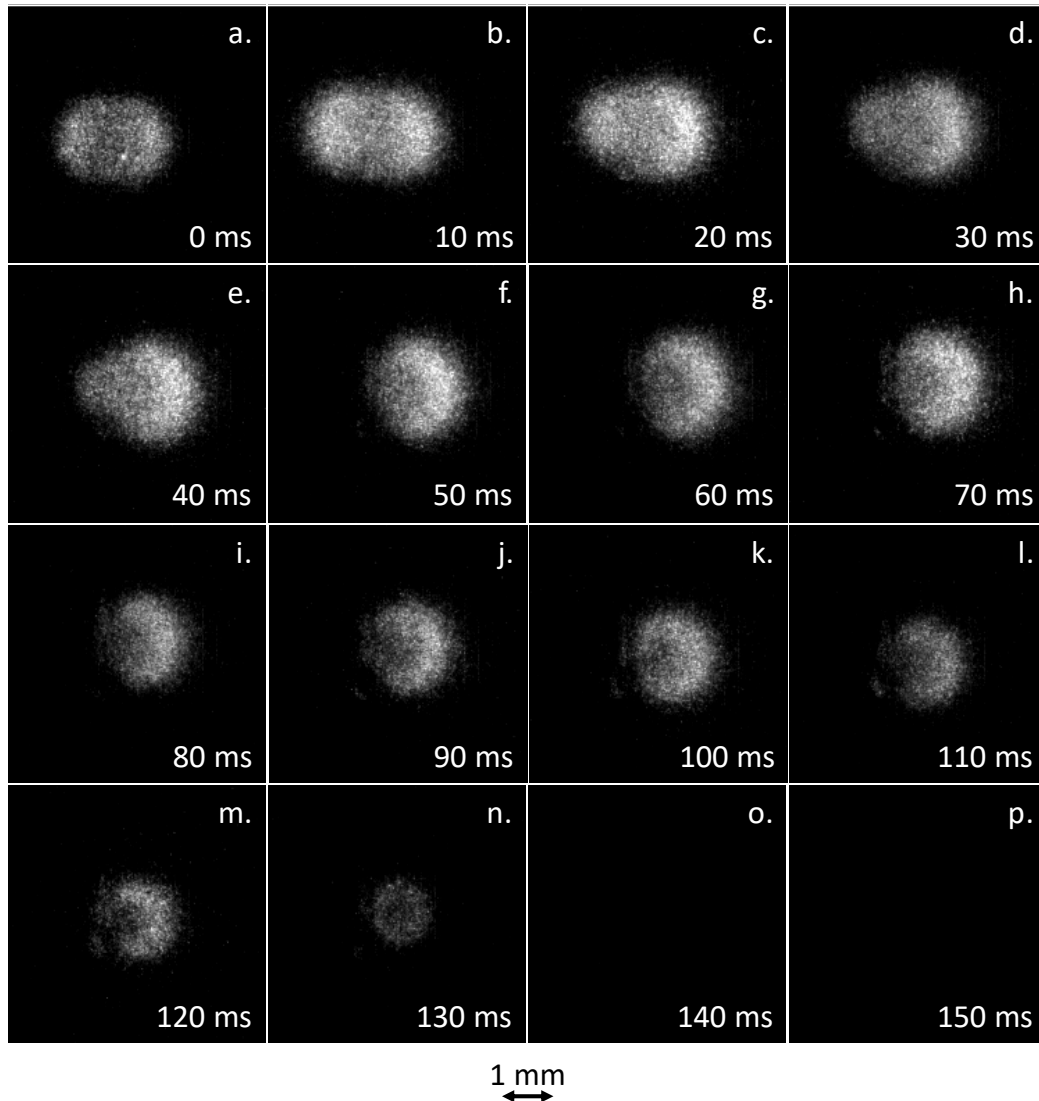


**Figure 80:** High-speed  $OH^*$  chemiluminescence sequence at 0.10 MPa ( $p_r = 0.02$ ). Ignition occurred at 0 ms. All images are shifted by  $60 \mu\text{s}$ . The intensifier gate time was  $5 \mu\text{s}$  and the camera gain was 1.

It can also be seen that the suspender had an effect on the  $OH^*$  signal, since the middle region of the signal is slightly attenuated. After complete detachment of the droplet from the suspender, see Figure 80f and Figure 78f, the sphericity of the  $OH^*$  signal suggests also a spherical flame shape. However, since the droplet burned behind the suspender from the point of view of the chemiluminescence optics, the signal was slightly attenuated by the suspender also in the further course of the combustion.

The attenuation of the signal is shown in more detail in Figure 81 as a pseudo-color image (corresponding to Figure 80h). The symmetry of the signal is slightly broken on the left side by the obscuring of the suspender. And also, the brightness values transformed into pseudo-colors, which represent the signal strength, are interfered by the suspender. The right side shows a relatively smooth signal transition to the dark blue background. Inside, a green ring is clearly separated from the smooth edge and suggests the position of the outer flame zone. The red pixels indicate the zone with the highest signal strength, which

is also affected by the suspender. A more detailed analysis of the flame based on the  $OH^*$  signal is given in chapter 6.5.

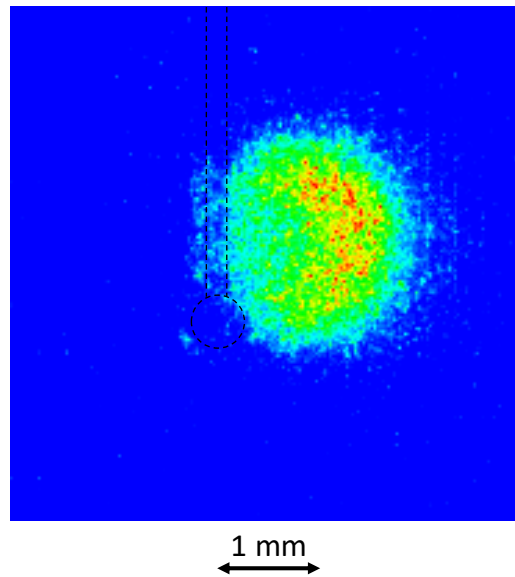


**Figure 81:** Pseudo-color  $OH^*$  chemiluminescence image at 0.10 MPa ( $p_r = 0.02$ ) 70.06 ms after ignition. The intensifier gate time was 5  $\mu$ s and the intensifier gain was 800 V. The position of the suspender is indicated by the dashed line.

Figure 82 shows the chemiluminescence images of the combustion process at 0.76 MPa ( $p_r = 0.15$ ), which is also shown in Figure 78. One major difference from the previous experiment at 0.10 MPa is that the signal intensity increased significantly due to the increased ambient pressure, although the camera settings are adjusted accordingly to compensate for this increase. The reasons for the increase in signal intensity and the camera settings for all experiments are discussed in chapter 6.5. Besides this difference, the combustion process looks very similar on the  $OH^*$  images. The flame was distorted during the droplet detachment from the suspender, as shown in Figure 82a-d. After complete detachment, Figure 82e, the flame took on a nearly spherical shape. However, in this experiment, the blockage from the suspender becomes very clear. As shown in Figure 78, the droplet moved very close to the suspender at the end of the combustion process, so that the flame heated the suspender. At this moment, the flame had already shrunk in diameter, so that the suspender completely covered the  $OH^*$  signal after 110 ms, as shown in Figure 82i, although the combustion ended not until 129.5 ms (indicated by the shadowgraph images).

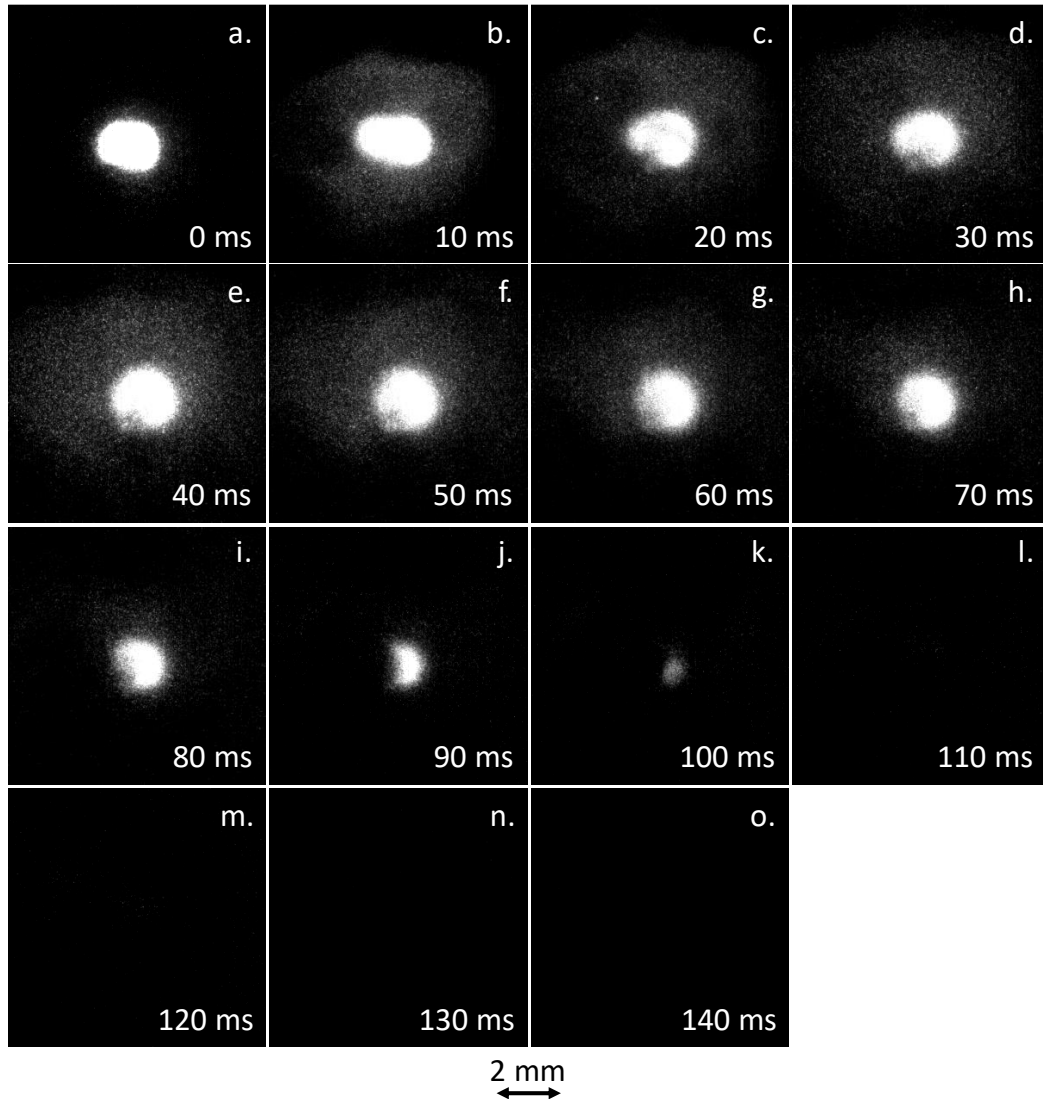


**Figure 82:** High-speed  $OH^*$  chemiluminescence sequence at 0.76 MPa ( $p_r = 0.15$ ). Ignition occurred at 0 ms. All images are shifted by 60  $\mu$ s. The intensifier gate time was 2.5  $\mu$ s and the camera gain was 1.

This was the only experiment, where the flame interacted directly with the suspender, as indicated by the glow of the suspender in the shadowgraph images in Figure 78. In all other experiments, no such interaction was observed. However, it can be assumed that the suspender was heated without glowing during the ignition and the detachment phase as well as by the hot gases outside the flame. Even without direct interaction, it appears that there was a minor influence on the combustion process caused by the suspender in the direct vicinity of the burning droplet. In some cases, the droplet floated horizontally away from the suspender and shortly thereafter back towards the suspender without floating vertically. The gasification of the droplet during combustion caused a bulk flow away from the droplet (Stefan flow), as discussed in chapter 2.1.2. When this gas flow hits a solid object in close proximity, an acceleration occurs that could have caused the horizontal movement away from the droplet. On the other hand, the local interaction of the flame with the suspender could lead to a slight reduction of the gasification rate on

this side of the droplet. This could have caused the gas flow from the droplet to become slightly unidirectional rather than radial, which would lead to a translational movement towards the suspender. Other reasons for the translational movement and rotation of the droplet during combustion are discussed in the following subsection. In summary, the unanticipated detachment of the burning droplet from the suspender resulted in some effects that exerted a small influence on the combustion process. On the other hand, it also created the situation where the droplets burned free-floating without the disturbing contact with the suspender in terms of heat conduction and sphericity. However, in some experiments the droplet motion reached a velocity of up to  $\sim 10$  mm/s during the main phase of the combustion process, which made the evaluation of the optical diagnostics much more complex and tracking algorithms had to be used.

### 6.3. Combustion process

The combustion process initiated by the ignition caused a pressure increase in the combustion chamber. Due to the rapid vaporization of the oxygen droplet and the high temperature rise, the pressure also increased rapidly after ignition. During the experimental campaigns, the pressure was measured by one or two sensors with different pressure ranges and thus resolutions, depending on the initial pressure. It should be noted that the pressure sensors were placed outside the cryogenic combustion chamber and were connected via pipes to the chamber, as described in chapter 4.1. Thus, the sensors could only receive a damped pressure signal. To determine the additional time delay of the signal, the speed of sound  $c$  in the hydrogen atmosphere can be calculated using the simple equation for ideal gases [193]:

$$c = \sqrt{\gamma R_s T} \quad (55)$$

where  $\gamma$  is the isentropic expansion factor and  $R_s$  is the specific gas constant. The temperature in the combustion chamber can be assumed to be 77 K, the boiling temperature of the liquid nitrogen cooling jacket. The temporary heating due to the combustion and the temperature rise up to the pressure sensors are not taken into account in this simple calculation. Using Equation (55), the speed of sound in pure hydrogen at 77 K can be calculated as follows:

$$c_{H_2, 77 K} = \sqrt{1.493 * 4124.482 \frac{J}{kg K} * 77 K} = 688.5 \frac{m}{s} \quad (56)$$

At higher temperature, the speed of sound increases, so this is the minimum value. The pressure wave in the combustion chamber propagates at the speed of sound through the gas medium in all directions. The sensors are located about 0.4 m from the center of the combustion chamber, which would result in a time delay of about 581  $\mu$ s. This is about an order of magnitude lower than the total combustion lifetime, which was in the range of 53.5 to 136.5 ms.

Figure 83 shows the pressure evolution in the combustion chamber during combustion at 0.10 MPa ( $p_r$  0.02). The droplet was ignited approximately 1.9 s after the capsule was dropped in the drop tower. Immediately after ignition, indicated by the dashed line, both sensors showed a clear increase in pressure, which reaches its maximum shortly after the end of combustion and then decays slowly. The timing of the laser pulse was selected as the ignition signal here. The pressure difference between the initial pressure and the maximum peak was 33.5 kPa.

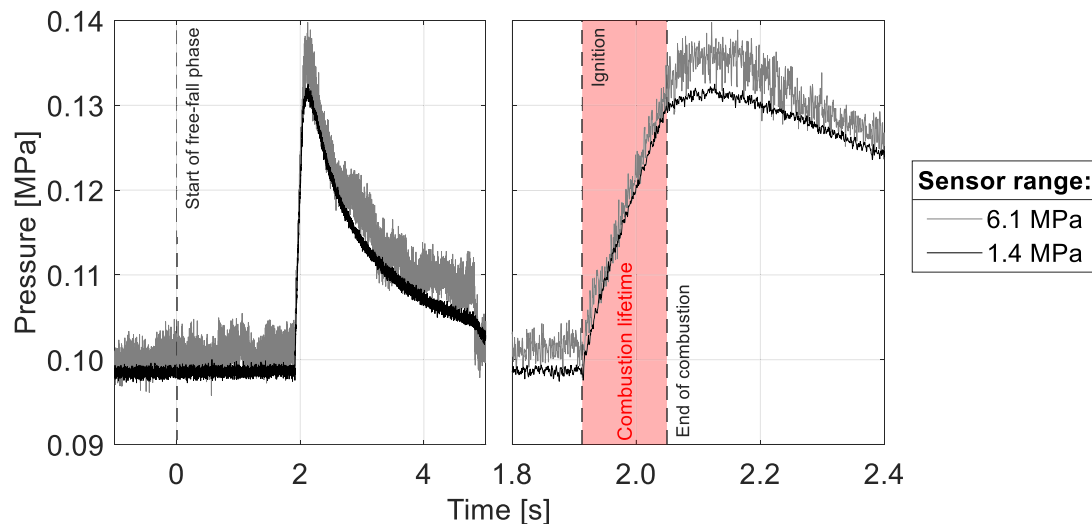


**Figure 83:** Combustion chamber pressure increase during combustion at 0.10 MPa ( $p_r$  0.02). Two different time intervals are shown.

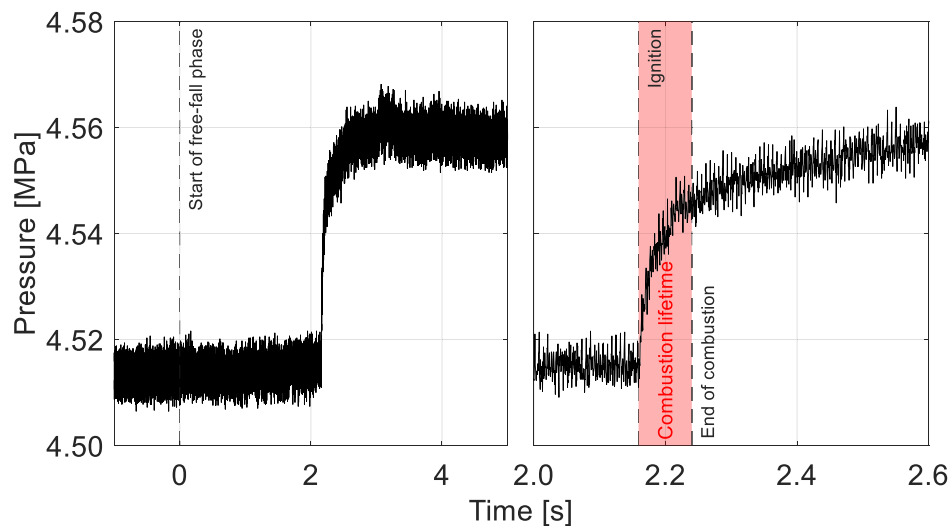


**Figure 84:** Combustion chamber pressure increase during combustion at 4.51 MPa ( $p_r$  0.90). Two different time intervals are shown.

A similar behavior could also be observed at a higher pressure. Figure 84 shows the pressure increase during combustion at 4.51 MPa ( $p_r$  0.90). In this case, the pressure increased rapidly with ignition, but continued to increase slightly even after the end of

combustion. The maximum pressure increase here was 46.2 kPa. In all experiments, the pressure profile and the order of magnitude of the maximum pressure peak were similar. However, it should be noted that the sensors have a natural frequency of  $< 100$  Hz and a typical response time of 1 ms. Thus, statements about highly dynamic pressure curves, such as during ignition, are limited by the sensor itself. In addition, there is the damping due to the spatial distance from the sensor to the droplet. For detailed pressure analysis during combustion, a high-speed pressure measurement system was installed directly in the cryogenic combustion chamber. The installation location as well as the high temporal resolution of up to 1 MHz of the sensors enables a more precise measurement. However, the high-speed measurement system presented in chapter 5.3 has not yet been used under  $\mu\text{g}$  conditions.

The effect of the detachment of the droplet from the suspender led to an influence of the combustion process by the deformation and movement of the droplet as well as by the heat conduction from the suspender into the liquid. Only after the complete detachment from the suspender a quasi-steady combustion process was formed. The hypothesized process of this quasi-steady combustion phase is shown schematically in Figure 85. Here, a diffusion flame forms around the vaporizing droplet. In the reaction zone, the fuel (the hydrogen gas) reacts with the oxidizer (the oxygen vapor), which leads to a stoichiometric flame ( $\phi = 1$ ). This continuous reaction generates the heat to maintain the rapid vaporization of the liquid and thus the flame at some distance from the droplet surface. The position of the flame is determined by the mass transport processes, i.e., at which distance the stoichiometric mixture is reached. The reactants are transported to the reaction zone mainly by diffusion. In the case of oxygen, the mass transport is supported not only by diffusion but also by the convective Stefan flow normal to the droplet surface. Heat transfer is by thermal radiation from the flame to the droplet surface as well as by thermal conduction, as described in chapter 2.5.1. The water produced in the reaction zone, as a product of combustion, is transported both outward, away from the droplet, and inward towards the droplet surface, as shown in Figure 10. Because of the high temperatures near the flame, the water is present as vapor in the gas phase. Outside the flame, however, the water is rapidly cooled down, so that the vapor can condense or even freeze. Inside of the flame, the temperature gradient is very steep between the hot flame and the cold droplet surface, which is close to the boiling temperature (between 90 and 154 K, depending on the pressure). This suggests that the water vapor can also condense and freeze on the inside of the flame sphere. Furthermore, this can lead to the formation of an ice layer near the droplet surface, as illustrated in Figure 85 and evidenced later. In fact, the formation of an ice layer around the burning droplet has been predicted in many studies [89-91, 95, 127]. The water vapor is transported towards the droplet surface by diffusion. On the other hand, the Stefan flow of the vaporizing droplet counteracts this movement. As soon as individual particles are formed, thermophoretic effects can also support mass transport by moving the ice particles to the cold droplet surface, as reported in the literature [90]. In this study, it was assumed that the overall effects of water condensation or even freezing on droplet vaporization are very small. Numerical studies on droplet vaporization revealed that in terms of the LOX droplet lifetime and the

distributions of temperature and species concentrations, no discernible changes were observed by varying the initial size of the condensed water droplets [90].

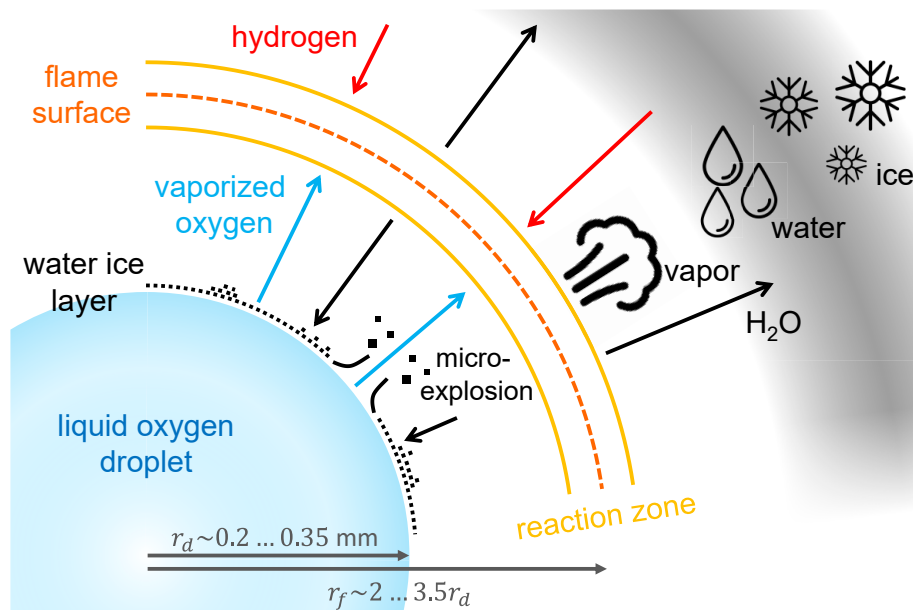


**Figure 85:** Schematic overview of the hypothesized combustion process in the subcritical pressure regime. Figure published in [179] and modified.

The shadowgraph sequence of the combustion at 0.10 MPa ( $p_r$  0.02) is shown in Figure 86. The images reveal that the shape of the oxygen droplet changed substantially during the combustion process. At the time of the detachment from the suspender, the droplet had a rather round and smooth shape, as shown in Figure 76f. As the combustion progressed (Figure 86), structures increasingly formed on the visible surface, making the surface less transparent and more irregular in shape (Figure 86f-1.). The change in shape is assumed to result from the inhomogeneous formation of ice structures close to the droplet surface due to the low droplet temperature, as hypothesized in Figure 85. This is the first time that experimental evidence for the presumed formation of water ice around a burning oxygen droplet in a hydrogen atmosphere is reported. The distance of the ice layer to the droplet surface could not be determined unambiguously from the shadowgraph images, since the ice formation obscured the view to the actual droplet surface. As in the literature [89], it is assumed that the ice layer was not directly on the droplet surface due to the high Stefan flow velocity at the surface and due to the cryogenic surface temperature, which is significantly lower than the condensation temperature of water. Furthermore, it is therefore assumed that despite the distinctly non-spherical external shape, the oxygen droplet inside the ice shell still had a spherical shape.

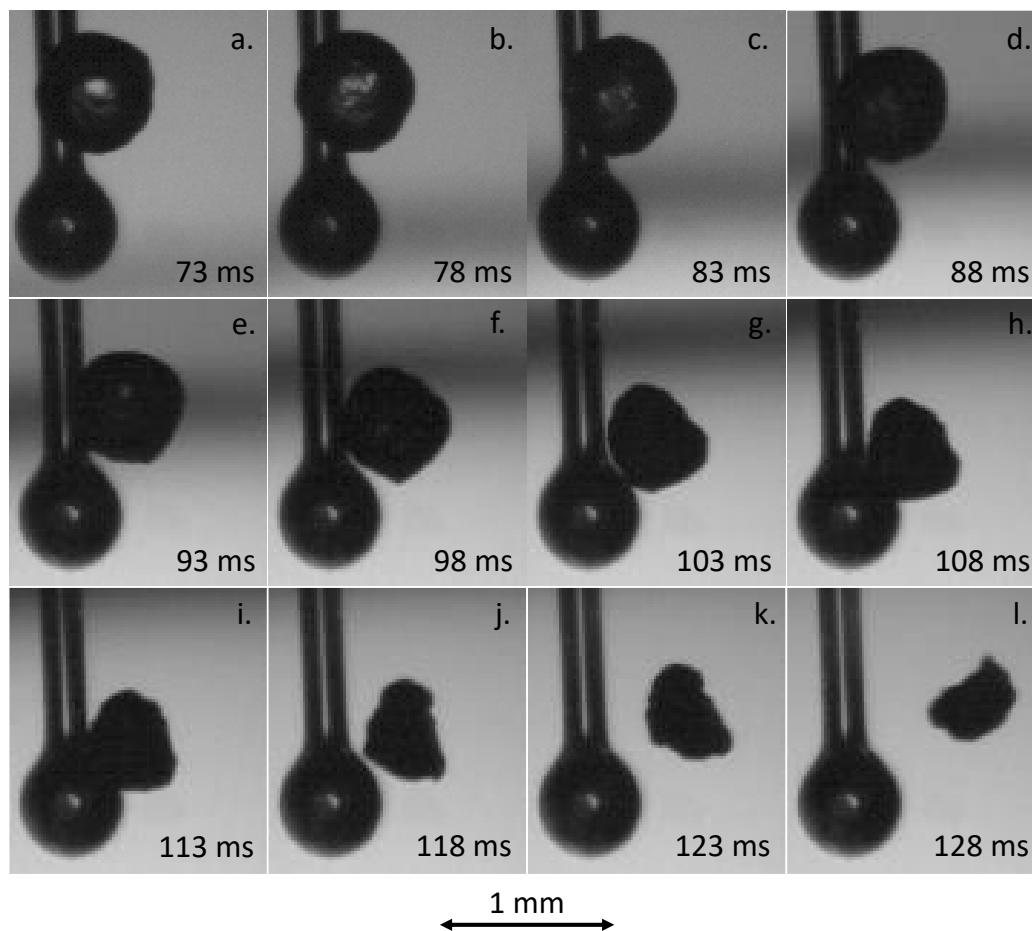


**Figure 86:** High-speed shadowgraph sequence of the building of an ice shell around the burning oxygen droplet at 0.10 MPa ( $p_r$  0.02). Ignition occurred at 0 ms.

In addition to the change in shape, the droplet began to rotate and translate irregularly, with the rotation and translational movement becoming more pronounced as the droplet mass decreased. The translational acceleration of the remaining ice particles at the end of combustion, e.g., visible in Figure 76o, and the increasing, irregular rotation of the droplet suggest that the ice layer induced a directionally inhomogeneous release of oxygen gas. Figure 87 suggests the occurrence of an additional micro-explosion at the end of the combustion at 0.10 MPa ( $p_r$  0.02). The sequence demonstrates on the one hand how an oxygen vapor jet erupted from the ice shell (Figure 87a-b) and on the other hand how the droplet was (additionally) accelerated by the unidirectional impulse against the direction of the micro-explosion (Figure 87c). Inside the ice shell, there was only a small amount of oxygen, so the inertia of the droplet was low. It is assumed that small oxygen-vapor jets issuing from pores in the irregular ice surface could therefore be sources of linear and angular momentum, which have led to the observed translational movement and rotation of the droplet. However, these micro-explosions occurred only at irregular intervals and were barely visible. The ice layer seemed to have been porous most of the time, as the  $OH^*$  measurements showed a homogeneous, spherical, and closed flame. Even though

the uneven motion of the droplet is indicative of directional vaporization, there appears to be an immediate compensation in the flame in the circumferential direction.

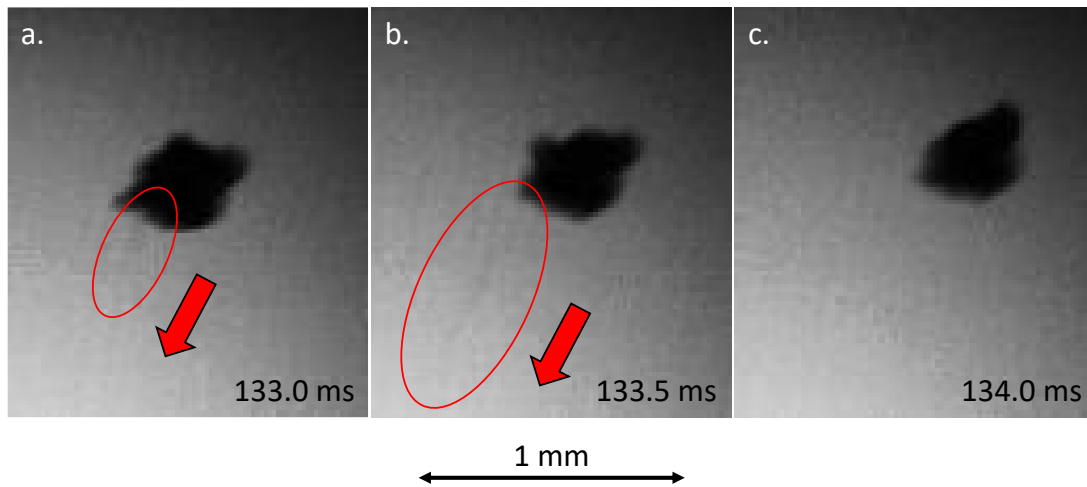


**Figure 87:** High-speed shadowgraph sequence of oxygen vapor jets (highlighted by red ellipses) breaking through the ice shell of the droplet at the end of combustion at 0.10 MPa ( $p_r$  0.02). Ignition occurred at 0 ms.

Stronger evidence for a micro-explosion could be observed in the combustion at 4.96 MPa ( $p_r$  0.98). As shown in Figure 88, a small water droplet or ice particle was ejected from the surface before it vaporized near the hot flame.

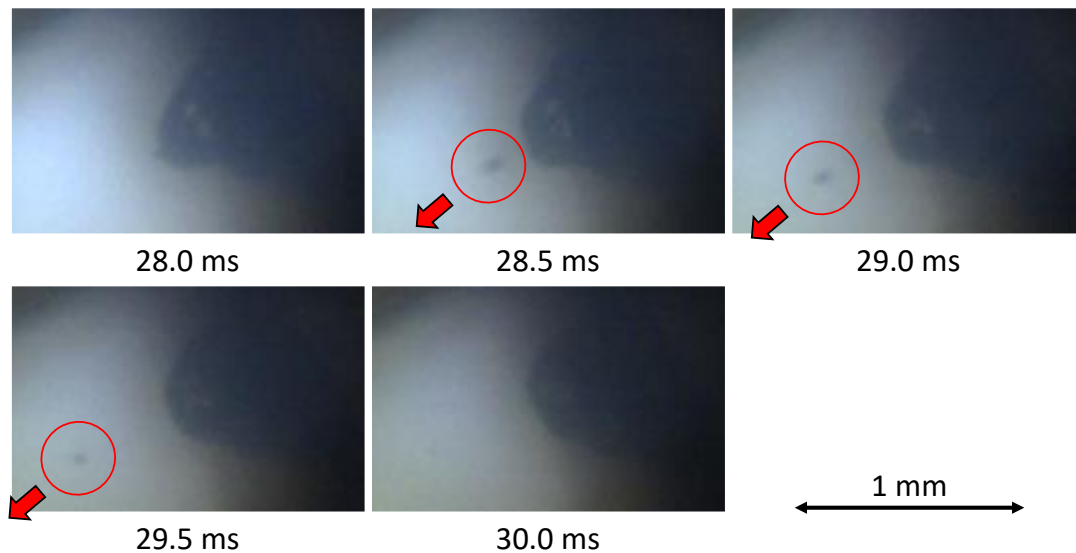


**Figure 88:** High-speed shadowgraph sequence of a micro-explosion ejecting a water droplet or ice particle (highlighted by red circles) from the droplet surface during the combustion at 4.96 MPa ( $p_r$  0.98). Ignition occurred at 0 ms.

Litchford & Jeng [91] predicted remaining ice particles after the burning process, which were observed in all experiments and can be seen in Figure 89. At the end of combustion, the breaking out of the ice layer, i.e., a micro-explosion, could be observed when, after

complete consumption of the LOX, a remaining ice fragment broke through the water cloud around the droplet.

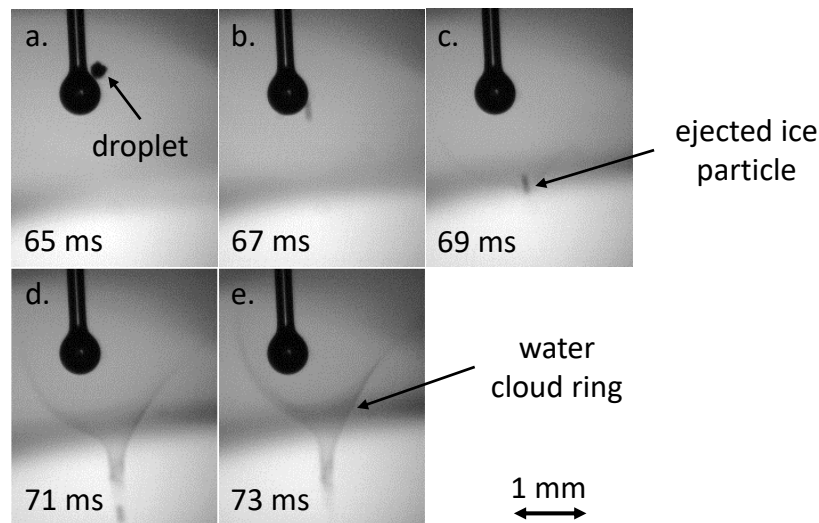


**Figure 89:** High-speed shadowgraph sequence of a remaining ice particle breaking through the water cloud ring due to micro-explosions at the end of combustion (all liquid consumed) at 0.18 MPa ( $p_r$  0.04). Ignition occurred at 0 ms. Figure published in [179].

The effect of ice formation around the burning droplet could be observed in most cases only after about half of the droplet lifetime, however, it is assumed that ice formation starts rapidly after ignition and only becomes visible at a certain stage using the applied diagnostics. Ice formation was most pronounced due to extreme shape deviations of the initially spherical droplet at low pressures  $< 0.75$  MPa ( $p_r < 0.15$ ). At higher pressures, such extreme shape deviation could no longer be detected. However, remaining ice particles were visible after combustion at any ambient pressure. The possible reasons for the observation of increased ice formation at low pressures are discussed in the following subsections.

Further evidence of ice formation inside the flame sphere was provided by the detachment of the droplet from the suspender. Figure 90 shows the process of detachment from the suspender at a pressure of 0.15 MPa ( $p_r$  0.03). The droplet migrated to the top of the suspender sphere after ignition (Figure 90a). It then detached from the sphere and the suspender needle as described in the previous subsection (Figure 90l). However, during this process, structures formed on the left side of the suspender needle (Figure 90b-e). As the detachment progressed, these structures separated from the rest of the liquid, so that the droplet slowly assumed a spherical shape (Figure 90f-j). The behavior of these separated structures (highlighted by red circles) indicates freezing of the water vapor at the relative cold suspender surface. A connection of water ice was formed between the suspender and the LOX. Only after the ice layer on the suspender melted and vaporized, the connection to the suspender broke and the droplet oscillated slightly and burned free-floating next to the suspender. The fact that no water vapor froze on the suspender after detachment suggests that the suspender surface was heated by the flame and hot gases.

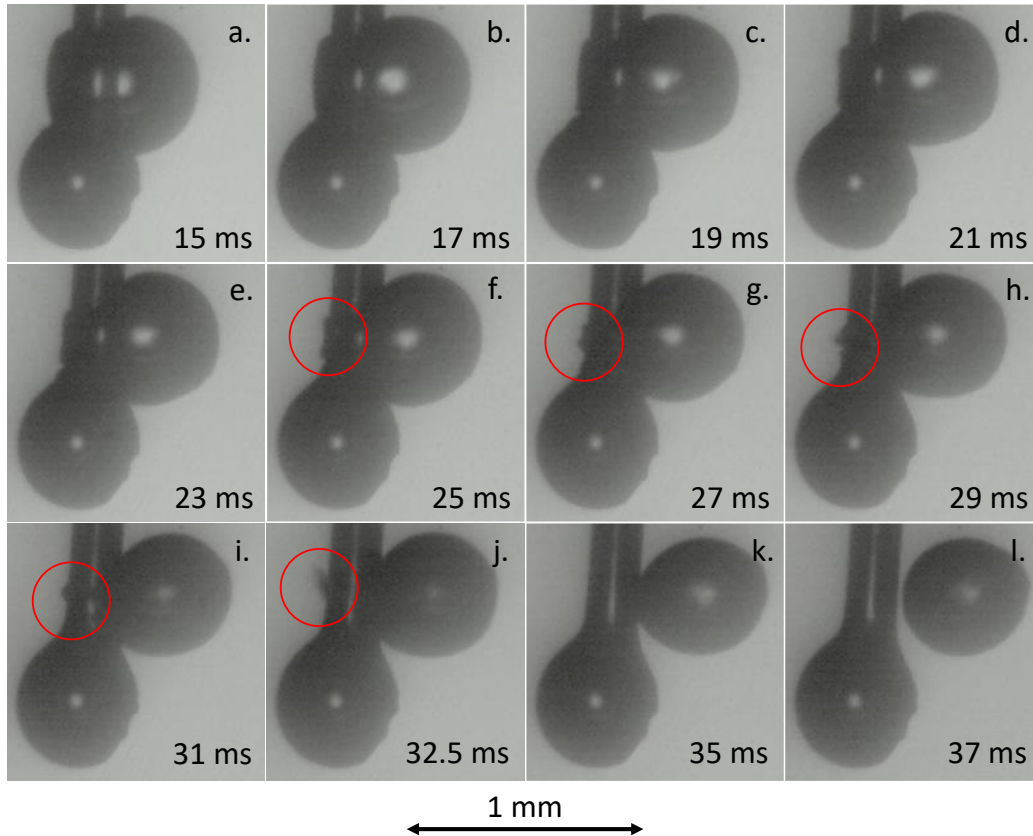


**Figure 90:** High-speed shadowgraph sequence of droplet detachment with ice structures (highlighted by red circles) at the suspender at 0.15 MPa ( $p_r$  0.03). Ignition occurred at 0 ms.

As hypothesized in Figure 85, a water cloud consisting of condensed or frozen water was formed in all experiments and was clearly visible as an evolving sphere/ring around the burning droplet, as can be seen in Figure 91. The diameter of this ring decreased and the cloud became opaque with increasing pressure. At a pressure of 0.10 MPa ( $p_r = 0.02$ ), this ring was outside the field of view of the camera and only became visible during the further course of the combustion. In all experiments, the cloud rings slowly shifted radially outward during combustion and become blurred as more water was produced.

In general, condensation occurs when the water vapor partial pressure is above the saturation pressure, which depends on the ambient temperature and pressure. As the ambient pressure increases, the saturation temperature also increases. This means that condensation occurs at higher temperatures, i.e., closer to the flame. In addition, as the ambient pressure increases, the diffusion rate in the gas phase also decreases significantly. This in turn means that the water vapor produced is transported more slowly to the outside and therefore higher water vapor concentrations can accumulate. Both effects led to the fact that the condensation of the water vapor, which was observed in the experiments by the water cloud ring, took place closer and closer to the flame and thus closer to the droplet. In addition to condensation, freezing could also have occurred, so that small ice particles were formed similar to the behavior inside the flame sphere. While ice formation near the droplet surface visibly leads to the growth and aggregation of a layer as a result

of radial convergence, it is conceivable that individual nucleation with the formation of a (cirrus-like) ice cloud may occur due to the radially diverging outward flow. However, this could not be clearly determined on the basis of the camera images. At least aggregation and formation of larger ice structures were never observed outside of the flame.

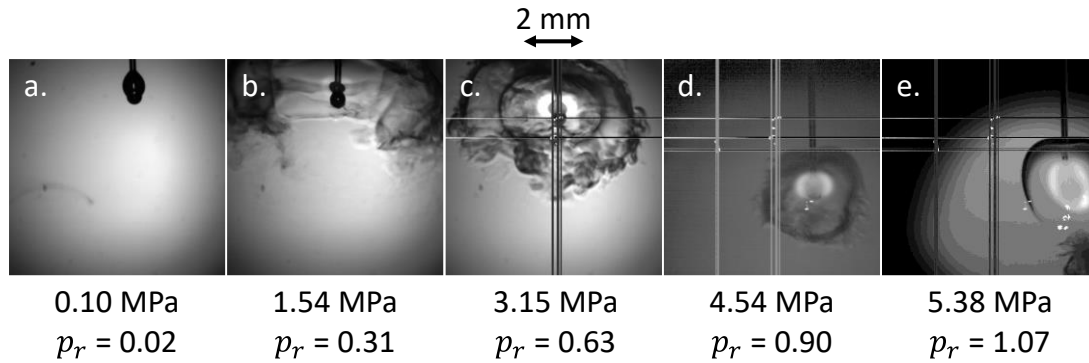


**Figure 91:** Shadowgraph images showing the outer water cloud ring at different ambient pressures in the subcritical and supercritical regime, each 5 ms after ignition. The lines and dots on the images are defects in the camera sensor.

#### 6.4. Droplet regression

After ignition, the process of droplet detachment from the suspender began. During this phase, the droplet and also the flame were distorted and had a non-spherical shape. Thus, the quasi-steady state of combustion was reached only after complete detachment, when the droplet burned free-floating next to the suspender. Quantitative evaluation of the experiments at different ambient pressures was therefore not started until the droplets were completely detached. In addition, the transient heating process, exemplified in Figure 17 for the case of vaporization, is not included in the evaluation, but only the quasi-steady part of the droplet regression.

In the subcritical pressure regime, a total of 16 experiments were evaluated. The initial diameters at the time of complete detachment from the suspender were  $0.53 \pm 0.08$  mm. The largest droplet had an initial diameter of 0.70 mm and the smallest droplet 0.42 mm. The droplet lifetimes calculated from the moment of complete droplet detachment were between 21.5 and 89.5 ms. The test matrix of the evaluated experiments including essential combustion parameters can be found in Appendix H.

To calculate the instantaneous droplet diameters, the shadowgraph images were processed using the MATLAB algorithm described in chapter 5.1. To present the results, the droplet diameters were normalized by the initial diameter  $d_0$ , which in the subcritical regime referred to the diameter at the time of complete detachment from the suspender. Secondly, the time  $t$  was normalized by the observed time of droplet disappearance  $t_1$ , which was calculated from the time of complete droplet detachment from the suspender. Accordingly,  $t/t_1 = 0$  was also defined at the time of complete droplet detachment.

Figure 92 shows an example of the droplet detection at four different times during the combustion at 0.10 MPa ( $p_r = 0.02$ ). The droplet detachment occurred 50 ms after ignition and at the beginning of the free-floating combustion phase, the droplet had a relatively spherical shape, as already described in the previous subsections. This is also evident from the droplet shape ratio  $R_d$  close to unity (Figure 92e). As the combustion progressed, the droplet shape deviated more and more from the spherical shape, and thus the calculated droplet shape ratio also increased (Figure 92f-h). The instantaneous droplet diameters were calculated as equivalent diameters based on the detected droplet area (2D).

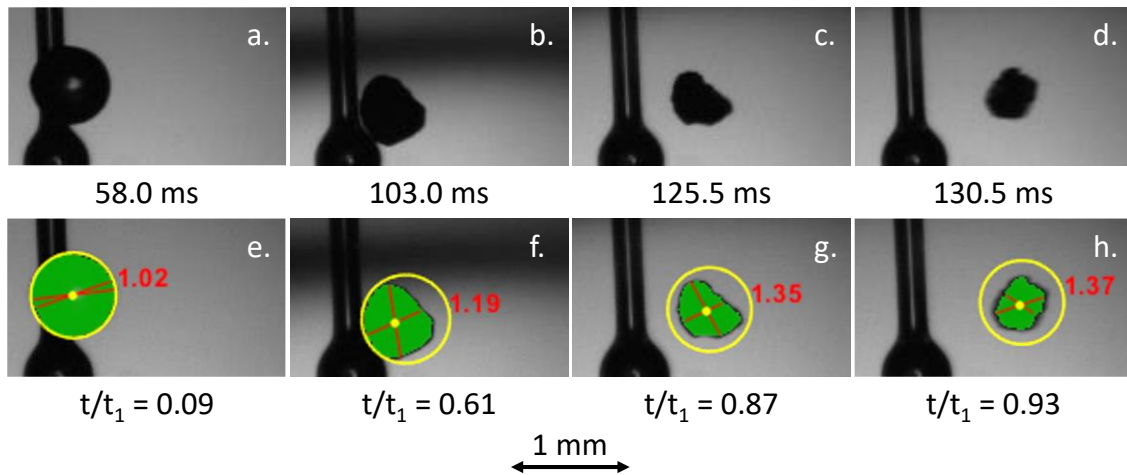


**Figure 92:** Equivalent droplet diameter detection for the combustion at 0.10 MPa ( $p_r = 0.02$ ). a-d. Original shadowgraph images. e-h. Evaluated images (yellow circle: manually selected evaluation area, green area: detected droplet area, yellow dot: calculated droplet origin, red lines: shortest and longest dimension line, red value: droplet shape ratio  $R_d$ ). The image pairs correspond to the same time, which is given in milliseconds after ignition and in dimensionless time  $t/t_1$ .

Figure 93 shows the course of the evaluated dimensionless droplet regression and the droplet shape ratio for the combustion at 0.10 MPa ( $p_r = 0.02$ ). After the droplet detached from the suspender, at  $t/t_1 = 0$ , the equivalent diameter initially remained almost constant until  $t/t_1 = 0.4$ . At the same time, the droplet shape was rather spherical in this first phase of combustion, indicated by the course of the droplet shape ratio. This suggests that the ice layer first grew quite uniformly around the droplet. This ice layer obscured the view of the actual droplet surface, so that the measured equivalent droplet diameter decreased only very slightly and remained almost constant. After  $t/t_1 = 0.4$ , the equivalent droplet diameter decreased quickly and the external shape increasingly deviated from the spherical shape. Overall, the observed droplet regression deviated significantly from the linear course expected for quasi-steady combustion. The reason for this was the previously described formation and growth of the water ice layer near the droplet surface. Hence, three-dimensional effects evidently affected the determination of the equivalent droplet/ice shell diameter in the subsequent evolution. In this experiment, the droplet was already burning for 50 ms, which was 36.6 % of the total droplet lifetime,

until detachment happened and the evaluation started. Due to the small flame distance to the droplet surface and due to the small temperature difference between the initial temperature of the droplet of 77 K and the boiling temperature of the droplet of 90 K, a very rapid heating phase can thus be assumed. Consequently, the initial phase of the combustion, in which the droplet regression is very slow, cannot be attributed to the droplet heating.

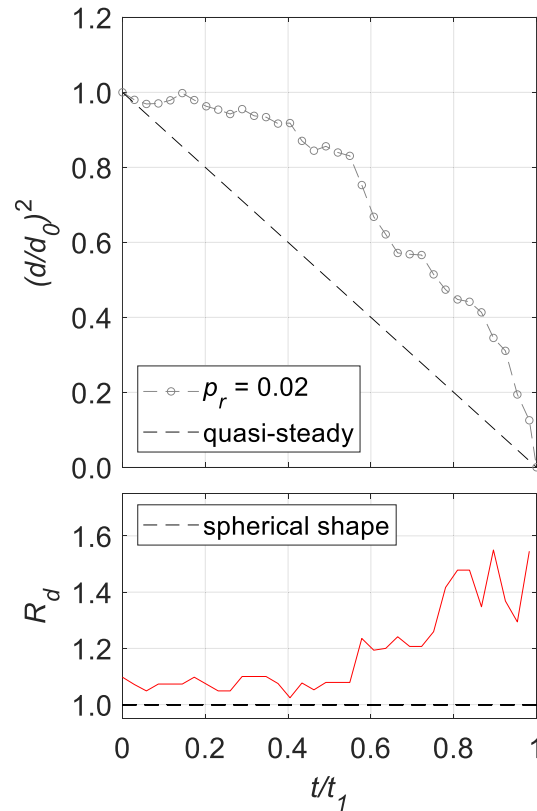


**Figure 93:** Dimensionless time evolution of dimensionless droplet diameter (top) and droplet shape ratio  $R$  (bottom) for the combustion at 0.10 MPa ( $p_r = 0.02$ ).

Figure 94 shows the time evolution of the equivalent droplet diameter for the combustion at a higher ambient pressure. The measured droplet regression approximately matched the expected quasi-steady linear response. The spherical shape was also maintained more or less throughout a major part of the combustion process. Only after  $t/t_1 = 0.75$ , the droplet shape ratio increased slightly above a value of 1.1. As previously discussed, ice formation around the burning droplet was much less visible over long periods of the combustion for pressures  $> 0.75$  MPa ( $p_r > 0.15$ ). Only at the end of the droplet lifetime, structures near the droplet surface appeared even at higher ambient pressures. Further discussions on the effect of pressure are given in chapter 6.7.

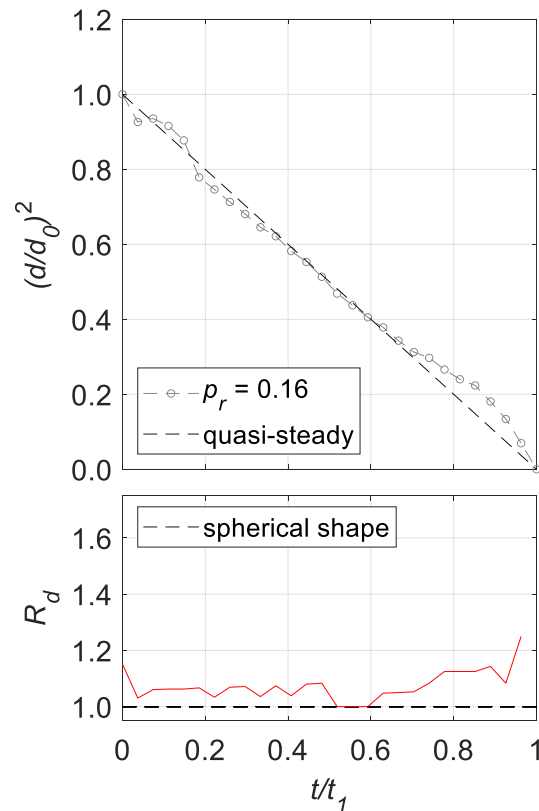


**Figure 94:** Dimensionless time evolution of dimensionless droplet diameter (top) and droplet shape ratio  $R$  (bottom) for the combustion at 0.83 MPa ( $p_r = 0.16$ ).

The plots shown here and all other droplet regression plots of the evaluated experiments in the subcritical pressure regime are given in Appendix J. The evaluations and analyses performed on the droplet regression refer only to the subcritical pressure regime. As explained in more detail in chapter 6.6, no spherical droplet shape was achieved in the supercritical regime and the LOX droplet was affected by the ignition spark throughout the entire combustion process.

## 6.5. Flame position

To determine the flame position relative to the droplet, the  $OH^*$  chemiluminescence images of each experiment were evaluated. The  $OH$  radical is excited during the reaction of hydrogen and oxygen. By detecting the excited radical, it is possible to determine the position of the reaction zone and thus the position of the flame. As shown in Figure 31, Marchese *et al.* [161] analyzed the  $OH^*$  signal during combustion of an n-heptane droplet. They detected an inner ring in the signal with high intensity, whereas the inner region in this ring had only a low signal strength. When comparing these line-of-sight images with data from detailed numerical simulations, it was found that the maximum  $OH^*$  emission occurred near the location of the maximum flame temperature [161].

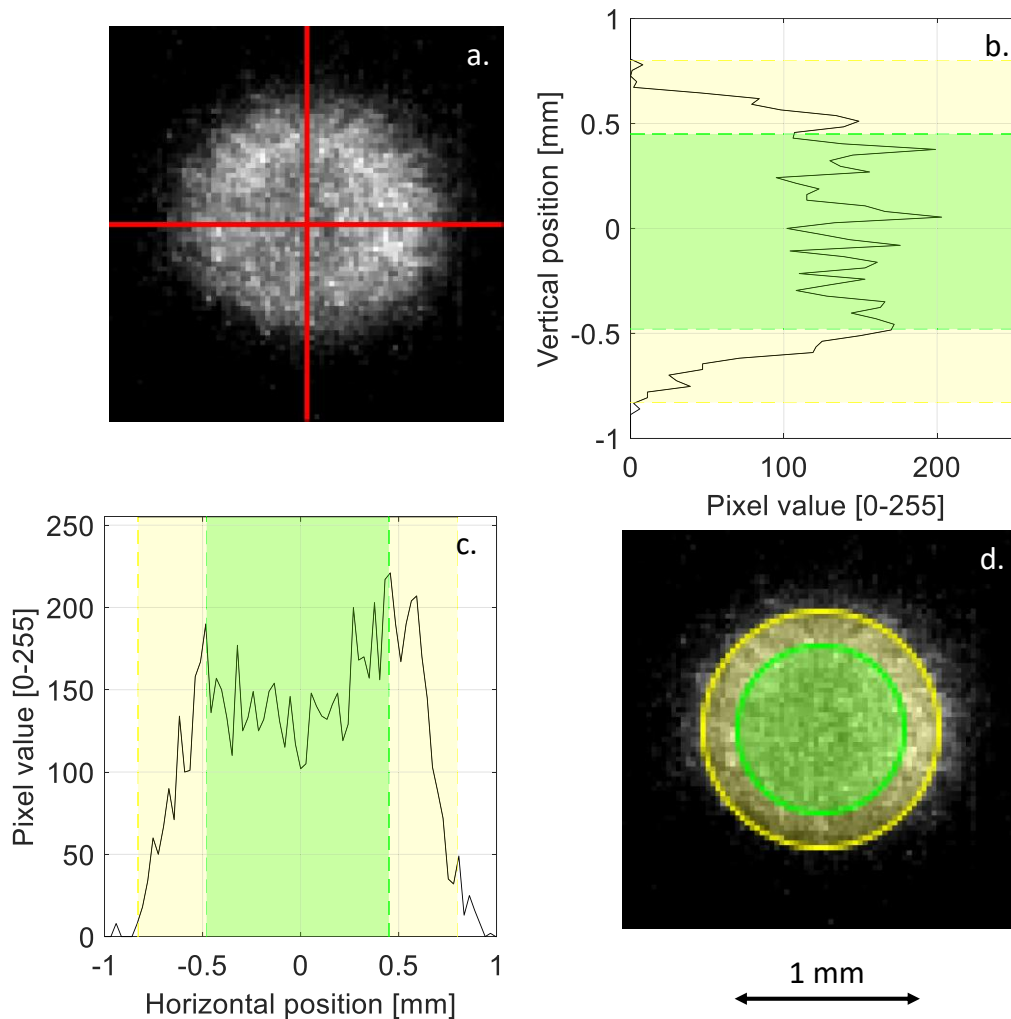


**Figure 95:** Analysis of the  $OH^*$  signal 56.310 ms after ignition at 0.20 MPa ( $p_r = 0.04$ ). a. Original image with selected evaluation lines in red. b-c. Intensity values along vertical and horizontal evaluation lines. The peak values of the left and right side of the origin are marked in green (based on the horizontal evaluation line). The evaluated edge values are marked in yellow. d. Original image overlaid with green circle based on the peak values and yellow circles based on the edge values along the horizontal evaluation line.

Figure 95 shows a detailed analysis of an  $OH^*$  chemiluminescence image during the combustion at 0.20 MPa ( $p_r = 0.04$ ). Overall, after the droplet detachment from the suspender, the signal was spherical and had a high signal-to-noise ratio resulting in high contrast to the background. This is also evident from the steep brightness gradients along the two evaluation lines in Figure 95b-c. Similar to the image obtained by Marchese *et al.* (Figure 31), the images of the hydrogen-oxygen flames also showed an inner ring with the maximum  $OH^*$  emission. However, on the one hand, the flames studied in this thesis were significantly smaller than those from the n-heptane experiments, which reduced the local resolution of the  $OH^*$  signal, which was comparable in both experimental studies. On the other hand, in some experiments the flame was obscured by the free-floating

droplet burning behind the suspender, as shown in Figure 80 and Figure 81. In addition, the  $OH^*$  intensity increased significantly with increasing ambient pressure, as already discussed in chapter 3.4. For example, experiments on hydrogen-oxygen diffusion flames showed that the  $OH^*$  emission increased by a factor of 400 when the pressure is increased from 0.1 to 4.0 MPa [156]. Table 6 shows the modified camera settings for the  $OH^*$  chemiluminescence measurements in relation to ambient pressure. Due to the rapid increase in signal intensity, the camera gain and intensifier gate time were reduced to maintain a constant brightness distribution.

**Table 6:** Modified settings of the intensified camera with increasing ambient pressure to compensate the  $OH^*$  intensity increase.

Pressure [MPa]	Camera gain	Intensifier gate time [ $\mu$ s]
0.10 – 0.46	1	5
0.76	1	2.5
1.10 – 3.15	0	1
5.51	0	0.1
5.56	0	0.04

However, due to the significant change in each experiment, an equal brightness distribution could not always be obtained, as experiments under 1g conditions were very limited. Some experiments were slightly overexposed, so that the inner ring as shown in Figure 95 (green circle) could not be detected. Similarly, it was not always possible to precisely determine the maximum intensity range in low-exposure images. For reasons of comparability in the context of the pressure effect and the partial occlusion by the suspender, the detection of the flame position using the  $OH^*$  chemiluminescence images was therefore calculated based on the signal gradient on the outer edge of the  $OH^*$  signal rather than the areas of maximum signal intensity, as indicated by the yellow circle in Figure 95.

Figure 96 shows an example of the procedure for determining the flame diameter. As described in more detail in chapter 5.2, an algorithm was used to automatically determine the threshold to separate the signal from the background (Figure 96b). The threshold allowed to determine the steep signal gradient at the outer edge. Based on this edge detection (Figure 96c), a Hough transformation was applied to detect a circular object. This method is based on the assumption that the observed flames were spherical and allowed to determine the position of the flame based on the flame diameter even in case of partial occlusion of the  $OH^*$  signal as shown in the example (Figure 96a).

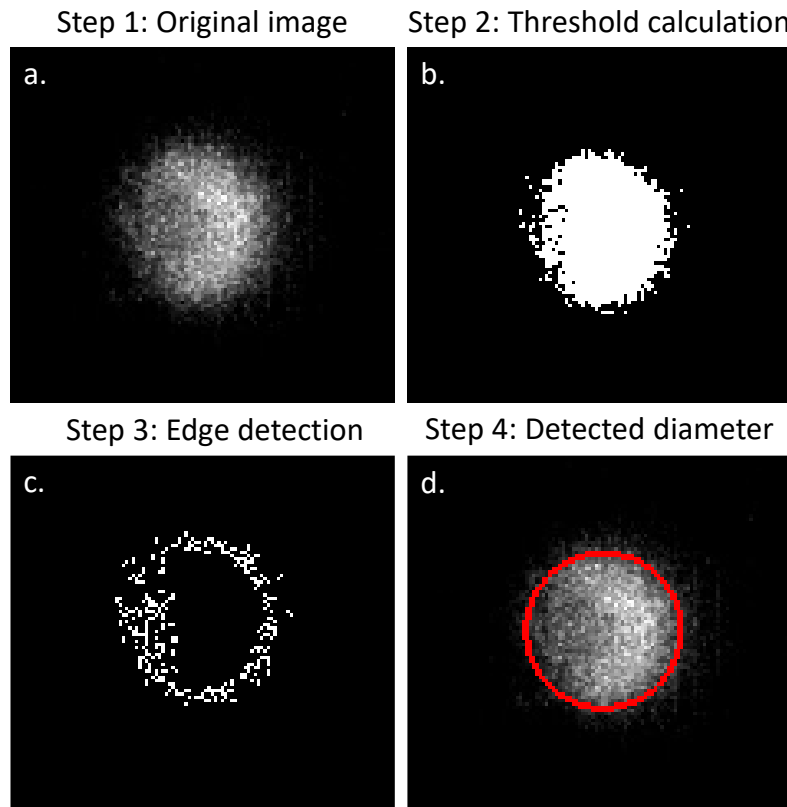


**Figure 96:** Flame diameter detection 50 ms after ignition for the combustion at 0.10 MPa ( $p_r = 0.02$ ). a. Original  $OH^*$  image. b-c. Automated threshold calculation (b.) and edge detection for actual image. d. Diameter detected based on Hough transformation.

With this method, the actual flame position – here assumed to be the zone of maximum flame temperature – was overestimated because the edge of the signal was detected rather than the position of maximum  $OH^*$  emission. With respect to the combustion at 0.20 MPa ( $p_r = 0.04$ ), the detected flame diameters were assumed to be about 45 % too large. This should be kept in mind when comparing these experimental results with other numerical or experimental studies. However, the results of overexposed experimental images were thus also evaluable and comparable within this study. Figure 97 shows the evolution of the flame diameter and the calculated flame standoff ratio  $f/d$  at two different pressures.

The determined flame diameter decreased in both experiments, first slowly and then more and more rapidly as the burning time progressed. The flame standoff ratio was calculated from the droplet diameter regression and the flame diameter. In the first example shown in Figure 97a, the flame standoff ratio was relatively constant up to  $t/t_1 = 0.7$ . After that, the ratio decreased briefly before increasing again significantly toward the end. This behavior can be explained by the previously described ice formation, which caused the measured equivalent droplet diameter to increase at about  $t/t_1 = 0.75$ . This indicates that the ice layer did not significantly affect the flame, because even though the fraction of the ice layer around the burning oxygen droplet increased strongly towards the end of the combustion, and thus even increased the equivalent droplet diameter (including the ice layer), the flame barely reacted to it. It seems that the flame position followed the liquid

surface and the porous ice layer had little effect on the oxygen vapor diffusion and the Stefan flow. Due to the high diffusion rate of hydrogen, local differences in the vaporization or transport rate around the droplet (induced by the ice shell) were quickly compensated, resulting in a spherical flame. However, due to the superposition of the liquid surface with the surrounding ice layer, the calculation of the flame standoff ratio was distorted at the end of the combustion. The steep increase at the end of almost any experiment is due to the fact that the droplet lifetime was minimally shorter than the combustion lifetime. As a result, the flame standoff ratio reached infinity at  $t/t_1 = 1$  ( $t_1$  is the time at which the droplet vanished). The correlation between droplet lifetime and combustion lifetime is discussed in more detail in chapter 6.7.

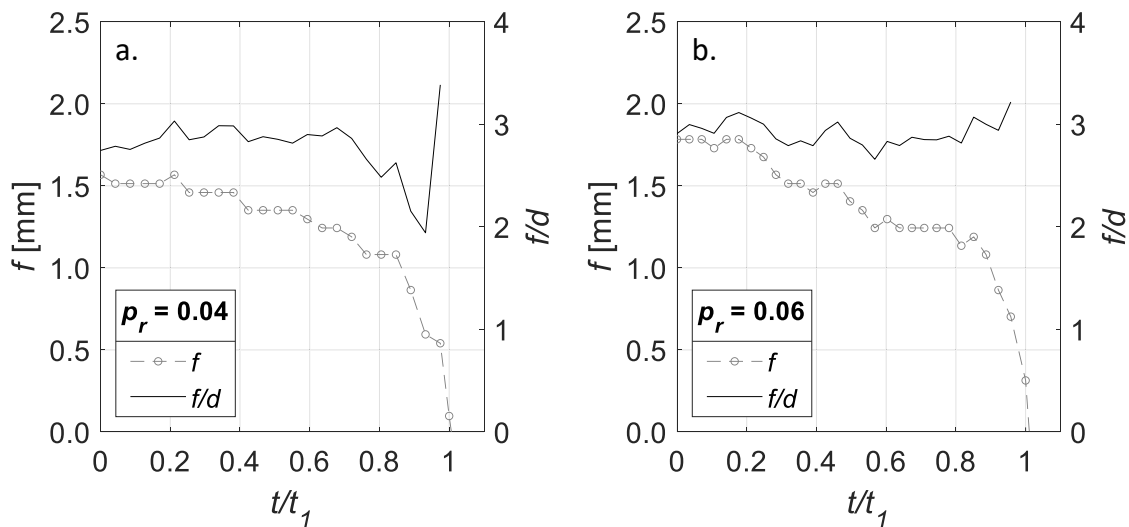


**Figure 97:** Dimensionless time evolution of measured flame diameter  $f$  and calculated flame standoff ratio  $f/d$  for combustions at 0.20 MPa ( $p_r = 0.04$ ) and 0.32 MPa ( $p_r = 0.06$ ).

The flame standoff ratio is much more constant in the second example shown, Figure 97b, although also in this experiment there was clearly visible ice formation around the droplet at the end. Without this ice layer, the flame standoff ratio would probably have increased slightly towards the end of combustion. Due to the errors in calculating the instantaneous flame standoff ratio in the last part of the combustion process, the last 10 % of the calculated values were not used to calculate the average flame standoff ratio for each experiment. The standard deviation from this average value was used to estimate the corresponding error bar, shown in Figure 110. Overall, the flame standoff ratio was nearly constant in all experiments. In experiments with hydrocarbons, the ratio was found to often increase with burning time. This was attributed to the transient accumulation of fuel vapor in the region between the droplet and the flame, which is dependent on the oxygen concentration in the ambiance [58]. Since the flame standoff ratio was constant in the experiments performed in the drop tower, a strongly reduced vapor accumulation can be assumed. This can be explained by the fact that the high diffusion rate of hydrogen results in a continuous supply of fuel in the reaction zone, so that all oxygen vapor is consumed almost immediately. The vaporization process and the transport of oxygen to the reaction

zone determine the combustion lifetime. In contrast, in hydrocarbon droplet combustion in normal air (with limited oxygen), mass transfer of oxygen from the gas phase can also be limiting, so that more fuel vapor is produced than can be burned, resulting in vapor accumulation [58].

As previously reported, the  $OH^*$  signal was obscured by the suspender during some experiments. Therefore, in some cases flame data were missing during the experiments. For this reason, the flame position was determined in these cases using the shadowgraph images. With increasing pressure, the luminosity of the flame on the shadowgraph images also increased so that, after simultaneous calibration with the  $OH^*$  images, these data could be used for experiments at high pressure without visible  $OH^*$  signal.

The plots shown here and all other flame diameter plots of the evaluated experiments are given in Appendix K. The evaluations and analyses performed on the flame detection refer only to the subcritical pressure regime. As explained in more detail in chapter 6.6, no spherical droplet shape and therefore no spherical flame shape was achieved in the supercritical regime and the LOX droplet was affected by the ignition spark throughout the entire combustion process.

## 6.6. Supercritical combustion effects

Figure 98 shows the shadowgraph sequence at an experimental pressure of 5.38 MPa ( $p_r = 1.07$ ), i.e., in the supercritical regime. One difference between subcritical and supercritical combustion is the behavior of the droplet immediately after ignition. In the subcritical regime, the droplet changed to a spherical shape almost immediately after ignition, because of the rapid damping of the oscillations triggered by the pressure spike due to the spark. In the supercritical regime, the droplet did not assume a spherical shape due to the lack of surface tension, which can be seen, e.g., in Figure 98e-f. The damping of the perturbations introduced by the ignition seems to have been strongly weakened, so that the droplet oscillated almost until the end of the combustion and changed shape repeatedly. For the supercritical case, the droplet confinement was presumably no longer determined by surface tension, but only by inertia [87]. During the transition to the supercritical pressure regime, the temperature played an essential role in reaching the supercritical state. Prior to ignition, i.e., during droplet generation, the LOX droplet was subjected to a reduced pressure greater than unity, but the temperature was 77 K ( $T_r = 0.50$ ), well below the critical temperature of 154.6 K. Thus, the droplet behavior did not change during droplet generation and vaporization period compared to the subcritical pressure regime. After ignition, the flame elevated the surface temperature of the droplet to the critical mixing temperature, resulting in a supercritical condition at the surface. However, the droplet interior may have remained liquid due to a subcritical temperature distribution [38]. In addition, above the critical pressure the droplet did not detach from the suspender in a controlled manner as in the subcritical experiments. This was due to the vanishing surface tension as soon as the droplet surface exceeded the critical temperature after ignition. Additionally, the strong perturbations of the droplet were caused by the very small distance between the ignition spark and the droplet surface needed to ignite the mixture around the droplet. As already shown in Figure 75, ignition

occurred in the supercritical pressure regime  $< 0.1$  mm below the suspender and thus just below the droplet surface. As a result, the droplet was subjected to a strong pressure wave and strongly deformed.

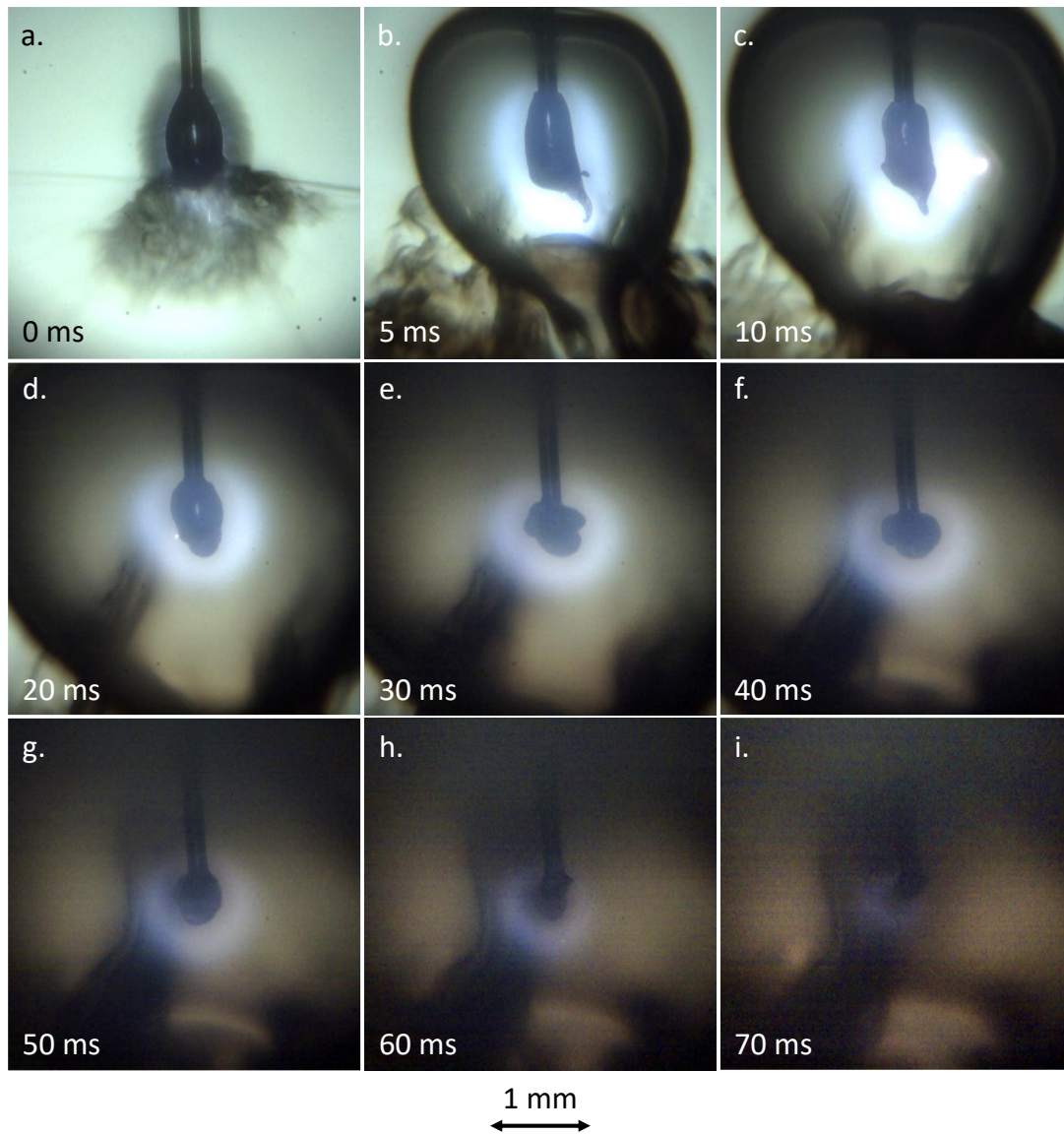


**Figure 98:** High-speed shadowgraph sequence at 5.38 MPa ( $p_r = 1.07$ ). Brightness correction progressively increased. Ignition occurred at 0 ms (a) and induced vortices below the droplet, which affected the shape of the water cloud ring around the droplet. The shape of the droplet is distorted by these vortices and remained non-spherical throughout the combustion.

In contrast to the experiments at subcritical ambient pressure, in which the experimental evaluation was performed only after complete droplet detachment from the suspender, the supercritical experiments had to be evaluated differently. Therefore, for the evaluation of the supercritical experiments, the diameter of the droplet on the suspender was measured optically just before ignition and the total burning time was measured. Using this method, the effects of ignition, the transient heating process, and the initially strong and persistent deformation of the droplet were included in the calculation and therefore

might have affected the gasification or burning rate. To precisely determine the size of the liquid droplet, first the volume of the suspender was determined. The LOX droplet was calculated as an ellipsoid and the covered volume of the suspender was subtracted accordingly, as described in chapter 5.1. With the determination of the initial equivalent droplet diameter and the droplet lifetime, the gasification rate constant could be calculated similar to the experiments under subcritical conditions, which will be compared and discussed in the following subsection. The described ice formation around the burning droplet, which was especially observed at low pressures, could no longer be clearly detected during combustion in the supercritical regime. However, after the end of the combustion, remaining ice particles were also visible as in subcritical conditions.

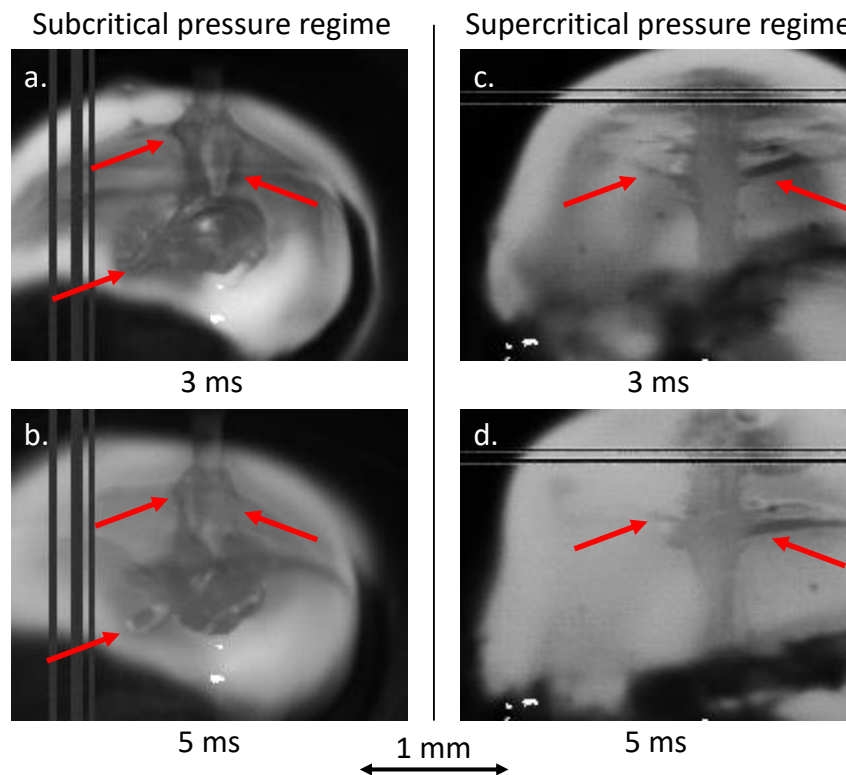


**Figure 99:** Comparison of the droplet behavior in the subcritical and supercritical regime after the ignition spark has hit the suspender tip. a-b. 4.51 MPa ( $p_r = 0.90$ ). c-d. 5.51 MPa ( $p_r = 1.09$ ). Red arrows mark special features of the oxygen fluid. Ignition occurred at 0 ms. The black lines and white dots on the images are defects in the camera sensor.

Another phenomenon observed by chance was the behavior of the LOX when a strong vibration was introduced into the suspender. This was accidentally achieved when the ignition spark hit the bottom of the suspender tip. The laser-induced plasma breakdown broke out part of the lower suspender tip. As a result, the suspender experienced a short but strong vibration. The behavior of the droplet on the suspender is shown in Figure 99. The left side of the figure shows the behavior of the droplet at subcritical pressure at two times. The right side also shows the behavior of the droplet after a suspension hit at the same times, but at supercritical conditions. In the subcritical regime, the liquid deformed significantly, but remained largely connected and began to contract again just 5 ms after

ignition (Figure 99a-b red arrows). At supercritical conditions, the fluid was drawn into long, thin threads (Figure 99c-d red arrows), which persisted for 5 ms (and longer) after ignition. Due to the lack of surface tension, the fluid dissolved as a result of the vibration and did not return to its original position. Comparing the two shadowgraph videos, significant differences could be observed in the behavior of the LOX in the different regimes.

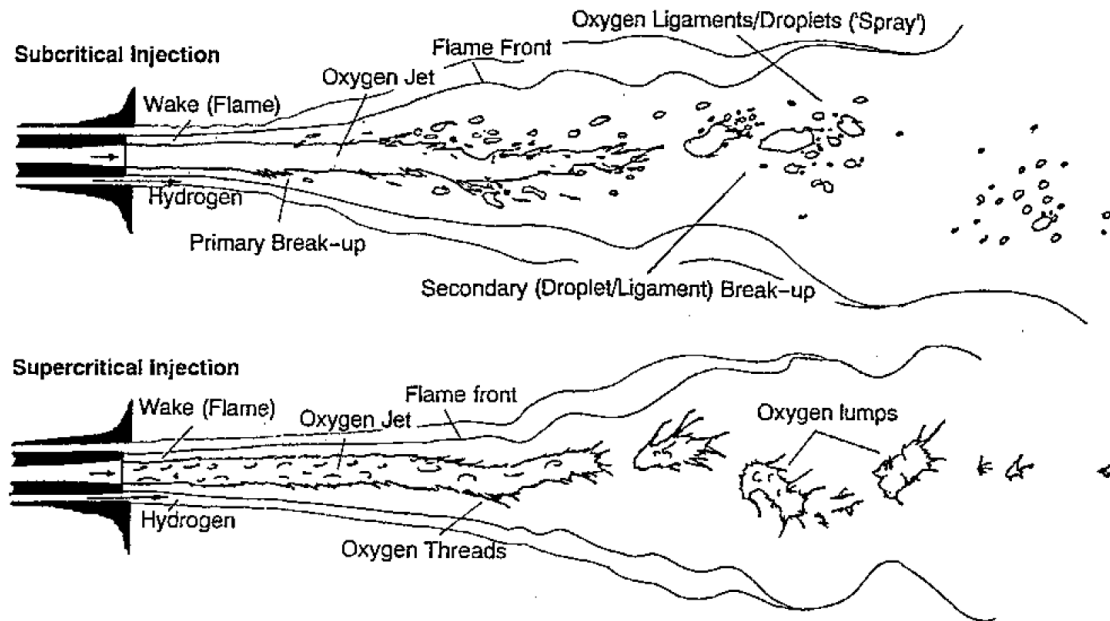


**Figure 100:** Schematic of the subcritical and supercritical injection process. Reprinted from [12] with permission from the American Institute of Aeronautics and Astronautics (AIAA).

The differences of the droplet behavior after a suspender hit are reminiscent of the studies of the subcritical and supercritical injection process. Figure 100 shows a schematic representation of this process based on the experimental study of Mayer & Tamura [12]. Similar to the findings in Figure 99, the oxygen jet breakup was different for each pressure regime. While in the subcritical regime the jet broke up into smaller and smaller droplets, in the supercritical regime oxygen lumps and small threads were formed similar to the results shown above. These structures can be seen even better in Figure 101, which shows two images from the second shadowgraph camera system from other experiments with a suspender hit.

However, these experiments were not suitable for quantitative evaluation. The surface area was extremely increased by spraying the droplet, which led to a significant increase in the gasification rate constant by a factor of about 2.5.

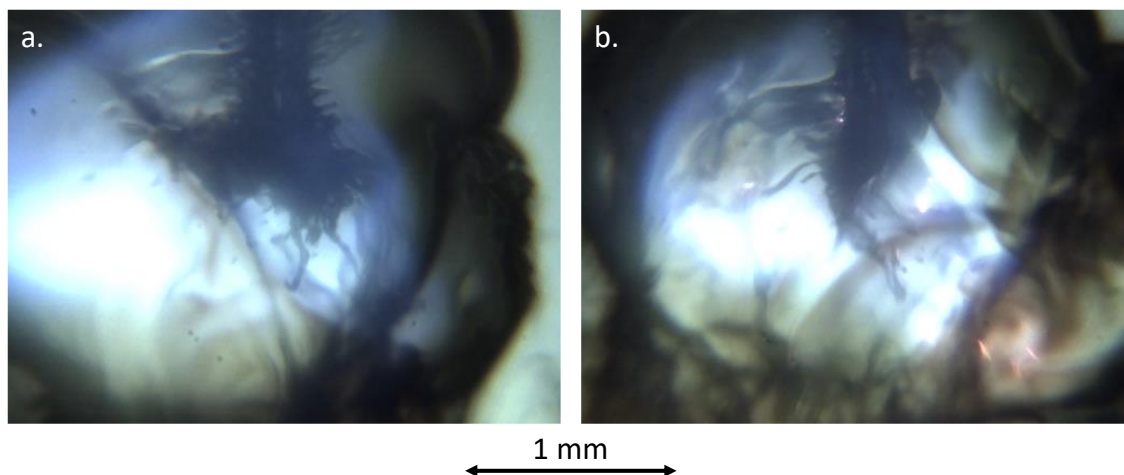


**Figure 101:** Droplet behavior in the supercritical regime 3.5 ms after the ignition spark has hit the suspender tip. a. 4.96 MPa ( $p_r = 0.98$ ). b. 4.94 MPa ( $p_r = 0.98$ ). In both cases the critical pressure was exceeded after ignition.

## 6.7. Pressure effects

This subchapter is divided into three sections. First, the repeatability of the experiments is discussed. Then, the results of the two main characteristics of droplet combustion, the burning rate constant and the flame standoff ratio, are shown and discussed individually.

### 6.7.1. Reproducibility

The main parameter of the experiments evaluated for this thesis is the ambient pressure in the combustion chamber, which is quantitatively evaluated and discussed below. First, the reproducibility of the experiments is considered and the errors are estimated accordingly. For this purpose, two experiments at approximately the same pressure are compared in the following figures. Figure 102 shows the calculated droplet regression in normalized units (left) and the calculated instantaneous flame standoff ratio over normalized time (right) at 1.10 and 1.12 MPa pressures. The droplet diameter regression was approximately linear in both experiments and the normalized droplet lifetime was 210.51 and 215.32 ms/mm<sup>2</sup>, respectively. In the experiment at  $p_r = 0.22$ , the suspender obscured the  $OH^*$  signal during the droplet lifetime, so that only partial data were available for the calculation of the flame standoff ratio. For the experiment at slightly higher pressure, the flame position could be evaluated over the entire burning time. The average values of both measurements were  $2.78 \pm 0.05$  and  $2.61 \pm 0.08$ , respectively. Figure 103 shows the comparison at a pressure of 1.97 and 1.99 MPa. The droplet regression, 192.02 and 190.22 ms/mm<sup>2</sup>, as well as the flame standoff ratio, 2.35 and 2.25, agree very well. Since the difference of the initial pressures in these two experiments was only 0.019 MPa, this comparison is very suitable to show the reproducibility of the experimental conditions.

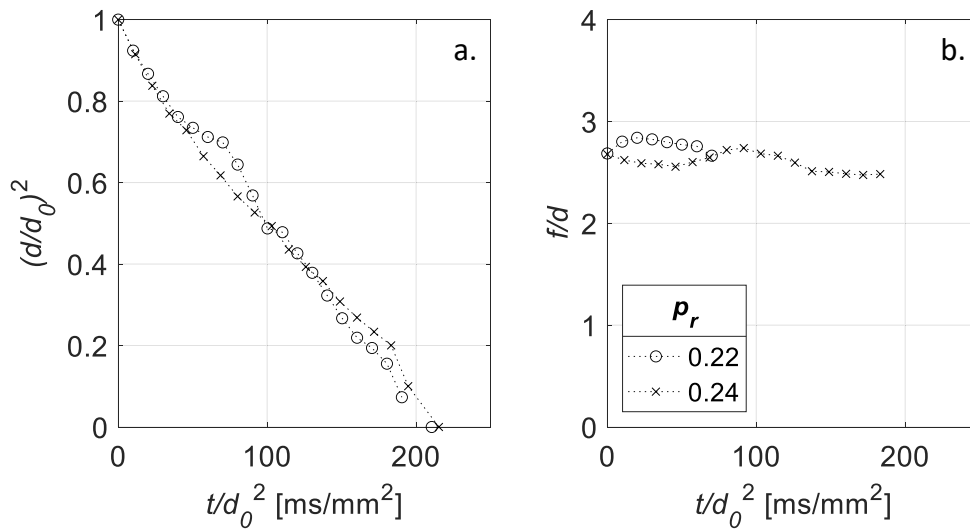


**Figure 102:** Comparison of the droplet regression (a) and flame standoff ratio (b) of two different experiments at  $p_r = 0.22$  and  $p_r = 0.24$ .

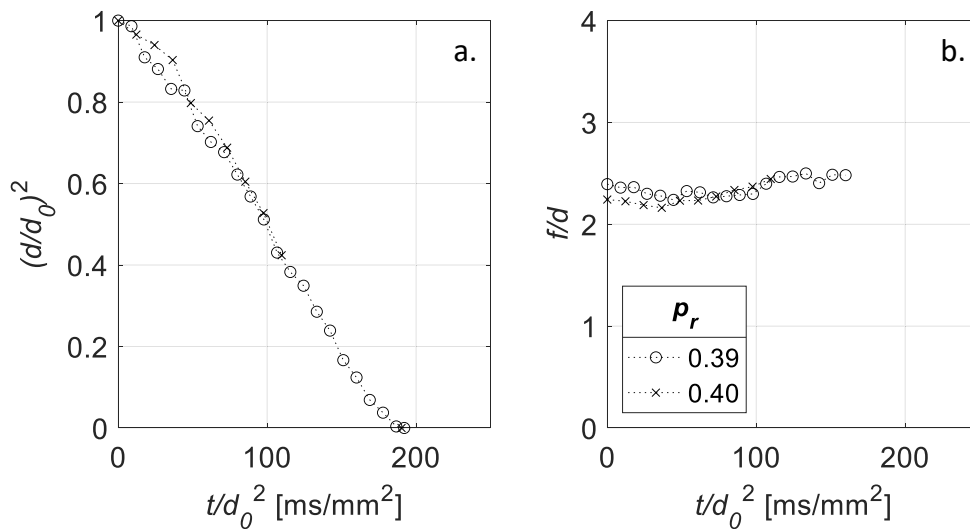


**Figure 103:** Comparison of the droplet regression (a) and flame standoff ratio (b) of two different experiments at  $p_r = 0.39$  and  $p_r = 0.40$ .

To cover the high-pressure region as well, Figure 104 shows the comparison of the experiments at 4.06 and 4.12 MPa. The normalized droplet lifetime was  $136.93$  and  $135.55$  ms/mm<sup>2</sup> and the flame standoff ratio was  $2.22 \pm 0.12$  and  $0.35 \pm 0.15$ , respectively. Overall, the comparisons show that the experiments were reproducible. The deviations between two experiments were comparatively small and corresponded to as the spatial and temporal resolution errors by the diagnostic systems used, as discussed in chapter 5. However, only experiments with reduced ice formation during the burning process were compared at this point. Increased ice formation around the LOX droplet was observed at pressures of  $p_r < 0.15$ . This significantly complicated the optical droplet diameter measurement and led to larger measurement errors, which was due to the complex shape of the droplet with the surrounding ice layer. With only one camera system, 3D effects

could not be captured. In addition, the rotation and translational movement of the droplet caused the detected shape to change very quickly. Therefore, experiments under the same pressure conditions with intense ice formation around the droplet could lead to a different evolution of the diameter regression.

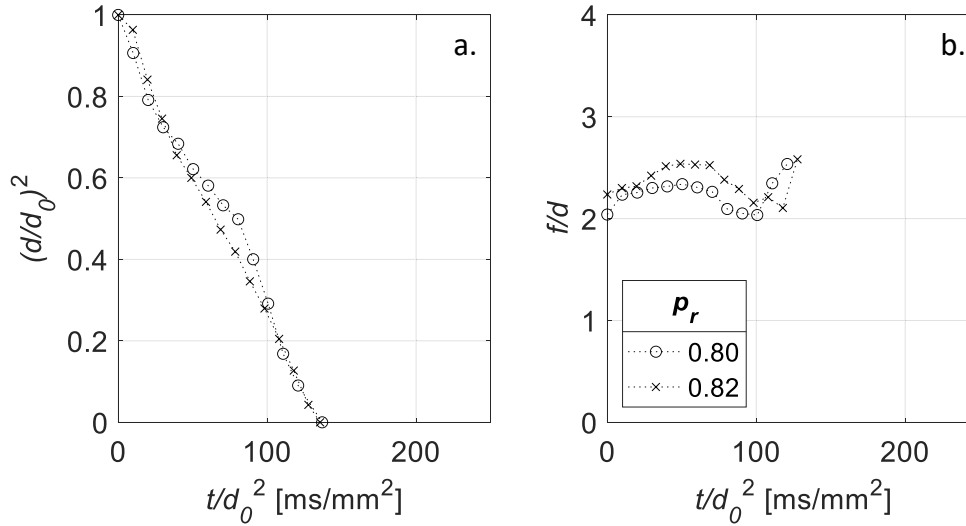


**Figure 104:** Comparison of the droplet regression (a) and flame standoff ratio (b) of two different experiments at  $p_r = 0.81$  and  $p_r = 0.82$ .

### 6.7.2. Burning rate constant

The burning rate was used to compare all experiments as a function of ambient pressure. In this thesis, a further differentiation was made between the burning rate constant  $k_c$  and the gasification rate constant  $k_g$ , as discussed in chapter 2.5.2. The difference between the two parameters is the reference time, which can be related either to the combustion lifetime or to the droplet lifetime. Due to the obscuring of the real droplet surface by the ice layer, which occurred especially at low pressures at the end of the droplet lifetime, an instantaneous burning rate could not be calculated from all experiments. However, since the experiments at higher pressures showed that the regression of the squared droplet diameter was linear and thus the  $d^2$ -law was valid, constant burning rates were assumed for all experiments. Based on the  $d^2$ -law, the gasification rate constant  $k_g$  could be calculated for each experiment from the initial equivalent droplet diameter  $d_0$  and the droplet lifetime  $\tau_g$  (both given in Appendix H):

$$k_g = \frac{d_0^2}{\tau_g} \quad (57)$$

For the evaluation in the subcritical pressure regime, both the initial equivalent droplet diameter and the droplet lifetime were defined with reference to the time of complete droplet detachment from the suspender. The experiments at supercritical conditions, on the other hand, were related to the complete combustion process, i.e., from ignition to extinction of the droplet. In all experiments where the flame was visible until extinction

– either in the  $OH^*$  signal or at higher pressure also in the shadowgraph images – the end of the combustion lifetime occurred within the next camera frame from the end of the droplet lifetime. This resulted in a maximum time offset of 875  $\mu\text{s}$  due to the different frame rates of the cameras. In relation to the droplet lifetimes, which were between 21.5 and 89.5 ms in all experiments after the suspender detachment, it can be assumed that the combustion lifetime roughly corresponds to the droplet lifetime. This is consistent with the numerical results of Lafon & Habiballah [89] which indicate no significant vapor accumulation due to the low flame standoff ratio, so they concluded that the droplet lifetime and the combustion lifetime are almost the same for the combustion of LOX droplets in hydrogen. This is in contrast to the results for hydrocarbon droplet combustion discussed in chapter 3.2.1. In addition to the vapor accumulation, the diffusion rate and the flame standoff ratio are decisive for the delay between droplet lifetime and combustion lifetime. Due to the high diffusion rate of hydrogen and oxygen compared to, e.g., n-heptane in air ( $D_{H_2,O_2} = 1196.3 \text{ mm}^2/\text{s}$  and  $D_{heptane,air} = 112.0 \text{ mm}^2/\text{s}$ , both at 0.1 MPa and 1500 K) and the resulting low flame standoff ratio (for the  $H_2/O_2$  system  $\sim 3$  and 10-15 for hydrocarbons in air [89]), the minimum delay between droplet lifetime and combustion lifetime is very small. For simplification, the following relationship is assumed with respect to the experiments on the combustion of LOX droplets conducted within the scope of this thesis:

$$k_g \sim k_c \quad (58)$$

The calculated gasification rate constants as a function of the reduced ambient pressure are shown in Figure 105a. In the subcritical pressure regime up to a pressure of about  $p_r = 0.15$ , the gasification rate constant appears to be essentially unaffected by ambient pressure and the values scatter widely. In this pressure range, ice formation around the burning droplet was most pronounced at the end of the droplet lifetime. At an ambient pressure greater than  $p_r = 0.15$ , the gasification rate initially decreases, but then increases significantly when the critical pressure is approached. Above the critical pressure, the gasification rate constant appears to be nearly constant with a value of  $\sim 8 \text{ mm}^2/\text{s}$ , however, the data do not extend very far into the supercritical regime due to the pressure limitation of the combustion chamber.

It should be mentioned that the calculation of the gasification rate constant was very sensitive to the initial droplet diameter. The error bars were therefore based on the quality of the initial diameter determination as well as the error that could occur due to the limited temporal resolution of 2000 fps. The ice formation around the droplet, especially at low pressures, may have led to a slight overestimation of the initial diameter, which in turn would lead to a significant overestimation of the gasification rate constant. Another possible influencing factor was the selected evaluation method in the supercritical regime as indicated by the red data points in Figure 105a. As already mentioned, the complete combustion was used for evaluation of these experiments and thus the effects of ignition, transient heating, and the suspender were included in the calculation. These effects could possibly have influenced the gasification rate constants. To verify this, all experiments

were additionally evaluated over the entire combustion process. Here, the initial droplet measurement was carried out shortly before ignition. The calculated gasification rates using this method are shown in Figure 105b.

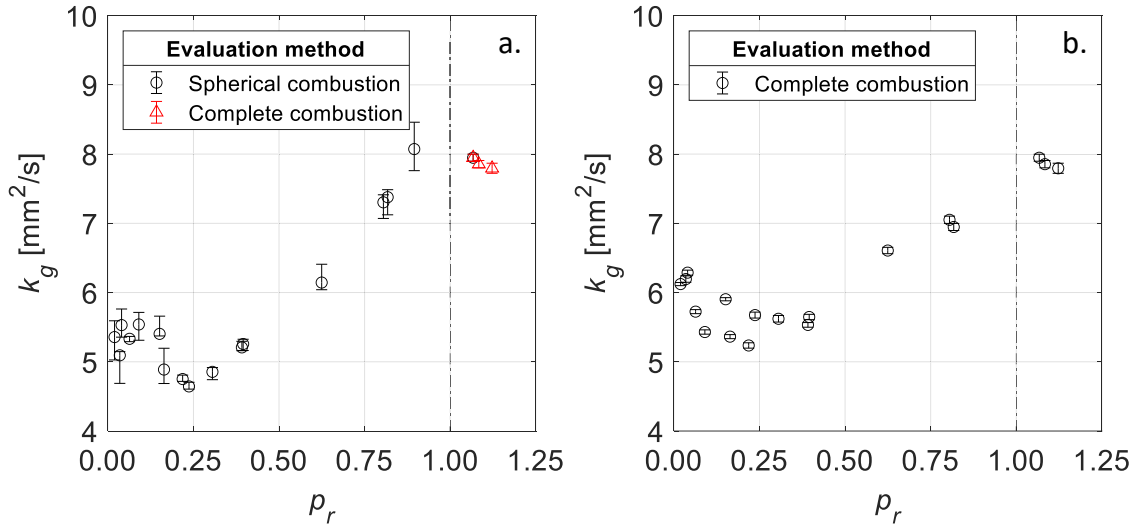


**Figure 105:** Variation in the gasification rate constant with reduced ambient pressure for LOX under  $\mu g$  conditions using different evaluation methods. Error bars are based on the longest and shortest detected dimension of the initial droplet (only for a.) as well as on the maximum time error of  $< 500 \mu s$ . a. Only supercritical experiments were evaluated based on the total combustion process. b. All experiments were evaluated based on the total combustion process. Experiment at  $p_r = 0.90$  not shown here, because the suspender was hit by the ignition spark.

Basically, both methods show a similar progression of gasification rates, although the absolute values are partly different. Also with this evaluation method, the gasification rates are initially increased in the lower pressure range, then decrease slightly. Using this method, ice formation during the combustion process could not have affected the determination of the gasification rate. This suggests that the spherical combustion evaluation method (after suspension detachment) was also not significantly affected by an inaccurate measurement of the initial equivalent droplet diameter due to early ice formation immediately after detachment, as hypothesized above. Thus, it can be assumed that the ice formation itself contributed to an increase in the gasification rate constant. Due to the phase change of water vapor in the direct vicinity of the droplet surface, additional heat is released by the enthalpy of condensation. The pressure effect and the difference between the enthalpy of vaporization of oxygen and the enthalpy of condensation of water is shown in Figure 106. The absolute value of enthalpy of condensation of water is significantly higher than the enthalpy of vaporization of oxygen. Therefore, much more energy is released during condensation of a given mass of water than is required to vaporize the same mass of oxygen. Thus, the energy release of even a small amount of condensed water vapor near the droplet surface can have a significant effect on the gasification rate constant. In addition, energy is also released during freezing (enthalpy of solidification), however, this is much less than the enthalpy of condensation.

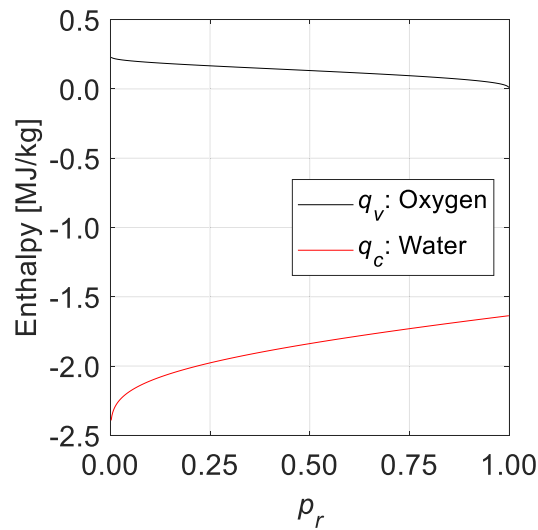


**Figure 106:** Effect of pressure on the enthalpy of vaporization  $q_v$  of oxygen and on the enthalpy of condensation  $q_c$  of water both at boiling temperature. Calculation based on the CoolProp database [194].

This effect was already suggested in the literature based on numerical studies, and it was found that the influence is in the order of 5-10 % [89, 90]. In the results from Figure 105a, an increase of about 35 % was found compared to the other curve in the subcritical pressure regime. In the numerical studies, however, droplets with a diameter of 100  $\mu\text{m}$  at a pressure of 10.1 MPa were investigated. For large droplets and significantly lower pressures this effect could be much stronger and lead to the observed increase in the gasification rate constants.

In contrast to the data in Figure 105a, the gasification rate in Figure 105b increases monotonically from about  $p_r = 0.15$  with slight scattering up into the supercritical regime. This suggests that the gasification rates in the supercritical experiments in Figure 105a compared to the other data in this figure were underestimated. One reason for this could have been, e.g., the transient ignition process or the interference of the flame with the suspender, which might have slowed down the combustion process. Although the spherical combustion evaluation method, shown in Figure 105a, provided better data on the quasi-steady combustion process in the subcritical regime, the qualitative course of the pressure effect on the gasification rates at the transition to the supercritical regime is likely to be more accurate from the complete combustion evaluation method, shown in Figure 105b.

It is pointed out in the literature on hydrocarbon combustion that with increasing pressure the difference between combustion lifetime and droplet lifetime increases [61, 80], as shown in Figure 25 and Figure 27. This is explained by the decreasing diffusion coefficient, which causes the vaporized gas to burn more slowly after reaching the droplet lifetime [80, 131]. However, in these experiments, the droplet lifetime and the combustion lifetime were approximately the same, which is consistent with the literature on LOX combustion in hydrogen [89]. It should be noted, however, that at the end of the droplet lifetime, no clear distinction between LOX and water ice can be seen in the

shadowgraph images. Therefore, errors in the determination of the droplet lifetime may have occurred, especially at higher pressures, such that the apparent droplet lifetime was closer to the combustion lifetime. However, due to the comparably high diffusion rate of hydrogen in oxygen and the low value of the flame standoff ratio, that error in determining the droplet lifetime is assumed to be rather small in relation to the combustion lifetime.

When comparing the results on LOX combustion with those from hydrocarbon combustion experiments, which are based on measured combustion lifetimes, e.g., [59, 80, 96, 98, 101], a similar progression of the burning rate constants can be seen in Figure 107. Based on the results presented in Figure 105a, it can be expected that the maximum burning rate is also reached near a reduced pressure of unity ( $p_r = 1$ ), which would be consistent with the hydrocarbon experiments.

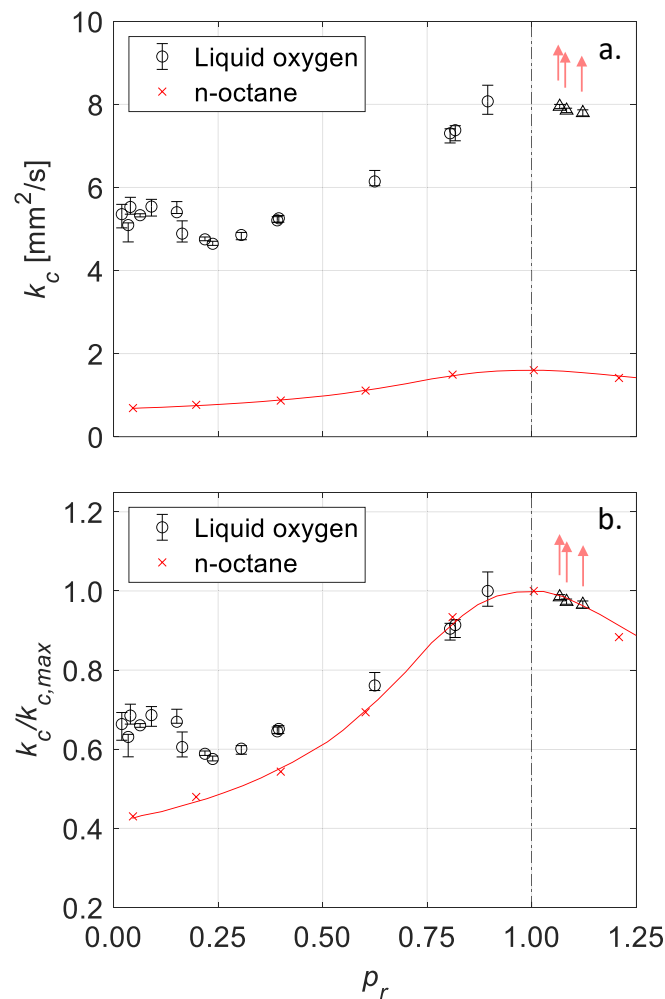


**Figure 107:** Variation in the burning rate constant with reduced ambient pressure for LOX and n-octane [101] under  $\mu\text{g}$  conditions. Error bars for LOX are based on the longest and shortest detected dimension of the initial droplet as well as on the maximum time error of  $< 500 \mu\text{s}$ . a. Absolute burning rate constant  $k_g$ . b. Normalized burning rate constant  $k_g/k_{g,max}$ . Red arrows indicate qualitative correction of data in supercritical regimes.

However, when the underestimation of the burning rates in the supercritical regime is taken into account, indicated by the red arrows, it becomes clear that the experimental series of droplet combustion of LOX and of hydrocarbons differ not only quantitatively (Figure 107a) but also qualitatively (Figure 107b).

For the hydrocarbon case, the combustion lifetime decreases with increasing pressure, and reaches a minimum near the critical pressure of the liquid fuel. As the pressure continues to increase, the combustion time increases due to the reduced mass diffusivity at high pressures. The droplet lifetime decreases continuously with pressure, while the single-phase combustion lifetime increases progressively with pressure. Therefore, at low pressures, the combustion process is primarily determined by gasification of the liquid, while in a supercritical environment transient gas phase diffusion plays a more important role [38].

In contrast, the corrected evaluated data in the case of LOX combustion in hydrogen do not suggest a minimum of the combustion lifetime at the critical point. This is primarily due to the strongly reduced vapor accumulation for the H<sub>2</sub>/O<sub>2</sub> system. Lafon & Habiballah explained this by the fact that the gasification process is mainly controlled by heat diffusion [89]. They attributed the increase in gasification rate to the increase in thermal conductivity and the decrease in enthalpy of vaporization. In the subcritical pressure regime, the enthalpy of vaporization takes a dominant role in the gasification of LOX [38, 87, 96]. Despite the significant decrease in the binary diffusion coefficient with increasing pressure, which would lead to a decrease in the burning rate, the decrease in the enthalpy of vaporization dominates and leads to the observed increase in the gasification/burning rate constant and decrease in the droplet/combustion lifetime, respectively. The enthalpy of vaporization at the respective boiling temperature in the subcritical regime is shown in Figure 108a.

Another pressure-dependent effect is the heating of the droplet. Since the initial droplet temperature in all experiments is 77 K (due to the cooling of the combustion chamber with LN<sub>2</sub>), the temperature difference to the boiling temperature  $\Delta T$  increases with increasing pressure, as shown in Figure 108b. Due to the larger temperature difference, the amount of energy used to heat the droplet to the boiling temperature (sensible heat) increases with ambient pressure. The ratio of the sensible heat and the enthalpy of vaporization (latent heat) can be calculated using the Jacob number given in Equation (36). Here the sensible heat is calculated by the temperature difference  $\Delta T$  and the heat capacity at the corresponding ambient pressure  $c_p$ , at 77 K each. The evolution of the Jacob number  $Ja$  in the subcritical regime is shown in Figure 109. Up to a pressure of  $p_r = 0.65$ , the enthalpy of vaporization is higher than the sensible heat ( $Ja < 1$ ), i.e., the energy required to heat the droplet to the boiling temperature is lower than the energy required for the phase change. Above this pressure, more energy is required for heating the droplet than for the vaporization process. However, it should be noted that the heating of the droplet is a transient process that takes more and more time in relation to the droplet lifetime as the pressure increases. In the spherical combustion evaluation method, a large part of the heating phase is not taken into account, whereas in the complete combustion

evaluation method, the entire heating phase is included. This could explain why the gasification rate constants at high pressures are lower with the complete combustion evaluation method compared to the spherical combustion method, as shown in Figure 105.

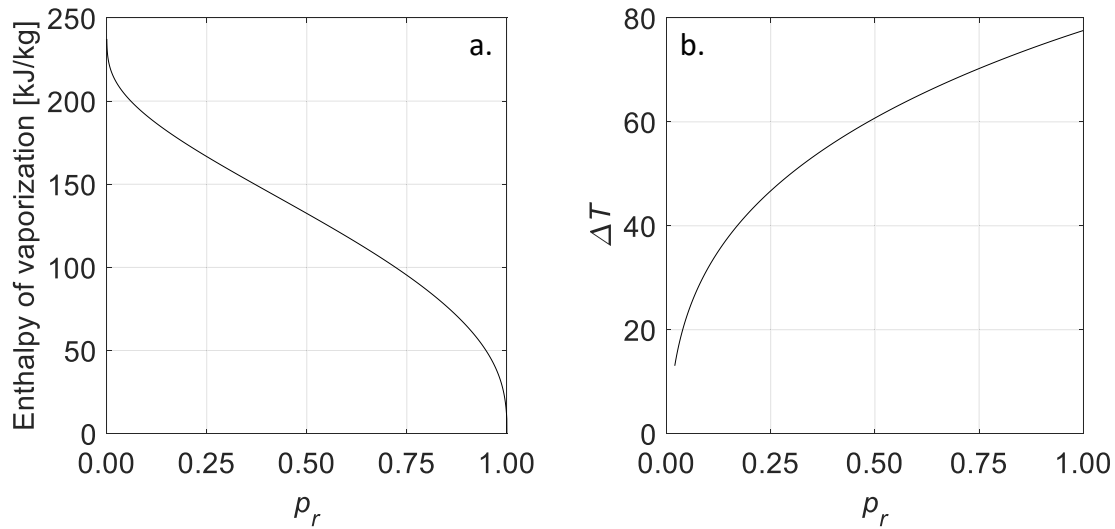


**Figure 108:** a. Effect of pressure on the enthalpy of vaporization of oxygen at boiling temperature. b. Temperature difference  $\Delta T$  between initial droplet temperature of 77 K and boiling temperature. Calculations based on the CoolProp database [194].

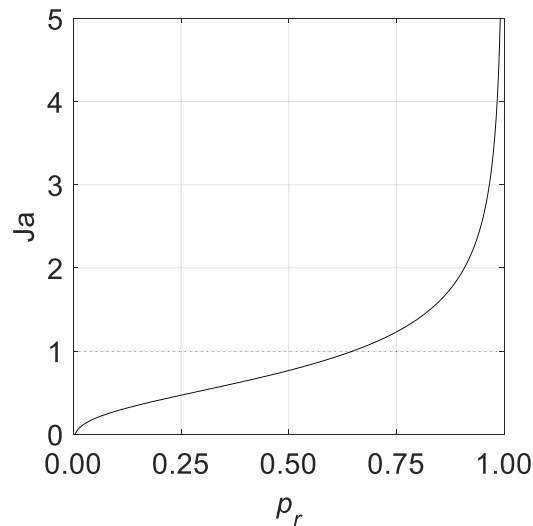


**Figure 109:** Effect of pressure on the Jakob number for a LOX droplet with an initial temperature of 77 K. Calculation based on the CoolProp database [194].

The enthalpy of vaporization at the droplet surface vanishes during the transition to the supercritical pressure regime, as shown in Figure 108a. When approaching the critical conditions, the divergence of the specific heat compensates for the effect of the reduction in the enthalpy of vaporization so that no abrupt change occurs during the critical

transition [38]. With a further increase in ambient pressure, the diffusivity decreases further, which would cause the droplet lifetime to increase again. This is counteracted by the decreasing critical mixing temperature with increasing pressure [38, 84], as shown in Figure 4. At a pressure above the critical point, the disappearance of the sharp distinction between gas and liquid occurs at the critical mixing temperature. Due to the pressure limitation of the combustion chamber, higher pressures could not be investigated within the scope of this thesis.

Since no single droplet experiments on  $H_2/O_2$  combustion have been performed prior to this thesis, the data from the drop tower experiments can only be compared with numerical studies from the literature. The results of Lafon & Habiballah [89], who performed numerical simulations on the combustion of a LOX droplet with a diameter of  $100\ \mu\text{m}$ , are in qualitative agreement with the corrected data from these experiments and are shown in Figure 26. The absolute values are of the same order of magnitude, but the effect of ambient pressure is significantly reduced, compared to the experimental data. However, in the numerical simulations, the ambient temperature varied between  $T_r = 4.85$  and  $T_r = 12.94$ , which was significantly higher than the initial ambient temperature in the drop tower experiments of  $T_r = 0.5$ .

### 6.7.3. Flame standoff ratio

Figure 110 shows the calculated mean flame standoff ratio as a function of the ambient pressure in the subcritical regime. The mean value was calculated from the instantaneous ratio of the flame diameter to the droplet diameter during combustion. Therefore, the intense ice formation at low pressures ( $p_r < 0.15$ ) could have affected the calculation of the flame standoff ratio because the droplet shape, i.e., the droplet diameter, changed significantly.

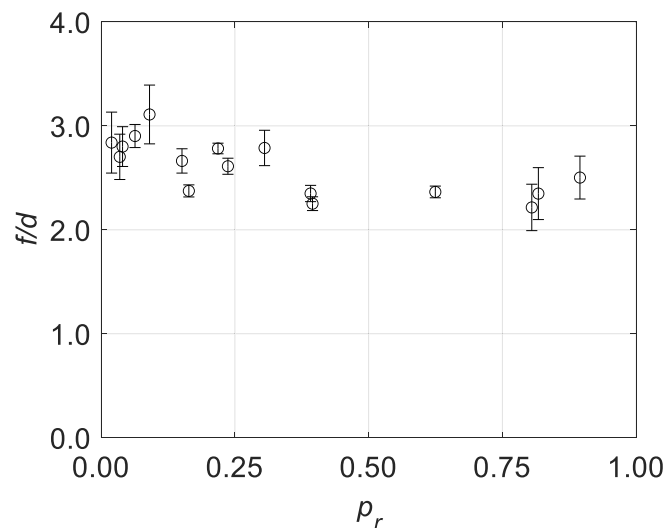


**Figure 110:** Effect of reduced ambient pressure on the mean flame standoff ratio in the subcritical regime under  $\mu\text{g}$  conditions. The error bars indicate standard deviation from the mean value.

In this pressure range, the calculated values scatter strongly over time, resulting in large standard deviations when calculating the mean value. In addition, increasing the pressure had a major effect on the luminosity of the flame in both the  $OH^*$  chemiluminescence and shadowgraph images, where the flame zone became apparent at high pressures.

The aperture, exposure, and gain settings of the different camera systems were correspondingly adjusted during the experimental campaign. This might account for some of the larger data scatter at higher pressures. Despite the scatter in the data, it appears that the ambient pressure had only a limited effect on the flame standoff ratio. With increasing pressure, the trend of the flame standoff ratio appears to decrease slightly, reaching a value of approximately 2.5 at a reduced pressure of about 0.9. The low values of the flame standoff ratio are due to the high diffusion rate of hydrogen and a value of 3 was reported in the literature for the  $H_2/O_2$  system [89] (a value of 2.3 for the combustion at  $p_r = 1.98$  [55]). In comparison, the flame standoff ratio for the combustion of hydrocarbons in air is between 15 and 20 [89].

The position of the flame is essentially determined by the transport processes. The flame is supplied with oxygen vapor from the inside, i.e., from the droplet surface, and with hydrogen from the outside. The transport process of oxygen vapor is essentially based on diffusion, but also on the Stefan flow. To estimate the velocity of the Stefan flow at different ambient pressures, Equation (12) can be used. For the calculation, saturation properties were assumed for the densities, i.e., a temperature of 90 K at 0.10 MPa ( $p_r = 0.02$ ), 115 K at 0.76 MPa ( $p_r = 0.15$ ), and 143 K at 3.15 MPa ( $p_r = 0.62$ ). The gasification rate constants and the initial droplet diameters were taken from the  $\mu g$  experiments.

$$v_{Stefan\ flow, p_r=0.02} = \frac{1141.8\text{ kg/m}^3 \cdot 5.357\text{ mm}^2/\text{s}}{4.4\text{ kg/m}^3 \cdot 8 \cdot 0.341\text{ mm}} = 509.6\text{ mm/s} \quad (59)$$

$$v_{Stefan\ flow, p_r=0.15} = \frac{1005.0\text{ kg/m}^3 \cdot 5.807\text{ mm}^2/\text{s}}{29.4\text{ kg/m}^3 \cdot 8 \cdot 0.361\text{ mm}} = 68.7\text{ mm/s} \quad (60)$$

$$v_{Stefan\ flow, p_r=0.62} = \frac{781.9\text{ kg/m}^3 \cdot 6.144\text{ mm}^2/\text{s}}{136.7\text{ kg/m}^3 \cdot 8 \cdot 0.266\text{ mm}} = 16.5\text{ mm/s} \quad (61)$$

The sole decrease of the Stefan flow with increasing pressure would have resulted in the stoichiometric point and thus the flame moving further towards the droplet, i.e., a decrease in the flame standoff ratio. However, an opposite effect was caused by the simultaneous strong decrease in diffusivity with increasing pressure, as exemplarily shown in Figure 111. Thus, both effects compensated each other, resulting in the observed nearly constant flame position.

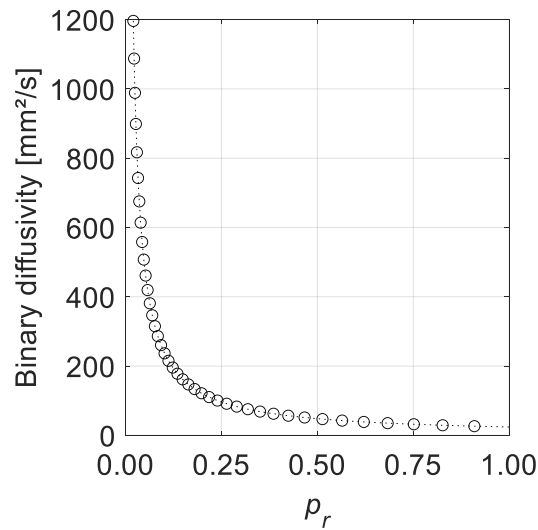


**Figure 111:** Pressure effect on the binary diffusion coefficient of hydrogen and oxygen at temperature of 1500 K. Calculated with Equation (2) based on [32].

The ambient pressure also has an effect on flame temperature. The adiabatic flame temperature  $T_f$  can be used to estimate this effect. It is calculated as the temperature that can be reached in a closed system by a combustible mixture in chemical equilibrium by means of an isobaric, adiabatic process [27]. The calculation depends primarily on the ambient pressure and the initial temperature, but also on the oxygen content and the equivalence ratio. The adiabatic flame temperature calculated for the  $H_2/O_2$  system is shown in Figure 112 as a function of ambient pressure. The initial ambient temperature was set to 77 K and an equivalence ratio of unity was chosen.

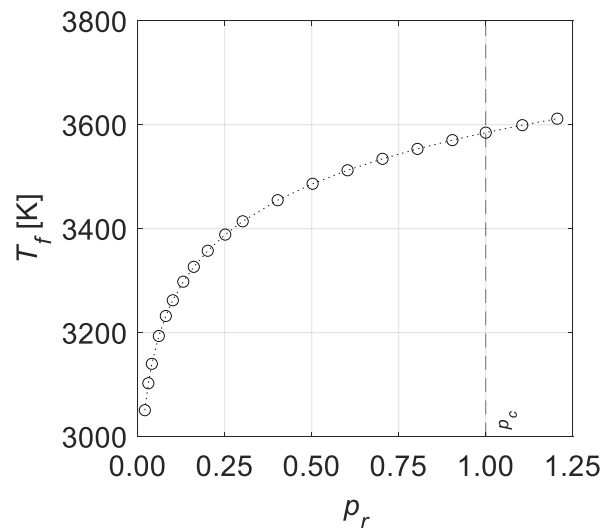


**Figure 112:** Variation in adiabatic flame temperature  $T_f$  of the  $H_2/O_2$  flame with reduced ambient pressure. Initial temperature was 77 K and the equivalence ratio was unity. Calculated with [195] and based on [10, 27, 196, 197].

The adiabatic flame temperature increases degressively from 3051 K at 0.1 MPa to 3610 K at 6.0 MPa. This degressive course could be an explanation for the increased ice formation at low pressures up to approximately  $p_r = 0.15$ . A steep temperature gradient was established between the cryogenic surface of the LOX droplet, which reached approximately the boiling temperature during combustion (between 90 and 154 K, depending on the pressure), and the hot flame. Only in the direct vicinity of the droplet surface was the temperature low enough for the produced water vapor to condense and freeze. At an ambient pressure of 0.1 MPa ( $p_r = 0.02$ ), this low-temperature zone was wide enough to allow clearly visible ice structures to form around the burning droplet, which had a significant effect on the droplet's external shape. With increasing ambient pressure, on the one hand, the surface temperature of the droplet increased slightly, but more importantly, the flame temperature also increased sharply, especially at low pressures. This caused the temperature gradient to become even steeper and the low-temperature zone to move even closer to the droplet surface. Other influencing factors were the flame standoff ratio, which decreased, albeit only slightly, with increasing ambient pressure, which also caused the temperature gradient to steepen as well as the shorter droplet lifetimes, which limited the accumulation and growth time of water droplets and ice particles near the droplet surface.

## 7. Conclusions

### 7.1. Summary of the experimental results

The experimental apparatus developed in this thesis was used to study the combustion of single LOX droplets in hydrogen under microgravity conditions. A parameter study was performed in which the ambient pressure was varied between 0.10 MPa ( $p_r = 0.02$ ) and 5.66 MPa ( $p_r = 1.12$ ). Using shadowgraph diagnostics, the initial droplet diameter and the droplet regression were measured. In addition, the recordings were used to identify regions in which water vapor condenses or freezes. The position and size of the flame zone was determined by  $OH^*$  chemiluminescence.

To ignite the mixture around the vaporizing droplet, the plasma spark had to be positioned very close to the droplet surface, despite the very wide ignition limits of the  $H_2/O_2$  system. Specifically, at an ambient pressure of 0.1 MPa, the minimum ignition distance was 0.8 mm from the droplet surface. Simplified numerical simulations were used to qualitatively evaluate the concentration field around the LOX droplet. The simulation indicated that a steep concentration gradient is established due to the high diffusion rate of hydrogen. With increasing ambient pressure, the necessary minimum distance between the spark and the droplet decreases even more. Due to the closely positioned plasma spark, the LOX droplet was strongly influenced by the resulting pressure wave during ignition. This was one reason for the observed droplet detachment from the suspender that occurred in all (subcritical) experiments. This reproducible behavior has not been reported in the literature and led to a free-floating LOX droplet, which was not affected by the suspender and (initially) assumed a perfectly spherical shape. The evaluation of the combustion process was started only after complete detachment from the suspender. Thus, the unexpected phenomenon of a defined droplet detachment unintentionally led to overcome the disadvantages of the suspender technique, such as the additional heat input into the droplet interior.

The shadowgraph images revealed that the initially spherical shape of the droplet was deformed progressively during the combustion process (most pronounced at low pressures,  $p_r < 0.15$ ). Structures near the surface indicated that the water vapor produced during combustion froze near the cold droplet surface and formed an ice shell around the LOX droplet. Some images revealed erupting jets as the result of micro-explosions. The formation of the ice layer was especially visible at low pressures and led to a clear deviation from the spherical shape of the droplet. However, the ice layer also obscured the view of the actual liquid surface, so that the investigation of the diameter regression towards the end of the combustion process was no longer possible. This led to significant deviations from the quasi-steady course of the droplet regression according to the  $d^2$ -law.

In contrast, the flame shape was not measurably affected by the ice layer and was spherical in all experiments. Due to the high diffusion rate of hydrogen, the flame was very close to the surface of the droplet compared to hydrocarbon systems. The flame standoff ratio was nearly constant in all experiments, which indicates that the transient vapor accumulation was very limited. At low pressures, the average flame standoff ratio

was 3 and decreased slightly to 2.5 with increasing ambient pressure. This effect, combined with the increase in flame temperature and reduced droplet lifetimes, led to the fact that ice formation no longer caused a significant change in the shape of the droplet at pressures  $p_r > 0.15$ . However, ice formation at the end of the droplet lifetime was also visible in this pressure range.

It was also found that the ambient pressure has a significant effect on the gasification rate. In the subcritical regime, despite a few deviations at low pressures,  $p_r < 0.15$ , the gasification rate increased significantly with increasing pressure. Above the critical pressure, the gasification rate appears to be nearly constant with a value of about 8 mm<sup>2</sup>/s. However, due to the vanishing of the surface tension in the supercritical regime, no defined detachment of the droplet from the suspender occurred. Hence, the evaluation of these experiments was started at the time of ignition (in contrast to the evaluated experiments in the subcritical regime). An alternative evaluation method yields a slight, but continuous increase in the combustion rate during the transition to the supercritical regime.

## 7.2. Progress and future work

Considerable progress has been made in the field of droplet combustion in recent years. Due to the increase in computational performance, more complex numerical simulations can be performed in shorter times. Regarding the development of new or the optimization of existing liquid rocket engines, a detailed understanding of spray combustion is necessary, which is characterized by the nonlinear interaction of individual sub-processes, such as atomization, droplet formation, or combustion. Detailed numerical models can help to maximize the combustion efficiency in rocket engines and thus to increase the payload-to-mass ratio of the rocket. However, for the development and validation of detailed fundamental models, experimental studies are essential. Especially experiments on single droplet combustion under microgravity conditions allow to study the fundamental processes of droplet vaporization, ignition, and combustion in detail and without superposition of convection processes. Regarding the H<sub>2</sub>/O<sub>2</sub> system, as a typical propellant combination for liquid rocket engines, no experimental database on single droplet combustion was available prior to this thesis. The experiments performed here reveal the fundamental characteristics of LOX droplet combustion in hydrogen. It was shown that an ice layer forms around the droplet, most significantly at low pressures. This ice layer leads on the one hand to a strong deformation of the droplet and on the other hand to an increase of the gasification rate constant. The existence of an ice shell around the burning droplet represents a new finding. Previously, it was suspected from numerical simulation results that water condensation could occur near the droplet surface. Moreover, the effect was considered to be very small, whereas the experimental results of this thesis show that this effect is significant.

With respect to the flame standoff ratio, numerical predictions from the literature could be confirmed. Due to the high diffusion rate of hydrogen, the flame formed very closely around the droplet. It should be noted that the mass transfer was not significantly affected by the ice shell. However, the determined gasification rate constants deviate from those

from numerical studies because of the presence of the ice layer and the enthalpy of condensation (and solidification) released. The experiments revealed both higher absolute rate constants and a stronger pressure effect (resulting in a stronger increase with increasing ambient pressure), although the ambient temperature in the experiments was significantly lower ( $T_r = 0.5$ ) than in the numerical studies ( $T_r = 4.9$  to  $13.0$ ). The gasification rate is the essential parameter in droplet or spray combustion, as it reflects the droplet lifetime and thus influences the size of the combustion chamber required for complete burnout. In contrast to hydrocarbons, the gasification rate continues to increase monotonically even in the supercritical regime (based on the investigated pressure range up to  $p_r = 1.12$ ). This is consistent with numerical studies on LOX droplet combustion.

The results of the conducted experiments on large droplets can be applied to technical combustion due to the similarity to very small droplets in convective environments through matching flow velocity and droplet diameter in the Grashof number. Therefore, the data in this thesis provide an initial database for the development and validation of fundamental numerical (sub-)models and thus can contribute to the development of future detailed spray combustion models. The main characteristics of droplet combustion, such as the combustion or gasification rate constant as well as the flame standoff ratio, can be used for comparison with the calculated values from the numerical simulations. The position of the flame is determined by the diffusive and convective transport mechanisms in the gas phase, which in turn are essentially influenced by the flame temperature and position. In addition, the experimental observation of significant ice formation around large LOX droplets at low pressure provides also valuable information for future model development. Neglecting water condensation leads to a significant overestimation of droplet lifetimes, especially in the low pressure range.

Of particular interest is the combustion behavior at supercritical conditions, since most rocket engines are operated in this pressure regime. Due to the small distance and the strong pressure wave during ignition, the LOX droplet was strongly deformed in the conducted experiments. In combination with the vanishing surface tension, it was very difficult to minimize the deformation of the droplet during combustion. Additional experiments in the supercritical pressure regime, especially at higher pressures, would be of great interest to investigate the pressure effects also in a large (supercritical) pressure range. These data are necessary to fully cover the relevant pressure range for liquid rocket engines. For this, the droplet ignition would have to be revised to avoid (or limit) a pressure wave. However, ignition must occur very close to the droplet surface, which greatly limits the use of conventional ignition techniques, such as heating wires or electrodes. Due to the very short droplet lifetimes ( $\sim 50$  ms), a very fast retraction of the ignition device is necessary to avoid affecting the combustion. Another approach is to use magnetic levitation to both hold the LOX droplet in position and maintain the spherical shape during ignition. However, this approach is technically very demanding and has so far only been considered theoretically by the author of this thesis and the cooperation partners. In summary, several technical hurdles still need to be overcome in order to extend the experimental investigation of single droplet combustion in the supercritical regime.

Another open scientific question is the detailed analysis of ice formation around the burning LOX droplet. Due to the significant water condensation inside and outside the flame, it was not possible to determine the exact position of the ice shell and the shape of the LOX droplet inside the ice layer with the shadowgraph diagnostics used. However, these data are necessary for a complete characterization of the ice formation phenomenon. Advanced optical diagnostics, such as differential optical absorption spectroscopy, could help determine these parameters in future experiments.

Overall, the development of the apparatus for conducting single droplet experiments in microgravity also represents a basis for further experimental studies and thus a technical advance. Despite the great importance for the development and optimization of rocket engines, no combustion experiments with isolated cryogenic droplets have been performed so far. This is mainly because the technical requirements for the experimental setup are very high, such as the generation of cryogenic droplets. During the development of the experimental setup, various techniques were tested and proven, which can be used to develop new experimental setups for studying cryogenic droplet combustion.

The investigations on the single droplet represent only the first step in the development of a detailed spray combustion model. Based on the results in this thesis, interactions of neighboring droplets can be taken into account in future (experimental) studies. The effects of the interactions of individual droplets allow individual parts of a spray combustion to be described in detail. The last step is the coupling of the droplet model with the trajectories and size distribution of a spray.

In addition to the experiments on LOX droplet combustion presented in this thesis, the project partner Prof. Hermanson from the University of Washington is working on a numerical simulation of the LOX droplet combustion in hydrogen based on the OpenFOAM platform. The author of this thesis is also working in collaboration with Dr. Ando from the Kyushu University on the adaptation of an existing numerical model for hydrocarbon autoignition to the H<sub>2</sub>/LOX case. Both development projects are to be supported in the future by specific experiments for validation, e.g., for pure vaporization. In this case, the experimentally determined vaporization rate constant (droplet lifetime) or, e.g., the concentration field around the vaporizing droplet (visualized with BOS diagnostics) would provide important data for comparison and fitting of numerical models. In addition, experiments with two neighboring droplets can be envisioned to investigate droplet interactions, which is an important next step towards spray combustion models, as explained above.

To conclude, the experiments on H<sub>2</sub>/LOX combustion revealed considerable differences compared with the intensively studied case of hydrocarbons. The transport properties of hydrogen cause a significant increase in the gasification rate constant and thus lead to a very fast combustion process. Not only with regard to rocket engines, but also with regard to future aircraft engines, stationary H<sub>2</sub> gas turbines, or internal combustion engines, fundamental research on hydrogen combustion (in terms of technical applications) is only just beginning to exploit the full potential of hydrogen for future mobility and energy production.

## References

- [1] C. K. Law, *Combustion Physics*, 1st Ed., Cambridge University Press (2006) pp. 2,9-10,15,126,146,195,211-224,552,569,575.
- [2] J. Mukhopadhyaya, D. Rutherford, *Performance Analysis of Evolutionary Hydrogen-Powered Aircraft*, The International Council of Clean Transportation - White Paper (2022).
- [3] P. Lott, U. Wagner, T. Koch, O. Deutschmann, *Der Wasserstoffmotor – Chancen und Herausforderungen auf dem Weg zu einer dekarbonisierten Mobilität* *Chemie Ingenieur Technik* 94, 217-229 (2022).
- [4] A. de Iaco Veris, *Fundamental Concepts of Liquid-Propellant Rocket Engines*, 1st Ed., Springer (2021) pp. 1,14-15,27,31,59,63-67,110-112,166-174,269,276-277.
- [5] Ariane Group, *HM7B Engine - Propulsion Solutions for Launchers*, Technical Data Sheet (2017).
- [6] United Launch Alliance, *Atlas V Launch Services, User's Guide* (2010).
- [7] M. Leonardi, F. Nasuti, M. Onofri, *Basic Analysis of a LOX/Methane Expander Bleed Engine*, 7th European Conference for Aeronautics and Aerospace Sciences EUCASS2017-332 (2017).
- [8] P. Caisso, A. Souchier, C. Rothmund, P. Alliot, C. Bonhomme, W. Zinner, *et al.*, *A liquid propulsion panorama*, *Acta Astronautica* 65, 1723-1737 (2009).
- [9] K. Dresia, S. Jentzsch, G. Waxenegger-Wilfing, R. D. S. Hahn, J. Deeken, M. Oschwald, F. Mota, *Multidisciplinary Design Optimization of Reusable Launch Vehicles for Different Propellants and Objectives*, *Journal of Spacecraft and Rockets* 58, 1017-1029 (2021).
- [10] K. K. Kuo, *Principles of Combustion*, 2nd Ed., John Wiley & Sons (2005) pp. 578, 569,590-591.
- [11] B. J. Hickey, M. Ihme, *Supercritical Mixing and Combustion in Rocket Propulsion*, Center for Turbulence Research, Annual Research Briefs (2013).
- [12] W. Mayer, H. Tamura, *Propellant injection in a liquid oxygen/gaseous hydrogen rocket engine*, *Journal of Propulsion and Power* 12, 1137-1147 (1996).
- [13] A. Lechtenberg, P. M. Gerlinger, *Numerical Investigation of Combustion Instabilities in a Rocket Combustion Chamber with Supercritical Injection Using a Hybrid RANS/LES Method*, AIAA Scitech 2020 Forum, AIAA 2020-1162 (2020).
- [14] N. N. Smirnov, V. B. Betelin, R. M. Shagaliev, V. F. Nikitin, I. M. Belyakov, Y. N. Deryuguin, S. V. Aksenov, D. A. Korchazhkin, *Hydrogen fuel rocket engines simulation using LOGOS code*, *International Journal of Hydrogen Energy* 39, 10748-10756 (2014).
- [15] V. B. Betelin, V. F. Nikitin, D. I. Altukhov, V. R. Dushin, J. Koo, *Supercomputer modeling of hydrogen combustion in rocket engines*, *Acta Astronautica* 89, 46-59 (2013).
- [16] M. Masquelet, S. Menon, Y. Jin, R. Friedrich, *Simulation of unsteady combustion in a LOX-GH2 fueled rocket engine*, *Combustion Science and Technology* 13, 466-474 (2009).

- [17] J. C. Oefelein, V. Yang, Modeling High-Pressure Mixing and Combustion Processes in Liquid Rocket Engines, *Journal of Propulsion and Power* 14, 843-857 (1998).
- [18] A. Yang, Kuo, K.K., Hsieh, W.H., Supercritical Evaporation and Combustion of Liquid Oxygen in an Axisymmetric Configuration, In: K. K. Kuo, *Recent Advances in Spray Combustion: Spray Atomization and Drop Burning Phenomena*, American Institute of Aeronautics and Astronautics, 439-480 (1996).
- [19] S. Kumagai, H. Isoda, Combustion of fuel droplets in a free falling chamber, *Symposium (International) on Combustion* 6, 726-731 (1957).
- [20] V. Nayagam, D. L. Dietrich, M. C. Hicks, F. A. Williams, Cool-flame extinction during n-alkane droplet combustion in microgravity, *Combustion and Flame* 162, 2140-2147 (2015).
- [21] C. Eigenbrod, V. Wagner, W. Paa, Spontaneous ignition of droplet pairs of n-Decane and n-Tetradecane in microgravity, *Proceedings of the Combustion Institute* 38, 3131-3139 (2021).
- [22] C. Eigenbrod, K. Klinkov, M. Peters, G. Marks, W. Paa, V. Wagner, W. Triebel, Formaldehyde LIF-Diagnostics of the Autoignition of n-Decane Droplet Pairs in Microgravity, *Int. J. Microgravity Sci. Appl.* 33 330306-1-8 2016 (2016).
- [23] M. Mikami, H. Kato, J. Sato, M. Kono, Interactive combustion of two droplets in microgravity, *Symposium (International) on Combustion* 25, 431-438 (1994).
- [24] M. Mikami, H. Watari, T. Hirose, T. Seo, H. Saputro, O. Moriue, M. Kikuchi, Flame spread of droplet-cloud elements with two-droplet interaction in microgravity, *Journal of Thermal Science and Technology* 12, JTST0028 (2017).
- [25] M. Mikami, Y. Yoshida, T. Seo, T. Sakashita, M. Kikuchi, T. Suzuki, M. Nokura, Space-Based Microgravity Experiments on Flame Spread over Randomly Distributed n-Decane-Droplet Clouds: Overall Flame-Spread Characteristics, *Microgravity Science and Technology* 30, 535-542 (2018).
- [26] D. B. Spalding, The combustion of liquid fuels, *Symposium (International) on Combustion* 4, 847-864 (1953).
- [27] F. A. Williams, *Combustion Theory*, 2nd Ed., The Benjamin/Cummings Publishing Company (1985) pp. 1,44-46,53-56,62,67-68,543.
- [28] H. D. Baehr, K. Stephan, *Wärme- und Stoffübertragung*, 8th Ed., Springer (2013) pp. 2-11,28-32,270-273,311.
- [29] A. Fick, On liquid diffusion, *The London, Edinburgh, and Dublin Philosophical Magazine and Journal of Science* 10, 30-39 (1855).
- [30] I. Glassman, R. A. Yetter, *Combustion*, 4th Ed., Academic Press (2008) pp. 1,22-23,43,252,333-359.
- [31] F. El-Mahallawy, S. E.-D. Habik, *Fundamentals and Technology of Combustion*, 1st Ed., Elsevier Science (2002) pp. 1,20-21,47-53,77.
- [32] R. B. Bird, W. E. Stewart, E. N. Lightfoot, *Transport Phenomena*, 2nd Ed., John Wiley & Sons (2002) pp. 516,525-528,553,864-866.
- [33] C. K. Law, Recent advances in droplet vaporization and combustion, *Progress in Energy and Combustion Science* 8, 171-201 (1982).
- [34] A. J. Marchese, F. L. Dryer, The effect of liquid mass transport on the combustion and extinction of bicomponent droplets of methanol and water, *Combustion and Flame* 105, 104-122 (1996).

- [35] M. J. Moran, H. N. Shapiro, D. D. Boettner, M. B. Bailey, *Fundamentals of Engineering Thermodynamics*, 8th Ed., Wiley (2014) pp. 99,265.
- [36] R. Schmidt, W. Wagner, A new form of the equation of state for pure substances and its application to oxygen, *Fluid Phase Equilibria* 19, 175-200 (1985).
- [37] National Institute of Standards and Technology (NIST), NIST Chemistry WebBook, SRD 69, <https://webbook.nist.gov/chemistry/fluid/>, October 28, 2021.
- [38] V. Yang, Modeling of supercritical vaporization, mixing, and combustion processes in liquid-fueled propulsion systems, *Proceedings of the Combustion Institute* 28, 925-942 (2000).
- [39] K. W. Ragland, K. M. Bryden, *Combustion Engineering*, 2nd Ed., CRC Press (2011) pp. 2-3,258.
- [40] F. Giese, Experimentelle Untersuchung der Verdampfung von Brennstofftropfen bei transkritischen Bedingungen, Diploma thesis, University of Bremen (2006).
- [41] W. Mayer, B. Ivancic, A. Schik, U. Hornung, Propellant atomization and ignition phenomena in liquid oxygen/gaseous hydrogen rocket combustors, *Journal of Propulsion and Power* 17, 794-799 (2001).
- [42] A. H. Lefebvre, V. G. McDonell, *Atomization and Sprays*, 2nd Ed., CRC Press (2017) pp. 6,8.
- [43] M. Micci, S. Lee, B. Vieille, C. Chauveau, I. Gökalp, Molecular dynamics calculations of near-critical liquid oxygen droplet surface tension, *Atomization and Sprays* 15, 413-422 (2005).
- [44] B. Vieille, Etude Experimentale de l'Atomisation Secondaire de Gouttes d'Oxygene Liquide, PhD thesis, University of Orleans (1998).
- [45] H. D. Baehr, S. Kabelac, *Thermodynamik*, 16th Ed., Springer (2016) pp. 195-197.
- [46] J. G. Chung, Estimation of vapor pressure of liquid oxygen between the triple and critical points, *Korean Journal of Chemical Engineering* 14, 209-212 (1997).
- [47] P. Boivin, C. Jiménez, A. L. Sánchez, F. A. Williams, An explicit reduced mechanism for H<sub>2</sub>-air combustion, *Proceedings of the Combustion Institute* 33, 517-523 (2011).
- [48] M. Ó Conaire, H. J. Curran, J. M. Simmie, W. J. Pitz, C. K. Westbrook, A comprehensive modeling study of hydrogen oxidation, *International Journal of Chemical Kinetics* 36, 603-622 (2004).
- [49] W. Pejpichestakul, E. Ranzi, M. Pelucchi, A. Frassoldati, A. Cuoci, A. Parente, T. Faravelli, Examination of a soot model in premixed laminar flames at fuel-rich conditions, *Proceedings of the Combustion Institute* 37, 1013-1021 (2019).
- [50] E. Ranzi, A. Frassoldati, A. Stagni, M. Pelucchi, A. Cuoci, T. Faravelli, Reduced Kinetic Schemes of Complex Reaction Systems: Fossil and Biomass-Derived Transportation Fuels, *International Journal of Chemical Kinetics* 46, 512-542 (2014).
- [51] E. Ranzi, C. Cavallotti, A. Cuoci, A. Frassoldati, M. Pelucchi, T. Faravelli, New reaction classes in the kinetic modeling of low temperature oxidation of n-alkanes, *Combustion and Flame* 162, 1679-1691 (2015).
- [52] S. Arrhenius, Über die Reaktionsgeschwindigkeit bei der Inversion von Rohrzucker durch Säuren, *Zeitschrift für Physikalische Chemie* 4U, 226-248 (1889).

- [53] K. J. Laidler, A Glossary of Terms Used in Chemical Kinetics - Including Reaction Dynamics, *Pure & App. Chem.* 68, 149-192 (1996).
- [54] B. Wang, W. Wei, S. Ma, G. Wei, Construction of one-step H<sub>2</sub>/O<sub>2</sub> reaction mechanism for predicting ignition and its application in simulation of supersonic combustion, *International Journal of Hydrogen Energy* 41, 19191-19206 (2016).
- [55] J. Daou, P. Haldenwang, C. Nicoli, Supercritical burning of liquid oxygen (LOX) droplet with detailed chemistry, *Combustion and Flame* 101, 153-169 (1995).
- [56] G. A. E. Godsave, Studies of the combustion of drops in a fuel spray - the burning of single drops of fuel, *Symposium (International) on Combustion* 4, 818-830 (1953).
- [57] R. Remsburg, *Advanced Thermal Design of Electronic Equipment*, Springer Science & Business Media (2011) p. 444.
- [58] C. K. Law, S. H. Chung, N. Srinivasan, Gas-phase quasi-steadiness and fuel vapor accumulation effects in droplet burning, *Combustion and Flame* 38, 173-198 (1980).
- [59] S. D. Givler, J. Abraham, Supercritical droplet vaporization and combustion studies, *Progress in Energy and Combustion Science* 22, 1-28 (1996).
- [60] H. Nomura, S. Nakaya, M. Tsue, Microgravity Research on Quasi-Steady and Unsteady Combustion of Fuel Droplet at High Pressures, In: J. Bellan, *High-Pressure Flows for Propulsion Applications*, AIAA, 1-47 (2020) pp. 20-21,39,41.
- [61] J. S. Shuen, V. Yang, C. C. Hsiao, Combustion of liquid-fuel droplets in supercritical conditions, *Combustion and Flame* 89, 299-319 (1992).
- [62] D. R. Kassoy, F. A. Williams, Variable property effects on liquid droplet combustion, *AIAA Journal* 6, 1961-1965 (1968).
- [63] A. H. Lefebvre, D. R. Ballal, *Gas Turbine Combustion*, 3rd Ed., CRC Press (2010) pp. 60,208-209,230.
- [64] J. Kuneš, *Dimensionless Physical Quantities in Science and Engineering*, 1st Ed., Elsevier (2012) pp. 69-70,81-82,175.
- [65] O. Moriue, S. Schnaubelt, C. Eigenbrod, H. J. Rath, Numerical Simulation of the Ignition of a Single Fuel Droplet in an Air with Finite Volume, *Proceedings of 9th International Conference on Liquid Atomization and Spray Systems*, 0701 (2003).
- [66] B. Topaloglu, *Theoretische und experimentelle Modellierung der Gas-Tröpfen-Strömung in Vormisch/Vorverdunstungszonen von Gasturbinenbrennern*, PhD thesis, Ruhr University of Bochum (1989).
- [67] A. Leipertz, S. Pfadler, R. Schießl, An Overview of Combustion Diagnostics, In: M. Lackner, F. Winter, and A. K. Agarwal, *Handbook of Combustion, Vol. 5: Combustion Diagnostics and Pollutants*, Wiley-VCH, 1-50 (2010) pp. 1-5,11,14-35.
- [68] W. Merzkirch, Y. Egami, Density-Based Techniques, In: C. Tropea, A. L. Yarin, and J. F. Foss, *Springer Handbook of Experimental Fluid Mechanics*, Springer Berlin Heidelberg, 473-486 (2007).
- [69] G. S. Settles, *Schlieren and Shadowgraph Techniques: Visualizing Phenomena in Transparent Media*, 1st Ed., Springer Berlin Heidelberg (2001) pp. 29-30.
- [70] M. Lackner, Á. B. Palotás, F. Winter, *Combustion - From Basic to Applications*, 1st Ed., Wiley-VCH (2013) pp. 149-150.

- [71] T. Fiala, Radiation from High Pressure Hydrogen-Oxygen Flames and its Use in Assessing Rocket Combustion Instability, PhD thesis, Technical University of Munich (2015) pp. 15-22,70-71.
- [72] E. Petersen, D. Kalitan, M. Rickard, Calibration and Chemical Kinetics Modeling of an OH Chemiluminescence Diagnostic, 39th AIAA/ASME/SAE/ASEE Joint Propulsion Conference and Exhibit, AIAA 2003-4493 (2003).
- [73] S. A. Ciatti, Light Emission from Flames, In: M. Lackner, F. Winter, and A. K. Agarwal, Handbook of Combustion, Vol. 1: Fundamentals and Safety, Wiley-VCH, 251-264 (2010).
- [74] S. A. Ciatti, B. Bihari, T. Wallner, Establishing combustion temperature in a hydrogen-fuelled engine using spectroscopic measurements, Proceedings of the Institution of Mechanical Engineers, Part D: Journal of Automobile Engineering 221, 6, 699-712 (2007).
- [75] G. E. A. Meier, Hintergrund-Schlierenmessverfahren, German patent, DE19942856A1 (1999).
- [76] M. Raffel, Background-Oriented Schlieren (BOS) Techniques, Experiments in Fluids 56, 60 (2015).
- [77] A. Williams, Combustion of Liquid Fuel Sprays, Butterworth-Heinemann (1990) p. 75.
- [78] A. Yang, W. Hsieh, K. Kuo, J. Brown, Evaporation of LOX under supercritical and subcritical conditions, 29th Joint Propulsion Conference, AIAA 93-2188 (1993).
- [79] X. Chesneau, C. Chauveau, I. Gökalp, Experiments on High Pressure Vaporization of Liquid Oxygen Droplets, 32nd Aerospace Sciences Meeting & Exhibit, AIAA 94-0688 (1994).
- [80] J. Sato, Studies on droplet evaporation and combustion in high pressures, 31st Aerospace Sciences Meeting & Exhibit, AIAA 93-0813 (1993).
- [81] H. Nomura, Y. Ujiie, H. J. Rath, J. i. Sato, M. Kono, Experimental study on high-pressure droplet evaporation using microgravity conditions, Symposium (International) on Combustion 26, 1267-1273 (1996).
- [82] H. Nomura, T. Murakoshi, Y. Suganuma, Y. Ujiie, N. Hashimoto, H. Nishida, Microgravity experiments of fuel droplet evaporation in sub- and supercritical environments, Proceedings of the Combustion Institute 36, 2425-2432 (2017).
- [83] J. P. Delplanque, W. A. Sirignano, Numerical study of the transient vaporization of an oxygen droplet at sub- and super-critical conditions, International Journal of Heat and Mass Transfer 36, 303-314 (1993).
- [84] M. Oswald, J. J. Smith, R. Branam, J. Hussong, A. Schik, B. Chehroudi, D. Talley, Injection of Fluids into Supercritical Environments, Combustion Science and Technology 178, 49-100 (2006).
- [85] K. Harstad, Bellan, J., Isolated fluid oxygen drop behavior in fluid hydrogen at rocket chamber pressures, International Journal of Heat and Mass Transfer 41, 3537-3550 (1998).
- [86] C. Nicoli, Haldenwang, P., Daou, J., Substitute mixtures for LOX droplet vaporization study, Combustion Science and Technology 112, 55-74 (1996).
- [87] P. Haldenwang, C. Nicoli, J. Daou, High pressure vaporization of LOX droplet crossing the critical conditions, International Journal of Heat and Mass Transfer 39, 3453-3464 (1996).

- [88] V. Yang, N. Nienchuan, S. Jian-Shun, Vaporization of Liquid Oxygen (LOX) Droplets in Supercritical Hydrogen Environments, *Combustion Science and Technology* 97, 247-270 (1994).
- [89] P. Lafon, M. Habiballah, Numerical analysis of droplet vaporization and burning under high-pressure conditions, 30th Joint Propulsion Conference, AIAA 94-2909 (1994).
- [90] P. Lafon, H. Meng, V. Yang, M. Habiballah, Vaporization of Liquid Oxygen (LOX) Droplets in Hydrogen and Water Environments under Sub- and Super-Critical Conditions, *Combustion Science and Technology* 180, 1-26 (2008).
- [91] R. Litchford, S.-M. Jeng, LOX vaporization in high-pressure, hydrogen-rich gas, 26th Joint Propulsion Conference, AIAA 90-2191 (1990).
- [92] J.-P. Delplanque, W. Sirignano, Oscillatory and transcritical vaporization of an oxygen droplet, 30th Aerospace Sciences Meeting and Exhibit, AIAA 1992-104 (1992).
- [93] H. Meng, G. C. Hsiao, V. Yang, J. S. Shuen, Transport and dynamics of liquid oxygen droplets in supercritical hydrogen streams, *Journal of Fluid Mechanics* 527, 115-139 (2005).
- [94] H. Meng, V. Yang, Vaporization of two liquid oxygen (LOX) droplets in tandem in convective hydrogen streams at supercritical pressures, *International Journal of Heat and Mass Transfer* 68, 500-508 (2014).
- [95] P. Lafon, H. Meng, V. Yang, M. Habiballah, Pressure-Coupled Responses of LOX Droplet Vaporization and Combustion in High-Pressure Hydrogen Environments, *Combustion Science and Technology* 186, 1191-1208 (2014).
- [96] B. Vieille, C. Chauveau, X. Chesneau, A. Odeïde, I. Gökalp, High-pressure droplet burning experiments in microgravity, *Symposium (International) on Combustion* 26, 1259-1265 (1996).
- [97] S. Kumagai, H. Isoda, Combustion of Fuel Droplets, *Nature* 166, 1111-1111 (1950).
- [98] G. M. Faeth, D. P. Dominicus, J. F. Tulpinsky, D. R. Olson, Supercritical bipropellant droplet combustion, *Symposium (International) on Combustion* 12, 9-18 (1969).
- [99] A. R. Hall, J. Diederichsen, An Experimental Study of the Burning of Single Drops of Fuel in Air at Pressures up to Twenty Atmospheres, *Symposium (International) on Combustion* 4, 837-846 (1953).
- [100] J. Bellan, Supercritical (and subcritical) fluid behavior and modeling: drops, streams, shear and mixing layers, jets and sprays, *Progress in Energy and Combustion Science* 26, 329-366 (2000).
- [101] J. Sato, M. Tsue, M. Niwa, M. Kono, Effects of natural convection on high-pressure droplet combustion, *Combustion and Flame* 82, 142-150 (1990).
- [102] C. Chauveau, X. Chesneau, I. Gökalp, High pressure vaporization and burning of methanol droplets in reduced gravity, *Advances in Space Research* 16, 157-160 (1995).
- [103] D. L. Dietrich, P. M. Struk, M. Ikegami, G. Xu, Single droplet combustion of decane in microgravity: experiments and numerical modelling, *Combustion Theory and Modelling* 9, 569-585 (2005).

- [104] D. L. Dietrich, V. Nayagam, M. C. Hicks, P. V. Ferkul, F. L. Dryer, T. Farouk, *et al.*, Droplet Combustion Experiments Aboard the International Space Station, *Microgravity Science and Technology* 26, 65-76 (2014).
- [105] M. Mikami, M. Kono, J. i. Sato, D. L. Dietrich, Interactive effects in two-droplet combustion of miscible binary fuels at high pressure, *Symposium (International) on Combustion* 27, 2643-2649 (1998).
- [106] K. Okai, O. Moriue, M. Araki, M. Tsue, M. Kono, J. Sato, D. L. Dietrich, F. A. Williams, Pressure effects on combustion of methanol and methanol/dodecanol single droplets and droplet pairs in microgravity, *Combustion and Flame* 121, 501-512 (2000).
- [107] H. Li, S. Pokhrel, M. Schowalter, A. Rosenauer, J. Kiefer, L. Mädler, The gas-phase formation of tin dioxide nanoparticles in single droplet combustion and flame spray pyrolysis, *Combustion and Flame* 215, 389-400 (2020).
- [108] H. Li, N. Riefler, T. Wriedt, L. Mädler, Reference data set for three-dimensional measurements of double droplet combustion of p-xylene, *Proceedings of the Combustion Institute* 38, 3151-3158 (2021).
- [109] H. Li, C. D. Rosebrock, Y. Wu, T. Wriedt, L. Mädler, Single droplet combustion of precursor/solvent solutions for nanoparticle production: Optical diagnostics on single isolated burning droplets with micro-explosions, *Proceedings of the Combustion Institute* 37, 1203-1211 (2019).
- [110] N. Fdida, Y. Mauriot, L. Vingert, A. Ristori, M. Théron, Characterizing primary atomization of cryogenic LOX/Nitrogen and LOX/Helium sprays by visualizations coupled to Phase Doppler Interferometry, *Acta Astronautica* 164, 458-465 (2019).
- [111] W. Mayer, Schik, A., Schaffler, M., Tamura, H., Injection and mixing processes in high-pressure liquid oxygen/gaseous hydrogen rocket combustors, *Journal of Propulsion and Power* 16, 823-828 (2000).
- [112] D. N. Klimenko, W. Clauss, M. Oswald, J. Smith, W. Mayer, CARS temperature mapping in a cryogenic LOX-H<sub>2</sub> rocket combustion chamber under supercritical conditions, *Journal of Raman Spectroscopy* 33, 900-905 (2002).
- [113] J. J. Smith, High Pressure LOx/H<sub>2</sub> Rocket Engine Combustion, PhD thesis, University of Adelaide (2007).
- [114] J. J. Smith, G. Schneider, D. Suslov, M. Oswald, O. Haidn, Steady-state high pressure LOx/H<sub>2</sub> rocket engine combustion, *Aerospace Science and Technology* 11, 39-47 (2007).
- [115] B. Yang, F. Cuoco, M. Oswald, Atomization and Flames in LOX/H<sub>2</sub>- and LOx/CH<sub>4</sub>- Spray Combustion, *Journal of Propulsion and Power* 23, 763-771 (2007).
- [116] A.-S. Yang, K. K. Kuo, W. H. Hsieh, Supercritical and subcritical combustion of lox with hydrogen in an axisymmetric laminar diffusion flame, *Symposium (International) on Combustion* 25, 1609-1618 (1994).
- [117] F. Meyer, C. Eigenbrod, J. C. Hermanson, J. Frydman, W. Paa, V. Wagner, Microgravity Experiments and Numerical Simulations on the Combustion of Single Oxygen Droplets in Hydrogen, 69th International Astronautical Congress (IAC), IAC-18-A2.2.7 (2018).

- [118] F. Meyer, C. Eigenbrod, V. Wagner, W. Paa, J. D. Hall, M. Zody, J. Frydman, J. C. Hermanson, Combustion of Single Oxygen Droplets in Hydrogen under Microgravity Conditions, AIAA SciTech 2021 Forum, AIAA 2021-0548 (2021).
- [119] Y. Aouina, U. Maas, E. Gutheil, U. Riedel, J. Warnatz, Mathematical Modeling of Droplet Heating, Vaporization, and Ignition Including Detailed Chemistry, *Combustion Science and Technology* 173, 1-23 (2001).
- [120] H. J. Kim, C. H. Sohn, S. H. Chung, J. S. Kim, Nonlinear acoustic-pressure responses of oxygen droplet flames burning in gaseous hydrogen, *KSME International Journal* 15, 510-521 (2001).
- [121] G. S. Canada, G. M. Faeth, Fuel Droplet Burning Rates at High Pressures, Symposium (International) on Combustion 14, 1345-1354 (1973).
- [122] O. Moriue, M. Mikami, N. Kojima, C. Eigenbrod, Numerical simulations of the ignition of n-heptane droplets in the transition diameter range from heterogeneous to homogeneous ignition, *Proceedings of the Combustion Institute* 30, 1973-1980 (2005).
- [123] M. Tanabe, M. Kono, J. Sato, J. Koenig, C. Eigenbrod, F. Dinkelacker, H. J. Rath Zarm, Two Stage Ignition of n-Heptane Isolated Droplets, *Combustion Science and Technology* 108, 103-119 (1995).
- [124] K. Klinkov, Eigenbrod, Ch., Giese, F., Rickmers, P., Reimert, M., Simulation of Spray Autoignition Introducing "Spraylets", *IGTI Turbo-Expo, Power for Land, Sea and Air*, (2012).
- [125] A. E. Saufi, A. Frassoldati, T. Faravelli, A. Cuoci, Interface-resolved simulation of the evaporation and combustion of a fuel droplet suspended in normal gravity, *Fuel* 287, 119413 (2021).
- [126] H. Sato, K. Watanabe, J. M. H. L. Sengers, J. S. Gallagher, P. G. Hill, J. Straub, W. Wagner, Sixteen Thousand Evaluated Experimental Thermodynamic Property Data for Water and Steam, *Journal of Physical and Chemical Reference Data* 20, 1023-1044 (1991).
- [127] E. A. Powell, Simulation of water vapor condensation on LOX droplet surface using liquid nitrogen, *NASA Technical Report* (1988).
- [128] G. S. Jackson, C. T. Avedisian, J. C. Yang, Observations of soot during droplet combustion at low gravity: heptane and heptane/monochloroalkane mixtures, *International Journal of Heat and Mass Transfer* 35, 2017-2033 (1992).
- [129] B. Knight, F. A. Williams, Observations on the burning of droplets in the absence of buoyancy, *Combustion and Flame* 38, 111-119 (1980).
- [130] C. Presser, C. Avedisian, A. Gupta, H. Semerjian, Combustion of methanol and methanol/dodecanol spray flames, *Journal of Propulsion and Power* 8, 553-559 (1992).
- [131] M. Mikami, O. Habara, M. Kono, J. Sato, D. L. Dietrich, F. A. Williams, Pressure Effects in Droplet Combustion of Miscible Binary Fuels, *Combustion Science and Technology* 124, 295-309 (1997).
- [132] H. Ulmke, T. Wriedt, K. Bauckhage, Piezoelectric droplet generator for the calibration of particle-sizing instruments, *Chemical Engineering and Technology* 24, 265-268 (2001).
- [133] C. Chauveau, M. Birouk, I. Gökalp, An analysis of the d2-law departure during droplet evaporation in microgravity, *International Journal of Multiphase Flow* 37, 252-259 (2011).

- [134] Y. C. Liu, Y. Xu, M. C. Hicks, C. T. Avedisian, Comprehensive study of initial diameter effects and other observations on convection-free droplet combustion in the standard atmosphere for n -heptane, n -octane, and n -decane, *Combustion and Flame* 171, 27-41 (2016).
- [135] A. J. Marchese, F. L. Dryer, R. O. Colantonio, V. Nayagam, Microgravity combustion of methanol and methanol/water droplets: Drop tower experiments and model predictions, *Symposium (International) on Combustion* 26, 1209-1217 (1996).
- [136] G. S. Jackson, C. T. Avedisian, Combustion of unsupported water-in-n-heptane emulsion droplets in a convection-free environment, *International Journal of Heat and Mass Transfer* 41, 2503-2515 (1998).
- [137] J. W. Bennewitz, A. Badakhshan, D. G. Talley, Systematic Measurement of Hydrocarbon Fuel Droplet Burning Rate Constants and Ignition Delays, *AIAA Aerospace Sciences Meeting, AIAA 2018-0672* (2018).
- [138] N. Ghata, B. D. Shaw, Computational modeling of the effects of support fibers on evaporation of fiber-supported droplets in reduced gravity, *8th US National Combustion Meeting, 070HE-0020* (2013).
- [139] Army Ballistic Research Lab Aberdeen Proving Ground, *Combustion Studies of Acoustically Suspended Liquid Droplets, Contract Report BRL-CR-594 AD-A193 892* (1988).
- [140] G. A. Ruff, S. Liu, I. Ciobanescu, *Droplet Vaporization in a Levitating Acoustic Field, NASA/CP 2003-212376/REV1* (2003).
- [141] Y. Wei, Y. Yang, J. Zhang, S. Deng, S. Liu, C. K. Law, A. Saha, Atomization of acoustically levitated droplet exposed to hot gases, *Applied Physics Letters* 116, 044101 (2020).
- [142] T. X. Phuoc, Laser Ignition, In: M. Lackner, F. Winter, and A. K. Agarwal, *Handbook of Combustion, Vol. 5: New Technologies, Wiley-VCH*, 95-123 (2010) pp. 95-96, 111-112.
- [143] T. I. Farouk, Y. C. Liu, A. J. Savas, C. T. Avedisian, F. L. Dryer, Sub-millimeter sized methyl butanoate droplet combustion: Microgravity experiments and detailed numerical modeling, *Proceedings of the Combustion Institute* 34, 1609-1616 (2013).
- [144] G. B. Yates, A. R. Perl, J. F. Loos, R. J. Sergeant, Spark Ignition Parameters of Cryogenic Hydrogen in Oxygen and Nitrogen Mixtures, *Advances in Cryogenic Engineering* 265-272 (1965).
- [145] V. Schröder, B. Emonts, H. Janßen, H.-P. Schulze, Explosionsgrenzen von Wasserstoff/Sauerstoff-Gemischen bei Drücken bis 200 bar, *Chemie Ingenieur Technik* 75, 914-918 (2003).
- [146] D. K. Srivastava, M. Weinrotter, K. Iskra, A. K. Agarwal, E. Wintner, Characterisation of laser ignition in hydrogen-air mixtures in a combustion bomb, *International Journal of Hydrogen Energy* 34, 2475-2482 (2009).
- [147] O. Gurliat, V. Schmidt, O. J. Haidn, M. Oschwald, Ignition of cryogenic H<sub>2</sub>/LOX sprays, *Aerospace Science and Technology* 7, 517-531 (2003).
- [148] M. De Rosa, Sender, J., Zimmermann, H., Oschwald, M., *Cryogenic Spray Ignition at High Altitude Conditions, 42nd AIAA/ASME/SAE/ASEE Joint Propulsion Conference & Exhibit, (2006).*

- [149] S. Soller, R. Behr, A. Preuss, W. Schwarz, Identification and Maturation of Technologies for Future Liquid Propellant Engines, 69th International Astronautical Congress (IAC), IAC-18-C4.10.11 (2018).
- [150] C. Schulz, A. Dreizler, V. Ebert, J. Wolfrum, Combustion Diagnostics, In: C. Tropea, A. L. Yarin, and J. F. Foss, Springer Handbook of Experimental Fluid Mechanics, Springer Berlin Heidelberg, 1241-1315 (2007) pp. 1243-1244,1262-1263.
- [151] K. Kobayasi, An experimental study on the combustion of a fuel droplet, Symposium (International) on Combustion 5, 141-148 (1955).
- [152] M. Tanabe, T. Kuwahara, K. Satoh, T. Fujimori, J. i. Sato, M. Kono, Droplet combustion in standing sound waves, Proceedings of the Combustion Institute 30, 1957-1964 (2005).
- [153] A. M.-D. Faik, Quantitative Investigation of the Multicomponent Fuel Droplet Combustion Using High Speed Imaging and Digital Image Processing, PhD thesis, University of Sheffield (2017) pp. 53,55,61,79-80,91-93,125-126.
- [154] Y. Ogami, S. Sakurai, S. Hasegawa, M. Jangi, H. Nakamura, K. Yoshinaga, H. Kobayashi, Microgravity experiments of single droplet combustion in oscillatory flow at elevated pressure, Proceedings of the Combustion Institute 32, 2171-2178 (2009).
- [155] G. Kirchhoff, R. Bunsen, Chemische Analyse durch Spektralbeobachtungen, Annalen der Physik und Chemie 110, 161-189 (1860).
- [156] J. Diederichsen, H. G. Wolfhard, A. C. Egerton, Spectrographic examination of gaseous flames at high pressure, Proceedings of the Royal Society of London. Series A. Mathematical and Physical Sciences 236, 89-103 (1956).
- [157] G. D. Liveing, J. Dewar, On the Influence of Pressure on the Spectra of Flames, Proceedings of the Royal Society of London 49, 217-225 (1891).
- [158] E. Petersen, M. Kopp, N. Donato, F. Güthe, Assessment of Current Chemiluminescence Kinetics Models at Engine Conditions, Journal of Engineering for Gas Turbines and Power 134, (2012).
- [159] B. Higgins, M. Q. McQuay, F. Lacas, J. C. Rolon, N. Darabiha, S. Candel, Systematic measurements of OH chemiluminescence for fuel-lean, high-pressure, premixed, laminar flames, Fuel 80, 67-74 (2001).
- [160] D. Klimenko, J. Smith, D. Suslov, Flame-Emission Spectroscopy at High Pressure Combustion in Combustor C, Technical Report DLR-LA-OD-RP003, DLR Lampoldshausen, (2004).
- [161] A. J. Marchese, F. L. Dryer, V. Nayagam, R. O. Colantonio, Hydroxyl radical chemiluminescence imaging and the structure of microgravity droplet flames, Symposium (International) on Combustion 26, 1219-1226 (1996).
- [162] S. Werner, W. Meier, Measurement of evaporation of hydrocarbon droplets by laser absorption spectroscopy, Applied Physics B 126, 13 (2019).
- [163] I. Düwel, J. Schorr, J. Wolfrum, C. Schulz, Laser-induced fluorescence of tracers dissolved in evaporating droplets, Applied Physics B 78, 127-131 (2004).
- [164] M. Koegl, K. Baderschneider, F. J. Bauer, B. Hofbeck, E. Berrocal, S. Will, L. Zigan, Analysis of the LIF/Mie Ratio from Individual Droplets for Planar Droplet Sizing: Application to Gasoline Fuels and Their Mixtures with Ethanol, Applied Sciences 9, 4900 (2019).

- [165] C. S. Connon, R. Dimalanta, C. Cho, M. D. Dunn-Rankin, LIF Measurements of Fuel Vapor in an Acetone Droplet Stream, *Combustion Science and Technology* 129, 197-216 (1997).
- [166] H. Renken, T. Bolik, C. Eigenbrod, J. Koenig, H. Rath, Digital high-speed camera system for combustion research using UV-laser diagnostic under microgravity at Bremen drop tower, *Electronic Imaging '97*, 3018 (1997).
- [167] K. Matsumoto, T. Fujii, K. Suzuki, D. Segawa, T. Kadota, Laser-induced fluorescence for the non-intrusive diagnostics of a fuel droplet burning under microgravity in a drop shaft, *Measurement Science and Technology* 10, 853-858 (1999).
- [168] V. Wagner, W. Paa, W. Triebel, C. Eigenbrod, K. Klinkov, M. Larionov, A. Giesen, C. Stolzenburg, Diode pumped solid state kilohertz disk laser system for time-resolved combustion diagnostics under microgravity at the drop tower Bremen, *Review of Scientific Instruments* 85, 033106 (2014).
- [169] A. Vincent-Randonnier, Combustion Enhancement and Stabilization: Principles of Plasma Assistance and Diagnostics Tools, In: M. Lackner, F. Winter, and A. K. Agarwal, *Handbook of Combustion, Vol. 5: New Technologies*, Wiley-VCH, 125-160 (2010) pp. 129-130.
- [170] W. D. Bachalo, Methods for Compressible Flows, In: A. J. Smits, *Flow Visualization: Techniques and Examples*, Imperial College Press, 227-265 (2012) p. 249.
- [171] M. Tanabe, T. Bolik, C. Eigenbrod, H. J. Rath, J. Sato, M. Kono, Spontaneous ignition of liquid droplets from a view of non-homogeneous mixture formation and transient chemical reactions, *Symposium (International) on Combustion* 26, 1637-1643 (1996).
- [172] O. Moriue, C. Eigenbrod, H. J. Rath, J. Sato, K. Okai, M. Tsue, M. Kono, Effects of dilution by aromatic hydrocarbons on staged ignition behavior of n-decane droplets, *Proceedings of the Combustion Institute* 28, 969-975 (2000).
- [173] W. P. Acker, A. Serpengüzel, R. K. Chang, S. C. Hill, Stimulated raman scattering of fuel droplets, *Applied Physics B* 51, 9-16 (1990).
- [174] L. Rousseau, C. Lempereur, M. Orain, O. Rouzaud, O. Simonin, Droplet spatial distribution in a spray under evaporating and reacting conditions, *Experiments in Fluids* 62, 26 (2021).
- [175] S. Aßmann, B. Münsterjohann, F. J. T. Huber, S. Will, Droplet sizing in spray flame synthesis using wide-angle light scattering (WALS), *Applied Physics B* 126, 92 (2020).
- [176] ZARM FAB mbH, Bremen Drop Tower Payload User's Guide, Version 1.1 (2022) pp. 16-18,27.
- [177] F. Meyer, C. Eigenbrod, V. Wagner, W. Paa, J. C. Hermanson, Apparatus to investigate liquid oxygen droplet combustion in hydrogen under microgravity conditions, *Review of Scientific Instruments* 91, 105110 (2020).
- [178] F. Meyer, C. Eigenbrod, V. Wagner, W. Paa, J. D. Hall, M. Zody, J. Frydman, J. C. Hermanson, Combustion of Single Liquid Oxygen Droplet in Hydrogen under Microgravity Conditions, *The 31st International Symposium on Transport Phenomena*, Virtual Event (2020).

- [179] F. Meyer, C. Eigenbrod, V. Wagner, W. Paa, J. C. Hermanson, S. Ando, M. Avila, Oxygen droplet combustion in hydrogen under microgravity conditions, *Combustion and Flame* 241, 112081 (2022).
- [180] F. Meyer, C. Eigenbrod, W. Paa, V. Wager, J. C. Hermanson, HYDRA - Untersuchung der Verbrennung einzelner LOX-Tropfen in einer Wasserstoffumgebung unter Mikrogravitationsbedingungen - Final Report, University of Bremen, BMWi 50 WM 1645 (2020).
- [181] 3M, Novec™ 7000 Engineered Fluid, Technical Data Sheet (2021).
- [182] 3M, Novec™ 7500 Engineered Fluid, Technical Data Sheet (2021).
- [183] Goodfellow GmbH, Material Properties for Quartz - Fused, <https://www.goodfellow.com/de/de/displayitemdetails/p/si61-tb-000141/quartz-fused-tube>, May 04, 2022.
- [184] Quantel Laser, Viron - Ultra compact pulsed diode pumped Nd:YAG laser, Technical Data Sheet (2016).
- [185] Quantel Laser, Viron - Ultra compact pulsed diode pumped Nd:YAG laser, Technical Data Sheet (2021).
- [186] F. Meyer, C. Eigenbrod, V. Wagner, W. Paa, J. C. Hermanson, HYDRA - Interim Report 2017, unpublished (2018).
- [187] A. Couairon, A. Mysyrowicz, Femtosecond filamentation in transparent media, *Physics Reports* 441, 47-189 (2007).
- [188] F. Meyer, C. Eigenbrod, V. Wagner, W. Paa, J. C. Hermanson, HYDRA II - Interim Report 2020, unpublished (2021).
- [189] Q. Composers, The Sapphire Plus - Dugutal Delay Pulse Generator, Technical Data Sheet, 1.1 (2016).
- [190] Schott, UG11, <https://www.schott.com/shop/advanced-optics/en/Matt-Filter-Plates/UG11/c/glass-UG11>, June 28, 2022.
- [191] P. V. C. Hough, Method And Means For Recognizing Complex Patterns, United States Patent Office, 3069654 (1962).
- [192] N. Otsu, A Threshold Selection Method from Gray-Level Histograms, *IEEE Transactions on Systems, Man, and Cybernetics* 9, 62-66 (1979).
- [193] H. Schade, E. Kunz, F. Kameier, *Strömungslehre*, 3rd Ed., de Gruyter (2007) p. 164.
- [194] I. H. Bell, J. Wronski, S. Quoilin, V. Lemort, Pure and Pseudo-pure Fluid Thermophysical Property Evaluation and the Open-Source Thermophysical Property Library CoolProp, *Industrial & Engineering Chemistry Research* 53, 2498-2508 (2014).
- [195] Centre Européen de Recherche et de Formation Avancée en Calcul Scientifique (CERFACS), Adiabatic Flame Temperature Calculator, <https://elearning.cerfacs.fr/combustion/tools/adiabaticflametemperature/index.php>, April 07, 2022.
- [196] Gregory P. Smith, David M. Golden, Michael Frenklach, Nigel W. Moriarty, Boris Eiteneer, Mikhail Goldenberg, C. Thomas Bowman, Ronald K. Hanson, Soonho Song, William C. Gardiner, Jr., Vitali V. Lissianski, and Zhiwei Q, University of California, Berkeley, GRI-MECH 3.0, <http://combustion.berkeley.edu/gri-mech/version30/text30.html>, April 07, 2022.

- 
- [197] T. Poinso, D. Veynante, Theoretical and Numerical Combustion, 2nd Ed., R.T. Edwards (2005).
- [198] N. Kleemann, Auslegung einer Schlierenfotografie zur Verdampfungsuntersuchung eines Tropfens, B.Sc. thesis, University of Bremen (2020).
- [199] G. Meier, Computerized background-oriented schlieren, Experiments in Fluids 33, 181-187 (2002).
- [200] Hough transform for circles, <https://www.mathworks.com/matlabcentral/fileexchange/26978-hough-transform-for-circles>, June 26, 2019.
- [201] ANSYS Inc., Ansys Fluent Theory Guide, ANSYS Inc. (2021) p. 222.

## List of figures

<b>Figure 1:</b>	Schematic of the subcritical injection process. Reprinted from [12] with permission from the American Institute of Aeronautics and Astronautics (AIAA).....	3
<b>Figure 2:</b>	Pressure-temperature phase diagram for oxygen. Data from [36] via NIST Chemistry WebBook [37]. .....	10
<b>Figure 3:</b>	Density-temperature diagram calculated with a modified Benedict-Webb-Rubin equation for oxygen at three different reduced pressures <i>pr</i> . Adapted from [38].....	11
<b>Figure 4:</b>	Pressure-temperature diagram for the phase behavior of the hydrogen-oxygen system in equilibrium. Adapted from [38]. .....	12
<b>Figure 5:</b>	a. Measured values of surface tension as a function of pressure for a LOX droplet in a gaseous oxygen environment at saturation temperature. Adapted from [43] based on [44]. b. Computed values of surface tension as a function of temperature for a LOX droplet in hydrogen. Adapted from [41].....	12
<b>Figure 6:</b>	Vapor pressure of oxygen as a function of temperature at 0.1 MPa. Data based on [46].....	13
<b>Figure 7:</b>	Schematic representation of spherically-symmetric oxygen droplet vaporization (divided into evaporation and boiling), where $pO_2$ is the partial pressure of oxygen, $pvap$ is the vapor pressure, $Ts$ is the surface temperature, and $Tb$ is the boiling temperature. Adapted from [33] and modified. ....	14
<b>Figure 8:</b>	Simplified qualitative profiles of the mass and heat transport processes during vaporization of a LOX droplet in hydrogen at subcritical ambient pressure. a. Temperature. b. Mole fraction. c. Stefan flow velocity. ....	16
<b>Figure 9:</b>	Schematic representation of spherically-symmetric oxygen droplet combustion. Adapted from [33].....	20
<b>Figure 10:</b>	Simplified qualitative profiles of the mass and heat transport processes during combustion of a LOX droplet in hydrogen at subcritical ambient pressure. I. Inside flame shell: a. Temperature. b. Mole fraction. c. Stefan flow velocity. II. Outside flame shell: d. Temperature. e. Mole fraction. f. Stefan flow velocity. Adapted from [27, 55].....	21
<b>Figure 11:</b>	Droplet regression during combustion according to the $d^2$ -law. a. Dimension-based diameter. b. Dimensionless diameter. Adapted from [10]. ....	24
<b>Figure 12:</b>	Schematic setup of the direct shadowgraph imaging technique. The density inhomogeneity causes a refraction of light with an	

	angle $\varepsilon$ , which leads to a displacement on the image plane from its original position by distance $\Delta y$ . The image plane is located at a distance of $l$ from the test region. Adapted from [68, 69].	30
<b>Figure 13:</b>	Spectral profile of hydrogen-air combustion in a car engine. Data adapted from [74] and filtered.	32
<b>Figure 14:</b>	Schematic BOS setup. The density inhomogeneity causes a refraction of light with an angle $\varepsilon$ , which leads to a displacement on the camera sensor from its original position by distance $\Delta y$ . The background pattern is located at a distance of $lBG$ and the camera lens at a distance of $lL$ from the density inhomogeneity, respectively. Adapted from [76] and modified.	33
<b>Figure 15:</b>	Effect of reduced ambient pressure on the vaporization rate of LOX in helium at 290 K with a purge flow velocity of 0.2 cm/s. Adapted from [78].	35
<b>Figure 16:</b>	Variation of the average vaporization rate constant of LOX droplets with pressure in helium at 300 K. Adapted from [79].	35
<b>Figure 17:</b>	Droplet regression of vaporizing n-heptane droplets at 2 MPa and 445 K under $\mu g$ and 1g. Adapted from [80].	36
<b>Figure 18:</b>	Effects of the ambient temperature on the vaporization rate constant of n-heptane droplets at 1 MPa under $\mu g$ and 1g. Adapted from [80].	37
<b>Figure 19:</b>	Effects of the ambient pressure on the vaporization rate constant of n-heptane droplets at different ambient temperatures under 1g. Adapted from [80].	37
<b>Figure 20:</b>	Comparison of different numerical studies on the effect of the ambient pressure on the vaporization rate constant of LOX droplets with a diameter of 1 mm at different ambient temperatures from 300 K to 2500 K. In the supercritical regime, the droplet surface is defined at position of the critical mixture composition. Adapted from Nicoli <i>et al.</i> [86] and Haldenwang <i>et al.</i> [87]. Vaporization rate constant calculated from droplet lifetimes based on Equation (41).	40
<b>Figure 21:</b>	Numerical results showing the effect of pressure and temperature on the enthalpy of vaporization of oxygen in an equilibrium mixture of oxygen and hydrogen. Adapted from [88].	41
<b>Figure 22:</b>	Numerical results on the effect of the ambient pressure on the vaporization rate constant of LOX droplets with a diameter of 100 $\mu m$ at different ambient temperatures. Vaporization rate constant calculated from droplet lifetimes based on Equation (41). Adapted from [89].	41
<b>Figure 23:</b>	Experimental results on the effect of the ambient pressure on the burning rate constant of n-decane droplets with a diameter of	

	875 $\mu\text{m}$ in air at room temperature under $\mu\text{g}$ . Combustion rate constant calculated from combustion lifetimes based on Equation (41). Adapted from Hall & Diederichsen [99] and Faeth <i>et al.</i> [98].	43
<b>Figure 24:</b>	Experimental results on the effect of the ambient pressure on the burning rate constant of n-octane droplets with a diameter between 0.6 to 1.0 mm in air under $\mu\text{g}$ . Adapted from [101].	44
<b>Figure 25:</b>	Comparison of the ambient pressure effects on the total time of combustion/gasification (a.) and on the burning/gasification rate constant (b.) of n-heptane droplets with a diameter of 0.8 mm in 13 % oxygen under $\mu\text{g}$ . Adapted from [80].	46
<b>Figure 26:</b>	Numerical results on the effect of the ambient pressure on the gasification rate constant of burning LOX droplets with a diameter of 100 $\mu\text{m}$ at different ambient temperatures. Gasification rate constant calculated from droplet lifetimes based on Equation (41). Adapted from [89].	48
<b>Figure 27:</b>	Numerical results on the effect of the ambient pressure on different time scales for the combustion of a n-pentane droplet with a diameter of 1 mm in air at a ambient temperature of 1000 K. Adapted from [61].	50
<b>Figure 28:</b>	a-c. Various experimental techniques to study droplet combustion. d-f. Different suspender configurations. Droplet shown idealized in blue without the effect of gravity or wetting forces. Adapted from [27, 82, 133].	56
<b>Figure 29:</b>	Normalized droplet time histories for the vaporization of n-decane droplets at an ambient temperature of 570 K and a pressure of 0.1 MPa under 1g. Adapted from [133].	58
<b>Figure 30:</b>	Pressure effect on the explosion limits of hydrogen-oxygen mixtures at 293 K between 0.1 to 20 MPa. Adapted from [145].	59
<b>Figure 31:</b>	$OH^*$ chemiluminescence image from a microgravity droplet flame surrounding a 1.9 mm n-heptane droplet in 40/60 % mixture of oxygen and helium at 0.025 MPa at 0.53 s after ignition. Reprinted from [161] with permission from Elsevier.	63
<b>Figure 32:</b>	Schematic illustration of the principle of the cryogenic combustion chamber.	66
<b>Figure 33:</b>	Cross-sectional CAD view of the cryogenic combustion chamber (outermost container diameter of 206 mm) with the different compartments and main inlets (helium line not shown). The dashed line indicates the optical axis. Figure published in [177].	67
<b>Figure 34:</b>	CAD exploded view of the combustion chamber. Inner diameter: 43 mm, inner height: 60 mm.	68

<b>Figure 35:</b>	Indium wire sealing of the quartz windows in the combustion chamber.....	68
<b>Figure 36:</b>	CAD representation of the combustion chamber piping without vacuum and liquid nitrogen container.....	69
<b>Figure 37:</b>	CAD view of the sealed tunnel between combustion chamber and LN <sub>2</sub> container for optical access to the combustion chamber.....	70
<b>Figure 38:</b>	CAD view of the spring energized PTFE lip sealings for cryogenic applications in a flange groove. ....	70
<b>Figure 39:</b>	CAD view of the nitrogen feedthrough. a. Feedthrough with funnel. b. Sectional view with funnel. c. Feedthrough with thermocouple.....	71
<b>Figure 40:</b>	a. Integration of the cryogenic combustion chamber (without piping). b. View through the cryogenic combustion chamber with dummy suspender. ....	72
<b>Figure 41:</b>	a. Cross-sectional CAD view of the LOX valve in closed state. Helium (He) is used to drive the valve. b. Manufactured valve stem with sealings. Figure published in [177] and modified. ....	74
<b>Figure 42:</b>	Simplified circuit diagram for the pressure control to generate a droplet. ....	76
<b>Figure 43:</b>	Schematic illustration of the pressure levels during the droplet generation process.....	77
<b>Figure 44:</b>	Schematic illustration of different approaches for separating a single droplet.....	78
<b>Figure 45:</b>	a. Cross-sectional CAD view of the suspender holder with a quartz suspender and actual suspender images. b. Suspender dimensions in mm. Figure published in [177]. ....	79
<b>Figure 46:</b>	a. Cross-sectional CAD view of the integrated suspender (highlighted) in the combustion chamber. b. Suspender detail view with the droplet generation process shown schematically (solid arrows: LOX flow path, ellipses: LOX accumulation, dashed arrow: falling path of the LOX droplet).....	80
<b>Figure 47:</b>	Pressure profile during droplet generation. The $\mu\text{g}$ phase starts at 0 s. ....	81
<b>Figure 48:</b>	Composite image of a LOX droplet backlit image and a suspender tip backlit image in 1g (the image with droplet is displayed semi-transparent to make the suspender tip visible). The droplet width is 0.88 mm and the length is 1.27 mm. Figure published in [177]. ....	81
<b>Figure 49:</b>	CAD illustration of the integrated laser ignition system with the schematic path of the laser beam in red. ....	83

<b>Figure 50:</b>	Initial concept for beam guidance and influence of the beam expansion on the focus dimensions. Focal lengths in mm. Modified figure from [186].	84
<b>Figure 51:</b>	Pressure effect on the position and shape of the ignition spark in helium. Laser enters from the left.	85
<b>Figure 52:</b>	New concept for beam guidance and influence of the beam expansion vs. smaller focus lens on the focus dimensions. Focal lengths in mm. Modified figure from [188].	86
<b>Figure 53:</b>	CAD representation of the motorized mirror and lens adjustment unit for remote-controlled and high-precision positioning of the ignition spark.	87
<b>Figure 54:</b>	Laser-induced plasma spark at 0.15 MPa to ignite the LOX droplet.	88
<b>Figure 55:</b>	Technical drawing of the standard drop tower capsule without pressure-tight capsule shell and experiment-specific hardware. Reprinted from [176] with permission from ZARM FAB mbH.	89
<b>Figure 56:</b>	CAD illustration of stacked experiment platforms integrated into drop capsule stringer setup.	89
<b>Figure 57:</b>	Top view of the fluid platform.	90
<b>Figure 58:</b>	CAD illustration of the combustion chamber and optics platform. a. Top view. b. Bottom view.	91
<b>Figure 59:</b>	Final experimental setup of the drop capsule platforms. a. Cross-sectional CAD view. b. Actual image.	92
<b>Figure 60:</b>	Timing diagram of the experiment sequence and the different measurement systems.	93
<b>Figure 61:</b>	Schematic overview of the optical setup. Red: ignition system with illustrated laser beam path (z-axis). Green: diagnostics with indicated optical beam paths (dashed lines, x/z-axis).	96
<b>Figure 62:</b>	CAD illustration of the integrated shadowgraph imaging diagnostics with indicated optical beam paths (dashed lines).	97
<b>Figure 63:</b>	CAD illustration of the functional principle and structure of the tiltable mirror. Optical path is shown as dashed line. a. Normal position of the mirror (rotary solenoid not powered). b. Alternative position of the mirror (rotary solenoid powered). c. Main components of the design.	97
<b>Figure 64:</b>	High-speed shadowgraph images of a suspended LOX droplet. a. Main camera system (monochrome). b. Second camera system (color).	98
<b>Figure 65:</b>	Equivalent droplet diameter detection algorithm demonstration. a-c. Generated example images. d-f. Evaluated images (yellow circle: manually selected evaluation area, green area: detected	

	droplet area, yellow dot: calculated droplet centroid, red lines: shortest $ld, s$ and longest $ld, l$ dimension line, red value: droplet shape ratio $Rd$ ).....	99
<b>Figure 66:</b>	Transmission characteristics of the UG11 UV-bandpass filter with a thickness of 3 mm. Adapted from [190]. .....	101
<b>Figure 67:</b>	CAD illustration of the integrated $OH^*$ chemiluminescence diagnostics with highlighted main components. ....	101
<b>Figure 68:</b>	Test image with the intensified camera for $OH^*$ chemiluminescence without UV filter attached. ....	102
<b>Figure 69:</b>	Flame diameter detection algorithm demonstration. a-c. Generated example images. d-f. Evaluated images (yellow circle: detected circle, yellow value: filling level).....	103
<b>Figure 70:</b>	Flame diameter detection algorithm demonstration on artificially generated example signal. a. Generated signal. b. Evaluated image (yellow circle: detected circle, yellow value: filling level).....	103
<b>Figure 71:</b>	Integrated high-speed pressure transducers into the combustion chamber main body. a. Exterior view of the combustion chamber base. b. View into the combustion chamber. ....	105
<b>Figure 72:</b>	Combustion chamber pressure increase during combustion at 0.14 MPa ( $pr$ 0.03) under 1g conditions using the high-speed pressure measurement system. Three different time intervals are shown. ....	105
<b>Figure 73:</b>	Shadowgraph sequence of an unsuccessful ignition of a $H_2/He$ mixture (50/50 %) at 0.16 MPa ( $pr = 0.03$ ). Time synchronized with laser-induced spark. ....	109
<b>Figure 74:</b>	Ignition sequence at 0.10 MPa ( $pr = 0.02$ ). a-d. $OH^*$ chemiluminescence images. e-h. Shadowgraph images. Time synchronized with laser pulse. ....	110
<b>Figure 75:</b>	Vertical spark distance needed to ignite the droplet at different pressures under $\mu g$ conditions. Measured from the bottom of the droplet to the center of the laser-induced plasma spark. Based on experimental data with a gradual decrease in the distance between the ignition spark and the droplet surface. ....	111
<b>Figure 76:</b>	High-speed shadowgraph sequence at 0.10 MPa ( $pr = 0.02$ ). Ignition occurred at 0 ms (a). ....	112
<b>Figure 77:</b>	High-speed shadowgraph sequence at 1.20 MPa ( $pr = 0.67$ ). Ignition occurred at 0 ms (a). Contact angle $\theta$ indicated in red. Complete droplet detachment after 19 ms. ....	113
<b>Figure 78:</b>	High-speed shadowgraph sequence at 0.76 MPa ( $pr = 0.15$ ). Ignition occurred at 0 ms (a). The flame made contact with the suspender after 80 ms, causing the suspender to glow. ....	114

- Figure 79:** High-speed shadowgraph sequence at 3.15 MPa ( $pr = 0.63$ ). Ignition occurred at 0 ms (a). The lines and dots on the images are defects in the camera sensor. .... 115
- Figure 80:** High-speed  $OH^*$  chemiluminescence sequence at 0.10 MPa ( $pr = 0.02$ ). Ignition occurred at 0 ms. All images are shifted by 60  $\mu$ s. The intensifier gate time was 5  $\mu$ s and the camera gain was 1..... 116
- Figure 81:** Pseudo-color  $OH^*$  chemiluminescence image at 0.10 MPa ( $pr = 0.02$ ) 70.06 ms after ignition. The intensifier gate time was 5  $\mu$ s and the intensifier gain was 800 V. The position of the suspender is indicated by the dashed line. .... 117
- Figure 82:** High-speed  $OH^*$  chemiluminescence sequence at 0.76 MPa ( $pr = 0.15$ ). Ignition occurred at 0 ms. All images are shifted by 60  $\mu$ s. The intensifier gate time was 2.5  $\mu$ s and the camera gain was 1. .... 118
- Figure 83:** Combustion chamber pressure increase during combustion at 0.10 MPa ( $pr$  0.02). Two different time intervals are shown..... 120
- Figure 84:** Combustion chamber pressure increase during combustion at 4.51 MPa ( $pr$  0.90). Two different time intervals are shown..... 120
- Figure 85:** Schematic overview of the hypothesized combustion process in the subcritical pressure regime. Figure published in [179] and modified. .... 122
- Figure 86:** High-speed shadowgraph sequence of the building of an ice shell around the burning oxygen droplet at 0.10 MPa ( $pr$  0.02). Ignition occurred at 0 ms. .... 123
- Figure 87:** High-speed shadowgraph sequence of oxygen vapor jets (highlighted by red ellipses) breaking through the ice shell of the droplet at the end of combustion at 0.10 MPa ( $pr$  0.02). Ignition occurred at 0 ms. .... 124
- Figure 88:** High-speed shadowgraph sequence of a micro-explosion ejecting a water droplet or ice particle (highlighted by red circles) from the droplet surface during the combustion at 4.96 MPa ( $pr$  0.98). Ignition occurred at 0 ms. .... 124
- Figure 89:** High-speed shadowgraph sequence of a remaining ice particle breaking through the water cloud ring due to micro-explosions at the end of combustion (all liquid consumed) at 0.18 MPa ( $pr$  0.04). Ignition occurred at 0 ms. Figure published in [179]..... 125
- Figure 90:** High-speed shadowgraph sequence of droplet detachment with ice structures (highlighted by red circles) at the suspender at 0.15 MPa ( $pr$  0.03). Ignition occurred at 0 ms..... 126

- Figure 91:** Shadowgraph images showing the outer water cloud ring at different ambient pressures in the subcritical and supercritical regime, each 5 ms after ignition. The lines and dots on the images are defects in the camera sensor..... 127
- Figure 92:** Equivalent droplet diameter detection for the combustion at 0.10 MPa ( $pr = 0.02$ ). a-d. Original shadowgraph images. e-h. Evaluated images (yellow circle: manually selected evaluation area, green area: detected droplet area, yellow dot: calculated droplet origin, red lines: shortest and longest dimension line, red value: droplet shape ratio  $Rd$ ). The image pairs correspond to the same time, which is given in milliseconds after ignition and in dimensionless time  $t/t_1$ . ..... 128
- Figure 93:** Dimensionless time evolution of dimensionless droplet diameter (top) and droplet shape ratio  $R$  (bottom) for the combustion at 0.10 MPa ( $pr = 0.02$ ). ..... 129
- Figure 94:** Dimensionless time evolution of dimensionless droplet diameter (top) and droplet shape ratio  $R$  (bottom) for the combustion at 0.83 MPa ( $pr = 0.16$ ). ..... 130
- Figure 95:** Analysis of the  $OH^*$  signal 56.310 ms after ignition at 0.20 MPa ( $pr = 0.04$ ). a. Original image with selected evaluation lines in red. b-c. Intensity values along vertical and horizontal evaluation lines. The peak values of the left and right side of the origin are marked in green (based on the horizontal evaluation line). The evaluated edge values are marked in yellow. d. Original image overlaid with green circle based on the peak values and yellow circles based on the edge values along the horizontal evaluation line..... 131
- Figure 96:** Flame diameter detection 50 ms after ignition for the combustion at 0.10 MPa ( $pr = 0.02$ ). a. Original  $OH^*$  image. b-c. Automated threshold calculation (b.) and edge detection for actual image. d. Diameter detected based on Hough transformation. .... 133
- Figure 97:** Dimensionless time evolution of measured flame diameter  $f$  and calculated flame standoff ratio  $f/d$  for combustions at 0.20 MPa ( $pr = 0.04$ ) and 0.32 MPa ( $pr = 0.06$ ). ..... 134
- Figure 98:** High-speed shadowgraph sequence at 5.38 MPa ( $pr = 1.07$ ). Brightness correction progressively increased. Ignition occurred at 0 ms (a) and induced vortices below the droplet, which affected the shape of the water cloud ring around the droplet. The shape of the droplet is distorted by these vortices and remained non-spherical throughout the combustion. .... 136
- Figure 99:** Comparison of the droplet behavior in the subcritical and supercritical regime after the ignition spark has hit the suspender

- tip. a-b. 4.51 MPa ( $pr = 0.90$ ). c-d. 5.51 MPa ( $pr = 1.09$ ). Red arrows mark special features of the oxygen fluid. Ignition occurred at 0 ms. The black lines and white dots on the images are defects in the camera sensor..... 137
- Figure 100:** Schematic of the subcritical and supercritical injection process. Reprinted from [12] with permission from the American Institute of Aeronautics and Astronautics (AIAA). ..... 138
- Figure 101:** Droplet behavior in the supercritical regime 3.5 ms after the ignition spark has hit the suspender tip. a. 4.96 MPa ( $pr = 0.98$ ). b. 4.94 MPa ( $pr = 0.98$ ). In both cases the critical pressure was exceeded after ignition..... 139
- Figure 102:** Comparison of the droplet regression (a) and flame standoff ratio (b) of two different experiments at  $pr = 0.22$  and  $pr = 0.24$ ..... 140
- Figure 103:** Comparison of the droplet regression (a) and flame standoff ratio (b) of two different experiments at  $pr = 0.39$  and  $pr = 0.40$ ..... 140
- Figure 104:** Comparison of the droplet regression (a) and flame standoff ratio (b) of two different experiments at  $pr = 0.81$  and  $pr = 0.82$ ..... 141
- Figure 105:** Variation in the gasification rate constant with reduced ambient pressure for LOX under  $\mu\text{g}$  conditions using different evaluation methods. Error bars are based on the longest and shortest detected dimension of the initial droplet (only for a.) as well as on the maximum time error of  $< 500 \mu\text{s}$ . a. Only supercritical experiments were evaluated based on the total combustion process. b. All experiments were evaluated based on the total combustion process. Experiment at  $pr = 0.90$  not shown here, because the suspender was hit by the ignition spark..... 143
- Figure 106:** Effect of pressure on the enthalpy of vaporization  $qv$  of oxygen and on the enthalpy of condensation  $qc$  of water both at boiling temperature. Calculation based on the CoolProp database [194]. ..... 144
- Figure 107:** Variation in the burning rate constant with reduced ambient pressure for LOX and n-octane [101] under  $\mu\text{g}$  conditions. Error bars for LOX are based on the longest and shortest detected dimension of the initial droplet as well as on the maximum time error of  $< 500 \mu\text{s}$ . a. Absolute burning rate constant  $kg$ . b. Normalized burning rate constant  $kg/kg, max$ . Red arrows indicate qualitative correction of data in supercritical regimes. .... 145
- Figure 108:** a. Effect of pressure on the enthalpy of vaporization of oxygen at boiling temperature. b. Temperature difference  $\Delta T$  between initial droplet temperature of 77 K and boiling temperature. Calculations based on the CoolProp database [194]..... 147

<b>Figure 109:</b>	Effect of pressure on the Jakob number for a LOX droplet with an initial temperature of 77 K. Calculation based on the CoolProp database [194].	147
<b>Figure 110:</b>	Effect of reduced ambient pressure on the mean flame standoff ratio in the subcritical regime under $\mu\text{g}$ conditions. The error bars indicate standard deviation from the mean value.	148
<b>Figure 111:</b>	Pressure effect on the binary diffusion coefficient of hydrogen and oxygen at temperature of 1500 K. Calculated with Equation (2) based on [32].	150
<b>Figure 112:</b>	Variation in adiabatic flame temperature $T_f$ of the $\text{H}_2/\text{O}_2$ flame with reduced ambient pressure. Initial temperature was 77 K and the equivalence ratio was unity. Calculated with [195] and based on [10, 27, 196, 197].	150
<b>Figure 113:</b>	Suspender design for the generation of LOX droplets based on the fiber arc method. Cross-sectional CAD view of the combustion chamber with an actual detail image of the suspender (without droplet).	193
<b>Figure 114:</b>	New droplet separation method equipped with a fiber bundle consisting of six silicon carbide fibers.	194
<b>Figure 115:</b>	Fiber arc with and without LOX droplet under 1g conditions. a. Without droplet. b. With droplet (width: 1.321 mm, height: 1.586 mm).	194
<b>Figure 116:</b>	Combustion test of the fiber arc suspender. High-speed shadowgraph sequence at 0.19 MPa under 1g conditions. Ignition occurred at 0 ms (a).	195
<b>Figure 117:</b>	New suspender design with a fiber bundle consisting of six silicon carbide fibers and a ceramic bead at the tip.	195
<b>Figure 118:</b>	Combustion test of the silicon carbide fiber bundle suspender. High-speed shadowgraph sequence at 0.10 MPa under 1g conditions. Ignition occurred at 0 ms (a).	196
<b>Figure 119:</b>	New suspender design with a quartz fiber and a molten tip.	197
<b>Figure 120:</b>	Combustion test of the quartz fiber suspender. High-speed shadowgraph sequence at 0.12 MPa under 1g conditions. Ignition occurred at 0 ms (a).	197
<b>Figure 121:</b>	LabVIEW graphical user interface for experiment control and monitoring.	199
<b>Figure 122:</b>	Microscope image of the printed PET film as a BOS background pattern and detail image of the smallest structure.	201
<b>Figure 123:</b>	Integration of the BOS background into the combustion chamber using a lens holder.	202

<b>Figure 124:</b>	Numerical modeling of droplet vaporization. Upper section of the 2D mesh in ANSYS Fluent® .....	213
<b>Figure 125:</b>	Numerical modeling of droplet vaporization under 1g conditions at 0.1 MPa in ANSYS Fluent®. a. Mole fraction of oxygen. b. Flow field. Only the upper section of the modeled domain is shown. ....	215
<b>Figure 126:</b>	Numerical modeling of droplet vaporization under $\mu$ g conditions on the basis of the simulation result under 1g conditions at 0.1 MPa in ANSYS Fluent®. a. Mole fraction of oxygen. b. Flow field. Only the upper section of the modeled domain is shown. Vertical line indicating the evaluation line. ....	216
<b>Figure 127:</b>	Numerical modeling of droplet vaporization under $\mu$ g conditions on the basis of the simulation result under 1g conditions at 0.1 MPa in ANSYS Fluent®. Oxygen mole fraction evolution along the y-axis (evaluation line). Negative positions values indicate positions on the y-axis below the droplet and positive position values indicate positions on the y-axis above the droplet. Gray sections indicate area around droplet with oxygen mole fraction $> 0.1$ . ....	217
<b>Figure 128:</b>	Dimensionless time evolution of dimensionless droplet diameter (top) and droplet shape ratio $R$ (bottom) for combustions between $0.02 \leq pr \leq 0.06$ . ....	218
<b>Figure 129:</b>	Dimensionless time evolution of dimensionless droplet diameter (top) and droplet shape ratio $R$ (bottom) for combustions between $0.09 \leq pr \leq 0.22$ . ....	219
<b>Figure 130:</b>	Dimensionless time evolution of dimensionless droplet diameter (top) and droplet shape ratio $R$ (bottom) for combustions between $0.24 \leq pr \leq 0.39$ . ....	220
<b>Figure 131:</b>	Dimensionless time evolution of dimensionless droplet diameter (top) and droplet shape ratio $R$ (bottom) for combustions between $0.62 \leq pr \leq 0.90$ . ....	221
<b>Figure 132:</b>	Dimensionless time evolution of measured flame diameter $f$ and calculated flame standoff ratio $f/d$ for combustions between $0.02 \leq pr \leq 0.06$ . ....	222
<b>Figure 133:</b>	Dimensionless time evolution of measured flame diameter $f$ and calculated flame standoff ratio $f/d$ for combustions between $0.09 \leq pr \leq 0.22$ . ....	223
<b>Figure 134:</b>	Dimensionless time evolution of measured flame diameter $f$ and calculated flame standoff ratio $f/d$ for combustions between $0.24 \leq pr \leq 0.39$ . ....	224

---

<b>Figure 135:</b> Dimensionless time evolution of measured flame diameter $f$ and calculated flame standoff ratio $f/d$ for combustions between $0.62 \leq pr \leq 0.90$ . .....	225
---	-----

## List of tables

<b>Table 1:</b>	Example calculation of the Grashof number for hydrogen-oxygen combustion in various cases.....	27
<b>Table 2:</b>	Example calculation of the Fourier number for hydrogen-oxygen combustion in various cases.....	28
<b>Table 3:</b>	Example calculation of the Reynolds number for hydrogen-oxygen combustion in various cases.....	28
<b>Table 4:</b>	Properties of different model fluids compared to LOX. ....	78
<b>Table 5:</b>	Main specifications of the Nd:YAG ignition laser system [184, 185]. ....	83
<b>Table 6:</b>	Modified settings of the intensified camera with increasing ambient pressure to compensate the $OH^*$ intensity increase. ....	132
<b>Table 7:</b>	Overview student work. ....	182
<b>Table 8:</b>	Lennard-Jones potential parameters. Adapted from [32]. ....	184
<b>Table 9:</b>	Collision integrals for use with the Lennard-Jones potential. Adapted from [32].....	184
<b>Table 10:</b>	Test matrix of experiments evaluated in this thesis. ....	211
<b>Table 11:</b>	Numerical modeling of droplet vaporization under 1g conditions. Basic model parameters in ANSYS Fluent® .....	213
<b>Table 12:</b>	Numerical modeling of droplet vaporization under $\mu g$ conditions on the basis of the simulation result under 1g conditions. Changed basic model parameters in ANSYS Fluent® . ....	215

## Student work

In connection with this thesis, a student bachelor thesis was supervised by the author of this thesis. In addition, work was carried out by student assistants. The student thesis and all student work were carried out at ZARM, in the faculty of production engineering at the University of Bremen. The author sincerely thanks the students listed below for their valuable work. This thesis contains results obtained in the course of supervising the following student work.

**Table 7:** Overview student work.

<b>Student</b>	<b>Type</b>	<b>Year</b>	<b>Title or work packages</b>
Nick Kleemann	Bachelor thesis	2020	Auslegung einer Schlierenfotografie zur Verdampfungsuntersuchung eines Tropfens [198]
Sepehr Ariaei	Student assistant	2020	MATLAB: Visual droplet regression code improvements
Nick Kleemann	Student assistant	2020	Lab assistance

## Appendices

A. Example calculation of binary diffusion coefficient.....	184
B. Drawings LOX valve (German language) .....	186
C. Test of alternative droplet suspension techniques.....	193
D. Fluid system schematic .....	198
E. LabVIEW program .....	199
F. Background oriented Schlieren measurement technique .....	201
G. MATLAB evaluation code: Droplet and flame diameter .....	203
H. Test matrix .....	211
I. Simplified vaporization model.....	212
J. Droplet regression plots .....	218
K. Flame regression and flame standoff ratio plots .....	222

### A. Example calculation of binary diffusion coefficient

To calculate the binary diffusion coefficient using the Chapman-Enskog theory based on the Lennard-Jones potential the following equations and material parameters are used [32]:

$$D_{AB} = 0.18583 \sqrt{T^3 \left( \frac{1}{M_A} + \frac{1}{M_B} \right) \frac{1}{p \Psi_{AB}^2 \Omega_{D,AB}}} \quad (2)$$

$$\Psi_{AB} = \frac{1}{2} (\Psi_A + \Psi_B) \quad (62)$$

$$\epsilon_{AB} = \sqrt{\epsilon_A \epsilon_B} \quad (63)$$

where  $\epsilon$  is the characteristic energy for the Lennard-Jones potential.

$$T_r = \frac{K_B T}{\epsilon_{AB}} \quad (64)$$

where  $K_B$  is the Boltzmann constant with a value of  $1.380649 \times 10^{-23}$  J/K.

**Table 8:** Lennard-Jones potential parameters. Adapted from [32].

Element	$\Psi$ [Å]	$\frac{\epsilon}{K_B}$ [K]	$M$ [g/mol]
O <sub>2</sub>	3.433	113	31.999
H <sub>2</sub>	2.915	38	2.016

**Table 9:** Collision integrals for use with the Lennard-Jones potential. Adapted from [32].

$T_r$	$\Omega_{D,AB}$
1.10	1.375
1.15	1.347
1.20	1.320
1.25	1.296
1.30	1.274

For example, the binary diffusion coefficient of oxygen and hydrogen at a pressure of 0.1 MPa and at a temperature of 90 K can be calculated using these equations and parameters:

$$\epsilon_{O_2,H_2} = \sqrt{\left(113 \text{ K} * K_B \frac{\text{J}}{\text{K}}\right) * \left(38 \text{ K} * K_B \frac{\text{J}}{\text{K}}\right)} = 9.0472 * 10^{-22} \text{ J} \quad (65)$$

$$\Psi_{O_2,H_2} = \frac{1}{2} (3.433 \text{ \AA} + 2.915 \text{ \AA}) = 3.174 \text{ \AA} \quad (66)$$

$$T_{r,O_2,H_2} = \frac{K_B \frac{\text{J}}{\text{K}} * 77 \text{ K}}{9.0472 * 10^{-22} \text{ J}} = 1.1751 \quad (67)$$

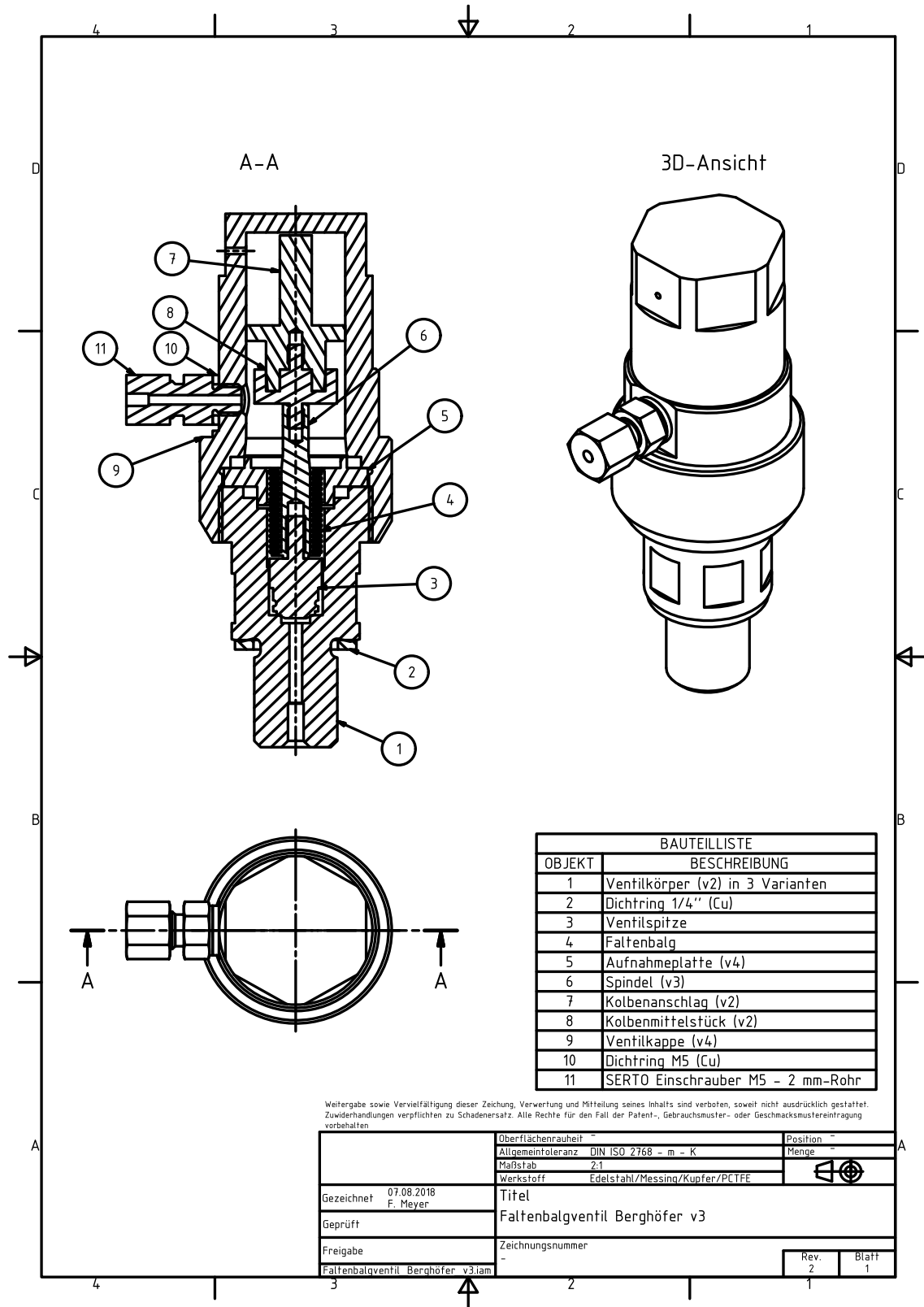
Using Table 9, this results in:

$$\Omega_{D,O_2,H_2} \approx 1.347 \quad (68)$$

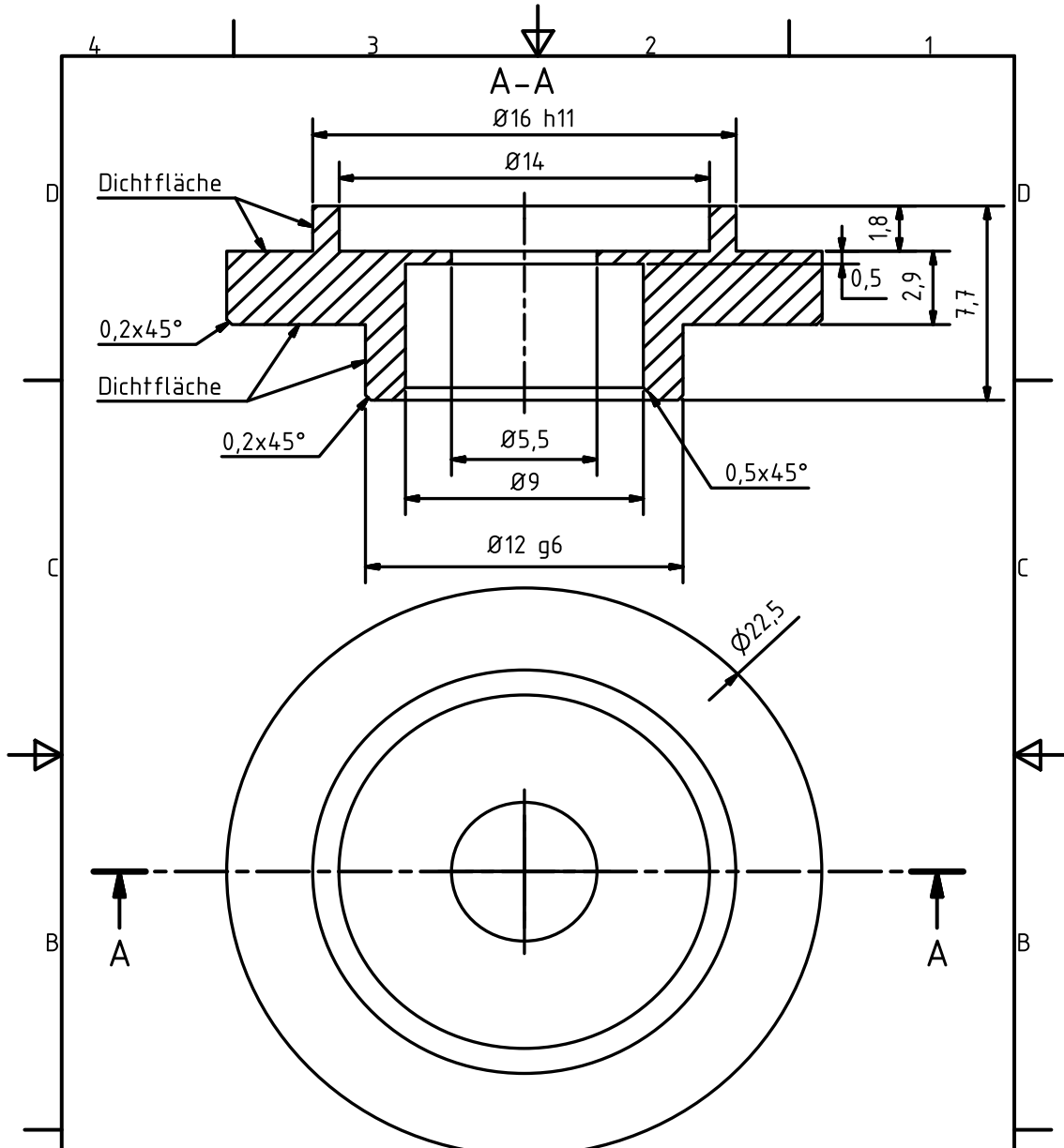
$$D_{O_2,H_2} = 0.18583 \sqrt{77^3 \text{ K}^3 \left( \frac{1}{31.999 \frac{\text{g}}{\text{mol}}} + \frac{1}{2.016 \frac{\text{g}}{\text{mol}}} \right)^*} \quad (69)$$

$$\frac{1}{0.987 \text{ atm} * 3.174^2 \text{ \AA}^2 * 1.347} = 6.8073 \frac{\text{mm}^2}{\text{s}}$$

B. Drawings LOX valve (German language)

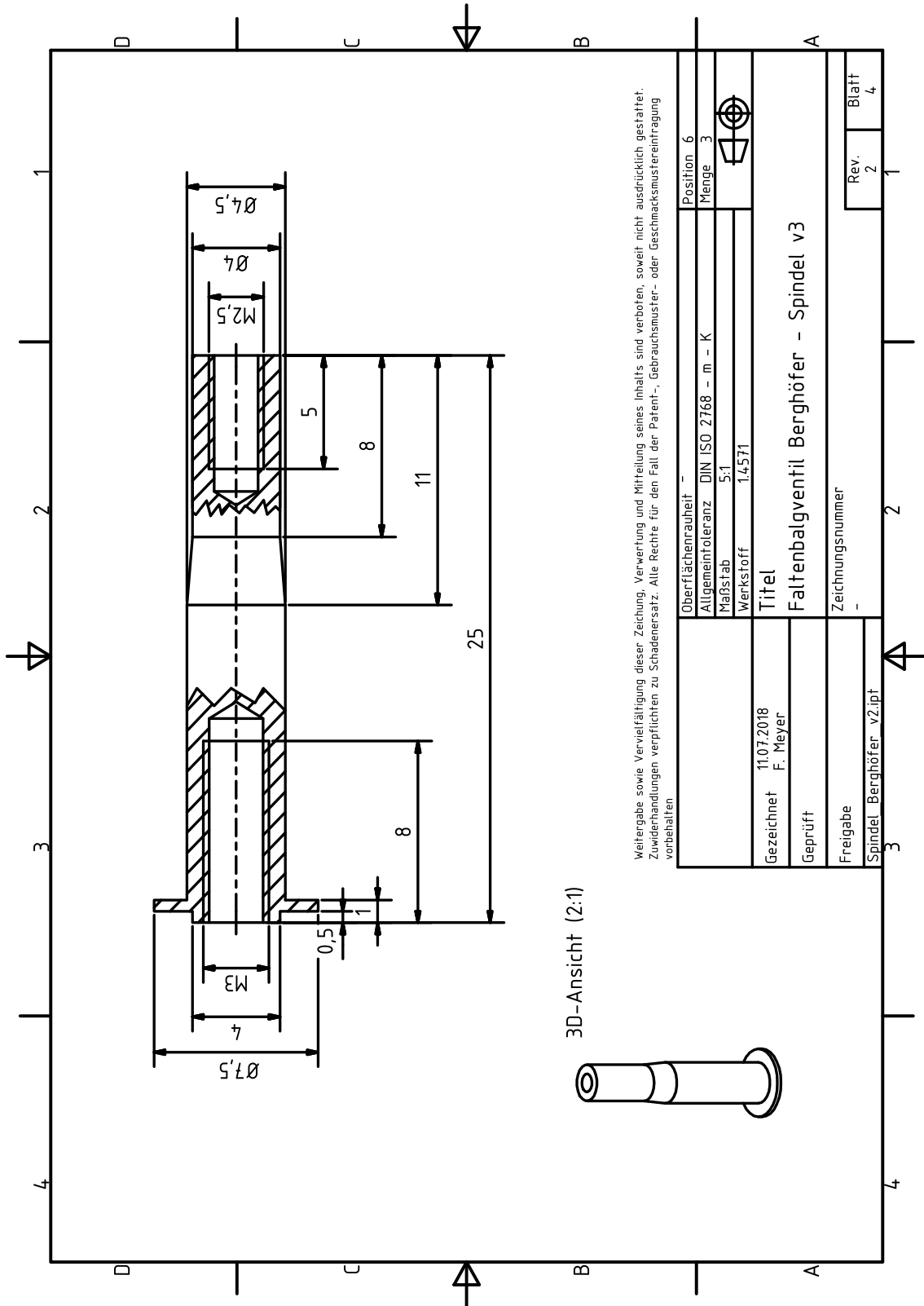




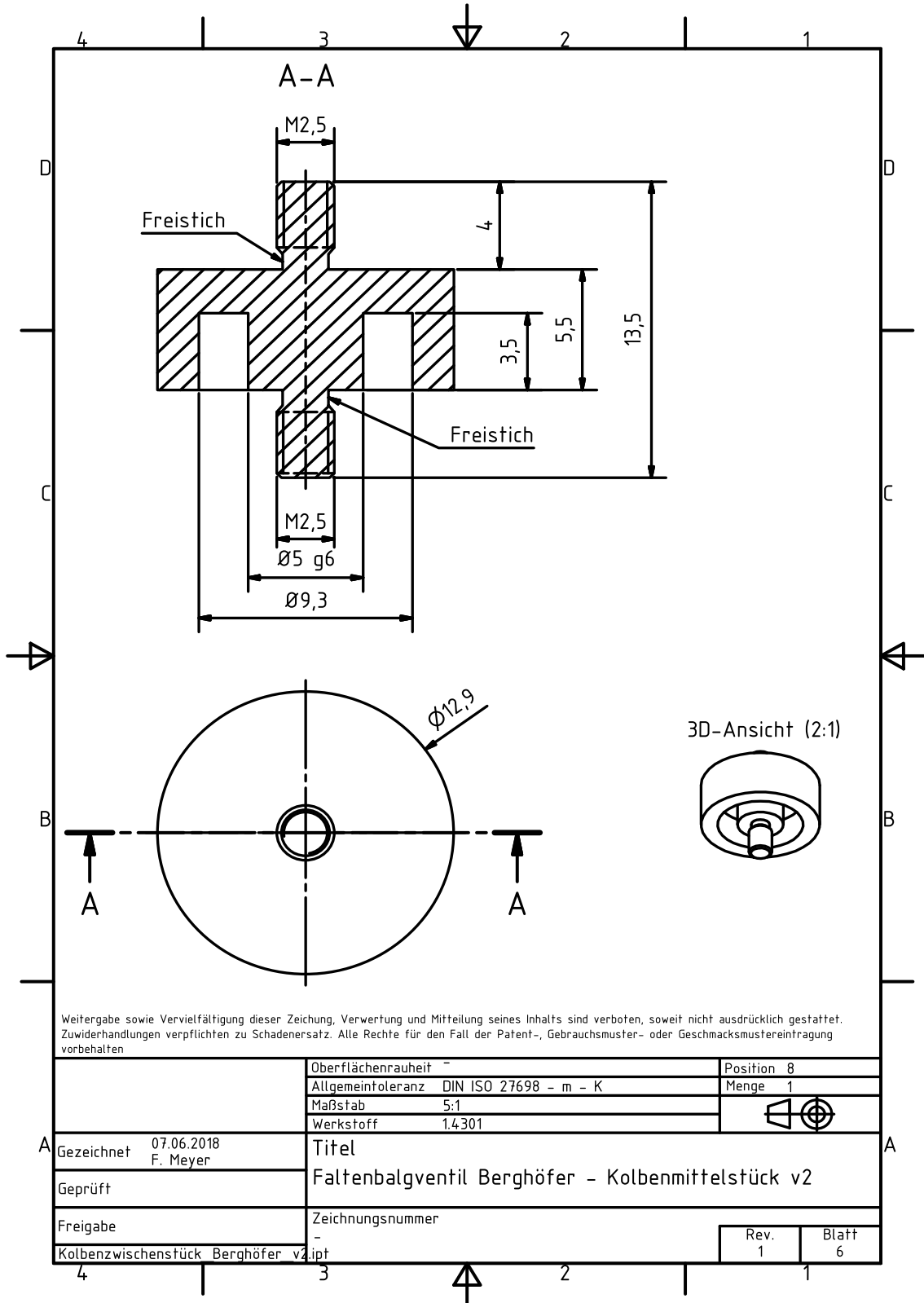


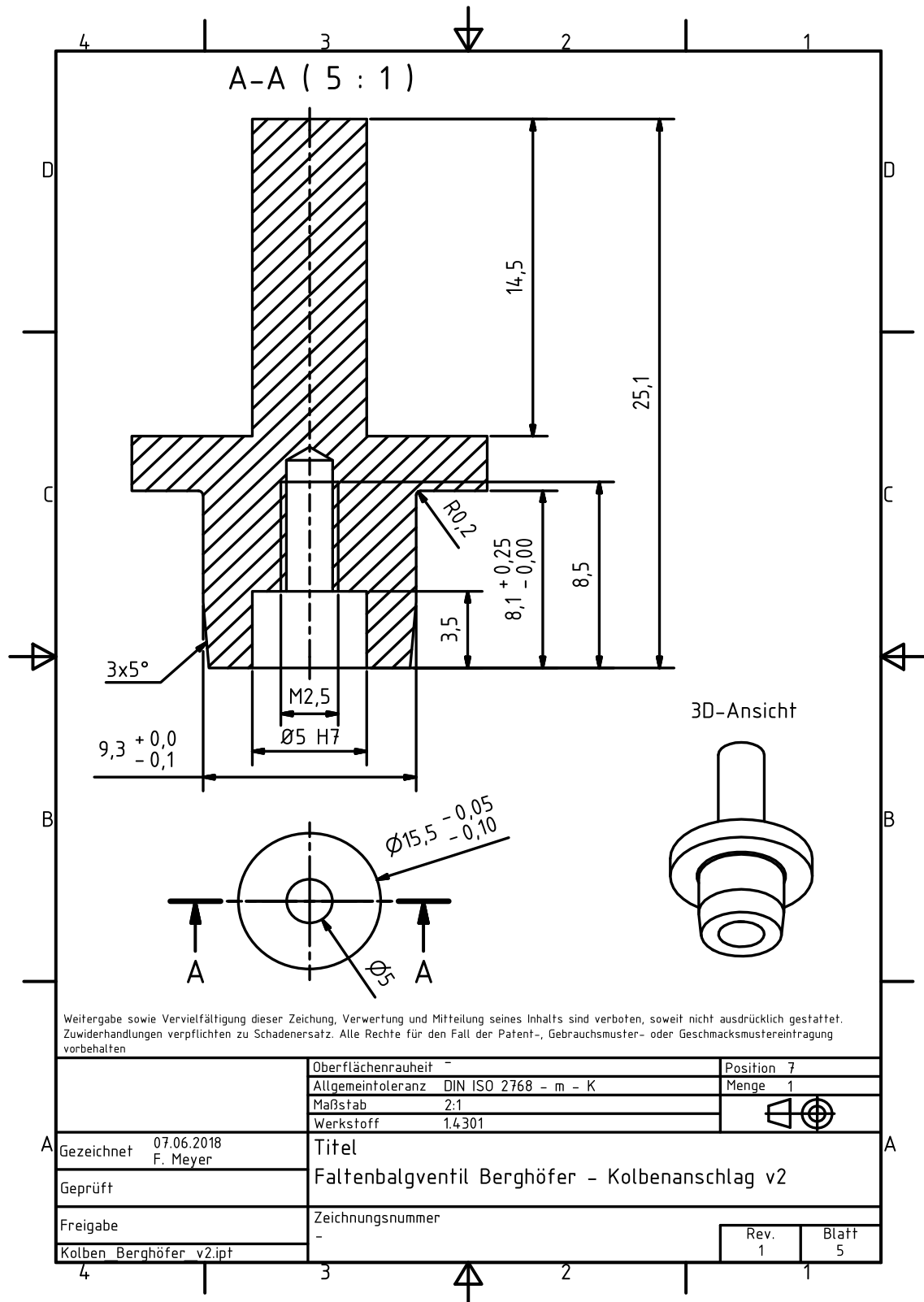
Weitergabe sowie Vervielfältigung dieser Zeichnung, Verwertung und Mitteilung seines Inhalts sind verboten, soweit nicht ausdrücklich gestattet. Zuwiderhandlungen verpflichten zu Schadenersatz. Alle Rechte für den Fall der Patent-, Gebrauchsmuster- oder Geschmacksmustereintragung vorbehalten.

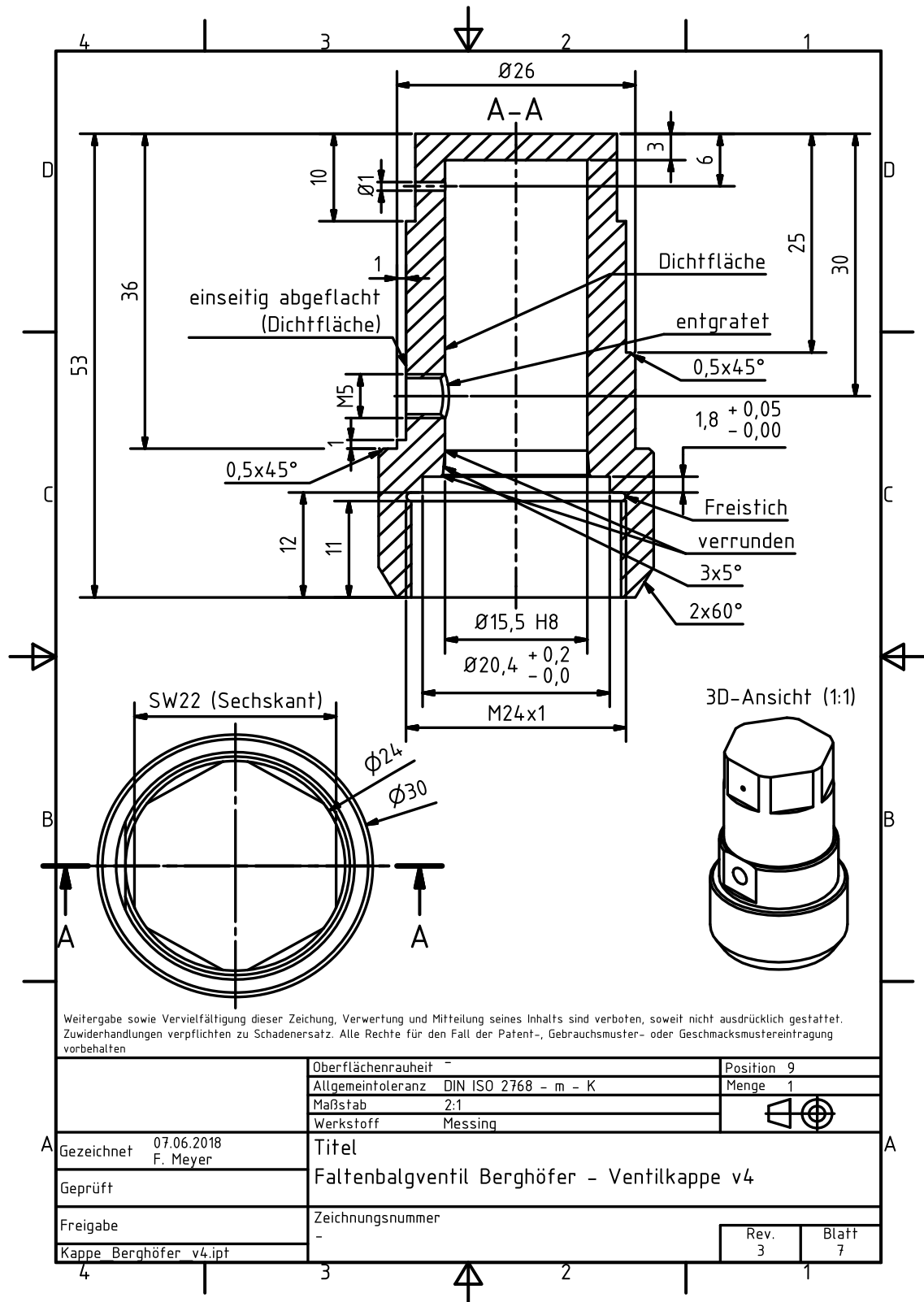
	Oberflächenrauheit -	Position 5		
	Allgemeintoleranz DIN ISO 2768 - m - K	Menge 3		
	Maßstab 5:1			
	Werkstoff 1.4571 oder 1.4301			
Gezeichnet 07.08.2018 F. Meyer	Titel			
Geprüft	Faltenbalgventil Berghöfe - Aufnahmeplatte v4			
Freigabe	Zeichnungsnummer			
Faltenbalg Mittelstück Berghöfer	v4.ipt	<table border="1" style="float: right;"> <tr> <td>Rev. 3</td> <td>Blatt 3</td> </tr> </table>	Rev. 3	Blatt 3
Rev. 3	Blatt 3			



Weitergabe sowie Vervielfältigung dieser Zeichnung, Verwertung und Mitteilung seines Inhalts sind verboten, soweit nicht ausdrücklich gestattet. Zuwiderhandlungen verpflichten zu Schadensersatz. Alle Rechte für den Fall der Patent-, Gebrauchsmuster- oder Geschmacksstoffeintragung vorbehalten







### C. Test of alternative droplet suspension techniques

The droplet generation of the LOX droplet is one of the most central elements of the entire experimental setup. Although the suspender used for these experiments allowed for repeatable droplet generation and was not damaged by the hot hydrogen-oxygen flame, this suspender design caused the LOX droplet to detach from the suspender shortly after ignition and then burned free-floating. As a result, optical diagnostics were sometimes more difficult, but sometimes not possible at all, e.g., when the droplet was obscured by the suspender. For this reason, after the experimental campaigns, some new suspender designs were developed and tested to improve future experiments. However, the combination with oxygen and hydrogen poses a particular challenge due to the very high flame temperatures and the simultaneously high oxygen concentrations.

The first design is based on the fiber arc method presented in chapter 3.3, which has already been successfully used for evaporation experiments on hydrocarbon droplets [60, 82]. In this method, the droplet is positioned by stretching two thin silicon carbide fibers into an arc and fixing them at the intersection point with a small glass bead. Since the droplet suspension fiber are very thin, the spherical shape of the droplet is rarely affected. Based on this method, a suspender design was created, which is shown in Figure 113.

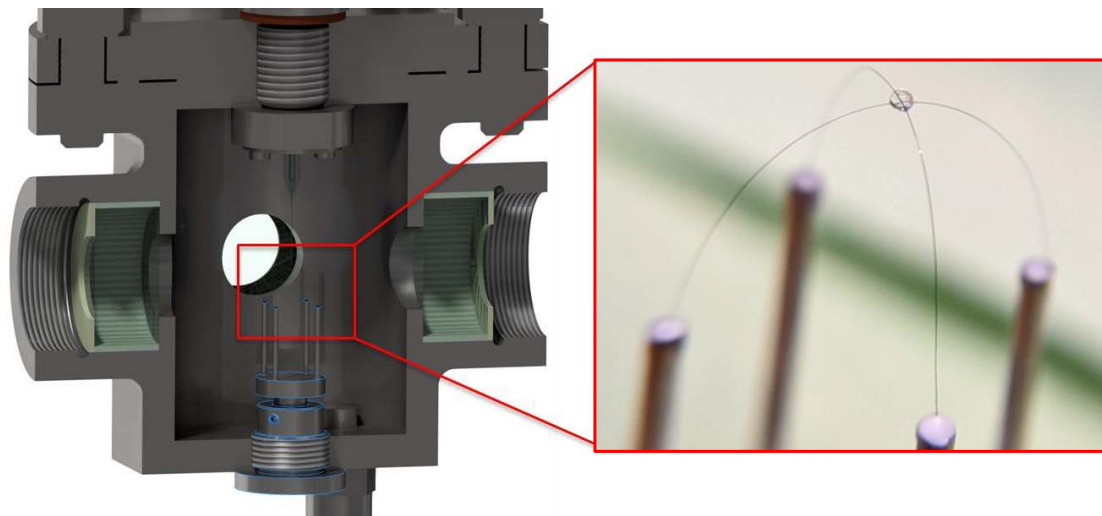
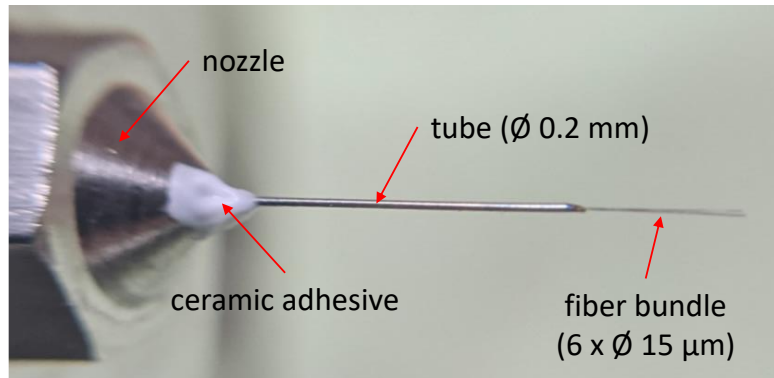


**Figure 113:** Suspender design for the generation of LOX droplets based on the fiber arc method. Cross-sectional CAD view of the combustion chamber with an actual detail image of the suspender (without droplet).

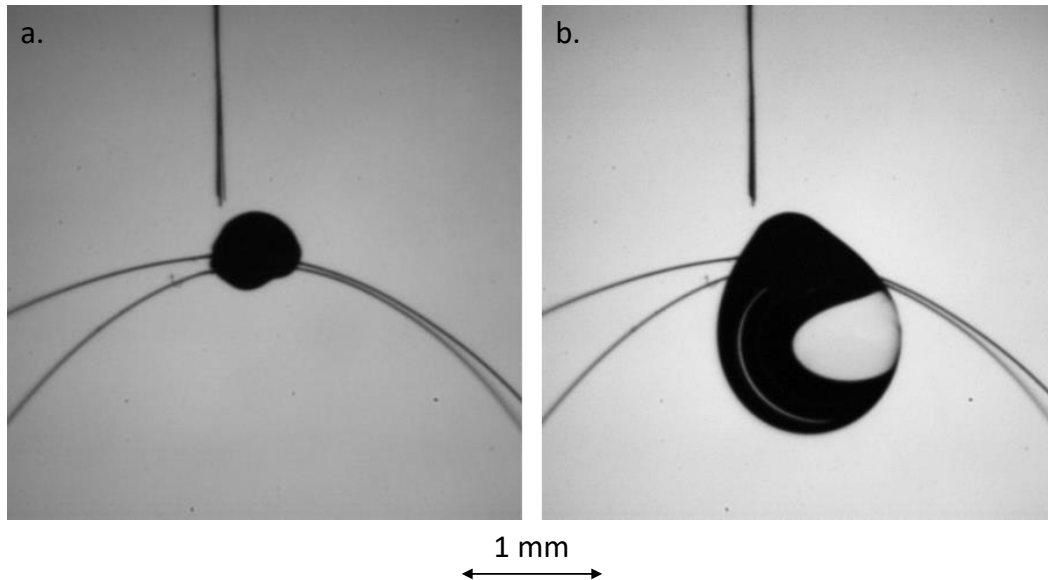
The suspender consists of a silicon carbide fiber arc with a fiber diameter of 15  $\mu\text{m}$ . The fibers are held in position by four stainless steel tubes with an outer diameter of 1 mm and are each bonded to the stainless steel tubes with a ceramic adhesive. At the connection point, the fibers are glued with an adhesive bead to fix the droplet position. The fiber arc can be adjusted in height and lateral directions and is screwed into the bottom of the combustion chamber.

The newly manufactured device for droplet separation is shown in Figure 114. Here, the LOX is drawn from the valve into a nozzle in which a stainless steel tube with a diameter

of 0.2 mm is bonded. Six silicon carbide fibers are fixed in this tube as a fiber bundle, which guides the falling droplet onto the bead of the fiber arc.



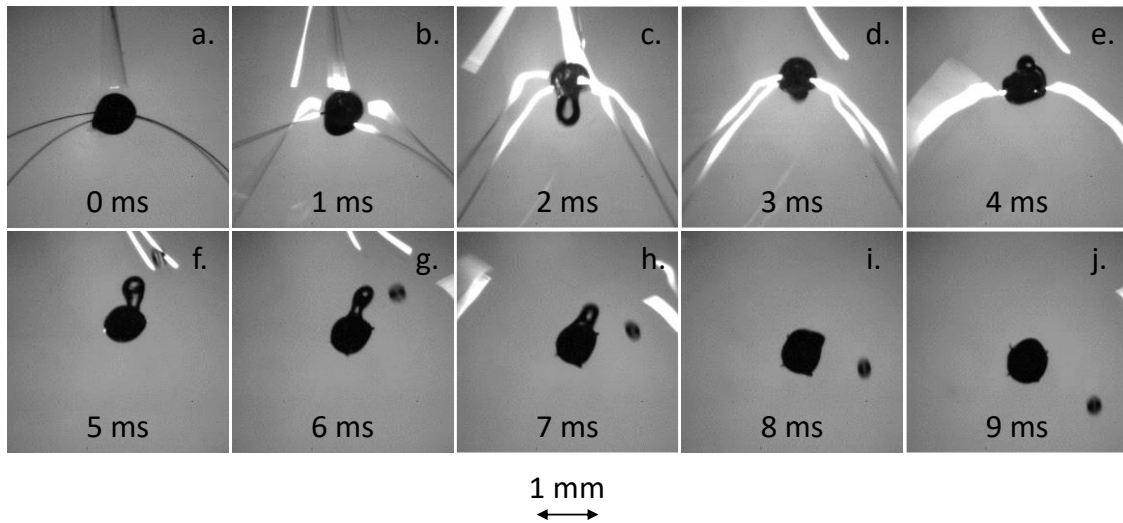
**Figure 114:** New droplet separation method equipped with a fiber bundle consisting of six silicon carbide fibers.



**Figure 115:** Fiber arc with and without LOX droplet under 1g conditions. a. Without droplet. b. With droplet (width: 1.321 mm, height: 1.586 mm).

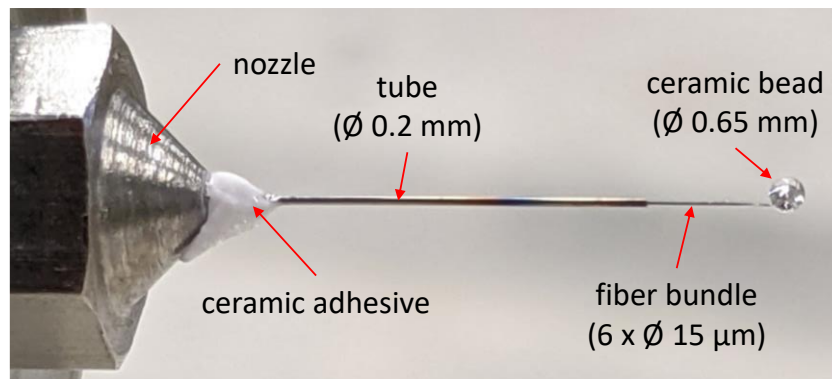
Figure 115 shows two shadowgraph images demonstrating the droplet generation process with the fiber arc suspender. This method allowed large LOX droplets to be generated that were barely affected by the individual fibers. In Figure 116, the combustion test of this suspender design conducted under 1g conditions is shown. The ignition occurred on the left side above the droplet. After ignition, the fiber bundle that guided the liquid to the suspender bead began to oscillate (Figure 116a). The flame around the burning LOX droplet heated the silicon carbide fibers and caused the suspender bead to move upwards (Figure 116c). 4 ms after ignition, the four fibers simultaneously detached from the bead and sped out of the field of view (Figure 116e-f). Due to the abrupt upward motion followed by the rupture of the fibers, the inertia of the liquid oxygen caused the liquid to elongate and even a satellite droplet to detach from the main droplet. Gravity

subsequently accelerated the now free-floating droplet downward out of the image frame (Figure 116f-j). Overall, this test showed that the single silicon carbide fibers could not withstand the high flame temperatures of the hydrogen-oxygen combustion.



**Figure 116:** Combustion test of the fiber arc suspender. High-speed shadowgraph sequence at 0.19 MPa under 1g conditions. Ignition occurred at 0 ms (a).

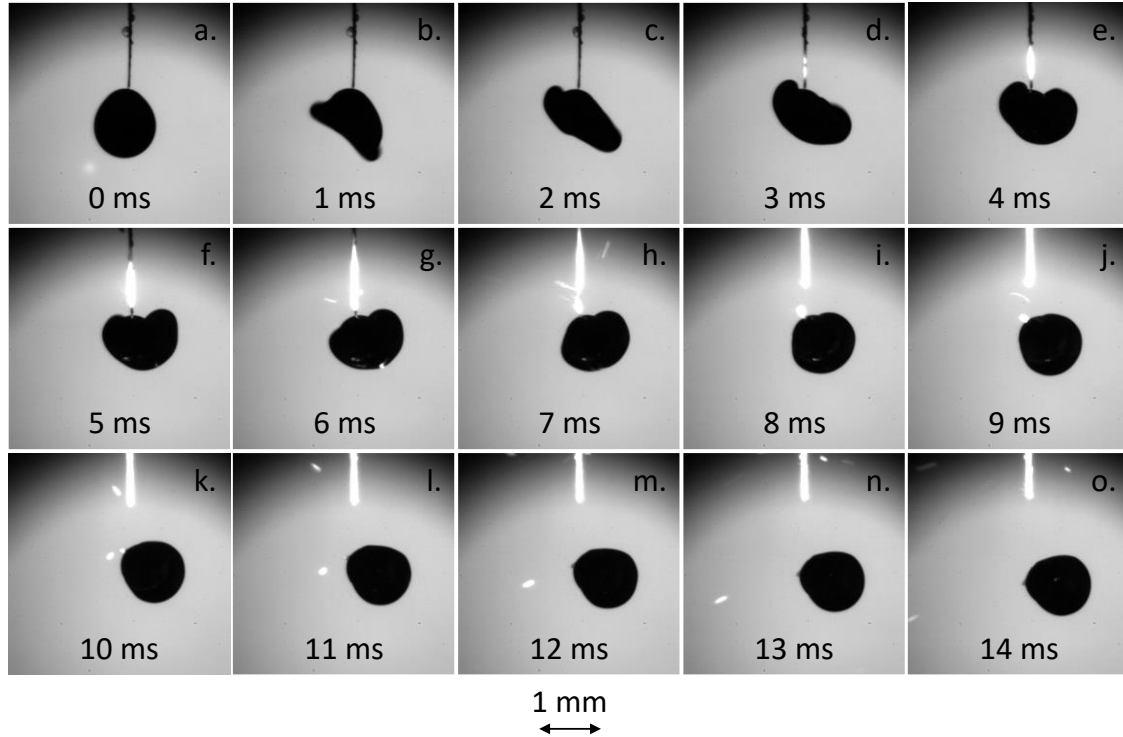
The next suspender design that was built and tested was a classic suspender, i.e., a thin fiber with a sphere at the tip. A silicon carbide fiber bundle was used for this purpose, with a sphere of ceramic adhesive attached to the tip. The new suspender design is shown in Figure 117.



**Figure 117:** New suspender design with a fiber bundle consisting of six silicon carbide fibers and a ceramic bead at the tip.

The image sequence of the combustion test is shown in Figure 118. In this test, the ignition occurred below the droplet (Figure 118a). The ignition spark, which was positioned very close, initiated a pressure wave that significantly deformed the liquid. The large contact angle between the LOX and the suspender sphere indicated that the top of the suspender sphere was dry shortly after ignition and was not rewetted by the liquid (Figure 118d-o). This behavior was also observed in the drop tower experiments with the old suspender and ultimately led to the detachment of the droplet from the suspender, as discussed earlier in chape 6.2. Approximately 3 ms after ignition, the silicon carbide fiber

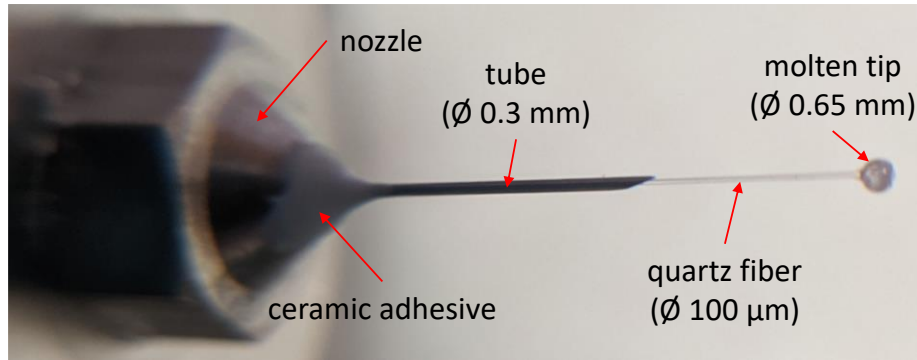
bundle above the suspender sphere began to glow. As combustion continued, the fiber bundle decomposed and detached the suspender sphere including the LOX droplet from the rest of the suspender (Figure 118g-i). This test showed that even a silicon carbide fiber bundle is not suitable to withstand the high temperatures that occur during combustion.



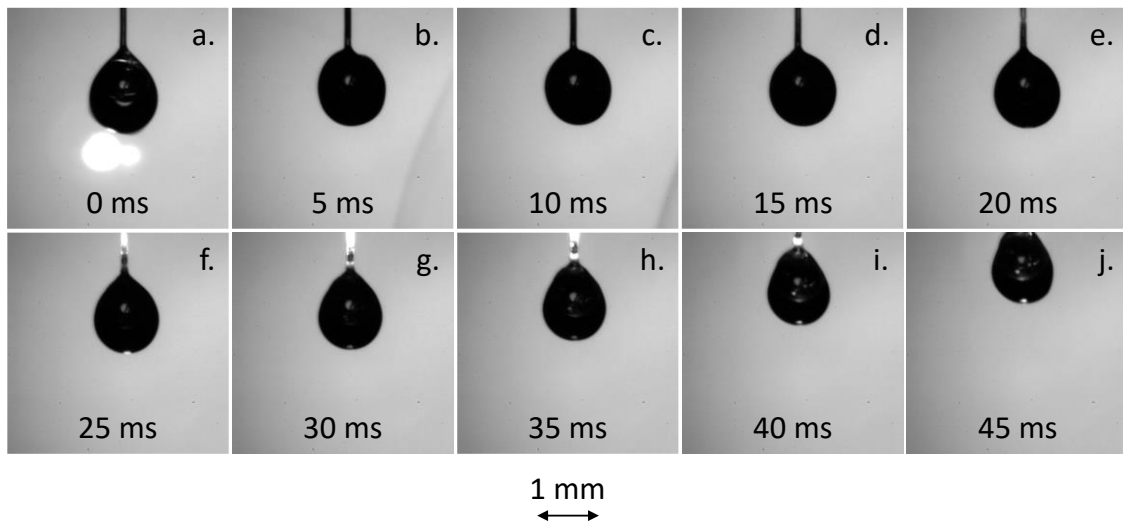
**Figure 118:** Combustion test of the silicon carbide fiber bundle suspender. High-speed shadowgraph sequence at 0.10 MPa under 1g conditions. Ignition occurred at 0 ms (a).

Figure 119 shows another suspender design that was built and tested. For this suspender, the fiber bundle was replaced with a single quartz fiber with a diameter of 100  $\mu\text{m}$ . A larger tube was also used to compensate for the larger fiber diameter.

The combustion process with the quartz suspender is shown in Figure 120. Again, the ignition was achieved with a laser-induced plasma breakdown below the droplet surface (Figure 120a). The droplet deformed slightly, but not as much as in the previous test. After about 20 ms, the quartz fiber above the suspender sphere began to glow (Figure 120e). This glow became increasingly intense before the suspender and with it the LOX droplet moved upward after about 35 ms. The LOX droplet burned at the top of the image frame and did not detach from the suspender sphere. After the combustion test, the combustion chamber was opened again and the suspender was examined. This revealed several possible reasons for the upward movement of the suspender. One was that the bonding of the quartz fiber inside the nozzle loosened slightly, allowing the fiber to move. Second, the quartz fiber was heated to such an extent that the section between the stainless steel tube and the suspender sphere melted. The accumulation of material significantly reduced the length of the suspender.



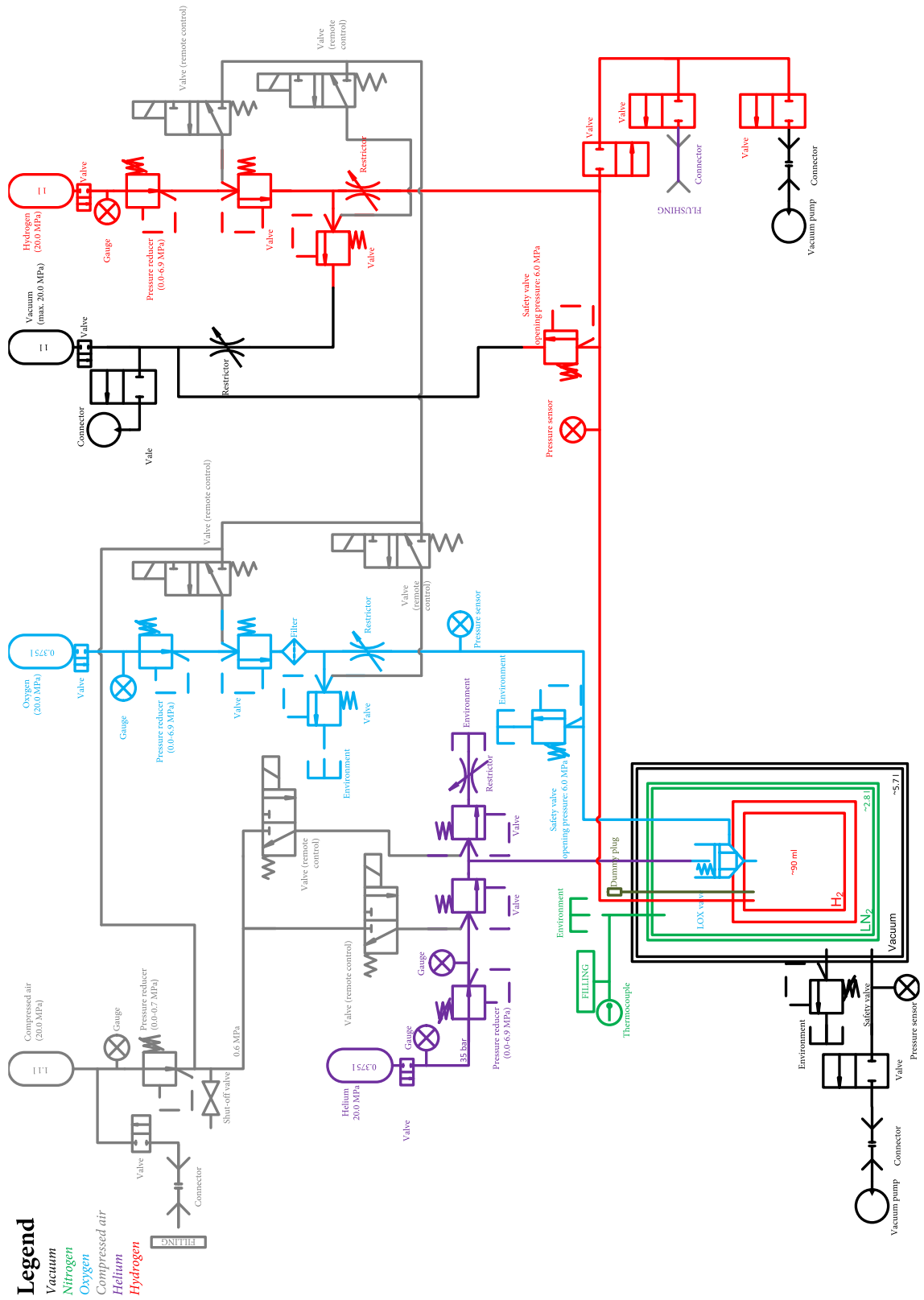
**Figure 119:** New suspender design with a quartz fiber and a molten tip.



**Figure 120:** Combustion test of the quartz fiber suspender. High-speed shadowgraph sequence at 0.12 MPa under 1g conditions. Ignition occurred at 0 ms (a).

Due to the very high flame temperatures in combination with the oxygen-rich atmosphere, it is very difficult to find a suitable suspender material which, on the one hand, is thinner than the previous suspender and, on the other hand, withstands the enormous stresses during combustion. It appears that droplet detachment during the drop tower experiments protected the old suspender from thermal damage. However, these tests provide a good basis for developing new suspender designs to improve the droplet generation and positioning process for future experiments.

### D. Fluid system schematic



## E. LabVIEW program

The entire drop tower experiment was controlled and monitored by a LabVIEW program. On the one hand, the program was used to read out, display, and store the sensor data as well as relay states. The data rate of the recorded data was 1 kHz during the experiment phase. On the other hand, the program allowed to control the experiment either manually, e.g., to open valves to adjust the combustion chamber pressure, or to automate processes or routines. The graphical user interface is shown in Figure 121.

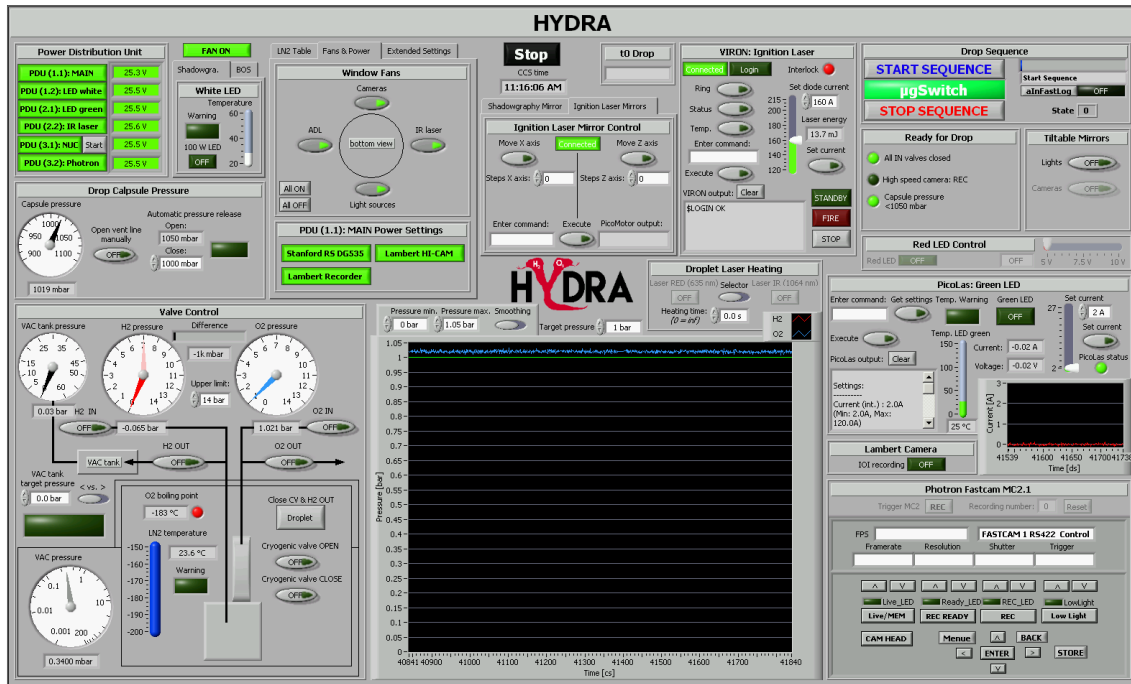


**Figure 121:** LabVIEW graphical user interface for experiment control and monitoring.

The control panel of the software was divided into individual sections, which can be classified into the following subgroups:

- Power distribution:**  
The power supply of the experiment capsule was divided into six main channels, which were individually switchable. In addition, some devices could be switched by relays, such as the intensified camera, the camera recorder, the Stanford delay generator, or the fans attached to the window flanges to prevent humidity condensation.
- Capsule pressure control:**  
By cooling the cryogenic combustion chamber with liquid nitrogen, the drop capsule pressure had to be controlled. Due to the vaporization of the nitrogen, the pressure in the drop capsule increased over time. To stay within the safety limits of the capsule structure (98 to 130 kPa [176]), the capsule pressure had to be released into the drop tower tube. This was ensured with an automatic routine. When the specified upper limit pressure was exceeded, the capsule pressure was released via a flow restrictor and a valve, which was automatically closed again

when the pressure dropped below the lower limit pressure. However, in order not to accelerate the capsule during the free-fall by releasing the pressure, the pressure was manually released before the drop and the routine was automatically stopped when the drop sequence was initiated.

- **Valve control and pressure plot:**

In this section, the fluid handling and the droplet generation were controlled. For this purpose, various pressure and temperature values were displayed, which were necessary for manual droplet generation. In addition, routines were developed that switch various valves in a specific sequence to facilitate the droplet generation. To prevent possible operator errors, safety routines were developed that, e.g., prevented the LOX valve from being opened when the oxygen inlet valve was open, which would have resulted in uncontrolled oxygen flow into the combustion chamber.

- **Ignition laser control:**

In order to be able to adjust and arm the laser system, a control panel was set up that based on a telnet communication interface. Thus, laser parameters could be changed and read out before the drop. The laser system was armed shortly before the drop and was triggered within the drop sequence. Other control panels included the adjustment of the laser optics, which could be adjusted in all three axes by stepper motors or piezo actuators. The vertical position of the plasma breakdown was adjusted by a stepper motor controller, which was controlled by another computer (NUC) via remote access.

- **Communication interfaces:**

A communication interface with the Photron MC 2 recorder was set up in order to be able to integrate the arming of the recording automatically into the drop sequence. In addition, a control panel for the power supply of a light source was integrated into the user interface.

- **Other controls:**

To control other elements, such as light sources or tiltable mirrors, corresponding control panels were integrated into the GUI.

- **Drop sequence:**

The drop sequence consists of several routines executed sequentially. Some routines were executed before the drop of the capsule, such as turning off fans, initiating the data logging, or switching on light sources. After these routines were executed, the actual drop was initiated, followed by the scripted experiment procedure. After a defined period of time corresponding to the  $\mu\text{g}$  time, the experiment was put back into a safe mode, e.g., by switching off the ignition laser so that the experiment could be recovered by the drop tower operators.

- **Extended settings:**

In order to be able to bypass certain security routines during laboratory testing under 1g conditions, extended settings have been implemented in the GUI.

## F. Background oriented Schlieren measurement technique

The BOS method is based on the local displacement of patterns in an image. The general setup consists of a camera system, a background pattern, and a background illumination system. A high-power LED (Luminus PT-121-G-L11-MPL) was used as the light source, which emits light with a wavelength of  $530\pm 10$  nm. The LED can reach a maximum power of almost 150 W in continuous wave mode with a luminous flux between 4400 and 6200 lm and is operated with 27 A. A bright backlight is necessary because typically a small aperture is used to reduce the geometric blur of the image [76]. The LED was screwed onto an aluminum heat sink and was integrated into the experimental setup as an additional light source. The light from the LED can be directed into the combustion chamber by actuating a tiltable mirror. A USB 3.0 camera from Basler (acA2040-90um) equipped with magnification optics is used as the camera system. The camera has a maximum resolution of  $2048 \times 2048$  px, but is operated at  $2048 \times 900$  px and 180 fps. The resolution achieved by the camera including the magnification optics is  $2.88 \mu\text{m}/\text{px}$ . Since precise droplet measurement prior to the drop is also possible with the BOS diagnostics, the previously used high-resolution shadowgraph imaging was replaced by the new camera system.

To test different backgrounds, several patterns (chess and grid pattern with different structure sizes and distances) were created, which were then printed on a  $200 \times 200$  mm PET film by the company JD Photodata. In the literature, an optimal structure size of 2-4 px on the image plane is recommended [199]. For this reason, a square with an edge length of  $9.75 \mu\text{m}$  was defined as the smallest structure. Figure 122 shows a microscope image of the printed pattern.

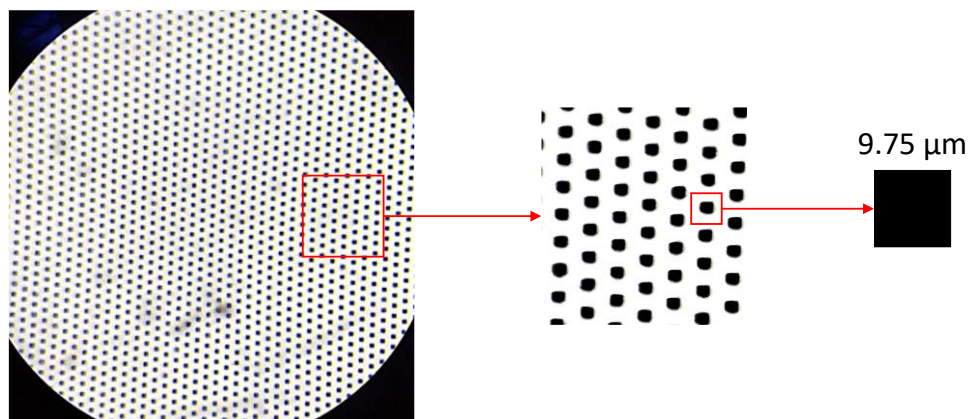


**Figure 122:** Microscope image of the printed PET film as a BOS background pattern and detail image of the smallest structure.

To integrate the BOS background into the combustion chamber, the PET film was clamped in a lens holder from Thorlabs. To fix this lens holder in the combustion chamber, the corresponding window flange was threaded so that the lens holder could be screwed into the window flange from the inside, as shown in Figure 123. The partially transparent background pattern is illuminated by the LED and captured by the BOS

camera from the opposite side. The distance between the droplet and the background can be changed by adjusting the lens mount.

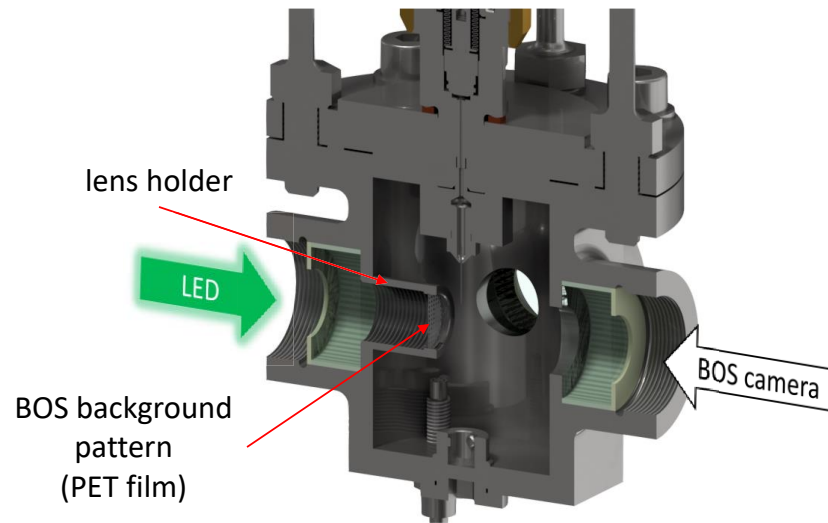


**Figure 123:** Integration of the BOS background into the combustion chamber using a lens holder.

The BOS diagnostic will be used in future drop tower experiments. For evaluation, an undisturbed reference image is computed with the experiment images. For this purpose, an algorithm originally developed for PIV evaluation is used to make the density-related displacement visible.

## G. MATLAB evaluation code: Droplet and flame diameter

### Parameter set for each experiment (shown for droplet diameter detection):

```

clear
clc
close all
tic

%% INPUTS - B.01

StartTime = 50; % Start time of video data in ms
ImageScale = 62; % Define image scale [px/mm]
EvaluationMethod = 1; % Select droplet detection (1) or flame detection (2)

ExportTracking = true; % Export the evaluated images

CropImage = true; % Define if images shall be cropped for evaluation
CropPositionCoordinates = true; % Define if you want to define the crop position manually (false) or
by giving coordinates (true)
CropPosition = [270,6.33,188,81.6]; % Coordinates for crop position (is ignored when using
CropPositionInteractive = true)

GammaEnhancement = true; % Activate fixed gamma enhancement for every image
Gamma = 1; % Define gamma value (1 is not enhanced)
TargetBrightness = 25; % Define the level of brightness for droplet area recognition, use
((TargetBrightness/255) ^ Gamma) * 255 for calculation of target value

Shadowgraphy = true; % For OH chemiluminescence = false (just affecting AutoThreshold
method [Ridler and Calvard / Otsu])
NoGrowth = true; % Limits the possibility for droplet growing
BoxSize = 5; % Define box size around detected circle for next image in px
ShowBox = true; % Show the evaluation box around the droplet & dimension lines

%% CALL FUNCTION

% Get current folder
Folder = cd;

Regression_v6(Folder, EvaluationMethod, CropImage, CropPositionCoordinates, CropPosition, Shadowgraphy,
NoGrowth, BoxSize, ShowBox, ExportTracking, StartTime, ImageScale, GammaEnhancement, Gamma, TargetBrightness)

toc

```

### Main function: Regression\_v6

```

function Regression_v6(Folder, EvaluationMethod, CropImage, CropPositionCoordinates, CropPosition,
Shadowgraphy, NoGrowth, BoxSize, ShowBox, ExportTracking, StartTime, ImageScale, GammaEnhancement, Gamma,
TargetBrightness)
%% INIT

% Select folder
folder = Folder;

% Load images
imageFiles = [dir([folder '*.jpg']);dir([folder '*.png'])];
numFiles = length(imageFiles);
data(1:numFiles,1:3) = NaN;

% Check if old tracking exist and make new folder
for trackingNo = 0:9
    if trackingNo == 0 && exist([folder '\Tracking'], 'dir')
        exportPath = ['\Tracking_' num2str(trackingNo+1)];
    elseif trackingNo == 0 && ~exist([folder 'Tracking'], 'dir')
        exportPath = ['\Tracking_' num2str(trackingNo+1)];
    end
    if trackingNo > 0 && exist([folder '\Tracking_' num2str(trackingNo)], 'dir')
        exportPath = ['\Tracking_' num2str(trackingNo+1)];
    end
end

mkdir(folder, exportPath);

%% LOOP

for x = 1:numFiles

    % Calculate actual time
    if Shadowgraphy == true
        time = (x-1)/2000*1000+StartTime;
    end
end

```

```

else
    time = (x-1)/1600*1000+StartTime;
end

% Load image & select cropping position
A = imread([folder '\ ' imageFiles(x).name]);

if CropImage == true && x == 1 && CropPositionCoordinates == false

    cropFigure = figure('Name','Crop Image: Draw a rectangle','NumberTitle','off');
    maximize(cropFigure);
    imshow(A);
    crop = imrect;
    addNewPositionCallback(crop,@(p) title(mat2str(p,3)));
    fcn = makeConstrainToRectFcn('imrect',get(gca,'XLim'),get(gca,'YLim'));
    setPositionConstraintFcn(crop,fcn);
    position = wait(crop);
    CropPosition = getPosition(crop);

    % Export cropped image position as png or txt (uncommend)
    csvwrite([folder exportPath '\Cropping-Image-Position.txt'],CropPosition);
    export_fig([folder exportPath '\Cropping-Image-Position.png']);

    close(cropFigure);

elseif CropImage == true && x == 1 && CropPositionCoordinates == true

    csvwrite([folder exportPath '\Cropping-Image-Position.txt'],CropPosition);
end

% Crop image
if CropImage == true

    CropPosition = round(CropPosition);
    A = imcrop(A,CropPosition);
end

%Gamma enhancement
if GammaEnhancement == true
    A = imadjust(A,[],[],Gamma);
end

% Treshold image
if AutoThreshold == true
    if Shadowgraphy == true
        threshold = isodata(A);
    else
        threshold = graythresh(A);
    end
end

% Flame evaluation
if EvaluationMethod == 2

    % Cut around previous center
    if x > 1
        cutPositionX = center.x - (radius + BoxSize);
        cutPositionXDelta = 0;

        if cutPositionX < 1
            cutPositionXDelta = abs(cutPositionX - 1);
            cutPositionX = 1;
        end

        cutPositionY = center.y - (radius + BoxSize);
        cutPositionYDelta = 0;

        if cutPositionY < 1
            cutPositionYDelta = abs(cutPositionY - 1);
            cutPositionY = 1;
        end

        B = imcrop(A,[cutPositionX,cutPositionY,(radius + BoxSize) * 2 - cutPositionXDelta,(radius +
BoxSize) * 2 - cutPositionYDelta]);
        Abox = insertShape(A,'Rectangle',[cutPositionX,cutPositionY,(radius + BoxSize) * 2 -
cutPositionXDelta,(radius + BoxSize) * 2 - cutPositionYDelta],'Color','blue');
    else
        cutPositionX = 0;
        cutPositionY = 0;
        B = A;
        if size(A,3) == 1
            Abox = cat(3, A, A, A);
        else
            Abox = A;
        end
    end
end

```

```

end

% Apply threshold
C = im2bw(B,threshold);

% Detect edges
D = edge(C);

% Generate range of radii + No Growth: The first 5 images are processed and then the max radius is
limited to the average of the last 20 radii + 1 px
if NoGrowth == true && x > 5
    limit = nanmean(data(x-5:x-1,2))/2 + 1;
    radii = limit-3:1:limit;
elseif NoGrowth == true && x > 10
    limit = nanmean(data(x-10:x-1,2))/2 + 3;
    radii = limit-5:1:limit;
else
    radii = 5:1:40;
end

h = circle_hough(D, radii, 'same');
[~,maxIndex] = max(h(:));
[i,j,k] = ind2sub(size(h), maxIndex);
radius = radii(k);
center.x = j + cutPositionX;
center.y = i + cutPositionY;

% Generate circle to overlay
N = 500;

theta = linspace(0,2*pi,N);
rho = ones(1,N) * radius;

% Cartesian coordinates of detected circle
[X,Y] = pol2cart(theta,rho);

% Get a mask of the detected circle
mask = poly2mask(X + center.x,Y + center.y,size(A,1),size(A,2));

if Shadowgraphy == true
    maskedImage = A(:, :, 1);
else
    maskedImage = imcomplement(A(:, :, 1));
end
maskedImage(~mask) = 255;
referenceArea = imbinarize(maskedImage,0.999);
actualArea = maskedImage;
actualArea(actualArea > ((TargetBrightness / 255) ^ Gamma) * 255) = 255;
actualArea = imbinarize(actualArea);

% Delete single pixels
actualArea = ~bwareaopen(~actualArea,floor(radius * 4));

% Fill holes in binary image
for row = 1:size(actualArea,1)
    first = 0;
    last = 0;
    for column = 1:size(actualArea,2)
        if actualArea(row,column) == 0
            if first == 0
                first = column;
            else
                last = column;
            end
        end
    end
    if first ~= 0
        actualArea(row,first:last) = 0;
    end
end

% Save data
data(x,1) = time;
data(x,2) = radius * 2;
data(x,3) = center.x + cutPositionX;
data(x,4) = center.y + cutPositionY;
data(x,5) = (radius - sqrt(nnz(~actualArea)/pi)) * 2 / ImageScale; % Error bar (negative)
data(x,6) = data(x,2) / ImageScale; % Diameter [mm]
data(x,7) = nnz(~actualArea) / nnz(~referenceArea); % Filling level
data(x,8) = sqrt(nnz(~actualArea)/pi) * 2 / ImageScale; % Detected area diameter [mm]

% Remove diameter tracking data with 0% filling level
if data(x,7) == 0
    data(x,2) = NaN;
end

```

```

        data(x,6) = NaN;
    end

    % Droplet evaluation
    elseif EvaluationMethod == 1

        % Message box: Manual position entry of specify given positions
        if x == 1
            SelectionModeBox = questdlg('Position selection mode:', 'Position Selection Mode', 'Manual
            Selection', 'From File', 'Manual Selection');

            switch SelectionModeBox
                case 'Manual Selection'
                    SelectionMode = 1;
                case 'From File'
                    SelectionMode = 2;

                    % Ask for txt file
                    [positionsFileName,positionsFilePath] = uigetfile('*.txt','Select "Diameter-
                    Regression.txt" File');
                    positionsFile = readmatrix([positionsFilePath positionsFileName]);
                    FileRow = 1;
            end
        end

        if SelectionMode == 1
            % Manual selection
            manualFigure = figure('units','normalized','outerposition',[0 0 1 1]);
            imshow(A);

            if x == 1
                circleData = [10 10 20 20];
            end

            circle = imellipse(gca,circleData);
            setFixedAspectRatioMode(circle,true);
            addNewPositionCallback(circle,@(p) title(mat2str(p,3)));
            fcn = makeConstraintToRectFcn('imellipse',get(gca,'XLim'),get(gca,'YLim'));
            setPositionConstraintFcn(circle,fcn);
            position = wait(circle);
            circleData = getPosition(circle);

            radius = circleData(3)/2;
            center.x = circleData(1) + radius;
            center.y = circleData(2) + radius;

            close(manualFigure);
        elseif SelectionMode == 2
            % Selection from file
            circleData(1) = positionsFile(FileRow,3) - positionsFile(FileRow,2) / 2;
            circleData(2) = positionsFile(FileRow,4) - positionsFile(FileRow,2) / 2;
            circleData(3) = positionsFile(FileRow,2);

            FileRow = FileRow + 1;

            radius = circleData(3)/2;
            center.x = circleData(1) + radius;
            center.y = circleData(2) + radius;
        end

        % Generate circle to overlay
        N = 400;

        theta = linspace(0,2*pi,N);
        rho = ones(1,N) * circleData(3)/2;

        % Cartesian coordinates
        [X,Y] = pol2cart(theta,rho);

        % Get a mask of the detected circle
        mask = poly2mask(X + center.x,Y + center.y,size(A,1),size(A,2));

        if Shadowgraphy == true
            maskedImage = A(:,:,1);
        else
            maskedImage = imcomplement(A(:,:,1));
        end
        maskedImage(~mask) = 255;
        referenceArea = imbinarize(maskedImage,0.999);
        actualArea = maskedImage;
        actualArea(actualArea > ((TargetBrightness / 255) ^ Gamma) * 255) = 255;
        actualArea = imbinarize(actualArea);

        % Fill holes in binary image - by row

```

```

for row = 1:size(actualArea,1)
    first = 0;
    last = 0;
    for column = 1:size(actualArea,2)
        if actualArea(row,column) == 0
            if first == 0
                first = column;
            else
                last = column;
            end
        end
    end
    if first ~= 0
        actualArea(row,first:last) = 0;
    end
end

% Fill holes in binary image - by column
for column = 1:size(actualArea,2)
    first = 0;
    last = 0;
    for row = 1:size(actualArea,1)
        if actualArea(row,column) == 0
            if first == 0
                first = row;
            else
                last = row;
            end
        end
    end
    if first ~= 0
        actualArea(first:last,column) = 0;
    end
end

% Detect center of droplet & calculate longest and shortest dimension
if size(A,3) == 1
    Abox = cat(3, A, A, A);
else
    Abox = A;
end

try
[longestLength,shortestLength,centerPolyX,centerPolyY,positionLongRot1,positionLongRot2,positionShortRot1,positionShortRot2] = dropletLines_v3(actualArea);

    % Mark droplet area & draw horizontal + vertical dimensions to image
    AboxGreenChannel = Abox(:,:,2);
    AboxGreenChannel(~actualArea) = 150;
    Abox(:,:,2) = AboxGreenChannel;
    Abox =

insertShape(Abox, 'Line', [flip(positionLongRot1),flip(positionLongRot2);flip(positionShortRot1),flip(positionShortRot2)], 'Color', 'red', 'Opacity',1);
    Abox = insertShape(Abox, 'FilledCircle', [centerPolyX,centerPolyY,2], 'Color', 'yellow', 'Opacity',1);
catch
end

% Save data
data(x,1) = time;
data(x,2) = circleData(3);
data(x,3) = circleData(1) + data(x,2)/2;
data(x,4) = circleData(2) + data(x,2)/2;
data(x,5) = (radius - sqrt(nnz(~actualArea)/pi)) * 2 / ImageScale; % Error bar (negative)
data(x,6) = data(x,2) / ImageScale; % Diameter [mm]
data(x,7) = nnz(~actualArea) / nnz(~referenceArea); % Filling level
data(x,8) = sqrt(nnz(~actualArea)/pi) * 2 / ImageScale; % Detected area diameter [mm]
try
    data(x,9) = longestLength/shortestLength; % Droplet-shape ratio (1 = sphere)
catch
end

end

% Export images with tracking
if ExportTracking == true

    figure;
    if ShowBox == true
        imshow(Abox);
    else
        imshow(A);
    end
    hold on

```

```

        plot(center.x-X,center.y-Y,'y-', 'linewidth',1);
        if Shadowgraphy == false
            text(center.x + radius,center.y,[num2str(data(x,7)*100,'%1f')
            '%'], 'HorizontalAlignment', 'left', 'Color', 'y');
        end
        try
            text(center.x + radius,center.y -
            10,num2str(data(x,9), '%.2f'), 'HorizontalAlignment', 'left', 'Color', 'r', 'FontWeight', 'bold');
        catch
            end
            %title(['Image ' num2str(x)], 'FontSize',16);
            title(['t = ' num2str(time) ' ms'], 'FontSize',16);
            export_fig([folder exportPath '\Tracking_' num2str(x) '.png']);
            close;
        end

        % Display progress in %
        Progress = round(x/numFiles*100)
    end

%% OUTPUT

% Create headlines for Excel export
titelsExcel = strings(1,9);
titelsExcel(1,1) = 'Time [ms]';
titelsExcel(1,2) = 'Diameter [px]';
titelsExcel(1,3) = 'Center X [px]';
titelsExcel(1,4) = 'Center Y [px]';
titelsExcel(1,5) = 'Errorbar Negative [mm]';
titelsExcel(1,6) = 'Diameter [mm]';
titelsExcel(1,7) = 'Filling Level [0-1]';
titelsExcel(1,8) = 'Pixel Sum Diameter [mm]';
titelsExcel(1,9) = 'Droplet-Shape Ratio';

% Export all data & clear data to get 1 kHz resolution (every full ms)
dataCut = data;

if floor(StartTime) == StartTime
    for i = 2:2:length(dataCut)
        dataCut(i,:) = NaN;
    end
else
    for i = 3:2:length(dataCut)
        dataCut(i,:) = NaN;
    end
end

% Clear all NaN rows
data = data(all(~isnan(data),2),:);
dataCut = dataCut(all(~isnan(dataCut),2),:);

% Convert data to cell array & insert headlines
dataExcel = cell(size(data));
dataExcel(1,:) = cellstr(titelsExcel);
dataExcel(2:end+1,:) = num2cell(data);

dataCutExcel = cell(size(dataCut));
dataCutExcel(1,:) = cellstr(titelsExcel);
dataCutExcel(2:end+1,:) = num2cell(dataCut);

% Safe results
writecell(dataExcel,[folder exportPath '\Regression.xlsx'],'Sheet','Regression - Full');
csvwrite([folder exportPath '\Regression.txt'], data);

end

```

### Function: circle\_hough [200]:

```

function [h, margin] = circle_hough(b, rrange, varargin)
% CIRCLE_HOUGH Hough transform for circles

% Copyright David Young 2008, 2010

% argument checking
opts = {'same' 'normalise'};
narginchk(2, 2+length(opts));
validateattributes(rrange, {'double'}, {'real' 'positive' 'vector'});
if ~all(ismember(varargin, opts))
    error('Unrecognised option');
end

```

```

end

% get indices of non-zero features of b
[featR, featC] = find(b);

% set up accumulator array - with a margin to avoid need for bounds checking
[nr, nc] = size(b);
nradii = length(rrange);
margin = ceil(max(rrange));
nrh = nr + 2*margin; % increase size of accumulator
nch = nc + 2*margin;
h = zeros(nrh*nch*nradii, 1, 'uint32'); % 1-D for now, uint32 a touch faster

% get templates for circles at all radii - these specify accumulator
% elements to increment relative to a given feature
tempR = []; tempC = []; tempRad = [];
for i = 1:nradii
    [tR, tC] = circlepoints(rrange(i));
    tempR = [tempR tR]; %#ok<*AGROW>
    tempC = [tempC tC];
    tempRad = [tempRad repmat(i, 1, length(tR))];
end

% Convert offsets into linear indices into h - this is similar to sub2ind.
% Take care to avoid negative elements in either of these so can use
% uint32, which speeds up processing by a factor of more than 3 (in version
% 7.5.0.342)!
tempInd = uint32( tempR+margin + nrh*(tempC+margin) + nrh*nch*(tempRad-1) );
featInd = uint32( featR' + nrh*(featC-1)' );

% Loop over features
for f = featInd
    % shift template to be centred on this feature
    incI = tempInd + f;
    % and update the accumulator
    h(incI) = h(incI) + 1;
end

% Reshape h, convert to double, and apply options
h = reshape(double(h), nrh, nch, nradii);

if ismember('same', varargin)
    h = h(1+margin:end-margin, 1+margin:end-margin, :);
    margin = 0;
end

if ismember('normalise', varargin)
    h = bsxfun(@divide, h, reshape(rrange, 1, 1, length(rrange)));
end

end

```

### Function: dropletLines\_v3:

```

function
[longestLength,shortestLength,centerPolyX,centerPolyY,positionLongRot1,positionLongRot2,positionShortRot1,positionShortRot2] = dropletLines_v3(actualArea)

% Detect center of droplet
regionArea = ~actualArea;
regionArea = regionprops(regionArea);
centerPolyX = round(regionArea.Centroid(1));
centerPolyY = round(regionArea.Centroid(2));

% Loop for angle variation
for angle = 0:1:180

    % Rotate image
    rotArea = rotateAround(actualArea,centerPolyY,centerPolyX,angle);

    % Define longest positions
    longestPosition(1) = 0;
    for horizontal = centerPolyX:-1:1
        if rotArea(centerPolyY,horizontal) == 1
            longestPosition(1) = horizontal + 1;
            break;
        end
    end
    longestPosition(2) = 0;
    for horizontal = centerPolyX:size(rotArea,2)
        if rotArea(centerPolyY,horizontal) == 1
            longestPosition(2) = horizontal - 1;
        end
    end
end

```

```

        break;
    end
end

% Define shortest positions
shortestPosition(1) = 0;
for vertical = centerPolyY:-1:1
    if rotArea(vertical,centerPolyX) == 1
        shortestPosition(1) = vertical + 1;
        break;
    end
end
shortestPosition(2) = 0;
for vertical = centerPolyY:size(rotArea,1)
    if rotArea(vertical,centerPolyX) == 1
        shortestPosition(2) = vertical - 1;
        break;
    end
end

% Check if new angle is longer/shorter than before
if angle > 0
    if longestPosition(2) - longestPosition(1) + 1 > longestLength
        longestLength = longestPosition(2) - longestPosition(1);
        angleLong = angle;
        positionLong = longestPosition;
    end

    if shortestPosition(2) - shortestPosition(1) + 1 < shortestLength
        shortestLength = shortestPosition(2) - shortestPosition(1) + 2;
        angleShort = angle;
        positionShort = shortestPosition;
    end
else
    % Data at first angle
    longestLength = longestPosition(2) - longestPosition(1);
    shortestLength = shortestPosition(2) - shortestPosition(1) + 2;
    angleLong = angle;
    angleShort = angle;
    positionLong = longestPosition;
    positionShort = shortestPosition;
end
end

% Calculation of longest/shortest end points in original coordinate system
centerPoly = [centerPolyY,centerPolyX];
positionLongRot1 = round([centerPolyY,positionLong(1)] - centerPoly) * [cosd(angleLong),-
sind(angleLong);sind(angleLong),cosd(angleLong)] + centerPoly;
positionLongRot2 = round([centerPolyY,positionLong(2)] - centerPoly) * [cosd(angleLong),-
sind(angleLong);sind(angleLong),cosd(angleLong)] + centerPoly;
positionShortRot1 = round([positionShort(1),centerPolyX] - centerPoly) * [cosd(angleShort),-
sind(angleShort);sind(angleShort),cosd(angleShort)] + centerPoly;
positionShortRot2 = round([positionShort(2),centerPolyX] - centerPoly) * [cosd(angleShort),-
sind(angleShort);sind(angleShort),cosd(angleShort)] + centerPoly;
end

```

H. Test matrix

**Table 10:** Test matrix of experiments evaluated in this thesis.

$p$ [MPa]	$p_r$	Complete combustion				Combustion after droplet detachment								
		Width	Droplet size [mm]	$\tau_g$ [ms]	$k_g$ [mm <sup>2</sup> /s] Value Error	$d_0$ [mm]	$\tau_g$ [ms]	$k_g$ [mm <sup>2</sup> /s] Value Error (-/+)	$f/d$ Value Error					
0.10	0.02	0.88	1.27	0.91	136.5	6.12	±0.02	0.68	86.5	5.36	-0.33	0.24	2.84	±0.29
0.20	0.04	0.75	1.10	0.74	86.5	6.29	±0.04	0.57	59.0	5.53	-0.17	0.23	2.80	±0.19
0.18	0.03	0.69	1.03	0.64	67.0	6.19	±0.05	0.47	43.0	5.09	-0.41	0.05	2.70	±0.22
0.32	0.06	0.77	1.11	0.75	98.0	5.72	±0.03	0.61	70.5	5.33	-0.04	0.03	2.90	±0.11
0.46	0.09	0.73	1.07	0.69	87.0	5.43	±0.03	0.57	59.5	5.54	-0.23	0.17	3.11	±0.28
0.76	0.15	0.87	1.22	0.87	129.5	5.90	±0.02	0.70	89.5	5.40	-0.03	0.26	2.66	±0.12
0.83	0.16	0.74	1.07	0.70	91.5	5.36	±0.03	0.57	67.5	4.89	-0.20	0.31	2.37	±0.06
1.10	0.22	0.66	1.00	0.59	67.5	5.24	±0.04	0.50	52.5	4.75	-0.03	0.06	2.78	±0.05
1.20	0.24	0.67	1.02	0.61	66.0	5.67	±0.04	0.47	47.0	4.64	-0.04	0.06	2.61	±0.08
1.54	0.31	0.65	0.99	0.58	59.0	5.62	±0.05	0.44	39.5	4.85	-0.11	0.06	2.79	±0.17
1.99	0.40	0.69	1.04	0.64	73.5	5.65	±0.04	0.45	39.0	5.26	-0.09	0.07	2.25	±0.07
1.97	0.39	0.71	1.06	0.67	82.0	5.53	±0.03	0.53	54.0	5.21	-0.05	0.09	2.35	±0.08
3.15	0.62	0.73	1.07	0.69	71.5	6.61	±0.05	0.53	46.0	6.14	-0.10	0.26	2.36	±0.06
4.12	0.82	0.73	1.07	0.69	68.0	6.95	±0.05	0.50	34.5	7.38	-0.25	0.11	2.35	±0.25
4.06	0.80	0.73	1.06	0.69	67.0	7.05	±0.05	0.50	34.0	7.30	-0.23	0.11	2.22	±0.22
4.51	0.90	0.93	1.20	0.92	81.0	10.49	±0.07	0.42	21.5	8.07	-0.31	0.39	2.50	±0.21
5.38	1.07	0.76	1.11	0.79	78.5	7.95	±0.05							
5.46	1.08	0.71	1.07	0.76	74.0	7.85	±0.05							
5.66	1.12	0.60	0.97	0.65	53.5	7.79	±0.07							

## I. Simplified vaporization model

A two-stage numerical simulation was performed to evaluate the concentration field around the LOX droplet before ignition. For this purpose, a simplified 2D model was developed using the ANSYS Fluent® 2021 R2 software package. The model represents the diffusion and convection processes in the gas phase around the droplet without including the actual vaporization process. Instead, the evolution of mass flow rate was determined from the diameter regression of a vaporization test under 1g conditions and 0.1 MPa as:

$$\dot{m}_{O_2}(t) = (-2.2997 * 10^{-10} \text{ kg/s}^2 * t + 2.0920 * 10^{-8} \text{ kg/s}) * 1500 \quad (70)$$

where a conversion factor of 1500 was used to transfer the 3D experimental results to the 2D model, which assumes a certain extension in the third dimension.

The mixing and transport of chemical species can be modeled by solving conservation equations that describe convection and diffusion for each species. For example, the local mass fractions of the species involved (oxygen and hydrogen) can be obtained by solving a convection-diffusion equation for  $i^{\text{th}}$  species. This mass conservation equation has the following general form [201]:

$$\frac{\partial}{\partial t}(\rho Y_i) + \nabla \cdot (\rho \vec{v} Y_i) = -\nabla \cdot \vec{j}_i + S_i \quad (71)$$

where  $Y_i$  is the mass fraction (of species  $i$ ) and  $S_i$  is the net rate of various sources. The diffusion flux is based on Fick's law as shown in Equation (1), and can be written as [201]:

$$\vec{j}_i = -\rho D_{m,i} \nabla Y_i \quad (72)$$

where  $D_{m,i}$  is the mass diffusion coefficient (for species  $i$ ). Since an isothermal temperature is assumed, thermal (Soret) diffusion effects are not considered.

The model represented a section of the combustion chamber with a width of 20 mm and a height of 50 mm around the droplet, which had a constant diameter of 1 mm. The boundary condition at the droplet surface was defined as a mass flow inlet with the experimentally determined mass flow rate, as shown in Equation (70). The single-phase domain was meshed with 4369 cells and is shown in Figure 124.

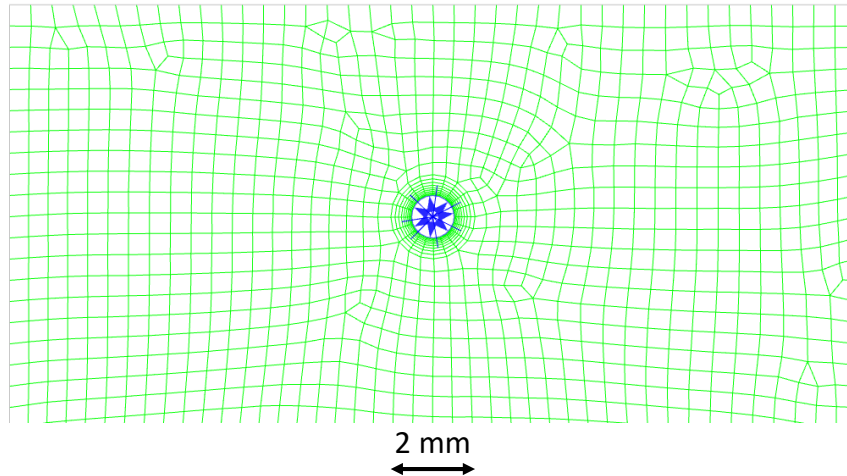


**Figure 124:** Numerical modeling of droplet vaporization. Upper section of the 2D mesh in ANSYS Fluent®.

The basic model settings and parameters used in the first step of the simulation for 1g conditions are shown in Table 11. Since this case can be assumed as isothermal (at 77 K) and isobaric (at 0.1 MPa), the specific material properties for hydrogen and oxygen were used as constants from the NIST Chemistry WebBook [37]. The process was first simulated for 1 s under 1g conditions to represent droplet generation prior to the free-fall phase in the drop tower.

**Table 11:** Numerical modeling of droplet vaporization under 1g conditions. Basic model parameters in ANSYS Fluent®.

Settings	Parameter	Unit
<b>General:</b>		
Solver type	Density-based	-
Time	Transient	-
Gravitational acceleration (y-axis)	-9.81	m/s <sup>2</sup>
<b>Models:</b>		
Viscous model	Laminar	-
Species model	Species transport with thermal diffusion	-
Number of volumetric species	2	-
Mixture density model	Ideal gas	-
Specific heat model	Mixing law	-
Thermal conductivity model	Ideal gas mixing law	-
Viscosity model	Ideal gas mixing law	-
Mass diffusivity	$6.8073 \times 10^{-6}$	m <sup>2</sup> /s
Thermal diffusion coefficient model	Kinetic theory	-

Settings	Parameter	Unit
<b>Boundary condition droplet:</b>		
Mass flow specification method	Mass flow rate: Equation (70)	-
Initial gauge pressure	0	
Direction specification method	Normal to boundary	Pa
Total temperature	77	K
Species mass fraction O <sub>2</sub>	1	-
<b>Boundary condition wall:</b>		
Wall motion	Stationary wall	-
Shear condition	No slip	-
Temperature	77	K
Species mass fraction O <sub>2</sub>	0	-
<b>Convergence criteria:</b>		
Continuity	$1.0 \times 10^{-4}$	-
X-velocity	$1.0 \times 10^{-5}$	-
Y-velocity	$1.0 \times 10^{-5}$	-
Energy	$5.0 \times 10^{-4}$	-
O <sub>2</sub>	$1.0 \times 10^{-5}$	-
<b>Initialization:</b>		
Gauge pressure	100000	Pa
X-velocity	0	m/s
Y-velocity	0	m/s
O <sub>2</sub>	0	-
Temperature	77	K
<b>Calculation:</b>		
Fixed number of time steps	10	-
Time step size	0.1	s
Max. iterations per time step	2500	-

The results of the first step of the simulation under 1g conditions are shown in Figure 125. It should be noted that due to the strong simplification of the vaporization case, the model gives rather qualitative results. Nevertheless, the results can serve a better understanding as well as visualization of the concentration field around the droplet prior to ignition. Figure 125b displays the flow field around the vaporizing droplet. It is apparent that the oxygen vapor is accelerated downward, i.e., in the negative y-direction, due to the approximately 16 times higher density compared to the surrounding hydrogen. This convection flow is clearly visible in the flow field below the droplet.

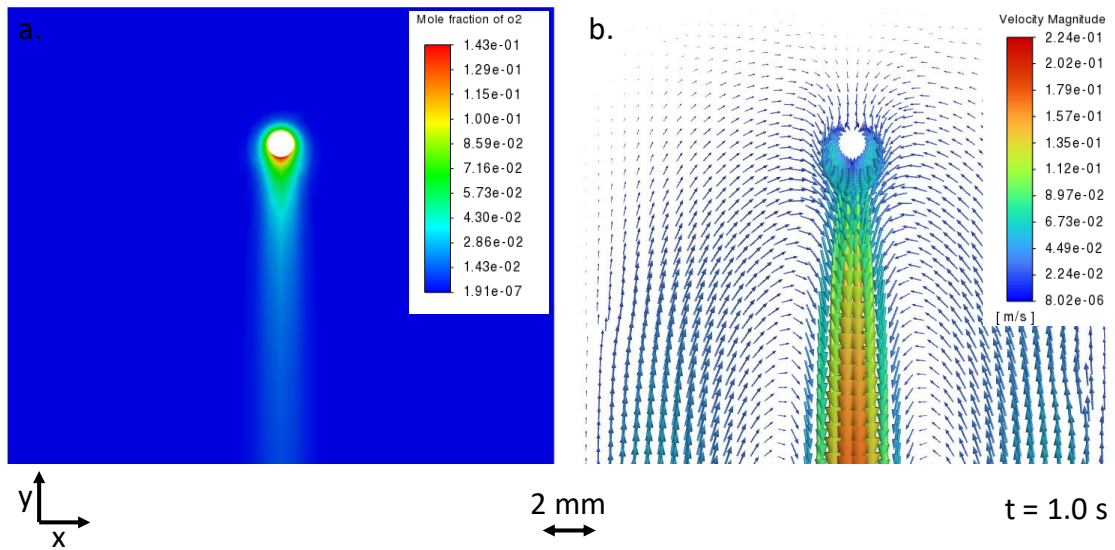


**Figure 125:** Numerical modeling of droplet vaporization under 1g conditions at 0.1 MPa in ANSYS Fluent®. a. Mole fraction of oxygen. b. Flow field. Only the upper section of the modeled domain is shown.

The concentration field, shown in Figure 125a, is strongly influenced by the convective flow and shows an accumulation of oxygen vapor below the droplet. In contrast, there is a steep concentration gradient above or to the side of the droplet, which causes oxygen vapor to accumulate only very close to the droplet surface. In the second step of the simulation, some parameters of the model were changed, as shown in Table 12. First, the gravitational acceleration along the y-axis was set to zero to match the  $\mu g$  case. The results of the first simulation step were taken as the initial conditions and the flow time was reduced to 0.3 s. This corresponds to the defined delay between the drop of the experiment in the drop tower and the laser ignition and a total time of 1.3 s.

**Table 12:** Numerical modeling of droplet vaporization under  $\mu g$  conditions on the basis of the simulation result under 1g conditions. Changed basic model parameters in ANSYS Fluent®.

Settings	Parameter	Unit
<b>General:</b>		
Gravitational acceleration (y-axis)	0	m/s <sup>2</sup>
<b>Initialization:</b>		
Initial conditions	1g simulation results	-
<b>Calculation:</b>		
Fixed number of time steps	3	-

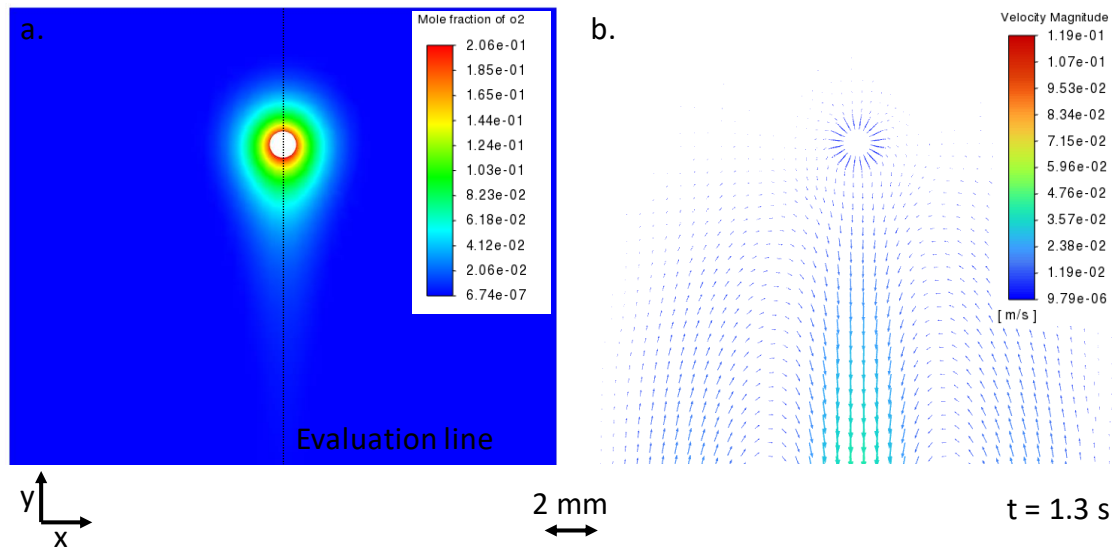


**Figure 126:** Numerical modeling of droplet vaporization under  $\mu\text{g}$  conditions on the basis of the simulation result under 1g conditions at 0.1 MPa in ANSYS Fluent<sup>®</sup>. a. Mole fraction of oxygen. b. Flow field. Only the upper section of the modeled domain is shown. Vertical line indicating the evaluation line.

The flow and the concentration field around the droplet, as shown in Figure 126, have become significantly more spherical in the simulated flow time of 0.3 s under  $\mu\text{g}$  conditions. Nevertheless, the influence of the vaporization under 1g conditions can still be seen, both in the flow and the concentration field. The concentration profile along the evaluation line (y-axis) is shown in Figure 127 and indicates a maximum oxygen vapor concentration of 20.6 % at the droplet surface. In the real system, the oxygen partial pressure in the gas phase can theoretically rise to a maximum of the vapor pressure, at which the gaseous state is in thermodynamic equilibrium with the liquid state. To calculate the vapor pressure, Equation (16) can be used. At an ambient pressure of 0.1 MPa and at a temperature of 77 K, the vapor pressure is 0.0196 MPa. In relation to the total pressure, this results in an oxygen saturation concentration of 19.6 %. Thus, the numerical simulation slightly overestimated the maximum oxygen vapor concentration. This is due to the fact that the vaporization of the droplet was only represented in a very simplified way and no real vaporization model was included. However, for the purpose of the (qualitative) visualization of the concentration field for the investigation of the ignitability of the gas mixture around the droplet, these simplified results are still applicable.

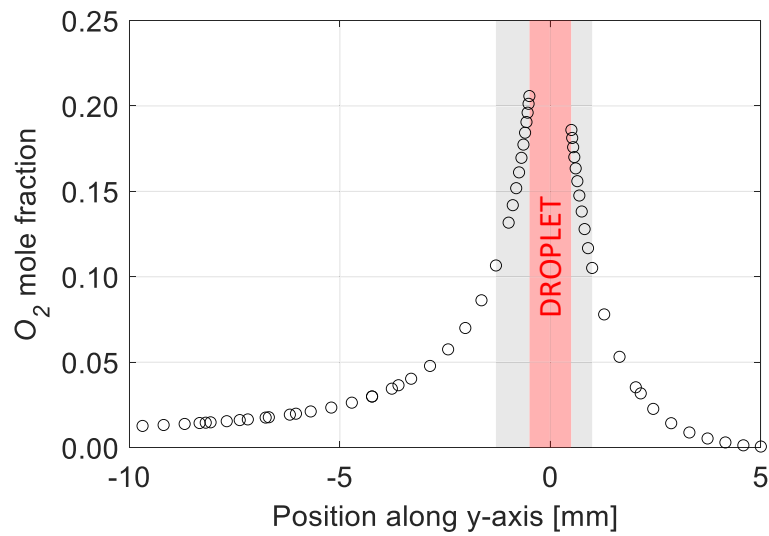


**Figure 127:** Numerical modeling of droplet vaporization under  $\mu\text{g}$  conditions on the basis of the simulation result under 1g conditions at 0.1 MPa in ANSYS Fluent<sup>®</sup>. Oxygen mole fraction evolution along the y-axis (evaluation line). Negative positions values indicate positions on the y-axis below the droplet and positive position values indicate positions on the y-axis above the droplet. Gray sections indicate area around droplet with oxygen mole fraction  $> 0.1$ .

**J. Droplet regression plots**

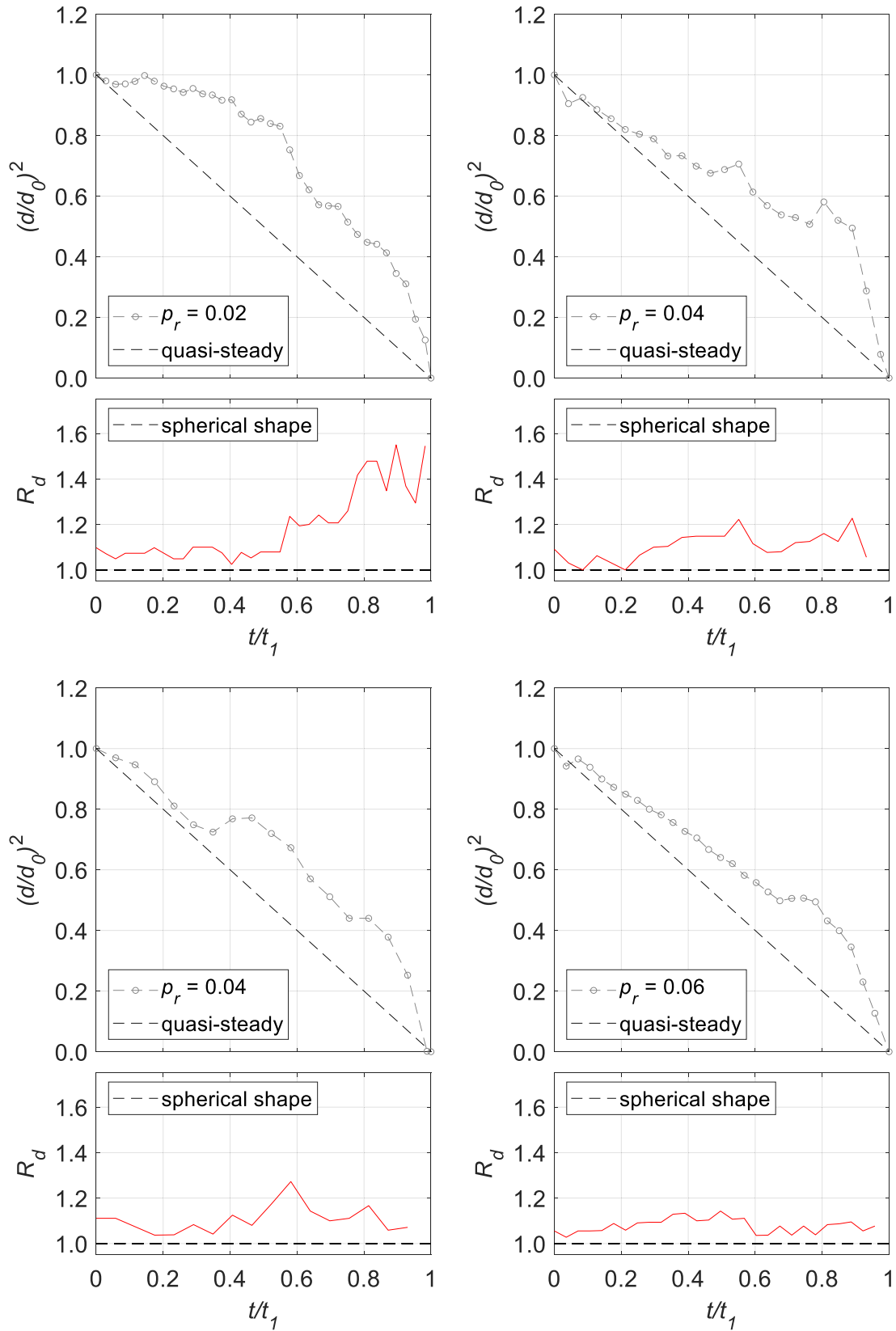


**Figure 128:** Dimensionless time evolution of dimensionless droplet diameter (top) and droplet shape ratio  $R$  (bottom) for combustions between  $0.02 \leq p_r \leq 0.06$ .

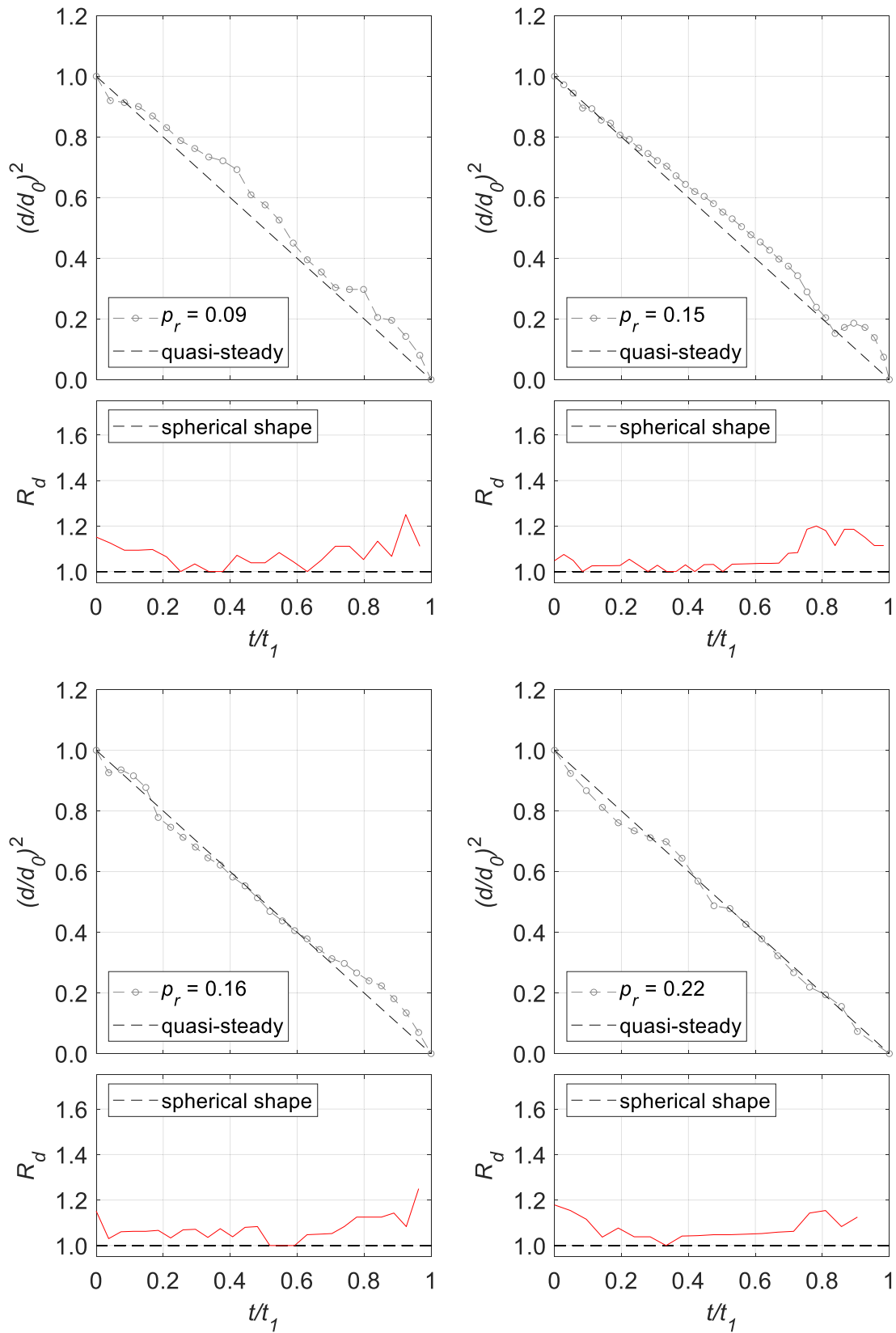


**Figure 129:** Dimensionless time evolution of dimensionless droplet diameter (top) and droplet shape ratio  $R$  (bottom) for combustions between  $0.09 \leq p_r \leq 0.22$ .

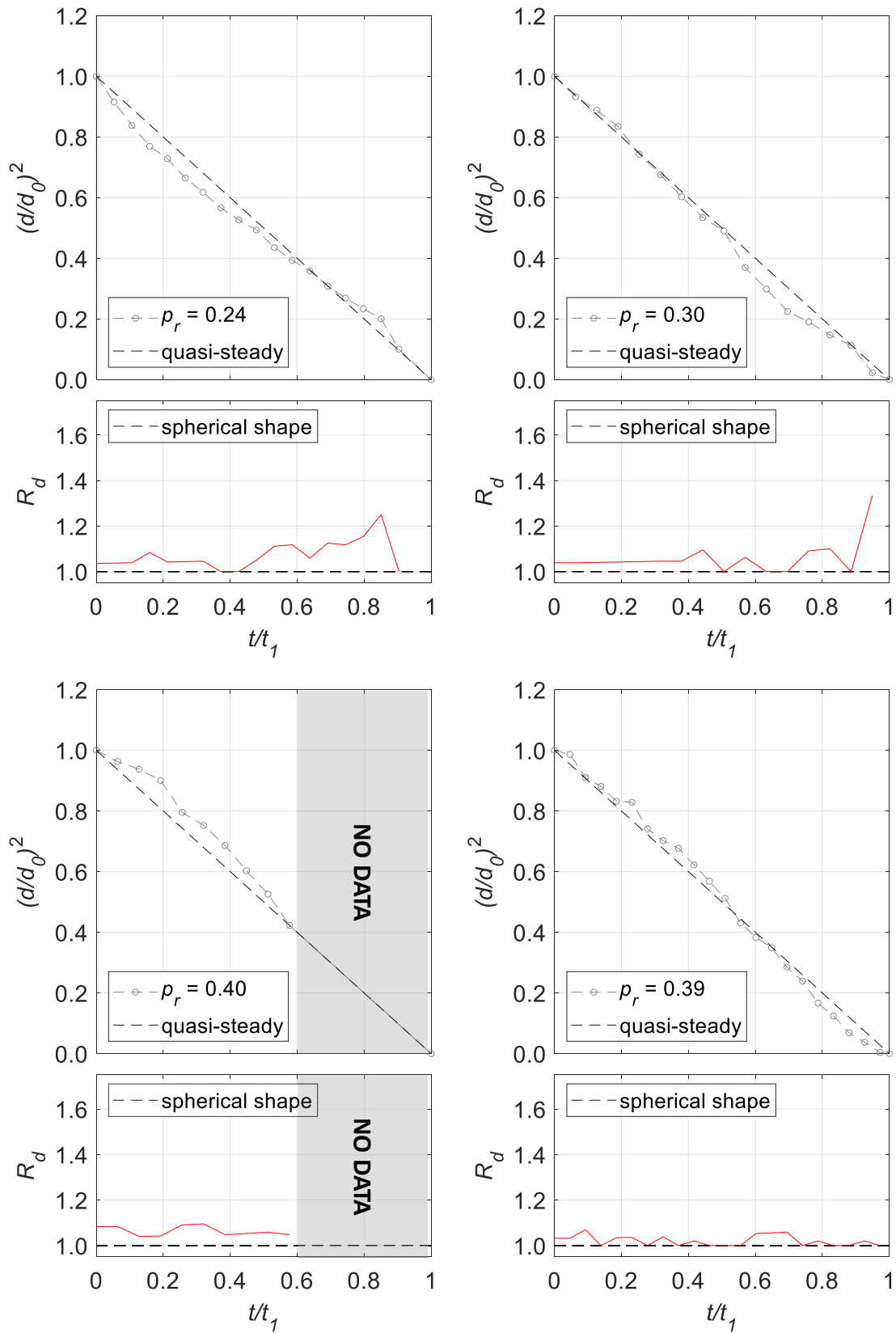


**Figure 130:** Dimensionless time evolution of dimensionless droplet diameter (top) and droplet shape ratio  $R$  (bottom) for combustions between  $0.24 \leq p_r \leq 0.39$ .

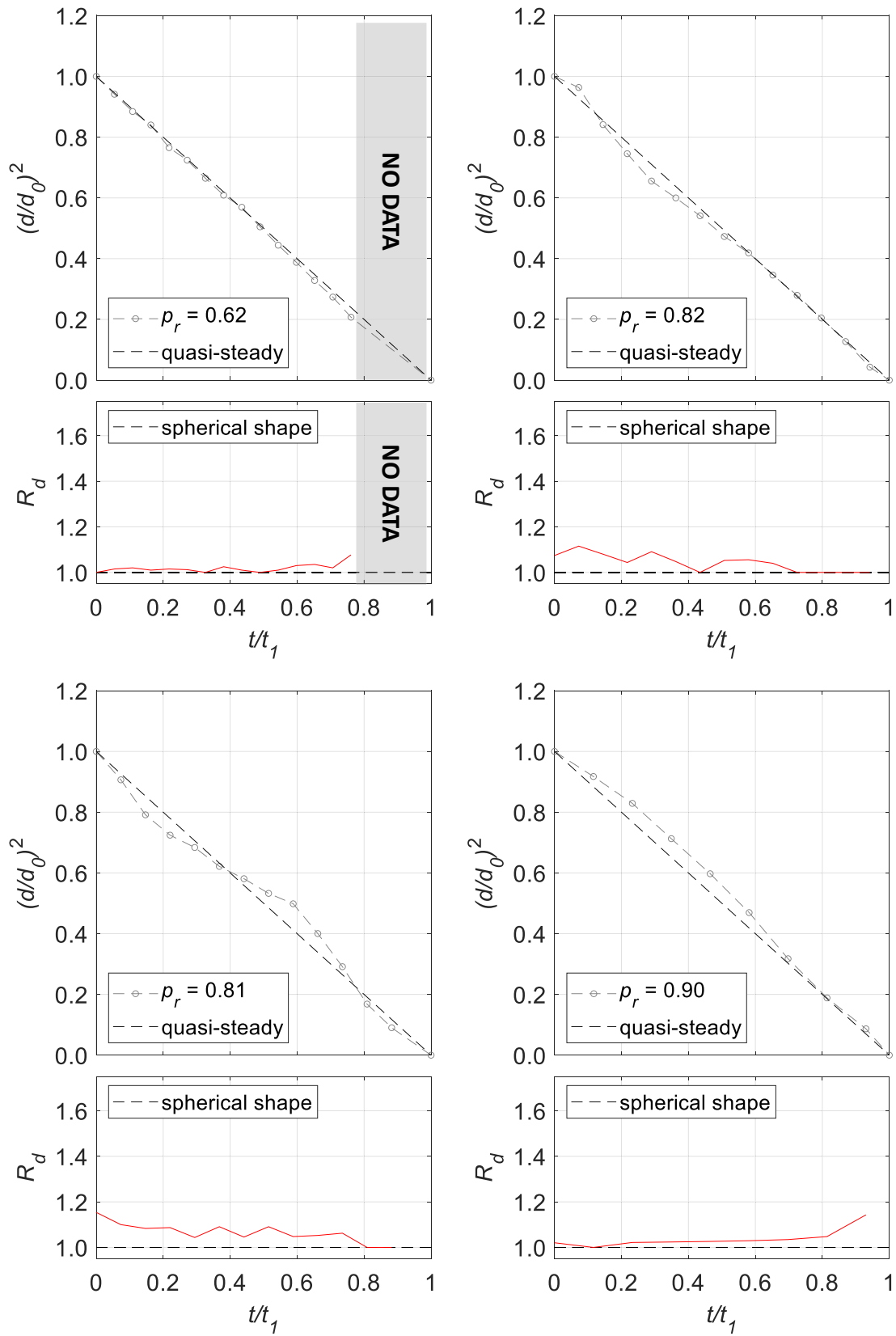


**Figure 131:** Dimensionless time evolution of dimensionless droplet diameter (top) and droplet shape ratio  $R$  (bottom) for combustions between  $0.62 \leq p_r \leq 0.90$ .

## K. Flame regression and flame standoff ratio plots

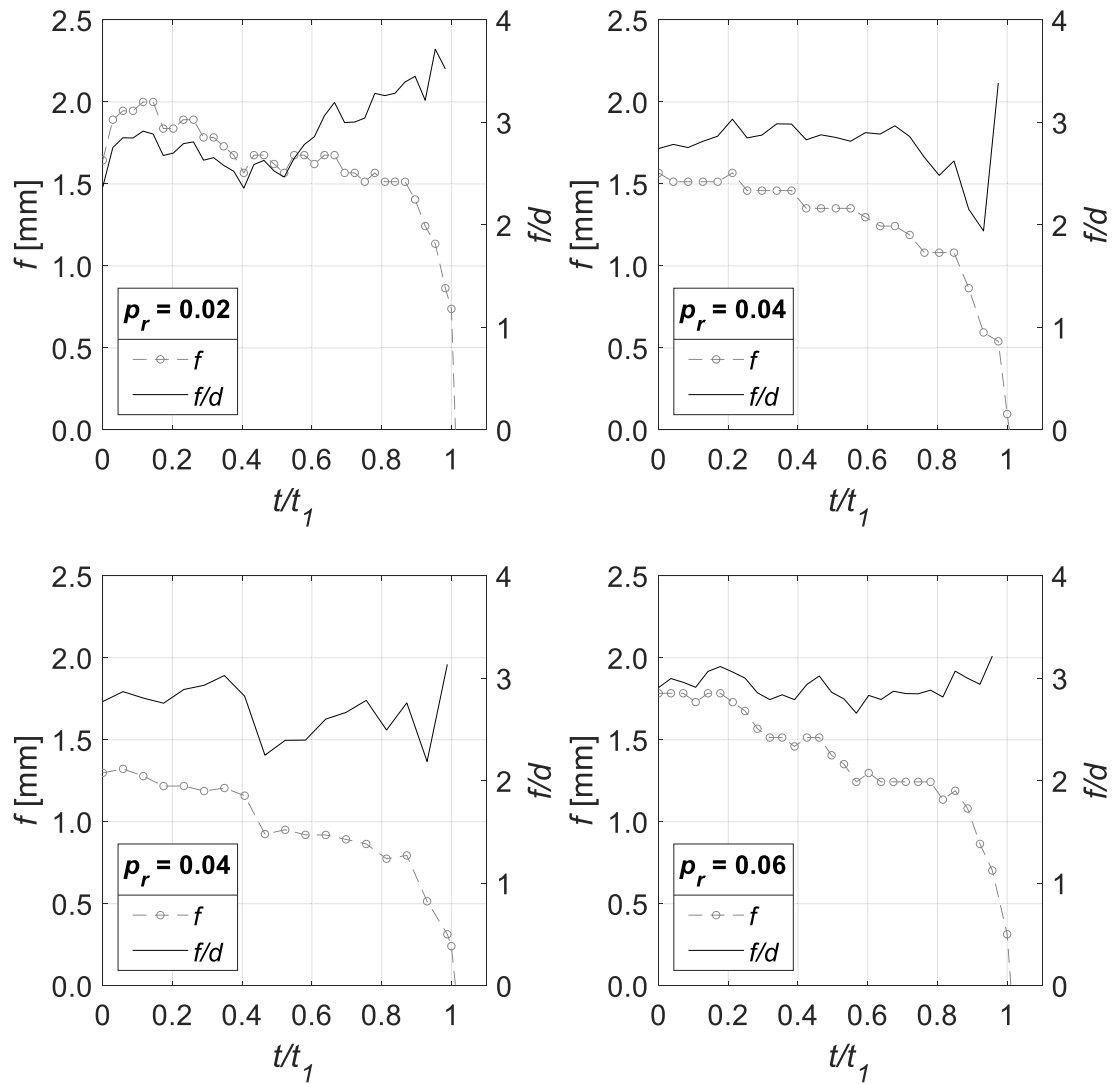


**Figure 132:** Dimensionless time evolution of measured flame diameter  $f$  and calculated flame standoff ratio  $f/d$  for combustions between  $0.02 \leq p_r \leq 0.06$ .

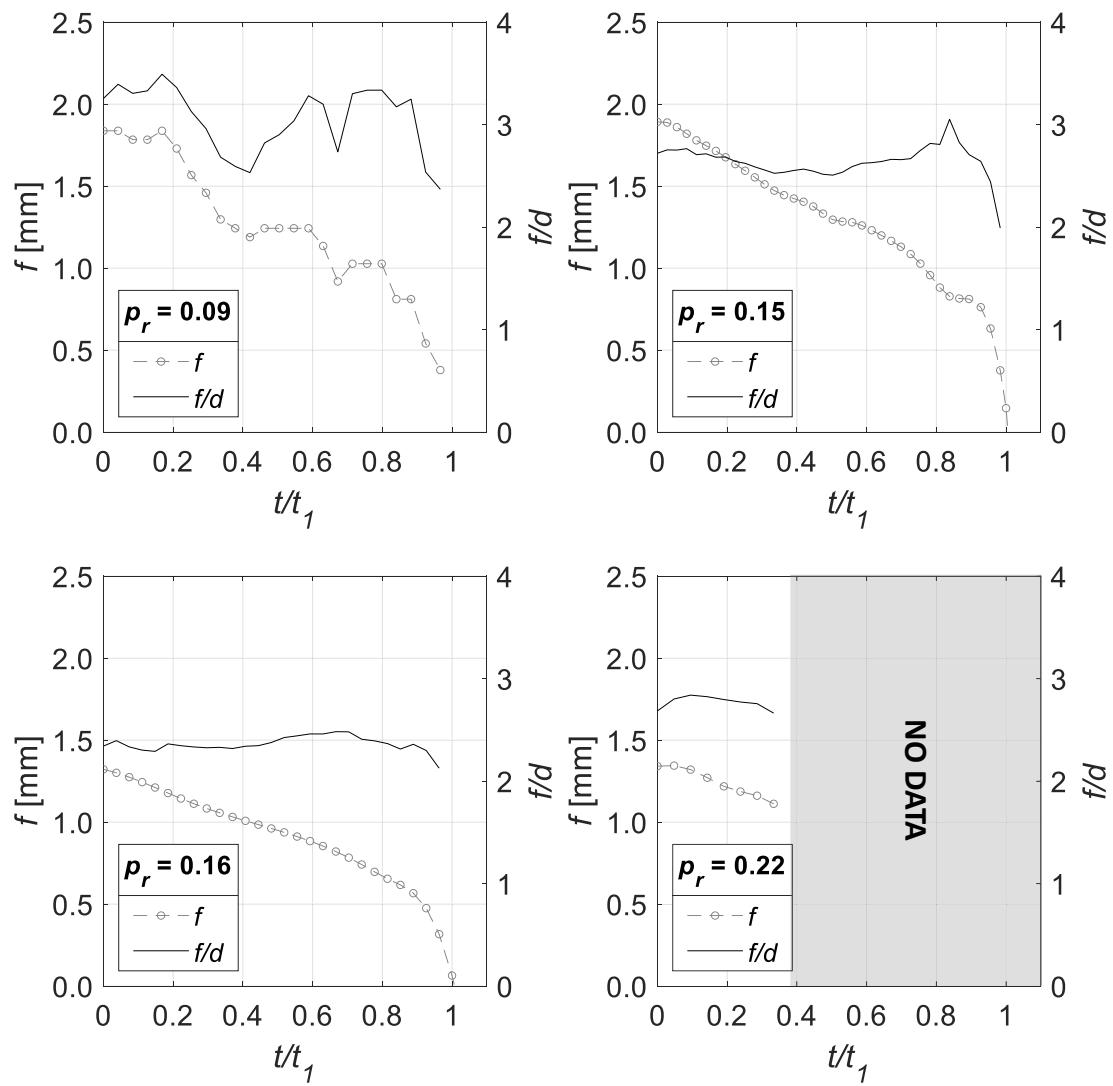


**Figure 133:** Dimensionless time evolution of measured flame diameter  $f$  and calculated flame standoff ratio  $f/d$  for combustions between  $0.09 \leq p_r \leq 0.22$ .

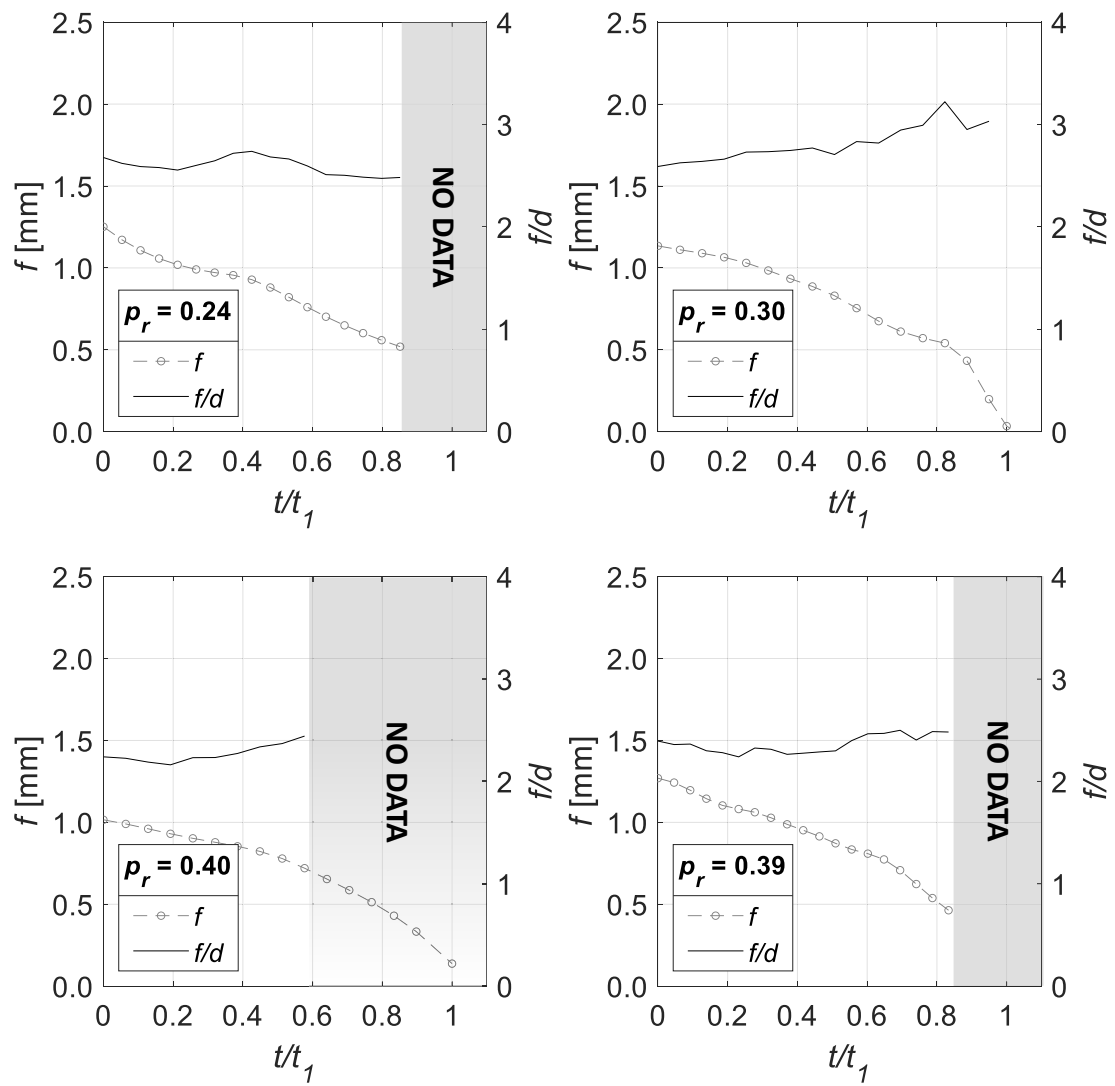


**Figure 134:** Dimensionless time evolution of measured flame diameter  $f$  and calculated flame standoff ratio  $f/d$  for combustions between  $0.24 \leq p_r \leq 0.39$ .

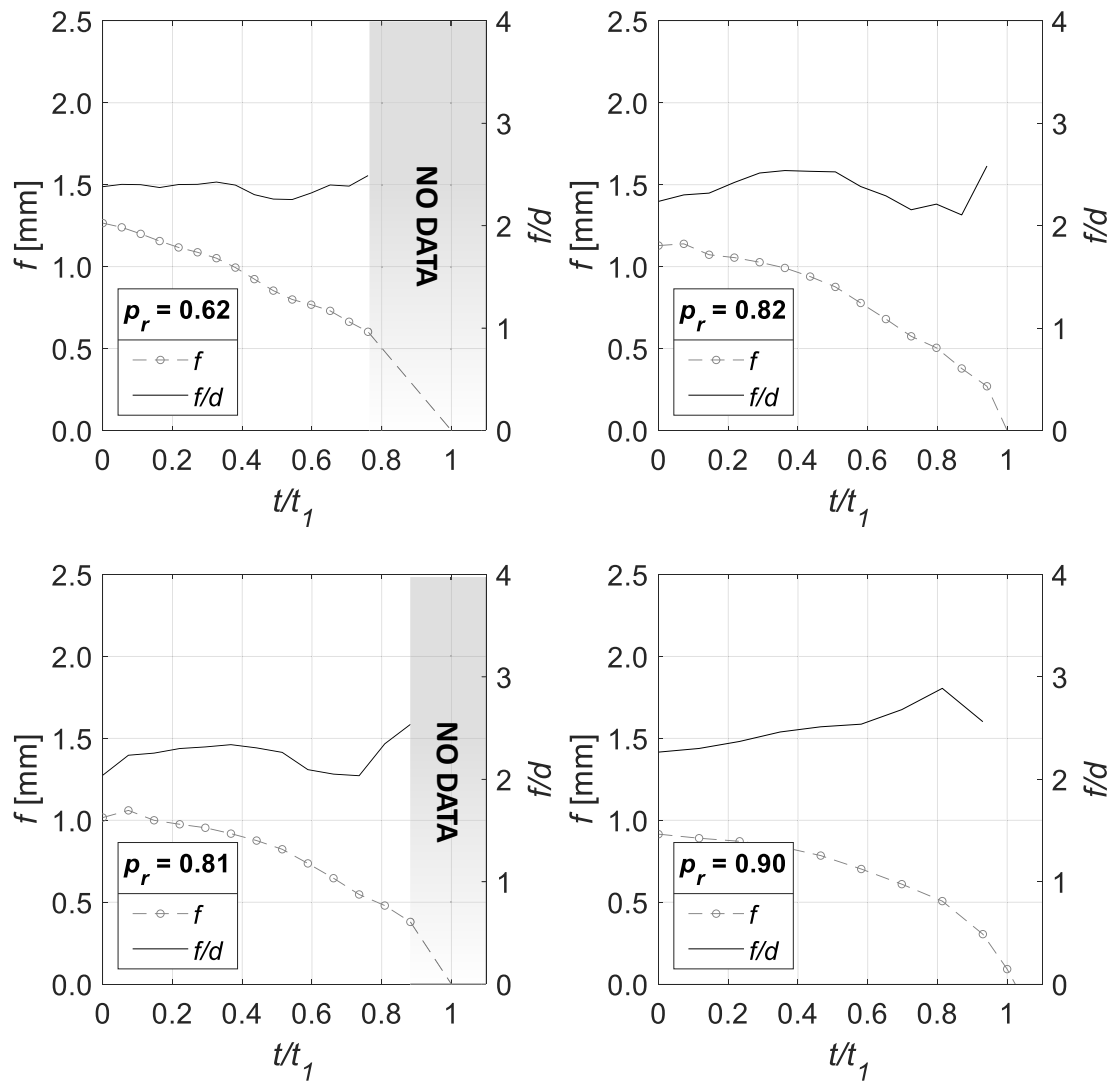


**Figure 135:** Dimensionless time evolution of measured flame diameter  $f$  and calculated flame standoff ratio  $f/d$  for combustions between  $0.62 \leq p_r \leq 0.90$ .